

VOLUME 80

AUGUST 26, 1976

NUMBER 18

JPCHAX

THE JOURNAL OF
PHYSICAL
CHEMISTRY



PUBLISHED BIWEEKLY BY THE AMERICAN CHEMICAL SOCIETY

THE JOURNAL OF PHYSICAL CHEMISTRY

BRYCE CRAWFORD, Jr., *Editor*
STEPHEN PRAGER, *Associate Editor*
ROBERT W. CARR, Jr., **FREDERIC A. VAN-CATLEDGE**, *Assistant Editors*

EDITORIAL BOARD: C. A. ANGELL (1973-1977), F. C. ANSON (1974-1978), V. A. BLOOMFIELD (1974-1978), J. R. BOLTON (1976-1980), L. M. DORFMAN (1974-1978), H. L. FRIEDMAN (1975-1979), H. L. FRISCH (1976-1980), W. A. GODDARD (1976-1980), E. J. HART (1975-1979), W. J. KAUZMANN (1974-1978), R. L. KAY (1972-1976), D. W. McCLURE (1974-1978), R. M. NOYES (1973-1977), W. B. PERSON (1976-1980), J. C. POLANYI (1976-1980), S. A. RICE (1976-1980), F. S. ROWLAND (1973-1977), R. L. SCOTT (1973-1977), W. A. STEELE (1976-1980), J. B. STOTHERS (1974-1978), W. A. ZISMAN (1972-1976)

Published by the
AMERICAN CHEMICAL SOCIETY
BOOKS AND JOURNALS DIVISION
D. H. Michael Bowen, *Director*

Editorial Department: **Charles R. Bertsch**,
Head; **Marianne C. Brogan**, *Associate*
Head; **Celia B. McFarland**, **Joseph E.**
Yurvati, *Assistant Editors*

Graphics and Production Department:
Bacil Guiley, Head

Research and Development Department:
Seldon W. Terrant, Head

Advertising Office: Centcom, Ltd., 50 W.
State St., Westport, Conn. 06880.

© Copyright, 1976, by the American
Chemical Society. No part of this publica-
tion may be reproduced in any form with-
out permission in writing from the Ameri-
can Chemical Society.

Published biweekly by the American
Chemical Society at 20th and Northamp-
ton Sts., Easton, Pennsylvania 18042. Sec-
ond class postage paid at Washington, D.C.
and at additional mailing offices.

Editorial Information

Instructions for authors are printed in
the first issue of each volume. Please con-
form to these instructions when submitting
manuscripts.

Manuscripts for publication should be
submitted to *The Journal of Physical*
Chemistry, Department of Chemistry, Uni-
versity of Minnesota, Minneapolis, Minn.
55455. Correspondence regarding **accepted**
papers and proofs should be directed to
the Editorial Department at the ACS East-
on address.

Page charges of \$60.00 per page are as-
sessed for papers published in this journal.
Ability to pay does not affect acceptance or
scheduling of papers.

Bulk reprints or photocopies of indi-
vidual articles are available. For informa-
tion write to Business Operations, Books
and Journals Division at the ACS Wash-
ington address.

Requests for **permission to reprint**
should be directed to Permissions, Books
and Journals Division at the ACS Wash-
ington address. The American Chemical
Society and its Editors assume no responsi-
bility for the statements and opinions ad-
vanced by contributors.

Subscription and Business Information

1976 Subscription rates—including sur-
face postage

	U.S.	PUAS	Canada, Foreign
Member	\$24.00	\$29.75	\$30.25
Nonmember	96.00	101.75	102.25
Supplementary material	15.00	19.00	20.00

Air mail and air freight rates are avail-
able from Membership & Subscription Ser-
vices, at the ACS Columbus address.

New and renewal subscriptions
should be sent with payment to the Office
of the Controller at the ACS Washington
address. **Changes of address** must include
both old and new addresses with ZIP code
and a recent mailing label. Send all address
changes to the ACS Columbus address. Please
allow six weeks for change to become effec-
tive. **Claims** for missing num-
bers will not be allowed if loss was due to
failure of notice of change of address to be
received in the time specified; if claim is

dated (a) North America—more than 90
days beyond issue date, (b) all other for-
eign—more than 1 year beyond issue date;
or if the reason given is "missing from
files". Hard copy claims are handled at the
ACS Columbus address.

Microfiche subscriptions are available
at the same rates but are mailed first class
to U.S. subscribers, air mail to the rest of
the world. Direct all inquiries to Business
Operations, Books and Journals Division,
at the ACS Washington address or call
(202) 872-4444. **Single issues** in hard copy
and/or microfiche are available from Spe-
cial Issues Sales at the ACS Washington
address. Current year \$4.75. Back issue
rates available from Special Issues Sales.
Back volumes are available in hard copy
and/or microform. Write to Special Issues
Sales at the ACS Washington address for
further information. **Microfilm** editions of
ACS periodical publications are available
from volume 1 to the present. For further
information, contact Special Issues Sales at
the ACS Washington address. **Supplemen-
tary material** must be ordered directly
from Business Operations, Books and Jour-
nals Division, at the ACS Washington ad-
dress.

	U.S.	PUAS, Canada	Other Foreign
Microfiche			
Photocopy	\$2.50	\$3.00	\$3.50
1-7 pages	4.00	5.50	7.00
8-20 pages	5.00	6.50	8.00

Orders over 20 pages are available only on
microfiche, 4 × 6 in., 24X, negative, silver
halide. Orders must state photocopy or mi-
crofiche if both are available. Full biblio-
graphic citation including names of all au-
thors and prepayment are required. Prices
are subject to change.

American Chemical Society
1155 16th Street, N.W.
Washington, D.C. 20036
(202) 872-4600

Member & Subscription Services
American Chemical Society
P.O. Box 3337
Columbus, Ohio 43210
(614) 421-7230

Editorial Department
American Chemical Society
20th and Northampton Sts.
Easton, Pennsylvania 18042
(215) 258-9111

THE JOURNAL OF
PHYSICAL CHEMISTRY

Volume 80, Number 18 August 26, 1976

JPCHAx 80(18) 1955-2048 (1976)

ISSN 0022-3654

Production of NO($A^2\Sigma^+, \nu = 0$) by Electronic Energy Transfer between Cd(1P_1) and NO($X^2\Pi$)	W. H. Breckenridge* and John FitzPatrick	1955
Near-Resonant Electronic Energy Transfer between Zn(1P_1) and NO($X^2\Pi$)	W. H. Breckenridge,* R. P. Blickensderfer, and John FitzPatrick	1963
Mechanism of the Formation of Cationic Species in the Radiolysis of Butyl Chlorides. 1.	Shigeyoshi Arai,* Akira Kira, and Masashi Imamura	1968
Dielectric Increments and the Conformations of Amino Acids and Betaines in Water	J. Kirchnerova, P. G. Farrell,* and J. T. Edward	1974
Allowance for Composition Dependence of Activity Coefficients in the Analysis of Sedimentation Equilibrium Results Obtained with Heterogeneously Associating Systems	L. W. Nichol* and D. J. Winzor	1980
Micellar and Nonmicellar Association of Antiacetylcholine Drugs in Aqueous Solution	D. Attwood	1984
Correlation between Melting Points of Alkanoic Acids and Krafft Points of Their Sodium Salts	Kozo Shinoda,* Yutaka Minegishi, and Haruhiko Arai	1987
Study of Metal Oxide Catalysts by Temperature Programmed Desorption. 1. Chemisorption of Oxygen on Nickel Oxide	Masakazu Iwamoto, Yukihiro Yoda, Makoto Egashira, and Tetsuro Seiyama*	1989
Infrared Studies of Reactions on Oxide Surfaces. 5. Lewis Acid Sites on Dehydroxylated Silica	B. A. Morrow* and I. A. Cody	1995
Infrared Studies of Reactions on Oxide Surfaces. 6. Active Sites on Dehydroxylated Silica for the Chemisorption of Ammonia and Water	B. A. Morrow* and I. A. Cody	1998
Integrated Infrared Intensities and Effective Charges in Acetylene	G. B. Mast and W. T. King*	2004
Charge Transfer Band of the Benzyl Radical-Halide Ion Formed by Dissociative Electron Attachment to Benzyl Halides in a Rigid Organic Matrix	Masahiro Irie, Masaaki Shimizu, and Hiroshi Yoshida*	2008
An Electron Paramagnetic Resonance Study of the $H_2S_2^-$ Radical on Magnesium Oxide	M. J. Lin and J. H. Lunsford*	2015
Pulse Radiolysis and Electron Spin Resonance Studies of Nitroaromatic Radical Anions. Optical Absorption Spectra, Kinetics, and One-Electron Redox Potentials	P. Neta,* M. G. Simic, and M. Z. Hoffman*	2018
The Internal Chemical Shift—A Key to Bonding in Aromatic Molecules. 2. Substituent Effects on the Carbon-13 Magnetic Resonance Spectra of the 1,4-Disubstituted Benzenes	D. W. Beistel* and W. Dan Edwards	2023
Sedimentation Coefficient and X-Ray Scattering of a Double-Helical Model for Deoxyribonucleic Acid	J. Garcia de la Torre and Arturo Horta*	2028
A Peroxy Isomer of Nitrogen Dioxide	H. F. Schaefer, III, C. F. Bender, and J. H. Richardson*	2035

คลังข้อมูล มหาวิทยาลัยเกษตรศาสตร์

18 ต.ค. 2519

Theoretical Calculation of Strong Complex Formation by the HO ₂ Radical: HO ₂ -H ₂ O and HO ₂ -NH ₃	E. J. Hamilton, Jr.,* and C. A. Naleway	2037
Tracer Diffusion Coefficients of Counterions in Homo- and Heteroionic Poly(styrenesulfonate) Resins	R. Fernández-Prini* and Mario Philipp	2041

COMMUNICATIONS TO THE EDITOR

Multiplicity of the Reacting State in the Photoaddition of Carbon Tetrachloride to Anthracene	Felix A. Carroll* and David G. Whitten*	2046
Effect of Ring Closure on the Diamagnetic Susceptibility Contributions of Oxygen Atoms	R. R. Gupta	2047

There is no supplementary material for this issue.

* In papers with more than one author, the asterisk indicates the name of the author to whom inquiries about the paper should be addressed.

AUTHOR INDEX

Arai, H., 1987	Farrell, P. G., 1974	Kirchnerova, J., 1974	Richardson, J. H., 2035
Arai, S., 1968	Fernández-Prini, R., 2041	Lin, M. J., 2015	Schaefer, H. F., III, 2035
Attwood, D., 1984	FitzPatrick, J., 1955, 1963	Lunsford, J. H., 2015	Seiyama, T., 1989
Beistel, D. W., 2023	Garcia de la Torre, J., 2028	Mast, G. B., 2004	Shimizu, M., 2008
Bender, C. F., 2035	Gupta, R. R., 2047	Minegishi, Y., 1987	Shinoda, K., 1987
Blickensderfer, R. P., 1963	Hamilton, E. J., Jr., 2037	Morrow, B. A., 1995, 1998	Simic, M. G., 2018
Breckenridge, W. H., 1955, 1963	Hoffman, M. Z., 2018		
	Horta, A., 2028		
Carroll, F. A., 2046	Imamura, M., 1968	Naleway, C. A., 2037	Whitten, D. G., 2046
Cody, I. A., 1995, 1998	Irie, M., 2008	Neta, P., 2018	Winzor, D. J., 1980
	Iwamoto, M., 1989	Nichol, L. W., 1980	
Edward, J. T., 1974	King, W. T., 2004		
Edwards, W. D., 2023	Kira, A., 1968	Philipp, M., 2041	Yoda, Y., 1989
Egashira, M., 1989			Yoshida, H., 2008

THE JOURNAL OF PHYSICAL CHEMISTRY

Registered in U. S. Patent Office © Copyright, 1976, by the American Chemical Society

VOLUME 80, NUMBER 18 AUGUST 26, 1976

Production of NO(A $^2\Sigma^+$, $\nu = 0$) by Electronic Energy Transfer between Cd(1P_1) and NO(X $^2\Pi$)

W. H. Breckenridge*¹ and John FitzPatrick

Department of Chemistry, University of Utah, Salt Lake City, Utah 84112 (Received January 5, 1976)

Publication costs assisted by the Petroleum Research Fund

The following energy transfer reaction, even though $\sim 450\text{-cm}^{-1}$ endothermic, has been shown to occur readily: $\text{Cd}(^1P_1) + \text{NO}(X ^2\Pi) \rightarrow \text{Cd}(^1S_0) + \text{NO}(A ^2\Sigma^+, \nu = 0)$. The NO $\gamma(0,x)$ fluorescence bands are sensitized when Cd vapor and NO(X $^2\Pi$) in a flow tube at 290 °C are illuminated with 2288-Å cadmium resonance radiation. By using NO $\gamma(1,x)$ band fluorescence (excited by direct absorption of the 2144-Å Cd⁺ spectral line from the electrodeless discharge lamp) as an internal actinometric standard, the branching ratio for NO(A $^2\Sigma^+$, $\nu = 0$) production in the overall quenching was determined to be only ~ 0.04 . Measurements of the sensitized $\gamma(0,x)$ fluorescence intensity as a function of added NO and N₂ pressures have resulted in the determination of the absolute total cross section for quenching of Cd(1P_1) by NO(X $^2\Pi$): 92 Å². The energy-transfer cross section for the production of NO(A $^2\Sigma^+$, $\nu = 0$), 3.4 Å², is much larger than would be predicted for a transition dipole-dipole interaction mechanism, using the theory of Gordon and Chiu. Possible mechanisms and favored exit channels are discussed for the efficient collisional quenching of Cd(1P_1) by nitric oxide as well as by other molecules. Particular attention is given to the possibilities of strong long-range van der Waal's attractive forces as well as intersecting charge-transfer potential surfaces. The surprising general importance of spin-forbidden exit channels resulting in the production of Cd(3P_J) is noted, and it is suggested that Cd(3P_J) production may be the dominant exit channel in the quenching of Cd(1P_1) by NO(X $^2\Pi$), since there are no spin restrictions.

Introduction

Electronic energy transfer reactions have been studied with increasing interest in the past few years,²⁻¹¹ and are known to be important in such disparate areas as the dynamics of planetary atmospheres,¹² photochemical air pollution,¹³ combustion,¹⁴ trace-metal analysis,¹⁵ photosynthesis,¹⁶ and laser action.^{17,18} Fundamental studies by chemists and physicists are currently directed toward a more comprehensive understanding of the rates and the detailed collisional mechanisms of such reactions.^{2,3,10} There has been long-standing interest, for example, in near-resonant energy transfer, whereby an acceptor molecule has an electronic energy level which can be populated by collision with a donor species in an excited state of similar energy.^{3-5,7-10,19,20}

The photophysics of such transfer processes has been widely investigated for large organic molecules, particularly where transitions between ground and excited states of both donor and acceptor are allowed by optical selection rules, i.e., singlet-singlet energy transfer.^{3,10} Both a long-range transi-

tion-dipole (Förster)²⁰ mechanism and a shorter-range electron exchange (Dexter)¹⁹ mechanism are applicable in rigid media. Lin²¹ and Lee³ have derived the analogous theoretical expressions for Förster- and Dexter-type energy transfer in the gas phase, and Lee and co-workers,³ as well as others,¹⁰ are gathering extensive experimental evidence for both types of mechanisms.

Studies of electronic energy transfer between less complex species, such as excited atoms and/or diatomic molecules, have also been reported,^{4-9,11,22} but the collisional mechanisms responsible for such processes are not yet well established. The results of the elegant isotopic experiments of Melton and Klemperer⁵ on the electronic energy transfer between NO(A $^2\Sigma^+$) and NO(X $^2\Pi$) have been successfully interpreted by Gordon and Chiu²³ using a Förster-like dipole-dipole theory derived from a theoretical treatment of rotational energy transfer.²⁴ Fink, Wallach, and Moore⁴ have utilized a similar theory to explain the sudden rise in cross section for energy-transfer processes near resonance in the production of H₂(B $^1\Sigma_u^+$, ν', J') in the collisional deactivation of excited argon

atoms by H₂. Jones and Bayes,⁶ however, have shown that energy transfer between O₂(¹Δ_g) and O₂ occurs at nearly every collision, even though the metastability of the ¹Δ_g state rules out any dipole-dipole interaction, and suggest that an electron exchange mechanism may explain the results in the O₂ and perhaps even the NO case.

There are numerous cases of transfer of electronic energy from excited atoms to diatomic molecules in which pronounced resonance effects have not been observed,^{2,22} and potential-surface crossing mechanisms have sometimes been invoked.

Transfer of energy from the first singlet excited state of the cadmium atom, Cd(¹P₁), to NO(X ²Π) to produce NO(A ²Σ⁺, ν = 0) is within *kT* of exact resonance at ~550 K.²⁵ As part of continuing investigations of the rates and mechanisms of collisional electronic energy dissipation of the low-lying excited states of Hg, Cd, Zn, and Mg atoms,²⁶ we report here the detection of NO(A ²Σ⁺, ν = 0) produced in such a transfer process and a determination of the absolute cross section. It is shown that the cross section is considerably larger than would be predicted on the basis of the Gordon-Chiu dipole-dipole theory, but is nevertheless small compared to the overall cross section for deactivation of Cd(¹P₁) by NO.

Experimental Section

All measurements were conducted using a quartz flow tube which passed through a furnace (equipped with quartz access windows on the top and side for excitation and detection) maintained at 285–300 °C. The gas stream was saturated with cadmium vapor by passage over a Cd reservoir at the upstream end of the furnace. Gas pressures were measured using an oil manometer (Halocarbon Corp. Oil No. 13–21). Cadmium(¹P₁ → ¹S₀) resonance radiation at 2288 Å was generated by microwave discharge, at ~35 W net power, of sealed quartz tubes (~50 mm length, 9 mm o.d.) containing a few milligrams of cadmium metal (ROC/RIC Ultrapure, 99.9999%) and ~4 Torr of argon. Fluorescence from the flowing gas was collected with a quartz lens and dispersed onto Kodak 103a-0 plates using a Hilger medium quartz spectrograph. The plates were sensitized with sodium salicylate and prefogged to the linear region of plate response to increase sensitivity and facilitate quantitative measurements of relative fluorescence intensities. The plate response factors at the wavelengths used for NO γ-band fluorescence measurements were determined by measuring plate optical densities as a function of exposure time to continuous radiation from a deuterium discharge lamp. The intensity of the D₂ lamp was adjusted so that the exposure times for these measurements were comparable to the exposure times necessary to obtain NO γ bands at roughly equivalent plate density. Relative fluorescence intensity at a particular wavelength was obtained from plate optical density:

$$I_f = 10^{\Delta D/\sigma} - 1 \quad (\text{A})$$

where *I_f* is the relative fluorescence intensity, Δ*D* is the plate optical density above background, and σ is the plate response proportionality constant, which varied smoothly from 0.8 to 1.2 over the 2400–3000-Å range. Integrated band intensities were obtained by graphical integration, using eq A to obtain *I_f* for each wavelength increment. Correction for the decreasing dispersion and increasing transmission of the spectrograph with increasing wavelength is only necessary when comparing widely separated bands.

Volume flow rates were calculated by timing the pressure

rise in a calibrated volume. Linear flow rates were usually on the order of 100–300 cm/s.

The argon (U.S. Welding) and N₂ (Matheson Prepurified Grade) were used without further purification. The nitric oxide (Linde Co.) was passed through a trap packed with silica gel and kept at –78 °C. Quantitative experiments with unpurified NO were difficult to perform because of rapid formation of a brownish film on the flow tube downstream from the cadmium reservoir (presumably CdO_(s)) formed by reaction of impurity NO₂ with cadmium).

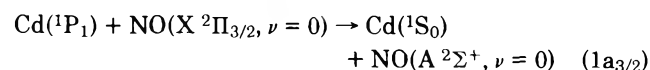
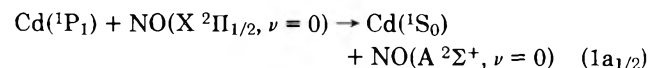
Results

When a stream of argon (~2 Torr) at 285–300 °C containing 0.1–0.5 Torr of NO and cadmium vapor is irradiated with 2288-Å cadmium resonance radiation, the NO γ bands²⁵ corresponding to fluorescence from both NO(A ²Σ⁺, ν = 1) and NO(A ²Σ⁺, ν = 0) (hereafter referred to as γ(1,*x*) and γ(0,*x*) bands, respectively) are observed with comparable intensity. When the experiment is repeated under the same conditions but with no cadmium metal in the stream (the cadmium metal was removed and the flow tube cleaned thoroughly, then preheated at 290 °C in a flow of argon for several hours), the γ(1,*x*) bands are again observed in fluorescence but the γ(0,*x*) bands are completely absent. (See Figure 1.) Subsequent addition of cadmium to the reservoir and repetition of the original experiment reproduces the relative intensities of the γ(0,*x*) and γ(1,*x*) bands.

If the experiment is run with the flow tube at room temperature, where the vapor pressure of cadmium is effectively zero, γ(1,*x*) bands but no γ(0,*x*) bands are observed. Repeating the experiment (at 285–300 °C) with a pyrex plate between the lamp and the furnace (which absorbs all radiation below 2900 Å, but passes a significant fraction of 3261 Å (³P₁ → ¹S₀) resonance radiation) results in complete elimination of γ-band fluorescence. Similar insertion of a NaCl plate (which blocks radiation below 2050 Å) had no effect on either the γ(1,*x*) or γ(0,*x*) band intensities.

These experiments can obviously be interpreted to indicate collisional electronic energy transfer from Cd(¹P₁) to NO(X ²Π_{3/2,1/2}), producing NO(A ²Σ⁺, ν = 0). Production of NO(A ²Σ⁺, ν = 1) results from direct excitation by the strong 2144-Å Cd⁺ spectral line from the lamp, which happens to be coincident with a particular rotational line in the γ(1,0) transition.^{5,9,27} Excitation of γ(1,*x*) bands by 2144-Å Cd⁺ radiation has been observed previously by several workers, and our γ(1,*x*) band profiles at moderate resolution are consistent with those observed by Carrington and Broida under similar pressure conditions and with a similar light source.⁹ Because rotational and vibrational relaxation by NO and Ar at these low pressures is slow compared to the radiative lifetime of NO(A ²Σ⁺, ν = 1),^{5,9,28,29} the only rotational lines observed in the γ(1,*x*) bands are those originating from the *K* = 13 level of NO(A ²Σ⁺, ν = 1).⁹

The following processes are only ~510- and ~390-cm⁻¹ endothermic, respectively (reasonable estimates made from the P band-head energies):²⁵



To gain even further proof that processes 1a were occurring in the experimental system, and to estimate the overall rate of quenching of Cd(¹P₁) by NO(X ²Π_{1/2,3/2}), experiments were

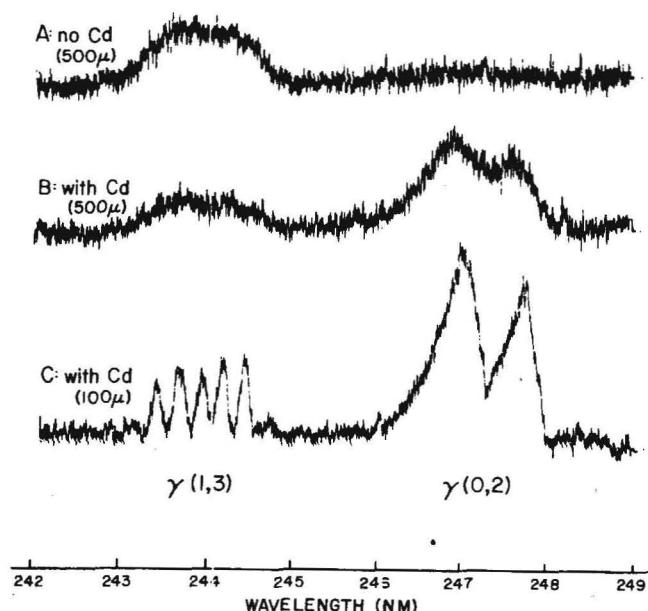


Figure 1. Microdensitometer traces of NO γ -band fluorescence. (A) Flow tube temperature $\sim 290^\circ\text{C}$. No cadmium vapor present, $P_{\text{NO}} = 0.2$ Torr; $P_{\text{Ar}} = 1$ Torr; spectrograph slit width $500\ \mu$. (B) Same conditions as A, but with Cd vapor present. (C) Same conditions as B, but with $100\text{-}\mu$ slit width. Exposure times and detection efficiencies differ for each case.

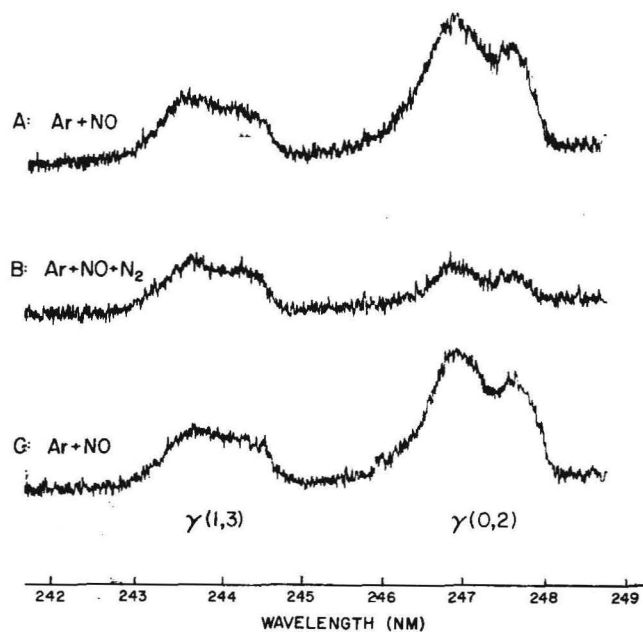


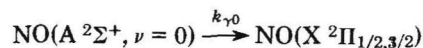
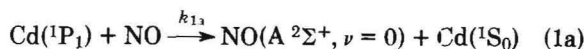
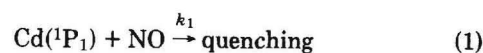
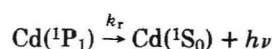
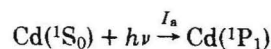
Figure 2. Microdensitometer traces of NO γ -band fluorescence. Effect of added N_2 : Slit width $500\ \mu$; flow tube temperature $\sim 290^\circ\text{C}$. (A) $P_{\text{Ar}} = 2.25$ Torr, $P_{\text{NO}} = 0.38$ Torr. (B) $P_{\text{Ar}} = 0.12$ Torr, $P_{\text{NO}} = 0.30$ Torr, $P_{\text{N}_2} = 2.22$ Torr. (C) $P_{\text{Ar}} = 2.20$ Torr, $P_{\text{NO}} = 0.40$ Torr. Measurements were taken consecutively, with same photographic plate.

conducted by adding N_2 , a gas which is known to be quite efficient^{26,30,31} in quenching $\text{Cd}(^1\text{P}_1)$ but relatively ineffective at pressures of a few torr in quenching $\text{NO}(\text{A } ^2\Sigma^+)$ in either the $\nu = 0$ or $\nu = 1$ vibrational level.^{9,29} When increasing amounts of Ar were replaced with N_2 , starting with 0.2 Torr of NO in 2 Torr of Ar, the intensity of the $\gamma(1,x)$ bands were essentially unaffected, while the intensity of the $\gamma(0,x)$ bands could be reduced nearly to the limits of detection. The dramatic selective reduction of the $\gamma(0,2)$ band intensity on addition of N_2 is shown in Figure 2.

The experiments reported here, therefore, show conclusively that $\text{NO}(\text{A } ^2\Sigma^+, \nu = 0)$ is formed by collisional energy transfer from $\text{Cd}(^1\text{P}_1)$ to $\text{NO}(\text{X } ^2\Pi_{1/2,3/2})$. It is important, however, to determine whether this energy-transfer mechanism is the dominant process by which $\text{Cd}(^1\text{P}_1)$ is quenched by NO, and if not, to estimate the absolute cross section for the overall quenching process as well as reaction 1a.

We first describe a determination of the absolute rate constant k_1 for the overall quenching process, then present the results of experiments which establish the fraction of quenching collisions of $\text{Cd}(^1\text{P}_1)$ with NO which produce $\text{NO}(\text{A } ^2\Sigma^+, \nu = 0)$, and therefore result in an absolute value for k_{1a} .

Determination of the Rate Constant for Quenching of $\text{Cd}(^1\text{P}_1)$ by $\text{NO}(\text{X } ^2\Pi_{1/2,3/2})$. The experiments involving addition of N_2 can be treated quantitatively in terms of the following processes:



where I_a is the rate of absorption of resonance photons at the concentration of $\text{Cd}(^1\text{S}_0)$ in the flow tube, k_r is the effective rate constant for first-order decay of $\text{Cd}(^1\text{P}_1)$ due to the eventual escape of resonant photons from the flow tube (substantially smaller than the natural fluorescent rate constant because of severe radiation imprisonment, see below), k_1 is the overall rate constant for quenching of $\text{Cd}(^1\text{P}_1)$ by an equilibrium mixture of $\text{NO}(\text{X } ^2\Pi_{3/2})$ and $\text{NO}(\text{X } ^2\Pi_{1/2})$ at the temperature of the flow tube, and $k_{\gamma 0}$ ($5.0 \times 10^6 \text{ s}^{-1}$)^{28,29} is the rate constant for spontaneous radiative decay of $\text{NO}(\text{A } ^2\Sigma^+)$. Assuming that steady-state concentrations of $\text{Cd}(^1\text{P}_1)$ and $\text{NO}(\text{A } ^2\Sigma^+)$ exist under the irradiation conditions, the following equation can be derived for treatment of the data for the decreased $\gamma(0,x)$ band intensity at any given NO pressure when N_2 is added:

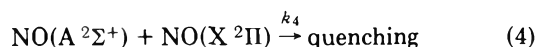
$$\frac{1}{[\text{NO}(\text{A } ^2\Sigma^+, \nu = 0)]} = \frac{1}{C_0 F_0} = \frac{k_{\gamma 0}}{I_a} \left(\frac{k_1}{k_{1a}} \right) \left(1 + \frac{k_r}{k_1[\text{NO}]} + \frac{k_2[\text{N}_2]}{k_1[\text{NO}]} + \frac{k_3[\text{Ar}]}{k_1[\text{NO}]} \right) \quad (B)$$

The variable F_0 is used to represent the relative intensity of the $\gamma(0,2)$ band, chosen because of moderate intensity and the absence of any interference from scattered atomic lines from the lamp, and C_0 is the detection proportionality constant.

We now discuss the relative importance of the terms in the right side of eq B. The $k_2[\text{N}_2]/k_1[\text{NO}]$ term is obviously large at higher pressures (~ 2 Torr) of N_2 because F_0 approaches zero. Phillips and co-workers,³⁰ using a phase-shift technique, have made direct measurements of k_2 and k_3 at 553 K of 2.2×10^{11} and $4.2 \times 10^9 \text{ M}^{-1} \text{ s}^{-1}$, respectively. The validity of

their measurements is given further support by the reasonable agreement of their value for the rate constant for Cd(1P_1) quenching by H_2 , $1.6 \times 10^{11} M^{-1} s^{-1}$, with that estimated by Breckenridge and Callear³¹ in a resonance-radiation flash-photolysis study at 508 K, $2.1 \times 10^{11} M^{-1} s^{-1}$. (No severe temperature dependence would be expected for such a rapid reaction.) This information, coupled with an estimate from the rough data that $k_2/k_1 \approx 0.5$, shows that the term $k_3[Ar]/k_1[NO]$ is small and can be ignored to a first approximation when $[Ar]$ is ≤ 2 Torr and $[NO]$ is ≥ 0.2 Torr.

The importance of the term $k_r/k_1[NO]$ in the equation can be evaluated from experiments in which the NO pressure in pure argon is varied. The $\gamma(0,x)$ intensity increased sharply with NO pressure to about 0.1 Torr of NO, was roughly constant from 0.1 to 0.4 Torr of NO, then dropped off continuously at higher NO pressures. The decrease in $\gamma(0,x)$ intensity at the higher NO pressures is undoubtedly due to the known self-quenching of NO($A^2\Sigma^+$) by NO($^2\Pi$). The self-quenching half-pressure at ~ 400 K has been measured as 0.5 Torr.⁹ The apparent constancy of the $\gamma(0,x)$ intensity in the 0.1–0.4 Torr of NO region may therefore result from the self-quenching of NO($A^2\Sigma^+$) roughly balancing the increasing production of NO($A^2\Sigma^+$) from quenching of Cd(1P_1) by NO:



In order to estimate k_r/k_1 under our conditions, allowance must therefore be made for reaction 4. It has been shown by others^{5,29} that the self-quenching rate for NO($A^2\Sigma^+$, $\nu = 1$) is virtually identical with that for NO($A^2\Sigma^+$, $\nu = 0$) (both rates correspond to quenching at effectively every hard-sphere gas kinetic collision).²⁹ We have therefore used measurements of the self-quenching of NO($A^2\Sigma^+$, $\nu = 1$) in our system to estimate the rate constant for self-quenching of NO($A^2\Sigma^+$, $\nu = 0$) at 560 K.

Measurements of the absorption of 2144-Å light by NO, described in more detail below, indicated that the percent absorption was small and essentially linear over NO pressures from 0.00 to 0.80 Torr with a 2-cm path length. Assuming linear production of NO($A^2\Sigma^+$, $\nu = 1$) and destruction only by $\gamma(1,x)$ band fluorescence or by self-quenching, the following equation should hold:

$$\frac{1}{F_1} = \frac{C_1 k_{\gamma 1}}{I_d [NO]} + \frac{C_1 k_4}{I_d} \quad (C)$$

where F_1 is the observed relative intensity of the $\gamma(1,3)$ bands, C_1 is the detection proportionality constant, I_d is the rate of absorption of 2144-Å photons at unit $[NO]$, and $k_{\gamma 1}$ ($= k_{\gamma 0}$) is $5.0 \times 10^6 s^{-1}$.^{28,29} From the slope-to-intercept ratio of a least-squares fit of the data to a plot of $1/F_1$ vs. $1/[NO]$, a value of k_4 was obtained which corresponded to a self-quenching half-pressure of 0.63 Torr. This may be compared to values of ~ 0.6 Torr determined at room temperature,^{5,29} and ~ 0.5 Torr at 400 ± 100 K. The cross sections for self-quenching of NO($A^2\Sigma^+$, $\nu = 0$) and NO($A^2\Sigma^+$, $\nu = 1$) are shown in Table I.

We assume that NO($A^2\Sigma^+$, $\nu = 0$) is also being quenched by NO($X^2\Pi$) with a quenching half-pressure of 0.63 Torr under our conditions and use this information to extract the effective value of k_r/k_1 from the observed variation of F_0 with $[NO]$ described above. Assuming that when $[NO] = 0.0$ – 0.8 Torr and $[Ar] \leq 2.5$ Torr the only process responsible for production of NO($A^2\Sigma^+$, $\nu = 0$) is (1) and that the only processes causing destruction of NO($A^2\Sigma^+$, $\nu = 0$) are $\gamma(0,x)$ band

TABLE I: Cross Sections for the Quenching of NO($A^2\Sigma^+$) by NO($X^2\Pi$)

Ref	Temp, K	Cross sections, Å ²	
		NO($A^2\Sigma^+$, $\nu = 0$)	NO($A^2\Sigma^+$, $\nu = 1$)
29	300	34	37
5	300	37	42
9	400 ± 100		.55 ± 7
This work	565 ± 10		52

emission and (4), the $\gamma(0,2)$ band emission intensity should fit an equation of the following form:

$$F_0 = \frac{k_{1a} I_a [NO]}{C_0 (k_r + k_1 [NO]) (k_{\gamma 0} + k_4 [NO])} \quad (D)$$

With a value of k_4 corresponding to an NO quenching half-pressure of 0.63 Torr, a plot of F_0 vs. $[NO]$ can only be fit to eq D adequately if a value of k_1/k_r is chosen corresponding to a half-pressure of NO for quenching Cd(1P_1) under these conditions of 0.04–0.07 Torr. A best fit is found at 0.050 Torr quenching half-pressure.

We may now return to eq B with sufficient knowledge to determine k_2/k_1 from measurements of F_0 with and without N_2 present. From eq B, the ratio of $\gamma(0,2)$ intensity without N_2 present, $F_0([N_2] = 0)$, to the $\gamma(0,2)$ intensity with N_2 present, $F_0(N_2)$, is:

$$\frac{F_0([N_2] = 0)}{F_0(N_2)} = \frac{1 + k_r/k_1[NO] + k_2[N_2]/k_1[NO] + k_3[Ar]/k_1[NO]}{1 + k_r/k_1[NO] + k_3[Ar]/k_1[NO]} \quad (E)$$

All quantities in the equation are known except k_2/k_1 . (Inclusion of the term involving Ar quenching results in a maximum change of 4% in calculated values of k_2/k_1 .) Equation B is valid at constant $[NO]$ despite self-quenching. Corrections were made for small changes in $[NO]$ with and without N_2 present.

The data from the N_2 addition runs is shown in Table II. Each experiment was conducted by measuring $F_0([N_2] = 0)$ under the specified conditions, then measuring $F_0(N_2)$ with the listed pressure of N_2 replacing a roughly equivalent pressure of Ar. The original $F_0([N_2] = 0)$ measurement was repeated immediately following to check reproducibility. Initial and final $F_0(N_2)$ values are seen to be constant to within 10% in these experiments. The average calculated rate constant ratio is $k_2/k_1 = 0.56 \pm 0.04$. From the value of $k_2 = 2.2 \times 10^{11} M^{-1} s^{-1}$ determined by Phillips and co-workers,³⁰ the following absolute value is determined: $k_1 = 3.9 \times 10^{11} M^{-1} s^{-1}$. This corresponds to a quenching cross section of ~ 92 Å².

It is appropriate here to rule out several possible sources of error. Vibrational deactivation of NO($A^2\Sigma^+$, $\nu = 1$) to NO($A^2\Sigma^+$, $\nu = 0$) by Ar, N_2 , and even NO($X^2\Pi$) will occur to a negligible extent under the conditions of these experiments.^{5,9,29} Even the relatively efficient vibrational relaxation by NO($X^2\Pi$) has a rate constant less than 5% of the total self-quenching rate constant. Net quenching by Ar or N_2 of either NO($A^2\Sigma^+$, $\nu = 1$) or NO($A^2\Sigma^+$, $\nu = 0$) is also completely negligible under our conditions.²⁹

Another process which should be considered is the possible quenching of NO($A^2\Sigma^+$, $\nu = 0,1$) by Cd vapor. At the temperature of the flow tube the maximum Cd vapor pressure is ~ 0.03 Torr. With an NO($A^2\Sigma^+$) lifetime of 2.0×10^{-7} s,

TABLE II: Determination of k_2/k_1 (See Text)^a

Expt	Pressures, Torr			F_1^b	F_0^b	k_2/k_1
	NO	N ₂	Ar			
A	0.23	0.00	2.14	0.80	3.51	0.51
	0.23	0.98	0.69	0.82	1.34	
	0.25	0.00	1.95	0.89	3.55	
B	0.43	0.00	1.91	1.19	3.46	0.59
	0.40	1.08	0.57	1.21	1.50	
	0.43	0.00	2.10	1.21	3.70	
C	0.40	0.00	2.31	1.12	3.52	0.58
	0.37	1.27	0.81	1.10	1.27	
	0.41	0.00	2.58	1.07	3.40	
D	0.38	0.00	2.25	0.92	3.53	0.56
	0.30	2.22	0.12	0.72	0.74	
	0.40	0.00	2.20	0.87	3.23	

$$\bar{A}_v = 0.56 \pm 0.04$$

^a F_1 and F_0 are the intensities of the $\gamma(1,3)$ and $\gamma(0,2)$ emission bands, respectively. $T = (565 \pm 10)$ K. ^b Arbitrary units.

quenching by Cd vapor would have to occur with a cross section greater than 200 \AA^2 for even 10% reduction of the $\text{NO}(\text{A } ^2\Sigma^+)$ concentration, and therefore is unlikely to cause any error in the measurements. The effects of radiation trapping of γ -band fluorescence (i.e., reabsorbance of a γ -band photon before reaching the cell wall), considered in detail by some workers,⁵ should be negligible with the dimensions of our reaction vessel and the pressure of NO used.³²

As a final consistency check on the validity of the procedure used to obtain k_2/k_1 , it is possible to calculate the "effective" lifetime of $\text{Cd}(^1\text{P}_1)$ under the severe radiation trapping conditions of these experiments, and therefore estimate k_1 from the k_2/k_1 ratio already determined.

The Holstein theory has been shown to predict accurately the lifetime of $\text{Hg}(^3\text{P}_1)$ under conditions of high opacity.³³ For these very high opacity conditions in the case of the totally allowed $\text{Cd}(^1\text{P}_1 \rightarrow ^1\text{S}_0)$ transition, however, photons can effectively only escape the vessel in the wings of the line-shape profile, which is entirely dominated by the Lorentzian contribution due to Heisenberg (natural) line broadening.³⁴ The modification by Walsh³⁵ of Holstein's theory to include simultaneous Doppler, Heisenberg, and Lorentz (pressure) broadening must therefore be employed. The effective lifetime of $\text{Cd}(^1\text{P}_1)$ at 0.030 Torr of Cd vapor, under Doppler + Heisenberg broadening conditions in an infinite cylinder of 1.1-cm radius (opacity = 10 700), is calculated *via* the Walsh treatment to be 1.6×10^{-6} s. According to the theory, at such high opacities the effective lifetime of $\text{Cd}(^1\text{P}_1)$ should vary only as $[\text{Cd}]^{1/2}$, minimizing the error due to the lack of precise knowledge of the pressure of Cd vapor in the flow tube. From the measured quenching half-pressure of NO of 0.050 Torr, k_1 can therefore be estimated as $4.3 \times 10^{11} \text{ M}^{-1} \text{ s}^{-1}$, in good agreement with the value determined above of $3.9 \times 10^{11} \text{ M}^{-1} \text{ s}^{-1}$.

Experimental confirmation of the use of the Walsh-Holstein theory for $\text{Cd}(^1\text{P}_1)$ effective lifetime predictions can be found in the phase-shift measurements of Phillips and co-workers³⁰ of apparent $\text{Cd}(^1\text{P}_1)$ fluorescence lifetimes. The theory predicts a lifetime, for their conditions of vapor pressure and vessel geometry, of 1.0×10^{-6} s, while their experimental value was $(1.3 \pm 0.4) \times 10^{-6}$ s.

The Cross Section for Production of $\text{NO}(\text{A } ^2\Sigma^+, \nu = 0)$ by Energy Transfer from $\text{Cd}(^1\text{P}_1)$ to $\text{NO}(\text{X } ^2\Pi)$. We now describe a measurement of the fraction of all net quenching

collisions of $\text{Cd}(^1\text{P}_1)$ with $\text{NO}(\text{X } ^2\Pi)$ which result in production of $\text{NO}(\text{A } ^2\Sigma^+, \nu = 0)$, the branching ratio k_{1a}/k_1 . The rate constant k_{1a} is likely to be measurably smaller than k_1 if only because of the endothermicity of (1a) and the fact that (1) occurs with a rate even greater than the hard-sphere collision rate. The ratio k_{1a}/k_1 was estimated by using the $\gamma(1,x)$ fluorescence, excited by direct excitation from the 2144- \AA Cd^+ line from the lamp, as an in situ actinometric standard. By measuring the ratio of the $\gamma(0,2)$ and $\gamma(1,3)$ band intensities, and knowing: (i) the fraction of the line intensities at 2144 and 2288 \AA absorbed by $\text{NO}(\text{X } ^2\Pi)$ and $\text{Cd}(^1\text{S}_0)$, respectively, (ii) the ratio of 2144- to 2288- \AA line intensities from the lamp, and (iii) the relative $\gamma(1,3)$ and $\gamma(0,2)$ radiative transition probabilities, it is possible to calculate the fraction of 2288- \AA photons originally absorbed by $\text{Cd}(^1\text{P}_1)$ which finally produce $\text{NO}(\text{A } ^2\Sigma^+, \nu = 0)$. Under conditions where all $\text{Cd}(^1\text{P}_1)$ is quenched by $\text{NO}(\text{X } ^2\Pi)$, this corresponds to the fraction of quenching collisions which produce $\text{NO}(\text{A } ^2\Sigma^+, \nu = 0)$, or k_{1a}/k_1 . Values of k_{1a}/k_1 were obtained using the following expression:

$$\left(\frac{k_{1a}}{k_1}\right) = \left(\frac{I_{2144}}{I_{2288}}\right) \left(\frac{L_{2144}}{L_{2288}}\right) \left(\frac{P(1,3)}{P(0,2)}\right) \left(\frac{1}{Q}\right) \left(\frac{E(0,2)}{E(1,3)}\right) \quad (\text{F})$$

where I_{2144} and I_{2288} are the total intensities of the 2144- and 2288- \AA emission lines from the lamp; L_{2144} is the fraction of I_{2144} absorbed by a certain pressure of NO in the flow tube; L_{2288} is the fraction of I_{2288} absorbed by Cd vapor in the flow tube; $P(1,3)$ and $P(0,2)$ are the absolute total emission strengths of the $\gamma(1,3)$ and $\gamma(0,2)$ bands; Q is the fraction of the $\text{Cd}(^1\text{P}_1)$ population which is quenched by NO at a particular NO pressure; and $E(0,2)$ and $E(1,3)$ are the measured integrated intensities of the $\gamma(0,2)$ and $\gamma(1,3)$ bands. The $\gamma(1,3)$ and $\gamma(0,2)$ bands were chosen because they are separated by only 30 \AA , minimizing errors due to variations in net detection efficiency with wavelength, and because there are no interfering line emissions scattered from the lamp in this wavelength region. Because the rate of reaction 4 is similar for $\text{NO}(\text{A } ^2\Sigma^+, \nu = 0)$ or $\text{NO}(\text{A } ^2\Sigma^+, \nu = 1)$, self-quenching has negligible effect on $E(0,2)/E(1,3)$.

The quantity I_{2144}/I_{2288} was determined using a Varian AA-5 atomic absorption spectrometer with a mechanical chopper and phase-sensitive detection. The observed intensities were corrected for a 20% difference in photomultiplier response, using the manufacturer's specifications. Flow-tube excitation conditions were simulated by running the lamp source at exactly the same power, and passing the light, before measurement, through the same quartz window at the same geometry and temperature as in the flow-tube experiments. These measurements were conducted immediately following the experiments in which $E(0,2)/E(1,3)$ were measured, to minimize error due to lamp deterioration.

L_{2144} was calculated from absorption measurements of the 2144- \AA Cd^+ line by NO, using the same lamp conditions and the atomic absorption spectrometer described above. The 2.0-cm path length of the cell was assumed to approximate the 2.2-cm i.d. cylindrical flow tube, and measurements were made with ~ 2 Torr of argon present to simulate flow-tube conditions. For the lamp used for the flow-tube measurements of $E(0,2)/E(1,3)$, absorption of NO up to ~ 1 Torr followed Beer's law, with an absorption coefficient of $0.025 \text{ cm}^{-1} \text{ Torr}^{-1}$ (log convention) at room temperature. These results indicated weak absorption under our conditions (i.e., less than 10% absorption of the 2144- \AA line) and are apparently comparable to those of Broida and Carrington for similar lamp and optical

density conditions (see Figure 4 of ref 9). The absorption coefficient at the temperature of the flow-tube experiments was assumed to be a factor of 1.9 greater than at room temperature, with the following justification. Flow-tube experiments performed at 300 and 560 K indicated that the $E(1,x)$ intensities at the same NO concentrations were about a factor of 1.65 higher at 560 K. The experimental intensities were further corrected for the differences in $\text{NO}(A^2\Sigma^+, \nu = 1)$ self-quenching at 300 and 560 K (see Table I), resulting in the overall factor of 1.9. Thus for 0.3 Torr of NO at 560 K, for example, $L_{2144} = 0.065$. The increase in absorptivity of the 2144-Å Cd^+ spectral line by NO with temperature is expected, since the output line from the low-power, low-pressure discharge source is quite narrow and is absorbed at the edge of a $\gamma(1,0)$ rotational transition.^{5,9} The increased Doppler width of the $\gamma(1,0)$ rotational transition at 560 K results in a greater effective absorption coefficient for the 2144-Å line. It was found that specific absorption at room temperature could also be increased by using higher lamp discharge powers, presumably because the 2144-Å emission line is broadened into greater overlap with the center portion of the Doppler rotational line absorption profile.

L_{2288} was assumed to be 1.00 for all experiments. At such high opacities, all the 2288-Å radiation should be absorbed by the cadmium vapor even if the lamp emission line is severely reversed, which it is almost certain to be (see ref 5 for a high-resolution spectrum of the $\text{Zn}(^1P_1 \rightarrow ^1S_0)$ 2138-Å emission line from a similar microwave lamp). However, this assumption was checked by measuring the absorption of a well-collimated beam of 2288-Å radiation from our lamp by cadmium vapor (~2 Torr of Ar) in a 0.7-cm i.d. quartz tube, using the atomic absorption spectrometer. The 2288-Å line intensity transmitted was first measured at room temperature, the cell was heated until the intensity dropped to zero, and was then cooled to room temperature to check that the original intensity could be reproduced. The transmitted 2288-Å intensity was effectively reduced to zero at ≤ 210 °C, corresponding to an opacity at least 100 times less than the flow-tube conditions.

The $P(1,3)/P(0,2)$ ratio was taken to be 0.30, corresponding to the ratio of the Franck-Condon factors for the $\gamma(1,3)$ and $\gamma(0,2)$ bands,³² corrected for the slight difference in intensity due to the fourth power wavelength dependence. Dependence of the electronic transition moment on the r-centroid has been shown to be negligible for these two transitions.³⁶

The value of Q for each pressure of NO was calculated using a quenching half-pressure of 0.050 Torr of NO.

$E(0,2)$ and $E(1,3)$ were obtained by graphical integration of each band for the same photographic plate exposure, using the plate response factor $\sigma = 0.80$ appropriate for the 2440–2480-Å region.

Values of k_{1a}/k_1 determined in several experiments are shown in Table III. The average value is

$$k_{1a}/k_1 = 0.034 \pm 0.004$$

Thus, using our determined values of $k_1 = 3.9 \times 10^{11} \text{ M}^{-1} \text{ s}^{-1}$, $\sigma_1 = 92 \text{ \AA}^2$:

$$k_{1a} = 1.4 \times 10^{10} \text{ M}^{-1} \text{ s}^{-1} \quad \sigma_{1a} = 3.4 \text{ \AA}^2$$

Discussion

Although the cross section determined for energy transfer process 1a, 3.4 \AA^2 , is substantial for an endothermic process, the total cross section for quenching of $\text{Cd}(^1P_1)$, $\sigma_1 = 92 \text{ \AA}^2$, is much larger. We now discuss these cross sections with ref-

TABLE III: Determination of k_{1a}/k_1 ^a

NO pressure, Torr	L_{2144}	Q	$E_{(0,2)}/E_{(1,3)}$	k_{1a}/k_1
0.078	0.017	0.61	13.1	0.033
0.168	0.037	0.77	9.3	0.036
0.23	0.050	0.82	7.7	0.036
0.33	0.072	0.87	4.7	0.030
0.41	0.088	0.91	5.8	0.043
0.55	0.117	0.92	4.9	0.044
				$\text{Av} = 0.037 \pm 0.004$

^a See eq F and text.

erence to current theories of quenching and energy transfer, and to the efficiency and mechanisms of quenching of excited Cd atoms by other molecules. It is convenient first to consider mechanisms for energy transfer reaction 1a as a separate minor exit channel, and then to discuss the overall quenching process and the other exit channels which must account for most of the energy disposal.

Dipole-Dipole Mechanism for $\text{NO}(A^2\Sigma^+)$ Production. If the energy transfer in reaction 1a is caused by long-range interaction of the transition dipole moments of the respective Cd and NO electronic transitions, the expected cross section can be calculated using the first-order theory of Gordon and Chiu,²³ developed to treat the data of Melton and Klemperer on analogous electronic energy transfer between isotopic NO molecules.^{5,32} A theory developed from essentially the same assumptions was published independently by Fink, Wallach, and Moore in their study of near-resonant energy transfer from Ar to H_2 .⁴

The probability of an exothermic electronic energy transfer transition can be expressed as:

$$P(b) = \frac{4\mu_1^2\mu_2^2(1 + 2X + \frac{3}{4}\pi X^2 + \pi X^3)e^{-2X}}{9\hbar^2\bar{V}^2b^4}$$

where μ_1 and μ_2 are the two transition dipole moments; b is the impact parameter of the collision; \bar{V} is the geometric mean of the relative velocities before and after collision:

$$\bar{V} = (\bar{V}_i\bar{V}_f)^{1/2}$$

where \bar{V}_i is the relative mean velocity and $\bar{V}_f = \bar{V}_i(E_f/E_i)^{1/2}$, with $E_i = \frac{3}{2}kT$, $E_f = E_i + \Delta E$, and ΔE is the energy transferred to translation (i.e., the energy off resonance); and $X = b\Delta E/\hbar\bar{V}$. A value b_c is found which satisfies $P(b_c) = E_f/(E_i + E_f) = P_c$, and the cross section is set equal to $2P_c\pi(b_c)^2$. The theory has been used to calculate cross sections which are consistent with those determined experimentally by Klemperer and Melton for NO^*-NO transfer,⁵ and is thought to be accurate to within a factor of 2. The principal approximations are neglect of rotational fine structure and of higher multipolar interactions.

We first calculate the expected cross sections for the reverse of each of the endothermic processes $1a_{1/2}$ and $1a_{3/2}$, then use the principle of microscopic reversibility to calculate the cross sections of interest. The value of μ_1 for NO $\gamma(0,0)$ was taken to be 0.19 D.²³ The value of $\mu_2 = 4.4$ D was calculated from the equation:³⁷ $\mu^2 = 3h/64\pi^4\bar{\nu}^3\tau$ where $\bar{\nu}$ is the frequency of the transition in wave numbers, and $\tau = 2.0 \times 10^{-9}$ s (the natural radiative lifetime of $\text{Cd}(^1P_1)$).³⁸ The quantity ΔE was taken to be 390 cm^{-1} for reaction $1a_{3/2}$ and 510 cm^{-1} for reaction $1a_{1/2}$. The resulting cross sections calculated for dipole-dipole energy transfer for the reverse of reactions $1a_{3/2}$ and $1a_{1/2}$ are 3.2 and 2.0 \AA^2 , respectively.

The ratios of electronic partition functions for reactions $1a_{3/2}$ and $1a_{1/2}$ are $\frac{1}{6}$ and $\frac{1}{3}$. Because the rotational partition functions for the $\frac{1}{2}$ and $\frac{3}{2}$ multiplets of $\text{NO}(X^2\Pi)$ are identical at the high temperature of the experiments, the ratio of rotational partition functions is $B_e(2\Pi)/B_e(2\Sigma^+) = 0.85$. The equilibrium constants for reactions $1a_{3/2}$ and $1a_{1/2}$ as written are calculated to be 0.053 and 0.077, respectively, at 560 K. The cross sections predicted for transfer of energy by dipole-dipole interaction for reactions $1a_{3/2}$ and $1a_{1/2}$ are therefore 0.17 and 0.15 \AA^2 , respectively, at this temperature. Since 99% of the $\text{NO}(X^2\Pi_{1/2,3/2})$ states are in the $V = 0$ vibrational level even at this temperature, no error is introduced by assuming that only the $V = 0$ level is thermally populated. Because the observed cross section for production of $\text{NO}(A^2\Sigma^+)$ in the deactivation of $\text{Cd}(^1P_1)$ by equilibrated $\text{NO}(X^2\Pi_{1/2,3/2})$ is a factor of 20 larger, another mechanism must be responsible.

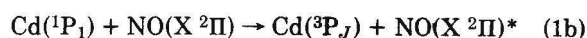
Direct Curve-Crossing Mechanism for $\text{NO}(A^2\Sigma^+)$ Production. For a simple potential-surface crossing mechanism to produce a cross section as large as 3.4 \AA^2 in an endothermic energy-transfer process, the crossing probability must be relatively large and the crossing point must not occur even slightly up on a repulsive wall of one of the $\text{Cd}(^1P_1) + \text{NO}(X^2\Pi)$ interaction surfaces. One or more of the surfaces which correlate with $\text{Cd}(^1P_1) + \text{NO}(X^2\Pi)$ may cross the surface correlating with $\text{Cd}(^1S_0) + \text{NO}(A^2\Sigma^+)$ at relatively large Cd-NO distances, where an amount of energy essentially no greater than the endothermicity of the reaction would be required for reaction 1a to proceed.

Because of the promotion of an electron from the 5s to the 5p orbital, the $\text{Cd}(^1P_1)$ state should have an effective size some 25–30% larger than $\text{Cd}(^1S_0)$.³⁹ Thus the repulsive part of any interaction potential between $\text{Cd}(^1P_1)$ and any molecule AB should in general set in at larger Cd-AB distances than the repulsive part of the $\text{Cd}(^1S_0)$ -AB interaction potential. Although the internuclear distance of $\text{NO}(A^2\Sigma^+)$ is 1.06 \AA compared to 1.15 \AA for ground-state $\text{NO}(X^2\Pi)$,⁴⁰ the $A^2\Sigma^+$ state is the first of a Rydberg series and the outer electron occupies a diffuse outer σ orbital.⁴¹ It is difficult to predict, therefore, whether the onset of the repulsive wall of the interaction of $\text{NO}(A^2\Sigma^+)$ with any atom M will occur at greater or smaller M-NO distances than that of $\text{NO}(X^2\Pi)$, although it seems unlikely that the repulsive wall would lie at a M-NO distance as much as 30% greater. It is possible, therefore, that the repulsive portions of the $\text{NO}(X^2\Pi)$ - $\text{Cd}(^1P_1)$ interaction potentials cross the $\text{NO}(A^2\Sigma^+)$ - $\text{Cd}(^1P_1)$ potential surface at moderately large Cd-NO distances. For a surface intersection at a Cd-NO distance of $\sim 4 \text{ \AA}$, for instance, allowing for a Boltzmann factor of ~ 0.3 , a successful crossing probability of ~ 0.1 would be required to explain the $3.4\text{-}\text{\AA}^2$ energy transfer cross section (assuming two crossings per trajectory). Any substantial attractive potential of $\text{Cd}(^1P_1)$ - $\text{NO}(X^2\Pi)$ and/or $\text{Cd}(^1S_0)$ - $\text{NO}(A^2\Sigma^+)$ could either enhance or inhibit the probability of surface crossings, of course.

A very similar mechanism has been proposed by Fink, Wallach, and Moore⁴ to account for the relative efficiency of endothermic production of certain $\text{H}_2(B^1\Sigma^+, \nu', J')$ states in the quenching of excited argon atoms by H_2 . Surface-crossing probabilities on the order of 0.01 to 0.15 were calculated based on a reasonable Ar- H_2 intermolecular crossing distance.

Collisional Mechanism and Exit Channels for Quenching of $\text{Cd}(^1P_1)$ by $\text{NO}(X^2\Pi)$. The fact that the quenching cross section for reaction 1 is roughly twice the cross section for a reasonable estimate of a $\text{Cd}(^1P_1) + \text{NO}(X^2\Pi)$ hard-sphere collision indicates that some kind of long-range attractive

forces exist between these two species. This, coupled with the fact that there must be several exit channel surfaces with probability density overlapping the $\text{Cd}(^1P_1)$ - $\text{NO}(X^2\Pi)$ interaction region, suggests that a kinetically parallel energy-transfer reaction 1a occurring via a separate long-range surface-crossing mechanism may be a drastic simplification of the real mechanism. The following additional exit channels must account for most of the energy disposal in reaction 1:



where the asterisk indicates vibrational-rotational excitation of unspecified distribution. Populations of the J states of $\text{Cd}(^3P_J)$ and the NO electronic states are also left unspecified for simplicity. The energies of the 3P_0 , 3P_1 , 3P_2 , and 1P_1 states of cadmium are 86.0, 87.6, 90.9, and 124.8 kcal/mol above that of $\text{Cd}(^1S_0)$, and the energy of $\text{NO}(a^4\Pi_i)$ above ground-state $\text{NO}(X^2\Pi_{1/2})$ is $\sim 108 \text{ kcal/mol}$.⁴²

No matter which exit channel is dominant, there must be some interaction between $\text{Cd}(^1P_1)$ and NO (besides the dipole-dipole effect) which is effective even for collisions with relatively large impact parameters, $\sim 5 \text{ \AA}$. We consider first the possibility that charge-transfer surfaces correlating with $\text{Cd}^+ + \text{NO}^-$, or $\text{Cd}^- + \text{NO}^+$, could intersect the $\text{Cd}(^1P_1)$ - $\text{NO}(X^2\Pi)$ surfaces at relatively large Cd-NO distances. If so, electron transfer would take place, with subsequent electrostatic attraction into the intermolecular region where net surface crossings to exit channels 1a–1d could occur with high efficiency before redissociation of the Cd-NO complex to $\text{Cd}(^1P_1) + \text{NO}(X^2\Pi)$ (i.e., a variation of the well-known "harpoon" mechanism).⁴³ A similar mechanism has been utilized successfully⁴⁴ in interpreting some quenching reactions of electronically excited alkali metal atoms, which of course have extremely low ionization potentials. Such a mechanism is also reasonable for the $\text{Cd}(^1P_1)$ -NO case because of the moderately low ionization potential of $\text{Cd}(^1P_1)$, 82 kcal/mol, and the slightly positive electron affinity of $\text{NO}(X^2\Pi)$, $\sim +1 \text{ kcal/mol}$.⁴⁵ A simple Coulombic calculation indicates that the Cd^+ - NO^- potential surface will cross the $\text{Cd}(^1P_1) + \text{NO}(X^2\Pi)$ asymptotic surface at a Cd-NO distance of 4.1 \AA . If every collision with impact parameter less than 4.1 \AA leads to net curve crossing and quenching, a cross section of 50 \AA^2 would result, as compared to the experimental value of $\sim 90 \text{ \AA}^2$. A polarizability contribution⁴⁶ to the Cd^+ - NO^- potential could increase the crossing-point distance, but a very large polarizability of 50 \AA^3 would be necessary to bring the approximate theory into agreement with experiment. Within the absolute uncertainty of the cross section, however, an ionic curve-crossing mechanism for $\text{Cd}(^1P_1)$ quenching by $\text{NO}(X^2\Pi)$ is probably viable.

The other charge-transfer surface, Cd^- - NO^+ , will be less important because of the higher ionization potential of NO vs. Cd, 213 vs. 207 kcal/mol, and the lack of a stable negative ion for Cd. Recent work⁴⁷ on shape resonances in Mg, Zn, Cd, and Hg indicates the existence of unstable low-lying negative ion states due to temporary electron occupation of the p orbital of the metal atom, however. The asymptotic energy of $\text{Cd}^- + \text{NO}^+$ could therefore be on the order of only 15 kcal/mol higher than that of $\text{Cd}^+ + \text{NO}^-$. Thus, although the Cd^- - NO^- curve would dominate with regard to collisions with the highest impact parameters, the Cd^- - NO^+ curve could contribute significantly to the quenching process by providing

another grid of vibrational-state potential surface intersections for efficient surface crossing.^{44,46}

Ionic surface crossing cannot properly account for the large Cd(¹P₁) quenching cross sections of molecules such as *n*-butane ($\sigma = 270 \text{ \AA}^2$),³⁰ however, because the electron affinity of the quencher is likely quite negative,⁴⁸ and the ionic surface crosses the neutral surface at Cd–quencher distances much too small to yield such large cross sections. The measured cross sections for quenching of Cd(¹P₁) by various molecules do show a reasonable correlation with *C*₆ van der Waal's parameters,² similar to that pointed out by Setser and co-workers for quenching of metastable argon atoms. Thus long-range van der Waal's dispersion interactions may play an important role in the quenching of Cd(¹P₁) by NO(*X* ²Π) as well as by other molecules. Lijnse⁴⁴ has successfully explained the temperature dependence of the cross sections for quenching of excited alkali atoms by N₂ and CO by including the van der Waal's long-range interaction in his modification of the ionic surface crossing mechanism.

A recent theoretical calculation⁴⁹ of *C*₆ parameters for long-range interactions of Hg(³P₁) and Hg(¹P₁) with the inert gases has indicated that the *C*₆ parameters for Hg(¹P₁) are a factor of 3.6–4.4 greater than those for ground-state Hg(¹S₀). In contrast the analogous *C*₆ parameters for the Hg(³P₁) are only a factor of 1.5–1.9 greater than those for Hg(¹S₀). Much of the difference between the singlet and triplet states of the sp excited configuration was shown to be due to a "correlation" effect arising from the differences in symmetry properties of the spatial parts of the wave functions. Analogous but somewhat smaller values of the *C*₆ parameters would be expected for Cd(¹P₁) and Cd(³P₁), so that long-range van der Waal's attraction could play a general role in the mechanism of quenching of Cd(¹P₁).

The cross sections for quenching of the equilibrated Cd(³P_{0,1}) states are usually smaller, and exhibit much wider variations from quencher to quencher, than those for Cd(¹P₁).²⁶ For example, the cross sections³⁰ for quenching of Cd(¹P₁) by N₂, NH₃, CO₂, propene, and *n*-butane are 50, 58, 150, 234, and 267 Å², respectively, while the same cross sections²⁶ at the same temperature for Cd(³P_{0,1}) are 0.024, 0.14, 38, 185, and 0.008 Å². Similar trends are found for Hg(¹P₁) and Hg(³P₁) quenching cross sections,⁵⁰ although the Hg(¹P₁) values have not yet been put on an absolute scale. For both Hg(¹P₁) and Cd(¹P₁), a major exit channel, unexpectedly, is the (usually) spin-forbidden production of Hg(³P_{*J*}) or Cd(³P_{*J*}),^{26,50,51} detected readily only when the ³P_{*J*} states are not themselves rapidly deactivated by the quenching molecule. It appears, therefore (though more detailed theoretical and experimental studies are obviously needed), that quenching of the ¹P₁ states may result from general long-range attractive forces as well as generally efficient mechanisms (still unknown) by which the ¹P₁ states are coupled into exit channel surfaces correlating with the ³P_{*J*} states (analogous to (1b)). Quenching cross sections for the ³P_{*J*} states are usually smaller because of less effective long-range interactions and show wider variations in magnitude because the coupling of the ³P_{*J*} states into exit channel surfaces correlating with the ground-state ¹S₀ atom is apparently not generally efficient, so that larger cross sections result from specific chemical (exchange) interactions. Studies of the ¹P₁ and ³P_{*J*} states of the lighter atoms zinc and (especially) magnesium may lead to a better general understanding of these quenching phenomena.²⁶

In the case of quenching of Cd(¹P₁) by NO(*X* ²Π), the production of Cd(³P_{*J*}), reaction 1b, does not even violate the rule

of overall conservation of spin angular momentum and consequently is expected to be particularly efficient. (Note that channel 1c is spin forbidden.) Unfortunately, Cd(³P_{*J*}) is also quenched rapidly by NO(*X* ²Π), so that quantitative estimation, or even detection, of the exit channel 1b is difficult, even using time-resolved techniques.²⁶

Because of the likely existence of Cd⁺NO⁻ and Cd⁻NO⁺ potential surfaces, as well as the surfaces correlating with product channels 1a–1d, in the Cd(¹P₁)–NO(*X* ²Π) interaction region, multiple crossing sites and severe perturbations are undoubtedly present. As a crude approximation, it is of interest then to inquire which exit channels would predominate if there are no special kinetic curve-crossing restrictions, i.e., if the exit channels were populated statistically. We have therefore performed a density-of-states⁵² calculation for channels 1a–1d, using known spectroscopic information.^{40,41}

The calculation was performed using the vibrating-rotor density function,⁵² with effective electronic degeneracies of 2, 54, 12, and 6 for channels 1a through 1d, respectively. An energy equal to $\frac{3}{2}kT$ at 560 K was added to the maximum electronic energy available in order to include channel 1a in the calculation. Energies of the Cd(³P_{*J*}) and NO(*X* ²Π) multiplets were approximated as the energies of Cd(³P₁) and NO(*X* ²Π_{1/2}).

This information theory analysis⁵² shows that channels 1a, 1b, 1c, and 1d would be populated statistically to the extent of 0.0015, 30, 3, and 67%. The measured efficiency of channel 1a is therefore much greater than any statistical mechanism could allow (as expected), and even if the exit channels 1b–1d are populated statistically, (1b) would be a major exit channel and predominate over (1c).

Acknowledgments. Acknowledgment is made to the donors of the Petroleum Research Fund, administered by the American Chemical Society, for partial support of this research. This research has also received support from the National Science Foundation (Grant No. MPS 75-12851).

The authors wish to thank Dr. Jack Simons and Dr. Roger Blickensderfer for helpful discussions, and Dr. Blickensderfer for assisting with the density-of-states calculation.

References and Notes

- (1) Dreyfus Foundation Teacher–Scholar.
- (2) L. G. Piper, J. E. Velazco, and D. W. Setser, *J. Chem. Phys.*, **59**, 3323 (1973).
- (3) G. L. Loper and E. K. C. Lee, *J. Chem. Phys.*, **63**, 3779 (1975), and references cited therein.
- (4) E. W. Fink, D. Wallach, and C. Bradley Moore, *J. Chem. Phys.*, **56**, 3608 (1972).
- (5) L. A. Melton and W. Klemperer, *J. Chem. Phys.*, **59**, 1099 (1973).
- (6) I. T. N. Jones and K. D. Bayes, *J. Chem. Phys.*, **57**, 1003 (1972).
- (7) A. B. Callear and J. D. Lambert, *Compr. Chem. Kinet.*, **3**, 261 (1969).
- (8) W. H. Breckenridge and T. A. Miller, *J. Chem. Phys.*, **56**, 465 (1972).
- (9) H. P. Broida and T. Carrington, *J. Chem. Phys.*, **38**, 136 (1963).
- (10) R. G. Brown, D. Phillips, and G. DasGupta, *J. Phys. Chem.*, **78**, 2407 (1974).
- (11) K. W. Chow and A. L. Smith, *Chem. Phys. Lett.*, **7**, 127 (1970).
- (12) T. G. Slanger and G. Black, *J. Chem. Phys.*, **55**, 2164 (1971).
- (13) J. N. Pitts, Jr., and B. J. Finlayson, *Angew. Chem., Int. Edit. Engl.*, **14**, 1 (1975).
- (14) M. F. R. Mulcahy, "Gas Kinetics", Nelson, London, 1973.
- (15) J. D. Winefordner, Ed., "Spectrochemical Methods of Analysis", Wiley-Interscience, New York, N.Y., 1971.
- (16) R. P. Wayne, "Photochemistry", Butterworths, London, 1970.
- (17) C. K. N. Patel, "Lasers", Vol. 2, A. K. Levine, Ed., Arnold, London, 1968.
- (18) "Dye Lasers", F. P. Schäfer, Ed., in "Topics in Applied Physics", Vol. 1, Springer-Verlag, New York, N.Y., 1973.
- (19) D. L. Dexter, *J. Chem. Phys.*, **21**, 836 (1953).
- (20) T. Förster, *Discuss. Faraday Soc.*, **27**, 7 (1959).
- (21) S. H. Lin, *Proc. R. Soc. London, Ser. A*, **335**, 51 (1973).
- (22) A. C. Vikis and D. J. LeRoy, *Chem. Phys. Lett.*, **21**, 103 (1973); **22**, 587

- (1973).
- (23) R. G. Gordon and Y. Chiu, *J. Chem. Phys.*, **55**, 1469 (1971).
- (24) R. J. Cross and R. G. Gordon, *J. Chem. Phys.*, **40**, 3571 (1966); H. Rabitz and R. G. Gordon, *ibid.*, **53**, 1815, 1831 (1970).
- (25) R. W. Pearse and A. G. Gaydon, "The Identification of Molecular Spectra", 3d ed, Chapman and Hall, London, 1965.
- (26) R. P. Blickensderfer, W. H. Breckenridge, and D. S. Moore, *J. Chem. Phys.*, **63**, 3681 (1975); W. H. Breckenridge, T. W. Broadbent, and D. S. Moore, *J. Phys. Chem.*, **79**, 1233 (1975); W. H. Breckenridge and T. W. Broadbent, *Chem. Phys. Lett.*, **29**, 421 (1974); W. F. Breckenridge, D. S. Moore, and A. Renlund, to be submitted for publication.
- (27) A. V. Kleinberg and A. N. Terenin, *Dokl. Akad. Nauk. SSSR*, **101**, 445, 1031 (1955); A. V. Kleinberg, *Opt. Spektrosk.*, **1**, 469 (1956).
- (28) It has been assumed in this work that there is negligible variation in radiative lifetime with vibrational ($V = 0, 1$) or rotational quantum state of NO(A²Σ⁺). A summary of relevant data may be found in O. Benoist d'Azy, R. López-Delgado, and A. Tramer, *Chem. Phys.*, **9**, 327 (1975). The agreement in the self-quenching cross sections for NO(A²Σ⁺) determined in ref 5, where individual rotational quantum states were excited, with those of ref 29, where Boltzmann distributions of rotational quantum states were populated, provides further justification for this assumption.
- (29) A. B. Callear and M. J. Pilling, *Trans. Faraday Soc.*, **69**, 1618 (1970).
- (30) P. D. Morten, C. G. Freeman, R. F. C. Claridge, and L. F. Phillips, *J. Photochem.*, **3**, 285 (1974).
- (31) W. H. Breckenridge and A. B. Callear, *Trans. Faraday Soc.*, **67**, 2009 (1971).
- (32) L. Melton, Ph.D. Thesis, Harvard University, 1972.
- (33) T. Holstein, *Phys. Rev.*, **72**, 1212 (1947); **83**, 1159 (1951); A. V. Phelps and A. O. McCoubrey, *ibid.*, **118**, 1561 (1960).
- (34) A. Mitchell and M. Zemansky, "Resonance Radiation and Excited Atoms", MacMillan, New York, N.Y., 1934.
- (35) P. J. Walsh, *Phys. Rev.*, **116**, 511 (1959).
- (36) A. B. Callear, M. J. Pilling, and I. W. M. Smith, *Trans. Faraday Soc.*, **62**, 2997 (1966).
- (37) G. Herzberg, "Atomic Spectra and Atomic Structure", Dover Publications, New York, N.Y., 1944.
- (38) A. Lurio and R. Novick, *Phys. Rev. A*, **134**, 608 (1964).
- (39) J. T. Waber and D. T. Cromer, *J. Chem. Phys.*, **42**, 4116 (1965).
- (40) G. Herzberg, "Spectra of Diatomic Molecules", Van Nostrand-Reinhold, New York, N.Y., 1950.
- (41) F. R. Gilmore, *J. Quant. Spectrosc. Radiat. Transfer*, **5**, 369 (1965).
- (42) J. Heicklen and N. Cohen, *Adv. Photochem.*, **5**, 157 (1968).
- (43) R. D. Levine and R. B. Bernstein, "Molecular Reaction Dynamics", Oxford University Press, New York, N.Y., 1974.
- (44) P. L. Lijnse, *J. Quant. Spectrosc. Radiat. Transfer*, **14**, 1143 (1974), and references therein.
- (45) P. W. Thulstrup, E. W. Thulstrup, A. Anderson, and Y. Ohru, *J. Chem. Phys.*, **60**, 3975 (1974), and references therein.
- (46) E. R. Fisher and G. K. Smith, *Appl. Opt.*, **10**, 1803 (1971); E. Bauer, E. R. Fisher, and F. R. Gilmore, *J. Chem. Phys.*, **51**, 4173 (1969).
- (47) P. D. Burrow and J. Comer, *J. Phys. B*, **8**, L92 (1975).
- (48) B. L. Earl and R. R. Herm, *Chem. Phys. Lett.*, **22**, 95 (1975).
- (49) H. A. Hyman, *Chem. Phys. Lett.*, **31**, 593 (1975).
- (50) V. Madhavan, N. N. Lichtin, and M. Z. Hoffman, *J. Phys. Chem.*, **77**, 875 (1973).
- (51) P. Young, G. Greig, and O. Strausz, *J. Am. Chem. Soc.*, **92**, 413 (1970).
- (52) A. Ben-Shaul, R. D. Levine, and R. B. Bernstein, *J. Chem. Phys.*, **57**, 5427 (1972).

Near-Resonant Electronic Energy Transfer between Zn(¹P₁) and NO(X²Π)

W. H. Breckenridge,*¹ R. P. Blickensderfer, and John FitzPatrick

Department of Chemistry, University of Utah, Salt Lake City, Utah 84112 (Received January 5, 1976)

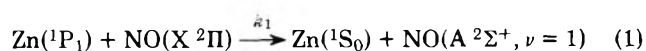
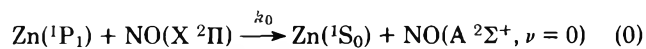
Publication costs assisted by the Petroleum Research Fund

It has been demonstrated that NO(A²Σ⁺) is produced by energy transfer from Zn(¹P₁), and that the production of the $\nu = 1$ vibrational level predominates over the $\nu = 0$ level by a ratio of 10 to 1: Zn(¹P₁) + NO(X²Π) → Zn(¹S₀) + NO(A²Σ⁺, $\nu = 0, 1$). The NO $\gamma(0, x)$ and $\gamma(1, x)$ fluorescence bands are sensitized when Zn vapor and NO(X²Π) in a flow tube at ~425 °C are illuminated with 2138-Å zinc resonance radiation. The preference for the near-resonant $\nu = 1$ exit channel is interpreted in terms of a mechanism involving the long-range interaction of transition dipoles, using the theory of Gordon and Chiu. Attempts to explain the necessarily large cross section for energy transfer as well as the ratio of observed vibrational level populations, using several other electronic-to-vibrational energy transfer models, were relatively unsuccessful. A minor parallel mechanism is likely, however, since the dipole-dipole theory predicts a larger exit-channel ratio than is observed experimentally.

Introduction

The production of NO(A²Σ⁺) by energy transfer from Cd(¹P₁) has been discussed in the preceding paper.² The quenching of Zn(¹P₁) by NO(X²Π) provides a potentially more interesting case study, because the Zn(¹P₁ → ¹S₀) atomic line at 2138 Å falls between rotational lines on the short-wavelength side of the NO $\gamma(1, 0)$ band.^{3,4} Efficient production of NO(A²Σ⁺, $\nu = 1$) by energy transfer from Zn(¹P₁) would therefore be predicted on the basis of near-resonant dipole-dipole theory.²⁻⁶ Measurements of $\gamma(1, x)$ and $\gamma(0, x)$ band intensities could provide interesting information concerning the actual energy-transfer mechanism. Higher resolution of the bands at low pressure would result in initial NO(A²Σ⁺, $\nu = 1$) rotational populations, possibly confirming the expected near-resonant dependence of dipole-dipole energy transfer.⁶

We report here an initial study of this energy transfer process, in which it is indeed shown that NO(A²Σ⁺) is produced in the quenching of Zn(¹P₁) by NO(X²Π), and that production of the $\nu = 1$ vibrational level greatly predominates over that of the $\nu = 0$ level:



Experimental Section

The general experimental apparatus and procedures have been described.² The Zn lamps require a higher temperature

to achieve 2138-Å intensity comparable to that of the 2288-Å intensity from Cd electrodeless discharge lamps. At the higher oven temperatures needed to produce sufficient Zn vapor in the flow tube ($T \geq 400$ C), the uncertainty in the actual gas temperature is greater because operating conditions are near the limit of the oven capabilities.

Results

When a stream of Zn vapor and NO (0.2–0.7 Torr) in argon (~ 2 Torr) at ~ 425 °C is subjected to 2138 Å ($^1P_1 \rightarrow ^1S_0$) zinc resonance radiation from the electrodeless discharge lamp, both the $\gamma(1,x)$ and $\gamma(0,x)$ fluorescence bands of NO are observed. When the experiment is then repeated under the same conditions, but with no zinc in the system (the flow tube was cleaned thoroughly with acid, then preheated several hours at ~ 450 °C with argon flowing), both the $\gamma(0,x)$ bands and $\gamma(1,x)$ bands are completely absent on the photographic plate. With Zn in the flow tube, the γ -band fluorescence intensity increases dramatically between about 390 and 420 °C, with little increase observed if the temperature is raised even further. Within an experimental error of $\sim 15\%$, the ratios of $\gamma(1,x)$ to $\gamma(0,x)$ band intensities do not vary with NO pressure or flow tube temperature above 420 °C. When the Ar is replaced by N_2 , both $\gamma(0,x)$ and $\gamma(1,x)$ band intensities are markedly and uniformly reduced. All these observations are consistent with the production of both $NO(A\ ^2\Sigma^+, \nu = 1)$ and $NO(A\ ^2\Sigma^+, \nu = 0)$ in the quenching of $Zn(^1P_1)$ by $NO(X\ ^2\Pi)$.

Unfortunately, quantitative experiments are more difficult to perform with $Zn(^1P_1)$ than with $Cd(^1P_1)$ with the present experimental system, for two main reasons. First of all, there is apparently no quantitative information available on cross sections for quenching of $Zn(^1P_1)$,^{7–10} although natural lifetime measurements have been made.¹¹ We assume, therefore, that N_2 does quench $Zn(^1P_1)$ efficiently, analogous to the $Cd(^1P_1)$ case,^{2,12} but have made no attempt at this stage to estimate absolute cross sections for either the energy-transfer channel leading to $NO(A\ ^2\Sigma^+)$ formation or for the total quenching of $Zn(^1P_1)$ by NO. From the known cross section for $NO(A\ ^2\Sigma^+)$ production by $Cd(^1P_1)$ in the same system, however, and the fact that the resonance lamp line intensities and excitation conditions are similar, it can be shown that the cross section for $NO(A\ ^2\Sigma^+)$ production by energy transfer from $Zn(^1P_1)$ must be at least $1\ \text{\AA}^2$.

The other source of difficulty in the present system is that pure NO apparently reacts with zinc vapor at these high temperatures to yield $ZnO_{(s)}$, which coats the detection portion of the flow tube and causes rapid and continuous attenuation of the NO γ -band fluorescence intensity. The $ZnO_{(s)}$ deposition should have negligible effect on measurements of relative emission intensities of contiguous bands such as the $\gamma(1,3)$ and $\gamma(0,2)$ bands, however, which are only separated by 30 Å. We have therefore concentrated in this paper on the measurement and interpretation of the primary yield of the $\nu = 1$ level vs. the $\nu = 0$ level of $NO(A\ ^2\Sigma^+)$ in the energy-transfer process. Several measurements of the $\gamma(1,3)$ vs. the $\gamma(0,2)$ integrated band intensities at different NO pressures have yielded an intensity ratio of $(3.1 \pm 0.5):1$. Normalization using the relative emission strengths² (essentially the Franck–Condon factors) for the two bands yields the following interesting result. The initial population of the $\nu = 1$ level is found to be a factor of 10.3 greater than that of the $\nu = 0$ level of $NO(A\ ^2\Sigma^+)$ in the energy transfer process, so that

$$k_1/k_0 = 10.3 \pm 1.7$$

It is appropriate here to discuss any possible systematic errors in the above determination, particularly since there is such a striking predominance of the near-resonant exit channel. As far as we can determine, only one source of possible experimental error causes any real concern, and arguments can be made to show that the effect is negligible. Even with the best ultrapure zinc available, the zinc discharge lamps emit Cd 2288-Å and Cd⁺ 2144-Å radiation, albeit at reduced intensity compared to cadmium lamps. Because the absorption coefficient by Cd vapor is so large, however, it is possible that 2288-Å radiation is absorbed appreciably even by the very small amounts of cadmium vapor impurity from the zinc in the heated flow tube. If so, some portion of the $\gamma(0,x)$ band intensity may result from sensitization by $Cd(^1P_1)$,² and the k_1/k_0 ratio of 10.3 would have to be considered a lower limit. While a larger k_1/k_0 ratio would only help the arguments presented below that a dipole–dipole mechanism appears to be the most reasonable way of explaining our data, experimental and theoretical evidence shows that the effect of the 2288-Å line from the lamp is negligible.

The cadmium impurity in the zinc cannot be greater than about one part in 10 000, and is probably less. It is likely that under the conditions of detection of the $Zn(^1P_1)$ sensitized γ bands, the opacity with regard to transmittance of 2138-Å radiation is similar to that for 2288-Å radiation in the Cd vapor flow system described earlier,² i.e., 10 000. If so, the opacity with regard to absorption of 2288-Å radiation by impurity cadmium in the zinc system could still be as high as 1.0, causing legitimate concern about $Cd(^1P_1)$ production and the resultant $NO(A\ ^2\Sigma^+, \nu = 0)$ sensitization. However, even with an opacity of 3.0, the effective (imprisoned) lifetime of $Cd(^1P_1)$ will be less than 10 ns,¹³ so that quenching of $Cd(^1P_1)$ by $NO(X\ ^2\Pi)$ at 0.16 Torr of NO should be inefficient (quenching half-pressure ≥ 5 Torr). At the very least, the absence of any variation in the ratio of $\gamma(1,3)$ to $\gamma(0,2)$ fluorescence intensity when the NO pressure was raised from 0.16 to 0.68 Torr (and when N_2 addition reduced the absolute magnitudes of the bands) would certainly not be expected. It appears, therefore, that the 2288-Å emission from the zinc lamps is too weak to cause appreciable error in any case.

Finally, an experiment was done in which the conditions necessary for $Cd(^1P_1)$ sensitized production of the NO $\gamma(0,x)$ bands were created in the flow tube (vapor pressure of cadmium at 290 °C, ~ 0.3 Torr of NO, 2 Torr of Ar).² Strong $\gamma(0,x)$ bands were again observed with cadmium lamp excitation, but immediate exposure of the flow tube to zinc lamp excitation for the same period of time produced no detectable NO $\gamma(0,x)$ band emission.

No evidence of NO β -band emission was observed in these experiments, even though $Zn(^1P_1)$ has sufficient electronic energy to populate $NO(B\ ^2\Pi_i, \nu = 0, 1)$. Because the lifetime of $NO(B\ ^2\Pi_i)$ is ~ 12 times longer than $NO(A\ ^2\Sigma^+)$, self-quenching would reduce markedly the detection efficiency for NO β -band emission.³

Discussion

The highly preferential formation of the $\nu = 1$ vibrational level of $NO(A\ ^2\Sigma^+)$ vs. the $\nu = 0$ level in the energy transfer from $Zn(^1P_1)$ is certainly suggestive of some kind of near-resonant coupling, and dipole–dipole interaction could be responsible. We show here that the dipole–dipole interaction does appear to offer the best explanation of such a favorable population of the $\nu = 1$ level, although some portion of the $\nu = 0$ (and possibly the $\nu = 1$) population likely results from

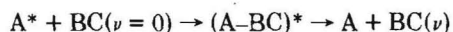
some other parallel mechanism. Considered first are the predictions of the Gordon–Chiu dipole–dipole theory.^{2–6} We then discuss other models for electronic-to-vibrational energy transfer, in an attempt to fit the $\nu = 1$ to $\nu = 0$ population ratio to any other reasonable model of the collisional transfer process.

Dipole–Dipole. Use of the Gordon–Chiu theory has been discussed previously.² The cross section for reaction 0 can be calculated in the same fashion as before, with the off-resonance energy, $\Delta E \approx 2600 \text{ cm}^{-1}$, resulting in the computed cross section $\sigma_0 = 0.40 \text{ \AA}^2$. (The radiative lifetime of Zn(¹P₁) was taken to be $1.4 \times 10^{-9} \text{ s}$.¹⁴) Because the Zn(¹P₁) electronic energy corresponds to a frequency which falls within the rotational band structure of the NO $\gamma(1,0)$ band, an accurate theoretical calculation of the overall cross section cannot be made without considering each of the rotational line energies and transition moments, then doing a collective sum over each rotational transition cross section weighted by the relative Boltzmann population of the particular rotational level of ground-state NO(X ²Π_{1/2}) or NO(X ²Π_{3/2}).⁶ For present purposes, however, such a calculation is unwarranted since we are interested only in showing that the dipole–dipole theory predicts a much greater cross section for reaction 1 than reaction 0. Elementary considerations of the Boltzmann rotational population, of the NO $\gamma(1,0)$ rotational band structure, and of the dependence of the dipole–dipole cross section on ΔE indicate that if we choose an average effective off-resonance energy $\langle \Delta E \rangle \approx 150 \text{ cm}^{-1}$, the calculated overall cross section will be correct to within a factor of 2. The estimated cross section is computed to be $\sigma_1 \approx 17 \text{ \AA}^2$, leading to the predicted ratio $k_1/k_0 = 43$. Even though this ratio cannot be directly reconciled with the smaller experimental value of 10.3, the dipole–dipole model, as expected, correctly predicts the predominant production of the $\nu = 1$ state. A minor competing collision mechanism in which the $\nu = 0$ level is the favored exit channel could easily rationalize the difference between the predicted and observed population ratios.

Franck–Condon. If the electronic energy is transferred in a manner similar to absorption of light energy of the appropriate wavelength (i.e., without regard to the amount of energy converted to translation), the ratio k_1/k_0 would simply be the ratio of the Franck–Condon factors for the NO $\gamma(1,0)$ and NO $\gamma(0,0)$ band, or $0.26/0.16 = 1.6$. This model is obviously incorrect, as might be expected in view of much data which are inconsistent with such a hypothesis.¹⁵

We now consider more sophisticated models which also utilize the Franck–Condon principle, but with reference to the process of sudden switching of potential surfaces in some region of the atom–diatomic interaction potential (i.e., at some point in a collision where the internuclear separation of the diatomic has been changed due to interaction with the excited atom). The models use adjustable parameters to fit observed vibrational population distributions.

Golden Rule (Berry).¹⁶ For the E-to-V energy transfer process



the (ABC)* complex may be characterized as a diatomic BC oscillator perturbed (“clothed”) by the presence of the A atom. If the B–C separation R^\ddagger in the complex is known, the force constant k^\ddagger of the clothed oscillator may be calculated using Badger’s rule.¹⁷ At that point in the collision when $R_{BC} = R^\ddagger$, the potential curve for the clothed oscillator is switched off, and the potential curve for the product BC state is switched on. With this “sudden approximation” the relative proba-

bilities for the different product levels may be calculated using a simple golden rule expression:

$$P_\nu = \frac{2\pi}{\hbar} |\langle 0|\nu \rangle|^2 \rho_\nu(\epsilon)$$

The overlap integrals $\langle 0|\nu \rangle$ are taken between the zeroth level of the clothed oscillator and various levels ν of the product oscillator. The statistical level densities ρ_ν depend on ϵ , the total energy released. Use of the sudden approximation implies that no exchange with the translational-continuum can occur during the second half of the collision, which is regarded as instantaneous.

Golden rule calculations were performed for the processes 0 and 1. This ratio P_1/P_0 was evaluated for a series of clothed NO oscillator separations. Agreement with the observed ratio $k_1/k_0 = 10.3$ was found for $R_{NO^\ddagger} > 2.2 \text{ \AA}$, which may be compared to the equilibrium distances 1.15 and 1.06 \AA for the X ²Π and A ²Σ⁺ states, respectively. Because the Franck–Condon factors for such a crossing are calculated to be $\sim 10^{-48}$, however, the absolute surface-crossing probability would be much too low to account for the large minimum cross section determined experimentally. Even adding an amount of translational energy equal to $\frac{3}{2}kT$ to the available energy (which improves the density-of-states probability of $\nu = 1$ vs. $\nu = 0$), R_{NO^\ddagger} must equal 1.50 \AA before $k_1/k_0 = 9.6$, with Franck–Condon factors which are still on the order of only 10^{-13} . Values of k_1/k_0 for calculations with several values of R_{NO^\ddagger} are shown in Table I. Note that for more reasonable R_{NO^\ddagger} distances, the k_1/k_0 ratios are less than one, so that such a parallel energy transfer path could well account for the lowering of the experimental k_1/k_0 value from that predicted by dipole–dipole theory. The Franck–Condon factors are also more reasonable for a moderate cross section; for example, the calculated Franck–Condon factors are still ~ 0.002 even when $R^\ddagger = 1.26 \text{ \AA}$.

Impulsive “Half-Collision” Model (Simons).¹⁸ The impulsive “half-collision” model combines both classical and quantum theory in the treatment of translation-to-vibration coupling of an atom with a diatomic oscillator. In contrast to the golden rule calculation, the excitation energy of the incident atom is partitioned between BC vibration and relative translation of the recoiling particles.

The formation of an initial complex (ABC)* is postulated, followed by a crossing to a repulsive surface which correlates with the product states of A and BC. The model allows for a change in the BC equilibrium internuclear distance in going to the new electronic state of the complex (which is repulsive only with respect to A + BC). This leads to a set of Franck–Condon factors for overlap of free BC with the BC oscillator ($R_{BC} = R^\ddagger$) as located in the repulsive ABC complex which determine an initial distribution over the levels “i”.

Oscillators initially in a given state “i” will be found in a range of states “f” after recoil. The recoil transition probabilities $P_{i \rightarrow f}$ are calculated using a quantum mechanical expression given in ref 18. The average energy transferred into vibration, a parameter used in the calculation of $P_{i \rightarrow f}$, is found classically from

$$\langle \Delta E \rangle = \frac{1}{2\mu} |f(\omega)|^2$$

where ω is the oscillator frequency, μ its reduced mass, and $f(\omega)$ the Fourier transform of the repulsive (normally exponential) force between A and BC during recoil. The final distribution is calculated by summing the probabilities $P_{i \rightarrow f}$ over initial states i , each weighted by the appropriate Franck–Condon

TABLE I: Experimental Determination of k_1/k_0 and Predictions of Theoretical Models (See Text)

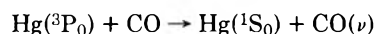
		k_1/k_0
Experimental (this work)		10.3 ± 1.7
Dipole-dipole model (Gordon-Chiu)		43 ± 21
Franck-Condon model		1.6
Single ionic curve-crossing model (see text)		1.8, 2.5
Golden rule model (Berry)		
ϵ, cm^{-1}	$R^\dagger, \text{\AA}$	
2546	1.00	0.024
2546	1.06	0.00
2546	1.15	0.048
2546	1.37	0.68
2546	2.20	8.9
3275	1.50	9.6
Impulsive half-collision model (Simons)		
$R^\dagger, \text{\AA}$	$L, \text{\AA}$	
1.00	0.12	4.7
1.08	0.12	1.0
1.15	0.12	0.0
1.21	0.12	0.760
1.37	0.12	10.1
1.37	0.20	10.1

factor. R^\dagger is treated as a variable parameter (along with the exponential range parameter L) to give the best agreement with experiment.¹⁸

This model provides a more plausible fit of the data, because for $k_1/k_0 = 10.1$, $R^\dagger \approx 1.37 \text{ \AA}$, and since the Franck-Condon overlap is in this case between the intermediate state and $\text{NO}(X^2\Pi)$, the absolute Franck-Condon factor for $\nu = 1$ production has a more reasonable value of 0.001. With a Franck-Condon factor as large as this, a cross section on the order of 1 \AA^2 might just be possible if the surface-crossing probability were high, but the model would seem to be inconsistent with a cross section larger than 1 \AA^2 .

The energy released in the process $\text{Zn}(^1P_1) + \text{NO}(X^2\Pi) \rightarrow \text{Zn}(^1S_0) + \text{NO}(A^2\Sigma^+)$ is the difference between the electronic terms for $\text{Zn}(^1P_1)$ and $\text{NO}(A^2\Sigma^+)$, or about 2600 cm^{-1} . This corresponds to an average energy transferred (ΔE) of less than 10^{-4} vibrational quanta. The energy transferred during recoil therefore has a negligible effect on the final distribution, which is determined solely by the Franck-Condon factors.

We have also made a direct comparison of the impulsive "half-collision" model and the golden rule model using recent experimental data¹⁹ for the quenching of $\text{Hg}(^3P_0)$ by CO:



The golden rule expression with $R_{\text{CO}^\dagger} = 1.32 \text{ \AA}$ gives a good fit¹⁶ of the CO vibrational distribution. It is also important to note that the average Franck-Condon factor for $\text{CO}(\nu = 2-9)$ calculated using the "golden rule" model and $R^\dagger = 1.32 \text{ \AA}$ is ~ 0.1 , which is consistent with a cross section of 2 \AA^2 for quenching of $\text{Hg}(^3P_0)$ by CO.¹⁹

On the other hand, the "impulsive half-collision" model overestimates the width of the $\text{CO}(\nu)$ distribution curve for all values R^\dagger . The exponential range parameter L was easily adjusted to fit the peak of the experimental distribution, but

the best fit of the width of the distribution was obtained with R^\dagger unchanged from free CO, so the Franck-Condon part of the model in *this* case only worsens the possible fit compared to a purely impulsive recoil model. We therefore believe that the use of the "impulsive half-collision" model for E-to-V energy transfer should be viewed with some skepticism in its present form, although the model has been applied successfully to bimolecular exchange reactions²⁰ and to photodissociation.¹⁸

Charge-Transfer Surface Crossing. A general mechanism involving the intersection of potential surfaces which correlate asymptotically with $M^+ + XY^-$ has been used successfully to treat quenching of excited alkali atoms M^* by certain quenchers XY .^{21,22} The model can also be used to predict the vibrational distribution of product XY^* .²² A series of repulsive potential curves $M + XY(\nu)$ (parallel at large R) is constructed up to the energy allowed by $M^* + XY(\nu = 0)$. Another set of attractive curves $M^+ + XY^-(\nu)$ (also parallel at very large R) is constructed, assuming a Coulombic (+ adjustable polarizability) attractive force, all of which cross both the $M^* + XY(\nu = 0)$ repulsive curve(s) as well as all the $M + XY(\nu)$ curves. A complicated grid of surface crossings leading to products $M + XY(\nu)$ is therefore constructed, and an incoming $M^* + XY$ is allowed to proceed statistically through this maze of crossings until there is a net exit as some $M + XY(\nu)$ state. Crossing probabilities are calculated using a Landau-Zener model. The transition matrix element is a product of an electronic component (derived from the Hasted-Chong correlation) and the vibrational overlap at the crossing point (obtained from estimated Franck-Condon factors). The likely importance of $\text{Cd}^+ - \text{NO}^-$ charge-transfer surface intersections in the quenching of $\text{Cd}(^1P_1)$ by $\text{NO}(X^2\Pi)$ has been discussed in the previous paper,² and there is no reason to believe that such surfaces will be any less important in the $\text{Zn}(^1P_1) + \text{NO}(X^2\Pi)$ case, since the ionization potentials of $\text{Zn}(^1P_1)$ and $\text{Cd}(^1P_1)$ are 83 and 82 kcal/mol, respectively.

The surface grid for the process $\text{Zn}(^1P_1) + \text{NO}(X^2\Pi) \rightarrow \text{Zn}(^1S_0) + \text{NO}(A^2\Sigma^+, \nu = 0, 1)$ is much simpler, with only four or six grid points being important (neglecting the fact that $\text{Zn}(^1P_1) + \text{NO}(X^2\Pi)$ can correlate with several repulsive states). All the other possible product exit channels must be included, however, for the model to be correct.² We therefore make no attempt to perform a detailed calculation using this model, but we do note that in the case of quenching of excited alkali atoms by N_2 , the near-resonant channel is always much lower in probability than other $\text{N}_2(\nu)$ exit-channel levels.²²

We have performed a calculation using the Simons "half-collision" model,¹⁷ but with $\text{Zn}^+ - \text{NO}^-$ as the intermediate complex, neglecting the repulsive half-collision. Spectroscopic information for NO^- was taken from experimental data ($R^\dagger = 1.26 \text{ \AA}$, $\omega_e \approx 1500 \text{ cm}^{-1}$).²³ For such a single-crossing model, then, we calculate $k_1/k_0 = 2.5$. This corresponds to neglecting differences in the electronic part of the transition matrix element and also ignoring the other grid points of the crossings $\text{Zn}^+ - \text{NO}^-(\nu)$, where $\nu > 0$, but inclusion of these factors would undoubtedly favor net production of $\text{NO}(A^2\Sigma^+, \nu = 0)$.²² A similar calculation using the Berry "golden rule" model (using actual NO^- data instead of relying on Badger's rule), yields $k_1/k_0 = 1.8$. A simple charge-transfer model cannot therefore rationalize the experimental ratio of $k_1/k_0 = 10.3$.

Summary

We have demonstrated that $\text{NO}(A^2\Sigma^+)$ can be produced by energy transfer from $\text{Zn}(^1P_1)$, and that the production of the $\nu = 1$ vibrational level, reaction 1, predominates over that

of the $\nu = 0$ level, reaction 0: $k_1/k_0 = 10.3 \pm 1.7$. The overwhelming preference for the near-resonant exit channel is likely due to a mechanism involving the long-range interaction of transition dipoles (dipole-dipole theory), but a minor parallel surface-crossing mechanism is probably involved, since dipole-dipole theory predicts a larger k_1/k_0 ratio than is determined experimentally.

Further work is planned with a more sophisticated fluorescence apparatus, and attempts will be made to obtain the initial rotational distributions in the $\nu = 0$ and $\nu = 1$ levels of NO(A $^2\Sigma^+$), as well as absolute cross sections for each exit channel and the overall process of quenching of Zn(1P_1) by NO(X $^2\Pi$). Such information is necessary to provide further evidence concerning the dipole-dipole mechanism.

The shape of the $\gamma(1,x)$ bands sensitized by Zn(1P_1) are apparently blue-shaded more than expected on the basis of a Boltzmann population, indicating a preferentially high initial rotational level distribution, which would be predicted since the Zn 2138-Å line lies closest to transitions terminating in higher rotational levels of NO(A $^2\Sigma^+$, $\nu = 1$)^{3,4,24} (i.e., R_1 ($22\frac{1}{2}$), Q_1 ($29\frac{1}{2}$), S_{21} ($17\frac{1}{2}$), etc.), but definite confirmation must await successful high-resolution experiments.

Acknowledgments. Acknowledgment is made to the donors of the Petroleum Research Fund, administered by the American Chemical Society, for partial support of this research. We also gratefully acknowledge support from the National Science Foundation (Grant No. MPS 75-12851).

The authors wish to thank Dr. Michael Berry for making available the computer program with which the calculations based on his model were performed, Dr. J. P. Simons (Birmingham University) for helpful correspondence, and Dr.

Jack Simons (University of Utah) for several stimulating discussions as well as for advice on the computer programs.

References and Notes

- (1) Dreyfus Foundation Teacher-Scholar.
- (2) W. H. Breckenridge and J. FitzPatrick, *J. Phys. Chem.*, preceding paper in this issue.
- (3) L. A. Melton and W. Klemperer, *J. Chem. Phys.*, **59**, 1099 (1973).
- (4) L. Melton, Ph.D. Thesis, Harvard University, 1972.
- (5) R. G. Gordon and Y. Chiu, *J. Chem. Phys.*, **55**, 1469 (1971).
- (6) E. W. Fink, D. Wallach, and C. Bradley Moore, *J. Chem. Phys.*, **56**, 3608 (1972).
- (7) H. Habeeb, D. J. LeRoy, and F. W. R. Steacie, *J. Chem. Phys.*, **10**, 261 (1942).
- (8) P. Bender, *Phys. Rev.*, **36**, 1543 (1930).
- (9) S. Hirokami and S. Sato, *J. Chem. Soc. Jpn.*, **41**, 2226 (1968).
- (10) P. J. Young, G. Greig, and O. P. Strausz, *J. Am. Chem. Soc.*, **92**, 413 (1970).
- (11) A. Landman and R. Novick, *Phys. Rev.*, **134**, A56 (1964).
- (12) P. D. Morten, C. G. Freeman, R. F. C. Claridge, and L. F. Phillips, *J. Photochem.*, **3**, 285 (1974).
- (13) R. P. Blickensderfer, W. H. Breckenridge, and J. Simons, *J. Phys. Chem.*, **80**, 653 (1976).
- (14) A. Lurio, R. L. de Zafra, and R. J. Goshen, *Phys. Rev. A*, **134**, 1198 (1964).
- (15) R. D. Levine and R. B. Bernstein, "Molecular Reaction Dynamics", Oxford University Press, New York, N.Y., 1974; A. C. Vikis and D. J. LeRoy, *Chem. Phys. Lett.*, **21**, 103 (1973); **22**, 587 (1973).
- (16) M. J. Berry, *Chem. Phys. Lett.*, **29**, 323, 329 (1974).
- (17) H. S. Johnston, "Gas Phase Reaction Rate Theory", Ronald Press, New York, N.Y., 1966, p 72.
- (18) J. P. Simons and P. W. Tasker, *Mol. Phys.*, **26**, 1267 (1973).
- (19) Y. Fushiki and S. Tsuchiya, *Chem. Phys. Lett.*, **22**, 47 (1973).
- (20) J. P. Simons and P. W. Tasker, *J. Chem. Soc., Faraday Trans. 2*, **70**, 1496 (1974).
- (21) P. J. Lijnse, *J. Quant. Spectrosc. Radiat. Transfer*, **14**, 1143 (1974), and references therein.
- (22) E. R. Fisher and G. K. Smith, *Appl. Opt.*, **10**, 1803 (1971); E. Bauer, E. R. Fisher, and F. R. Gilmore, *J. Chem. Phys.*, **51**, 4173 (1969).
- (23) P. W. Thulstrup, E. W. Thulstrup, A. Anderson, and Y. Ohru, *J. Chem. Phys.*, **60**, 3975 (1974), and references therein.
- (24) G. Bourg-Heckly, M. Petitdidier, and S. Cieslik, *J. Quant. Spectrosc. Radiat. Transfer*, **15**, 405 (1975).

Mechanism of the Formation of Cationic Species in the Radiolysis of Butyl Chlorides. 1

Shigeyoshi Arai,* Akira Kira, and Masashi Imamura

The Institute of Physical and Chemical Research, Wako-shi, Saitama 351, Japan (Received December 8, 1975)

Publication costs assisted by The Institute of Physical and Chemical Research

Radiation chemical studies have been carried out on *n*- and *sec*-butyl chlorides using low-temperature pulse radiolysis and matrix isolation techniques. The pulse radiolysis of *n*-butyl chloride at 133 K yields the same absorption spectrum as observed for γ -irradiated *n*-butyl chloride at 77 K. The initial spectrum has a peak at 520 nm, however, the peak shifts to 450 nm within 80 μ s. The absorption decay behavior indicated that the initial spectrum is due to a long-lived species with a peak at 450 nm as well as a short-lived species with a peak at about 550 nm. The effects of additives on both species suggest that the long- and short-lived species are butene cations and *n*-butyl chloride cations, respectively. The spectra of butene-1, *cis*-butene-2, and *trans*-butene-2 cations obtained using a matrix isolation technique also show peaks in the vicinity of 450 nm. In a solution of 0.031 mol % biphenyl at 133 K, a significant amount of biphenyl cations is produced simultaneously with pulse irradiation, although they are also produced slowly by charge transfer between biphenyl molecules and *n*-butyl chloride and butene cations. Addition of biphenyl to *n*-butyl chloride at 77 K reduces the formation of both butene and *n*-butyl chloride cations by the same ratio, and is accompanied by the formation of biphenyl cations. Therefore, butene and *n*-butyl chloride cations must originate from a common precursor, which reacts with biphenyl forming its cation. The nature of the precursor is discussed on the basis of the observed results. It is probably a vibrationally excited *n*-butyl chloride cation. Radiolysis of *sec*-butyl chloride gives results similar to *n*-butyl chloride.

Introduction

Molecular radical cations of aromatic compounds are efficiently produced in the radiolysis of their alkyl halide solutions in both solid^{1,2} and liquid^{3,4} phases. The formation mechanism of solute cations in solids at 77 K has been concisely discussed in a recent review by Hamill.⁵ The first step of the radiolysis is the formation of solvent cations. Although molecular diffusion is hindered in solids, positive charges of solvent cations definitely migrate and finally localize on solute molecules. The high yield of solute cations for even 0.1 mol % solutions indicates that positive charges must migrate over many solvent molecules. However, fundamental understanding of carriers of migrating positive charges, or holes, has not advanced appreciably since the innovative studies by Hamill and his colleague.^{1,5}

The mechanism of the formation of solute cations in liquids has not yet been investigated carefully, although the formation is well established by several pulse radiolysis studies.^{3,4,6} One of the studies⁴ demonstrated that the rates of the formation of aromatic hydrocarbon cations in 1,2-dichloroethane are much faster than those one could expect from a diffusion-controlled reaction.

Steady γ -irradiation of solid pure *n*-butyl chloride at 77 K produces a broad absorption spectrum with a peak at 520 nm.¹ This spectrum must be caused by either cations or products formed by reactions of cations because addition of cation scavengers such as alcohols and amines reduces the spectrum significantly. Thus, it is interesting to elucidate the relationship between these cationic species and the formation of solute cations when a solute is added.

In the present paper solvent cations and the formation mechanism of solute cations have been studied for *n*-butyl chloride and less extensively for *sec*-butyl chloride using low-temperature pulse radiolysis and matrix isolation techniques. We conclude from the effects of scavengers that the spectrum of irradiated pure *n*-butyl chloride is due to *n*-butyl

chloride cations and butene cations. Furthermore, the effect of biphenyl on the spectrum of irradiated solid *n*-butyl chloride at 77 K suggests that both *n*-butyl chloride and butene cations originate from a common precursor, which produces a biphenyl cation on encounters with biphenyl. In a *n*-butyl chloride solution of biphenyl at 133 K, solute cations are formed in a rapid process which occurs simultaneously with pulse irradiation and in a slow process which occurs concurrently with the decays of *n*-butyl chloride and butene cations. The former process may be the same as that occurs in a solution at 77 K; the latter is ascribed to charge transfer from *n*-butyl and butene cations to biphenyl. The nature of the precursor is discussed in the light of the observed results.

Experimental Section

The pulse radiolysis methods in our laboratory and the low-temperature apparatus for pulse radiolysis have been described in detail in previous papers.⁷⁻⁹ The source of electron pulses was a Mitsubishi Van de Graaff accelerator. The energy was 2.7-2.8 MeV; the width was selected among 0.5, 1, 2, and 5 μ s. The current was adjusted in the range up to 200 mA to give suitable intensities of transient absorptions for observation. Two different types (denoted by A and B) of apparatus were used for pulse radiolysis at low temperatures. The diagram and device have also shown in previous papers.^{8,9} The temperature was variable down to 120 K for the A type and was constant at approximately 100 K for the B type. Dimensions of an optical cell for the A type (optical cell A) were 1.2 cm in the direction of the electron beam and 2.2 cm in the direction of the analyzing light beam; those for the B type (optical cell B) were 1.0 cm in both directions. Analyzing light beams passed twice through an optical cell. The optical detection system used here was exactly the same as described previously.⁷⁻⁹

In the matrix isolation experiment samples were sealed in an optical cell with a thickness of 1.5 mm and irradiated at 77

K with γ rays from ^{137}Cs - ^{60}Co at a dose rate of $41\,000$ rad min^{-1} . The absorption spectra of irradiated samples were measured at 77 K on a Cary spectrometer Model 14R.

Butyl chlorides and bromides from Wako Pure Chemical Industries were repeatedly shaken with concentrated sulfuric acid and washed with water and a solution of sodium bicarbonate. Then the butyl halides were shaken with a solution of sodium hydroxide, washed with water, dried with calcium chloride, and fractionally distilled. Biphenyl (zone refined) from Tokyo Kasei Co. and butenes from Takachiho Shoji Co. were used without further purification. All samples were sealed in vacuo.

Results

Pulse irradiation of *n*-butyl chloride at low temperatures produces intense transient absorptions throughout the visible and uv regions. Figure 1 presents time-resolved spectra of *n*-butyl chloride irradiated at 133 K . The spectrum determined at $2\ \mu\text{s}$ after the pulse has a peak at 520 nm and resembles the spectrum of γ -irradiated solid *n*-butyl chloride at 77 K (see Figure 7). The peak, however, shifts to 450 nm within approximately $80\ \mu\text{s}$ and thereafter remains at the same wavelength. The observed spectral change indicates that the initial spectrum is caused by several absorbing species with different lifetimes. A detailed analysis of the decay behavior of the absorption at each wavelength makes it possible to specify the absorbing species. Figure 2 shows the decay curves of absorptions at 600 , 525 , 450 , and 310 nm . Absorptions at wavelengths above 600 nm disappear within $150\ \mu\text{s}$ in a similar manner, and therefore they are ascribed to a single absorbing species. The absorptions below 600 nm consist of two components, one with the same lifetime as the above mentioned species and the other with a longer lifetime. The former is, no doubt, due to the same species that absorbs light above 600 nm ; the latter is due to a species with an absorption maximum at 450 nm . In decay curves below 350 nm there is a contribution due to another absorbing species with a lifetime much longer than those of the other two species, although its absorption is negligibly small in the early spectrum in Figure 1. This long-lived absorption is observable at room temperature in the presence of methanol, and therefore ascribed to a neutral radical. The species was not subject to further study because it is probably a radical.

Figure 3 presents the spectra obtained at 133 K on the pulse radiolysis of a *n*-butyl chloride solution of 0.055 mol \% biphenyl. The initial spectrum comprises the absorption due to biphenyl cations and those observed for pure *n*-butyl chloride. The subsequent spectrum, however, involves only biphenyl cations. Comparison of the decay curves in the presence and absence of biphenyl shows that biphenyl reduces the lifetimes of both short- and long-lived species produced from *n*-butyl chloride. Furthermore, their decays are concurrent with the formation of a certain portion of biphenyl cations, as explained later in detail. This fact suggests that both short- and long-lived species are definitely cations and produce biphenyl cations by reactions with biphenyl.

The two species produced from *n*-butyl chloride differ remarkably from each other in reactivity toward butene-1 and *n*-butyl bromide. Several decay curves and the absorption spectra in the presence of these compounds are shown in Figures 4 and 5. The decay rates of absorptions at longer wavelengths increase with increasing concentration of butene-1 or *n*-butyl bromide. On the other hand, the decay rate of the absorption at 450 nm scarcely changes on addition of these compound with the exception of the component due to

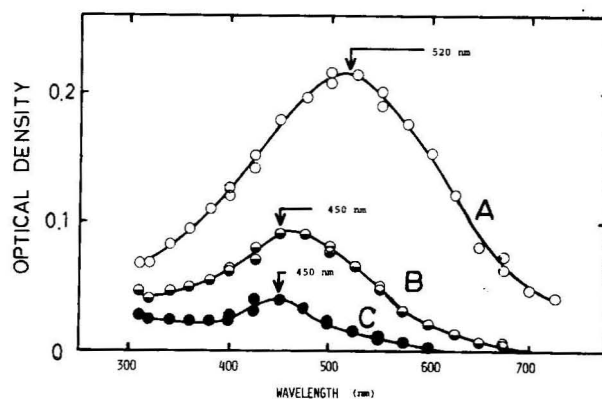


Figure 1. Transient absorption spectra for *n*-butyl chloride irradiated at 133 K with $2\text{-}\mu\text{s}$ pulses at 180 mA .²¹ The spectra were determined at $2\ \mu\text{s}$ (A), $80\ \mu\text{s}$ (B), and $305\ \mu\text{s}$ (C) after the pulse. Optical cell A was used.

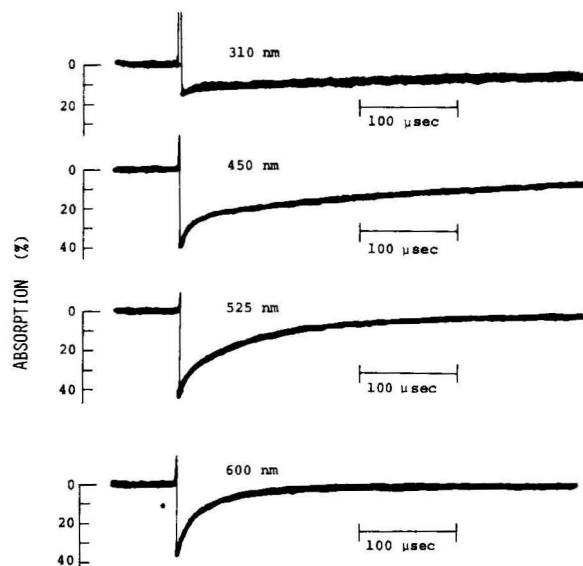


Figure 2. Decay curves of absorptions for *n*-butyl chloride irradiated at 133 K with $2\text{-}\mu\text{s}$ pulses at 180 mA .

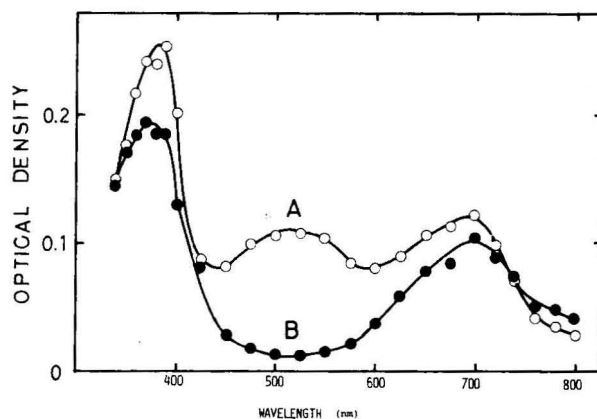


Figure 3. Transient absorption spectra for a *n*-butyl chloride solution of 0.055 mol \% biphenyl irradiated at 133 K with $2\text{-}\mu\text{s}$ pulses at 180 mA . These spectra were determined immediately (A) and at $55\ \mu\text{s}$ (B) after the pulses. Optical cell A was used.

the species observed at longer wavelengths. The difference in reactivity is reflected on the spectra of solutions. In a solution of 0.11 mol \% *n*-butyl bromide an absorption peak is initially located at 500 nm as shown in Figure 5. The peak shifts to 450

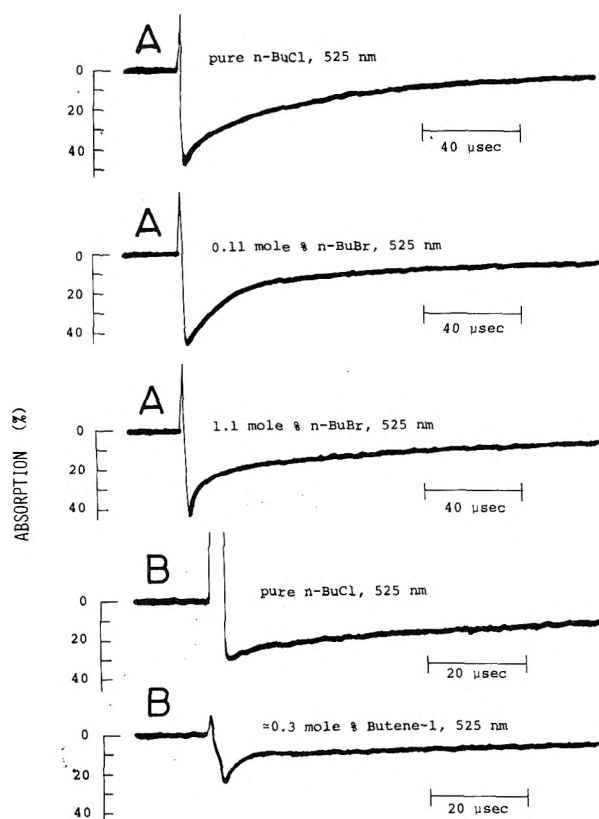


Figure 4. Decay curves obtained at 133 K for pure *n*-butyl chloride and its solutions of *n*-butyl bromide (series A) and butene-1 (series B). The concentration of butene-1 was calculated on the assumption that all butene-1 added was dissolved into *n*-butyl chloride. Series A and B were under different pulse conditions. Optical cell A was used.

nm after 55 μ s. In a solution of 1.1 mol % *n*-butyl bromide or 0.3 mol % butene-1, however, the peak is located in the vicinity of 450 nm even at 2 μ s after the pulse. The absorbing species at longer wavelengths may be scavenged efficiently in these solutions before determination of the spectra. There seems to be an intense absorption band below 400 nm in an irradiated concentrated solution of *n*-butyl bromide. The identification has not been made at this moment.

$C_4H_8^+$ is the most abundant in the mass spectrum of *n*-butyl chloride bombarded with 75-V electrons.¹⁰ Therefore, we consider that a butene cation is one of the cations produced in the radiolysis of *n*-butyl chloride. The mass spectrometric study, however, cannot indicate whether butene-1 or butene-2 cations are produced, although experimental results¹¹ suggest the occurrence of 1,3 elimination of HCl from *n*- $C_4H_9Cl^+$ rather than 1,2 elimination.

1,3 elimination might result in the formation of *cis*- or *trans*-butene-2 cations. For the purpose of obtaining the spectra of all butene cations, *n*-butyl chloride solutions of butene-1, *cis*-butene-2, and *trans*-butene-2 were irradiated with γ rays at 77 K. In these solutions holes are expected to be trapped by butenes forming their cations. As seen in Figure 6 all spectra have peaks at around 440 nm and almost similar spectral shapes. It is important that the spectra of butene cations obtained here resemble the spectrum of the long-lived species produced in the pulse radiolysis of *n*-butyl chloride at 133 K. This fact strongly supports an assignment of the long-lived species to a butene cation. The spectra of butene solutions imply the existence of large bands below 300 nm. These bands correspond to species other than butene cations,

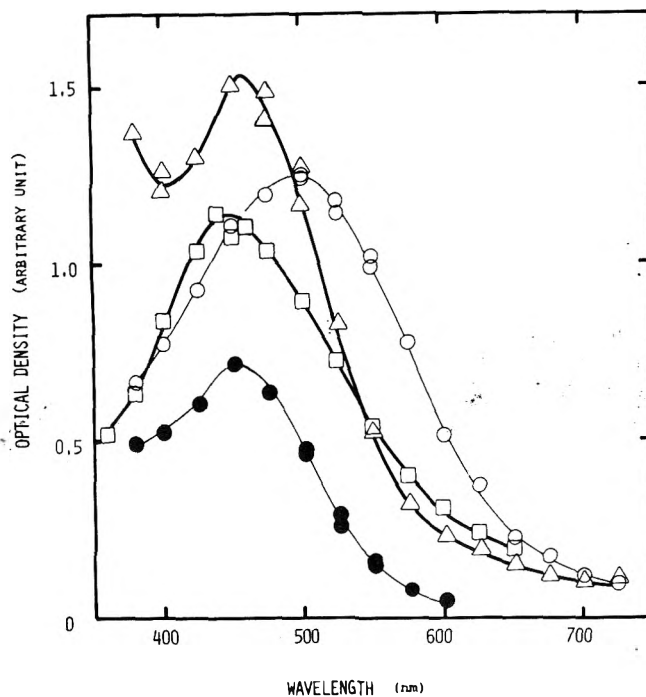


Figure 5. Transient absorption spectra obtained at 133 K for *n*-butyl chloride solutions of *n*-butyl bromide and butene-1. Circles and solid circles show the spectra determined at 2 and 55 μ s after the pulse for 0.11 mol % *n*-butyl bromide solution, respectively; triangles and squares show the spectra determined at 2 μ s after the pulse for 1.1 mol % *n*-butyl bromide and about 0.3 mol % butene-1 solutions, respectively. The spectrum for butene-1 was under different pulse conditions from those used for *n*-butyl bromide. Optical cell A was used.

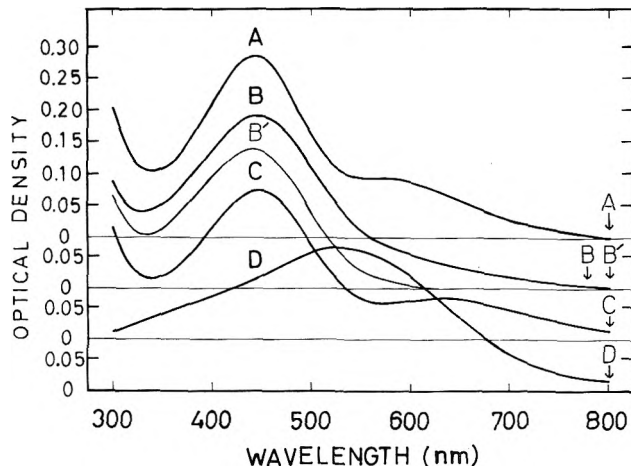


Figure 6. Absorption spectra for *n*-butyl chloride solutions of 2 mol % *cis*-butene-2 (A), 2 mol % butene-1 (B), and 2 mol % *trans*-butene-2 (C), and for pure *n*-butyl chloride (D). Spectrum B' was measured after illumination of spectrum B with a tungsten lamp for 1 min.¹² The base line of each spectrum is indicated by an arrow. All samples were irradiated at 77 K with γ rays to a dose of 2.1×10^5 rads. The concentrations of butenes were calculated on the assumption that butenes were completely dissolved into *n*-butyl chloride.

probably to neutral radicals. The pulse radiolysis of a *n*-butyl chloride solution of butene-1 at 133 K showed that absorptions around 300 nm decay much more slowly than the absorption at 450 nm does. Small peaks around 600 nm observed for *cis*- and *trans*-butene-2 in Figure 6 may be ascribed to dimer cations of these butenes.^{13,17}

The pulse radiolysis of *n*-butyl chloride at 133 K gives a broad spectrum due to both short- and long-lived species. The

decay behavior of the short-lived species is directly shown in decay curves at long wavelengths, for example, at 625 nm where there is no contribution due to the long-lived species. The decay curve fits neither first- nor second-order kinetics, indicating that the decay may be caused by a combination of several different reactions. The decay curve at 450 nm can be resolved into a long-lived component which approximately fits first-order kinetics, and a short-lived component which exhibits the same decay as observed at 625 nm. However, first-order kinetics is applicable to only an initial half of the whole decay of the long-lived component. Therefore, the corresponding species disappears in a complicated mechanism, too. As mentioned before, the long-lived component is caused by butene cations. The intensity of the component at 2 μ s after the pulse can be estimated to be 60% of the total optical density. Figure 7b presents the initial spectrum for pulse-irradiated *n*-butyl chloride as well as the spectrum of butene-1 cations obtained in the matrix isolation experiment. (Since all butene cations have almost similar spectral shapes, the spectrum of butene-1 cations has been tentatively used in Figure 7b as that of the long-lived species.) The intensity of the spectrum of butene-1 cations is normalized to 60% of the initial spectrum at 450 nm. The difference between both spectra corresponds to the spectrum of the short-lived species, which has a peak at 550 nm.

The results obtained here correlate well with findings in the photobleaching experiment.¹ Illumination of γ -irradiated solid *n*-butyl chloride at 77 K with a tungsten lamp remarkably reduces the absorption at longer wavelengths and results in a peak at 450 nm as shown in Figure 7a. The bleached component corresponds to the species with a shorter lifetime in pulse radiolysis; the remaining absorption corresponds to the species with a longer lifetime as it also has a peak at 450 nm. The difference between the spectra before and after illumination gives an absorption with a maximum at 550 nm, which agrees with the spectrum of the species with a short lifetime in pulse radiolysis.

The previous study has demonstrated¹ that γ irradiation of a *n*-butyl chloride solution of biphenyl at 77 K results in the formation of biphenyl cations. At concentrations lower than 0.15 mol %, irradiation gives the absorption of biphenyl cations as well as the absorption observed for pure solid *n*-butyl chloride. Figures 8 and 9 present the results obtained with 0.052 and 0.095 mol % solutions. These spectra apparently involve biphenyl cations and the absorbing species originating from *n*-butyl chloride. It must be emphasized in Figures 8 and 9 that the spectral component originating from *n*-butyl chloride decreases without change in shape with increasing concentration of biphenyl. Illumination of the spectra in Figures 8 and 9 with a tungsten lamp reduced the component originating from *n*-butyl chloride and enhanced appreciably the component due to biphenyl cations. Such an enhancement was observed more clearly when *trans*-stilbene was used as a solute.

The pulse radiolysis of *n*-butyl chloride solution of 0.052 mol % biphenyl was carried out at 100 K in order to obtain information on the formation process of biphenyl cations in the solid phase. Figure 10 shows the rate curves of absorptions at 520 and 700 nm. The absorption at 520 nm is almost entirely due to the absorbing species arising from the solvent; the absorption at 700 nm is mainly due to biphenyl cations. The absorptions at both wavelengths grow simultaneously with pulse irradiation and show neither a growth nor decay after the pulse. All the species observed at 100 K are produced within 1 μ s.

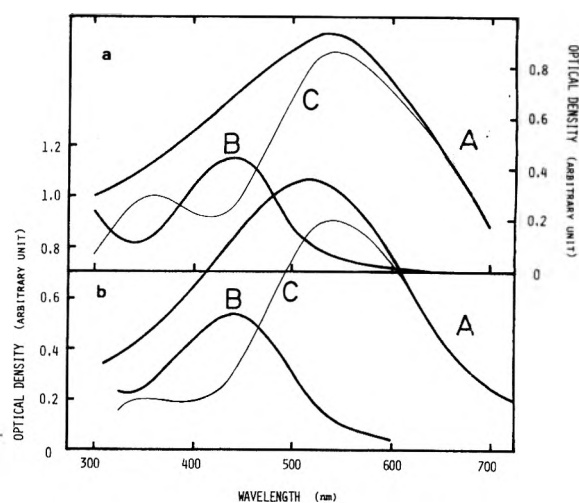


Figure 7. (a) Absorption spectra for γ -irradiated solid *n*-butyl chloride before (A) and after (B) photoillumination as well as the difference spectrum (C).¹ (b) Total absorption spectrum (A) as well as the spectra of long-lived (B) and short-lived (C) species when *n*-butyl chloride was irradiated at 133 K with electron pulses. Since the long-lived species was identified with a butene cation, the spectrum of the butene-1 cation was used for B (see text).

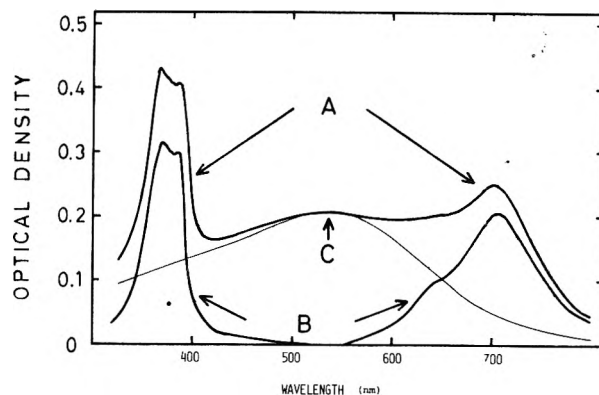


Figure 8. Absorption spectrum of a γ -irradiated solid *n*-butyl chloride solution of 0.052 mol % biphenyl (A), spectrum of a biphenyl cation (B), and spectrum of the component produced from *n*-butyl chloride (C). The dose was 2.1×10^5 rads.

As shown in Figure 3 the initial spectrum of a *n*-butyl chloride solution of biphenyl at 133 K consists of both absorptions of biphenyl cations and of species arising from the solvent. In addition the spectral shape seems similar to that observed at 77 K for the solid solution at similar concentrations. As shown in Figure 10, the formation process of biphenyl cations apparently consists of the rapid portion simultaneous with the pulse irradiation and a slow component concurrent with the decays of the absorptions at 450 and 520 nm. We ascribe the rapid formation to the same mechanism that occurs in a solid solution. The slow formation can be simply interpreted in terms of reactions between biphenyl and the species with long and short lifetimes produced from *n*-butyl chloride. The resemblance of the decay behavior of the absorptions at 450 and 520 nm suggests that both species react with biphenyl at a similar rate.

The results obtained with *sec*-butyl chloride are essentially the same as for *n*-butyl chloride. The pulse radiolysis of *sec*-butyl chloride at 123 K gives the spectra shown in Figure 11. Although the shift is rather small compared with that in the case of *n*-butyl chloride, several independent observations

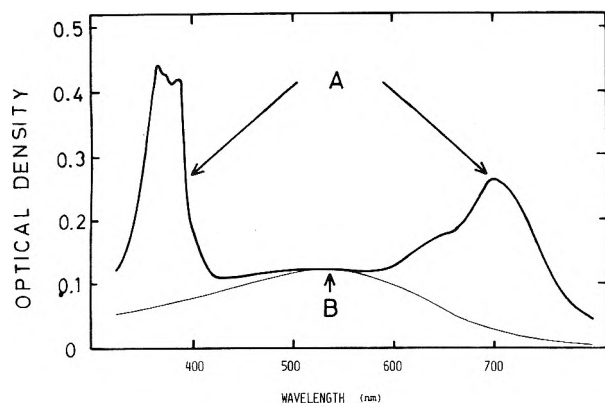


Figure 9. Absorption spectrum of a γ -irradiated solid *n*-butyl chloride solution of 0.095 mol % biphenyl (A) and spectrum of the component produced from *n*-butyl chloride (B). The dose was 2.1×10^5 rads.

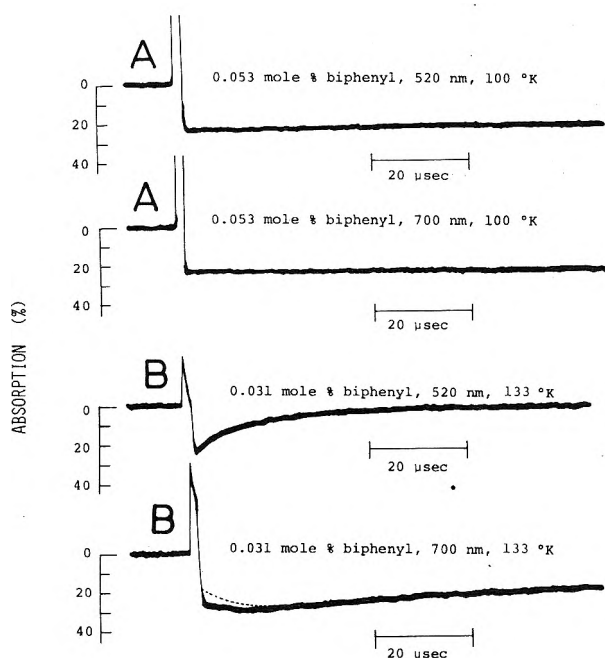


Figure 10. Decay curves for *n*-butyl chloride solutions of biphenyl at 100 (A) and 133 K (B). Dotted line shows the correction for the absorption due to a species produced from *n*-butyl chloride. Apparatus A and B were used for series B and A, respectively.

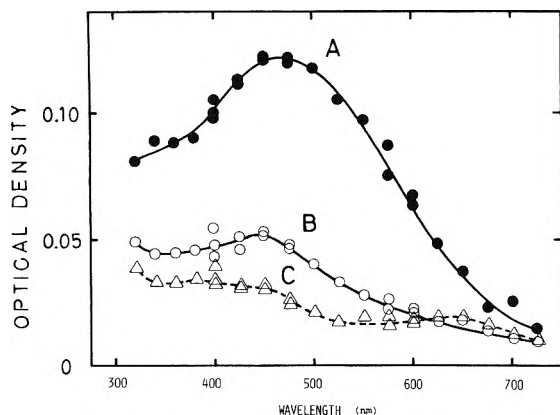


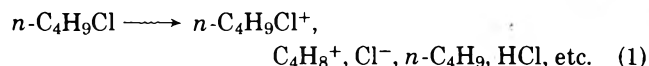
Figure 11. Absorption spectra for *sec*-butyl chloride irradiated at 123 K with 2- μ s pulses at 110 mA. The spectra were determined at 2 (A), 55 (B), and 110 (C) μ s after the pulse. Apparatus A and optical cell A were used.

confirmed that the peak shifts from 480 to 440 nm with time. Decay curves of absorptions at various wavelengths indicate the presence of two absorbing species with peaks at 440 and 540 nm. This finding is consistent with the photobleaching experiment on γ -irradiated solid *sec*-butyl chloride. The spectrum determined at 110 μ s after the pulse has a small peak at 650 nm, as seen in Figure 11. The peak probably arises from impurities because the *sec*-butyl chloride used without purification gives a more intense absorption at the same wavelength.

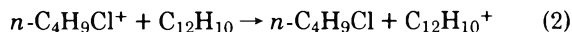
Discussion

A number of studies^{5,14,15} on the radiation chemistry of alkyl halides supports the occurrence of dissociative attachment of secondary electrons to alkyl halides. Therefore, the only initial negative species expected in irradiated *n*-butyl chloride should be chloride anions which absorb far-uv light. Cl_2^- could be formed at a later stage by the reaction between Cl^- and Cl . The absorption maximum of Cl_2^- is, however, located at 350 nm and is different from the spectra in Figure 1. The process of dissociative attachment also yields a *n*-butyl radical. In addition, dissociation of excited molecules and abstraction of H or Cl by atomic species yield various radicals including *n*-butyl radicals. Such alkyl radicals, even if with a chlorine atom as a substituent, usually absorb below 400 nm. In fact, we observed absorbing species which may correspond to neutral radicals below 350 nm.

The results obtained with *n*-butyl chloride solutions of biphenyl indicate that the absorptions in the uv and visible regions are cationic. We conclude from the effects of butene-1 and *n*-butyl bromide on the absorptions that the absorbing species are *n*-butyl chloride and butene cations. The former has a peak at 550 nm with a short lifetime and the latter has a peak at 450 nm with a long lifetime. The primary process of the radiolysis of *n*-butyl chloride is as follows



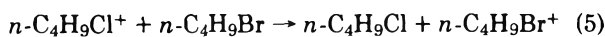
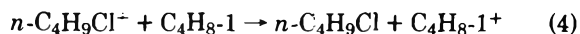
The ionization potentials of *n*- $\text{C}_4\text{H}_9\text{Cl}$, $\text{C}_4\text{H}_8\text{-1}$, *n*- $\text{C}_4\text{H}_9\text{Br}$, and biphenyl ($\text{C}_{12}\text{H}_{10}$) in the gas phase are 10.7, 9.58, 10.13, and 8.27 eV, respectively.¹⁶ We assume that the order of ionization potentials for these compounds will also apply to liquid and solid phases. Therefore, the following charge transfers are expected to occur:



These reactions can account for the reduction of the lifetimes of absorptions at 520 and 450 nm and the concurrent growth of the absorption at 700 nm in the presence of biphenyl. The γ irradiation of solid *n*-butyl chloride solutions of butenes at 77 K gives spectra with peaks at 440 nm. On the basis of numerous previous studies using a matrix isolation technique, the observed spectra are concluded to be due to butene cations. One of olefin cations, a cyclohexene cation, was found to have an absorption band at 430 nm.¹⁷ Satisfactory agreement between the subsequent spectrum in the pulse radiolysis (Figure 1) and the spectra in the matrix isolation experiment provides strong evidence for the assignment of the 450-nm band to butene cations. Since all butene cations have almost similar spectral shapes, we cannot specify the kind of butene cations produced in the radiolysis at the present moment. In the case where *cis*- or *trans*-butene-2 cations are produced, electron transfer such as reaction 3 will occur in the presence

of biphenyl. The nonreactivity of the absorption at 450 nm toward butene-1 or *n*-butyl bromide is understandable because charge transfer reproduces butene cations or, energetically, it cannot take place.

In contrast with the absorption due to butene cations, the absorptions above 600 nm are very reactive toward butene-1 and *n*-butyl bromide. We can ascribe the results to the following reactions

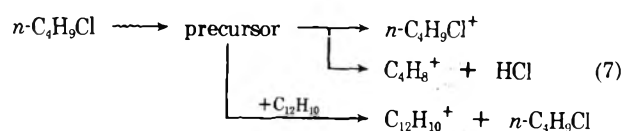


where *n*-C₄H₉Cl-Br represents a charge transfer complex between *n*-C₄H₉Cl and Br. Our pulse radiolysis and matrix isolation studies on *n*-butyl bromide show that irradiated *n*-butyl bromide gives absorption bands at 375 and 580 nm at low temperatures. Previous studies^{14,15,19} as well as our results¹⁸ suggest that the band at 375 nm is assigned to a charge transfer complex and that at 580 nm to a *n*-butyl bromide cation. Upon adding *n*-butyl bromide to *n*-butyl chloride, the absorptions around 580 nm were not observed but those below 400 nm were clearly enhanced. Therefore, we think reaction 6 is more acceptable as a reaction between *n*-C₄H₉Cl⁺ and *n*-C₄H₉Br. A detailed study on butyl bromide will be published shortly.

It is interesting that cations produced in the radiolysis of *n*-butyl chloride, *sec*-butyl chloride, *n*-butyl bromide, and *sec*-butyl bromide have some correlation with the mass spectra of these compounds.¹⁰ Relative abundances of C₄ ions in their mass spectra are as follows: *n*-butyl chloride, C₄H₈⁺ (100), C₄H₉⁺ (7), and C₄H₉Cl⁺ (0.7); *sec*-butyl chloride, C₄H₈⁺ (100), C₄H₉⁺ (88), and C₄H₉Cl⁺ (0.6); *n*-butyl bromide, C₄H₉⁺ (100), C₄H₈⁺ (13), and C₄H₉Br⁺ (13); *sec*-butyl bromide, C₄H₉⁺ (100), C₄H₈⁺ (5), and C₄H₉Br⁺ (0.3). The numbers in parentheses indicate relative abundances normalized to the most prominent ion. Major ions are explained by either the loss of HX or the loss of X from parent ions. The former process predominates in chlorides and the latter is favored in bromides. The abundances of parent ions are extremely low owing to fragmentation. The radiolysis of liquids or solids, as is generally accepted, rapid deactivation of excited parent ions by surrounding molecules may result in an enhancement in yields of parent ions. The peaks at around 450 nm obtained with *n*- and *sec*-butyl chlorides are butene cations arising from the loss of HCl from parent ions. In contrast with chlorides, no peaks are observed for *n*- and *sec*-butyl bromides around 450 nm.¹⁸ This fact suggests that butyl carbonium ions are probably formed instead of butene ions.

It is conceivable in solid *n*-butyl chloride that the positive charge is transferred from a ground-state *n*-butyl chloride cation to a neighboring neutral *n*-butyl chloride molecule and is eventually trapped by a solute molecule. This mechanism is, however, ruled out in solutions at 100 K because the absorptions due to *n*-butyl chloride and biphenyl cations show neither growth nor decay after the pulse. All biphenyl cations are formed during pulse irradiation even at this temperature. The broad spectrum produced from pure *n*-butyl chloride at 77 K is caused by both *n*-butyl chloride and butene cations. Upon adding biphenyl, only its intensity decreases without any change in spectral shape (Figures 8 and 9), although the spectrum of biphenyl cations overlaps. In other words the concentrations of *n*-butyl chloride and butene cations decrease by the same ratio with increasing concentration of biphenyl. This result indicates that both cations originate from

a common precursor, which reacts with biphenyl forming its cation. The reaction scheme can be written as follows:



The hole proposed by Hamill probably corresponds to the precursor in this scheme. We presume that the precursor, evidently cationic, is a presolvated *n*-butyl chloride cation, or vibrationally or electronically excited *n*-butyl chloride cation.

In a *n*-butyl chloride solution of biphenyl at 133 K we observed rapid formation of a significant amount of biphenyl cations. Furthermore, the initial spectrum for the pulse-irradiated solution was similar to that of the γ -irradiated solid solution at the same concentration. These findings suggest that the rapid formation at 133 K occurs according to the same mechanism as in the solid phase at 77 K. Since the rate of the solvation process of ions increases remarkably depending on temperature, the amount of biphenyl cations formed should decrease at a higher temperature if the precursor is a presolvated cation. The possibility of the presolvated cation is excluded because of similar formation efficiency of biphenyl cations at both temperatures. Shank and Dorfman⁴ showed that the rate of the formation of biphenyl cations in 1,2-dichloroethane at 25 °C is much faster than that expected from a diffusion-controlled reaction. They suggested that the formation involves an electron jump process, even in liquid 1,2-dichloroethane at this temperature.

A recent mass spectrometric study¹¹ reports that electron impact of alkyl chlorides usually produces metastable ions which decompose into hydrogen chloride and olefin ions. Such metastable ions are considered to be vibrationally excited *n*-butyl chloride ions.^{11,20} In fact, the ionization potential of *n*-butyl chloride¹⁶ and the appearance potential of its metastable ion¹¹ were determined to be 10.67 and 11.0 eV, respectively. The difference is comparable to vibrational excitation energy. Generally speaking, ionization of molecules by electrons yields vibrationally excited ions according to the Franck-Condon principle. If the incident electron gives additional energy to the molecule, the resulting ion may be in a higher excited state. The ionization in irradiated *n*-butyl chloride is caused by secondary electrons with various amounts of energy leading to the formation of vibrationally excited ions. These ions transfer positive charges and energy to neighboring neutral molecules. The migration may be a succession of such transfers. During migration, vibrationally excited *n*-butyl chloride ions either decompose into butene cations and HCl, or transfer charges to solute molecules on encounters. When the excited ions are deactivated below a certain level, the ions are trapped in a solid or liquid, and/or are then solvated. The ions stabilized in this manner cause the absorption with a peak at 550 nm. Experimental results indicate that photoillumination of the 550-nm band reproduces the precursor of a solute cation, although the efficiency has not yet been determined. The photoexcitation of a *n*-butyl chloride cation may either lead to the formation of a vibrationally excited cation via an electronically excited one, or promote electron transfer from a neighboring neutral molecule. The latter process results in the formation of a *n*-butyl chloride cation in the Franck-Condon state. In conclusion, it is quite probable that the precursor is a vibrationally excited *n*-butyl chloride cation although the possibility of an electronically excited cation cannot be excluded.

References and Notes

- (1) T. Shida and W. H. Hamill, *J. Chem. Phys.*, **44**, 4372 (1966).
- (2) T. Shida and S. Iwata, *J. Am. Chem. Soc.*, **95**, 3473 (1973).
- (3) S. Arai, H. Ueda, R. F. Firestone, and L. M. Dorfman, *J. Chem. Phys.*, **50**, 1072 (1969).
- (4) N. E. Shank and L. M. Dorfman, *J. Chem. Phys.*, **52**, 4441 (1970).
- (5) W. H. Hamill, "Radical Ions", E. T. Kaiser and L. Kevan, Ed., Interscience, New York, N.Y., 1968, pp 321-416.
- (6) H. Ueda, *Bull. Chem. Soc. Jpn.*, **41**, 2578 (1968).
- (7) A. Kira, S. Arai, and M. Imamura, *Rep. Inst. Phys. Chem. Res.*, **47**, 139 (1971).
- (8) S. Arai, S. Tagawa, and M. Imamura, *J. Phys. Chem.*, **78**, 519 (1974).
- (9) S. Arai, M. Hoshino, and M. Imamura, *J. Phys. Chem.*, **79**, 702 (1975).
- (10) F. W. McLafferty, *Anal. Chem.*, **34**, 2 (1962).
- (11) K. C. Kim, J. H. Beynon, and R. G. Cooks, *J. Chem. Phys.*, **61**, 1305 (1974).
- (12) Small absorptions due to incomplete scavenging of holes by butene were seen at long wavelengths in the spectra for all butene solutions. The absorptions were removed by photoillumination.
- (13) S. Arai, unpublished results.
- (14) R. F. C. Claridge and J. E. Willard, *J. Am. Chem. Soc.*, **88**, 2404 (1966).
- (15) R. F. C. Claridge and J. E. Willard, *J. Am. Chem. Soc.*, **89**, 510 (1967).
- (16) J. L. Franklin, J. G. Dillard, H. M. Rosenstock, J. T. Herron, K. Draxl, and F. H. Field, *Natl. Stand. Ref. Data Ser., Natl. Bur. Stand.*, No. 26 (1969).
- (17) B. Badger and B. Brocklehurst, *Trans Faraday Soc.*, **65**, 2575 (1969).
- (18) S. Arai, to be submitted for publication.
- (19) R. E. Buhler, *Radiat. Res. Rev.*, **4**, 233 (1973).
- (20) S. Ikuta, K. Yoshihara, and T. Shiokawa, *Bull. Chem. Soc. Jpn.*, in press.
- (21) The previous measurement showed that a 1- μ s pulse at 100 mA gives a dose of 9000 rads to an aqueous system at room temperature. This result leads to $\sim 3.2 \times 10^4$ rads for a 2- μ s pulse at 180 mA. However, an aluminum window and heat insulation material may reduce the dose in low-temperature pulse radiolysis.

Dielectric Increments and the Conformations of Amino Acids and Betaines in Water

J. Kirchnerova, P. G. Farrell,* and J. T. Edward

Department of Chemistry, McGill University, Montreal, Canada H3C 3G1 (Received February 12, 1976)

Publication costs assisted by the National Research Council of Canada

Molar dielectric increments at 25 °C for several aliphatic amino acids and betaines have been determined from the dielectric constants of their dilute aqueous solutions. These have been used to examine the predictions of various theories, particularly with regard to dipole moments and the corresponding interchange distances. The calculated interchange distances of zwitterionic molecules possessing flexible aliphatic chains imply that, in water, the average molecular conformation corresponds to some coiling of the chain.

Introduction

Dielectric measurements made upon aqueous solutions of aminocarboxylic acids were of especial importance in the early studies of the nature of these compounds, and provided unequivocal evidence for their zwitterionic structure in water.¹ The dielectric increments (δ) of amino acids, peptides, and other zwitterionic compounds have been extensively used to derive values of their dipole moments (μ), often calculated from Kirkwood's theory for a spherical unpolarizable point dipole.² In its simplified form, Kirkwood's theory leads to an expression for μ ($= 3.3 \delta^{1/2}$) and the values obtained using this simple relationship have been interpreted in terms of predominantly randomly coiled conformations of the molecular chains.^{3,4}

More recently, Buckingham⁵ has developed a theory which permits the calculation of μ values for polar solutes in polar solvents, assuming that the solutes are polarizable, ellipsoidal molecules. For spherical molecules, this theory becomes formally identical with the earlier theory of Onsager.^{2,6} Buckingham has shown his theory to be successful for the calculation of dipole moments of a number of pure polar liquids, binary mixtures, and aqueous solutions of two aminocarboxylic acids.⁷

A more extended study of dielectric increments for the homologous series of α,ω -aminocarboxylic acids together with some rigid or pseudorigid amino acids was recently reported.⁸ Dipole moments for these compounds were also calculated using both Kirkwood's and Buckingham's theories⁹ and em-

pirical correction factors for these theories were obtained by comparing the theoretical and calculated dipole moments for 4-aminobicyclo[2.2.2]octanoic acid. When applied to the dipole moments of flexible molecules, these correction factors gave interchange distances indicating a fully extended conformation of the aliphatic chain in water. These results were in sharp contrast with both earlier conclusions for amino acids based on dielectric constant measurements and the conformations of long-chain aliphatic molecules in water.¹⁰⁻¹²

In order to further examine the validity of these conclusions regarding the conformations of aliphatic amino acids, and to test the limitations of the three available theories of dielectric polarization, we have measured the dielectric increments for a number of α -amino acids, taurine, 3-aminopropanesulfonic acid, and five α,ω -aminocarboxylic acid betaines. Literature data for other zwitterionic compounds with rigid, symmetrical structures^{1,13} have also been examined in the light of these theories.

Dielectric increments may be directly related to dipole moments through the derivatives of the orientational polarization with respect to concentration. Those relationships have been obtained and used to show that the dielectric increments for α -amino acids, and therefore their calculated dipole moments in water, depend strongly on partial molar volumes.

Buckingham's theory⁵ has been shown to reproduce well the interchange distances of zwitterions possessing pseudorigid structures. This theory has been used, therefore, to obtain interchange distances for flexible aliphatic α,ω -zwitterions in water. These interchange distances suggest that the average

conformation of such molecules corresponds to some coiling of the chain.

Experimental Section

Materials. The α,ω -aminocarboxylic acids and the two aminosulfonic acids were commercial products of the best quality available. They were repeatedly recrystallized from deionized water, or a mixture of deionized water and methanol, until their 0.1 M aqueous solutions had acceptable specific conductivities ($<5 \times 10^{-6} \Omega^{-1} \text{ cm}^{-1}$). Betaines of the α,ω -aminocarboxylic acids were prepared by methylation of the acids with methyl iodide, following standard literature procedures.¹⁴ The neutral zwitterionic betaines were obtained by passing aqueous solutions of the hydriodides over a weak-base resin (Fisher Rexyn 201), followed by evaporation of the solvent. The betaines were crystallized from ethanol-ether and analyzed for complete methylation by NMR. They were then repeatedly recrystallized from small portions of deionized water-methanol to give 0.05 M solutions of acceptable conductivity.

Water. Doubly distilled water was freshly deionized by passing it over a mixed-bed resin (Rexyn I300); the resulting conductivity was less than $10^{-6} \Omega^{-1} \text{ cm}^{-1}$.

Calibration Solvents. Acetone (Fisher Spectroanalyzed) was dried before use over Linde molecular sieves (Type AA). Nitrobenzene (Fisher certified) was twice fractionally crystallized; before use it was dried in the same way as the acetone.

Measurements. All measurements were made at $25 \pm 0.02^\circ \text{C}$. Densities were determined using a Precision density meter, Type DMA 02C. Refractive indices were determined using a thermostatted Abbé refractometer. Dielectric constant values were obtained from capacitance data, measured using a dipolmeter, Type DM01 (Wissenschaftlich-Technische Werkstätten) fitted with a water-jacketed cell (Type MFL3/S), which functions in the dielectric constant range 21–120. Care was taken to ensure thermal equilibrium of the cell before measurements were taken. A calibration plot obtained using water, nitrobenzene, and acetone was used to calculate the unknown dielectric constants, ϵ , of the solutions. In addition to capacitance measurements, specific conductivities of the solutions were also determined.

Results

Dielectric Increments. These were evaluated from the linear variations of dielectric constants, ϵ , with concentration and are listed in Table I. (Table I also includes literature data.^{1,13}) For the sulfonic acids and the betaines these δ values are represented in Figure 1, as a function of the number of methylene groups, n , separating the charged ends. For comparison, this figure also includes data for some α,ω -aminocarboxylic acids. From this figure it can be seen that the variation of δ with n for the betaines parallels that for the α,ω -aminocarboxylic acids and it is possible that a similar trend would be observed for the sulfonic acids. This suggests that the different charged end groups induce no significant differences in the conformations of the aliphatic chains of these zwitterions. It is particularly noteworthy that the δ values for $n = 1$ appear to be constant. However, the nature of the acid group is presumably responsible for the appreciable differences between the absolute values of δ for sulfonic acids and carboxylic acids for a given value of n .

Orientational Polarization. Kirkwood's model of a molecule as an unpolarizable point dipole leads to eq 1 for the orientational polarization²

$$\frac{(\epsilon - 1)(2\epsilon + 1)}{9\epsilon} = \sum \bar{C}_i P_i^K = \frac{4}{3} \pi N_0 \sum \bar{C}_i \left(\alpha_i + \frac{g_i \bar{\mu}_i^2}{3kT} \right) \quad (1)$$

where \bar{C}_i is the concentration of the component i in mol/cm^3 , α_i is the corresponding molecular polarizability, $\bar{\mu}_i$ is the molecular dipole moment of i in solution, including any enhancement due to the reaction field, and g_i is a correlation factor to allow for coupling between the orientations of the given dipole and those of surrounding molecules. For non-associated liquids the value of g_i is generally close to unity.

By taking into account the total local field acting on the polarizable spherical molecule, Fröhlich¹⁵ derived a slightly different expression, viz.

$$\frac{(\epsilon - n^2)(2\epsilon + n^2)}{3\epsilon} = \sum \bar{C}_i P_i^{KF} h_i = \frac{4\pi N_0}{3kT} \sum \bar{C}_i \left[g_i \mu_i^2 \left(\frac{n_i^2 + 2}{3} \right)^2 \right] \quad (2)$$

where μ_i refers to the dipole moment in the gas phase and $h_i = [(n_i^2 + 2)/3]^2$. This is often referred to as the Kirkwood-Fröhlich equation.

Onsager's theory⁶ was modified by Buckingham⁵ to include an ellipsoidal cavity containing the solute molecule, thus allowing for the influence of molecular shape on the static dielectric constant of a liquid in terms of a shape factor, A_i :

$$\frac{(\epsilon - n^2)(2\epsilon + 1)}{3(2\epsilon + n^2)} = \sum \bar{C}_i P_i^B f_i g_i^B = \frac{4\pi N_0}{9kT} \sum \bar{C}_i \mu_i^2 f_i g_i^B \quad (3)$$

where

$$f_i = \frac{(2\epsilon + 1)[1 - A_i + n_i^2 A_i]}{3[\epsilon(1 - A_i) + n_i^2 A_i]}$$

and

$$g_i^B = \frac{\epsilon[1 - A_i + n_i^2 A_i]}{[\epsilon(1 - A_i) + n_i^2 A_i]}$$

Note that Buckingham's g_i^B factor does not correspond to Kirkwood's correlation factor, denoted by g_i . For Buckingham's theory to be strictly applicable to associated liquids, Kirkwood's g_i factor should be taken into account; then for spherical molecules, where $A_i = 1/3$, eq 2 and 3 would become equivalent.

Dipole Moments. For binary solutions the derivatives of eq 1–3 with respect to molar concentration lead, at infinite dilution, to expressions for the dipole moment of the solute in terms of the dielectric increment, δ . Thus for aqueous solutions at 25°C eq 1–3 yield eq 4–6, respectively, where subscript 1 refers to solvent and subscript 2 to solute.

$$\bar{\mu}_2^* = \bar{\mu}_2 g_2^{1/2} = 3.297 \left[\delta + 0.078(V_2 - 0.058 \frac{\delta P_1^K}{\delta x_2} - 0.058 R_2) \right]^{1/2} \quad (4)$$

R_2 is the molar refraction of the solute and $\delta P_1^K / \delta x_2$ represents the change of the orientation polarization of water, caused by the solute. From the Kirkwood-Fröhlich equation μ_2^* may be expressed as

$$\mu_2^* = \mu_2 g_2^{1/2} = \frac{9.89}{n_2^2 + 2} \left\{ \delta - \frac{39.8 V_2}{1000} \frac{\delta n}{\delta x_2} + 0.078 \left(V_2 - 0.092 \frac{\delta P_1^{KF}}{\delta x_2} \right) \right\}^{1/2} \quad (5)$$

Finally Buckingham's equation leads to

TABLE I: Dielectric Increments, δ , Partial Molar Volumes, V_2 , Squares of the Estimated Refractive Indexes, n_2^2 , and Maximum Intercharge Distances, R_{\max} , Calculated from Known Bond Lengths and Angles for Amino Acids and Betaines

Compound	δ	V_2 , ml	n_2^2	R_{\max} , Å
1 Glycine	24 ^a	43.3	2.177	2.95
2 Sarcosine	23.4 ^a	52.6	2.166	2.95
3 α -Alanine	23.5 ^a	60.6	2.166	2.95
4 Serine	22.5 ^a	60.3	2.122	2.95
5 α -Aminoisobutyric acid	21.8 ^a	77.2	2.159	2.95
6 Valine	23.3 ^a	91.3	2.154	2.95
7 Leucine	22.6 ^a	107.5	2.151	2.95
8 Norleucine	20.3 ^a	108.4	2.151	2.95
9 Phenylalanine	16.9 ^a	121.2	2.376	2.95
10 Proline	21.0 ^b	81.0	2.164	2.95
11 Hydroxyproline	22.0 ^b	84.4	2.282	2.95
12 1-Aminocyclopentanecarboxylic acid	20.8 ^c	93.9	2.207	2.95
13 4,4-Diphenylbetaine	155 ^b	240 ^d	2.362	10.53
14 p -Me ₃ ⁺ NC ₆ H ₅ CH=CBrCOO ⁻	102 ^b	218 ^d	2.292	8.45
15 p -Me ₃ ⁺ NC ₆ H ₅ CH=CHCOO ⁻	100 ^b	192.6 ^d	2.281	8.45
16 p -Sulfanilic acid betaine	73 ^b	162 ^d	2.259	6.43
17 p -Benzbetaine	72 ^b	141.3	2.264	6.36
18 4-Aminobicyclo[2.2.2]octanoic acid	71.6 ^c	125	2.227	6.10
19 Glycinebetaine	21.8 ^a	98	2.052	2.95
20 4-Aminobutanoic acid betaine	44.4 ^a	122.9	2.057	5.45
21 5-Aminovaleric acid betaine	60 ^b	138	2.064	6.93
22 6-Aminohexanoic acid betaine	73.5 ^a	155	2.069	7.96
23 7-Aminoheptanoic acid betaine	89.2 ^a	171	2.075	9.38
24 Taurine	40.4 ^a	71.7	2.180	4.45
25 3-Aminopropanesulfonic acid	56.8 ^a	87.1	2.170	5.51
26 β -Alanine	33 ^e	58.7	2.166	4.32
27 4-Aminobutyric acid	53 ^e	73.4 ^d	2.159	5.45
28 5-Aminovaleric acid	63 ^e	87.9	2.154	6.93
29 6-Aminohexanoic acid	82 ^e	102.6 ^d	2.151	7.96
30 7-Aminoheptanoic acid	93 ^c	117.3 ^d	2.148	9.38
31 8-Aminooctanoic acid	109 ^c	132.0 ^d	2.146	10.48
32 9-Aminononanoic acid	131 ^c	146.7 ^d	2.144	11.86
33 10-Aminodecanoic acid	153 ^c	162	2.143	12.99

^a This work. ^b Reference 1. ^c Reference 8. ^d Estimated. ^e Average of the best available values.

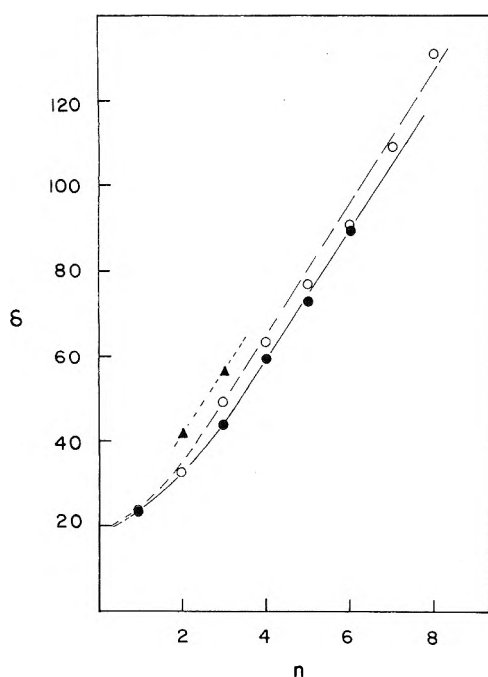


Figure 1. The variation of the dielectric increment, δ , with the number of $-\text{CH}_2-$ groups, n , separating the charged functions: (▲) aminosulfonic acids, this work; (●) betaines, this work; (○) aminocarboxylic acids, the average values obtained from the literature data.^{8,13}

$$\mu_2 = 4.945 \frac{(1 - A_2)}{[1 + (n_2^2 - 1)A_2]} \left[\delta - \frac{1.45V_2}{1000} \frac{\delta n}{\delta x_2} + 0.0758 \left[V_2 \left(1 + 0.0255 \frac{n_2^2 A_2}{1 - A_2} \right) - 0.095 \frac{\delta P_1^B}{\delta x_2} \right]^{1/2} \right] \quad (6)$$

To calculate the numerical values in eq 4-6 the following data for water at 25 °C were used: $V_1 = 18.07 \text{ cm}^3$, $\epsilon = 78.54$, $n_1^2 = 1.7756$, $P_1^K = 313.35 \text{ cm}^3$, $P_1^{KF} = 196.82 \text{ cm}^3$, $A_1 = 0.340$, and $P_1^B = 192.22 \text{ cm}^3$,²⁶ by assuming a water molecule to be spherical $A_1 = 0.333$, and then $P_1^B = P_1^{KF}$.

Partial molar volumes, V_2 , have been taken from the literature,³ where available, or were calculated from measured densities; in few cases estimates were used. Molar refractivities, R_2 , were estimated from the data tabulated by Vogel.¹⁶ From these values of R_2 , and estimated molar volumes,¹⁷ the squares of indices of refraction were calculated (Table I).

The refractive index of a solution is usually related to those of its components^{7,13} by

$$n^2 = n_1^2 + (n_2^2 - n_1^2)x_2 \quad (7)$$

although our own studies, and those of others,⁸ suggest that a better approximation is

$$n^2 = n_1^2 + (n_2^2 - n_1^2)\phi_2 = n_1^2 + (n_2^2 - n_1^2)x_2 \frac{V_2}{V} \quad (8)$$

Thus $\delta n/\delta x_2$ can be approximated by

TABLE II: Dielectric Increments, Molar Volumes, Refractive Indexes and the Calculated Values of $\delta P_1/\delta x_2$ (Eq 5) for Several Polar and Nonpolar Solutes in Water

Compound	δ^a	$V_2,^c$ ml	n_2^{2c}	$0.0758V_2$	μ^c	$\delta P_1/\delta x_2$
Methyl alcohol	-1.4	40.7	1.770	3.1	1.87	50.6
Ethyl alcohol	-2.6	58.7	1.848	4.5	1.66	114.9
<i>tert</i> -Butyl alcohol	-6.3	94.9	1.919	7.2	1.66	-26.7
Acetone	-3.2	74.1	1.839	5.6	2.69	-56.8
Aniline	-7.6	91.5	2.508	6.9	1.51	-241.5
Phenol	-6.6	83.1	2.380	6.3	1.45	-171.0
Pyridine	-4.2	80.9	2.272	6.1	2.37	84.7
Acetonitrile	-1.7	52.8	1.800	4.0	3.44	-312.0
Nitromethane	-2.0	54.0	1.903	4.1	3.56	-402.9
Methyl acetate	-5	79.8	1.853	6.1	1.66	9.7
Dioxane	-7.7 ^b	69	2.016	5.2	0	-347.1
Pyrazine	-6.4	82.5 ^d	2.278 ^d	6.3	0	-13.9
2-Methylpyrazine	-7.3	99.5 ^d	2.252 ^d	7.5	0	27.8
2,6-Dimethylpyrazine	-8.5	116.5 ^d	2.233 ^d	8.8	0	41.7
Quinoxaline	-9.3	116.2 ^d	2.684 ^d	8.8	0	-69.4
2-Methylquinoxaline	-11.1	133.2 ^d	2.608 ^d	10.1	0	-138.9
1,4-Diazabicyclo[2.2.2]octane	-7.4	116.4 ^d	2.201 ^d	8.8	0	194.4

^a Reference 12. ^b J. B. Hasted, G. H. Haggis, and P. Hutton, *Trans. Faraday Soc.*, 47, 577 (1951). ^c From the data in J. A. Riddick and W. B. Bunger, "Techniques of Chemistry, Vol. 11. Organic Solvents", 3d ed, Wiley, New York, N.Y., 1970. ^d Estimated values.

$$\frac{\delta n}{\delta x_2} = (n_2^2 - n_1^2) \frac{V_2}{V}$$

where V is the average molar volume of a solution. However, it is evident that in eq 6 the term including $\delta n/\delta x_2$ is negligible.

The shape factor A_2 represents the dimensions of an ellipsoid containing the molecule and is a function of the axial ratios, c/a and b/a , where $a \geq b \geq c$. Values of A_2 were obtained from the published data of Osborn.¹⁸ For the α -amino acids and those zwitterions having pseudorigid structures, interchange distances, R , and the lengths of the major axes of the ellipsoids circumscribing the molecules were calculated using known bond lengths, angles,¹⁹ and van der Waals radii.¹⁷ The positive charge was assumed to be located on the nitrogen atom of the alkylammonium group, and the negative charge to be symmetrically between the oxygen atoms in the plane containing these atoms and in line with the methylene-carboxyl bond or methylene-sulfonate bond.

For the α,ω -zwitterionic molecules, values of R_{\max} and the lengths of the major axes (a) were determined as described above, assuming full chain extension. A_2^{\min} values²⁷ for these compounds were then determined using these a values together with partial molar volumes in water (to obtain values for the lengths of the minor axes, $b = (6V_2/N\pi a)^{1/2}$).

To evaluate the quantity $\delta P_1^B/\delta x_2$ Buckingham used dielectric data for acetone-water mixtures and obtained a value of 85.3 cm³.⁷ He then assumed that the value of $\delta P_1/\delta x_2$ is constant for different solutes.

Using eq 5 and known values of dielectric decrements,¹³ etc. we have calculated values of $\delta P_1/\delta x_2$ for several polar and nonpolar nonelectrolytes and these are shown in Table II. Inspection of this table shows that the value of $\delta P_1/\delta x_2$ depends strongly on the character of the solute. Thus, among polar solutes $\delta P_1/\delta x_2$ is positive for methanol, ethanol, pyridine, and methyl acetate, whereas it is negative for all others in Table II. The negative values range from -26.7 for *tert*-butyl alcohol to -402.9 for nitromethane. For nonpolar solutes, $\delta P_1/\delta x_2$ shows a range of both positive and negative values which undoubtedly reflects the effects of these solutes on the structure of water.²⁰

It is, however, difficult to use these data to predict $\delta P_1/\delta x_2$ for amino acids. Inspection of eq 5 and 6 indicates that, for molecules with large dipole moments, any $|\delta P_1/\delta x_2| < 300$ cm² will have no significant effect on the calculated dipole moments. As the zwitterionic molecules studied will have large dipole moments and the values of $\delta P_1/\delta x_2$ of Table II are in general relatively small, we have assumed that these terms can be ignored (i.e., ≈ 0) for the purposes of calculation.

Intercharge distances ($R = \mu/4.803 \times 10^{-18}$ Å) have been calculated using eq 4-6 and the results are shown in Table III.

Discussion

Partial Molar Volumes. An examination of either eq 4 or 5 suggests that there should be an approximately linear correlation between the measured δ values and the partial molar volumes for molecules having identical dipole moments. A similar relationship is predicted by eq 6 when the term involving A_2 is constant. If one ignores both the polar effects of the side chains, and any changes in geometry induced by them, then the α,α -aminocarboxylic acids provide a series of molecules whose dipole moments should be effectively constant. The major contribution to the observed dipole moments for these zwitterions derives from the separated charges and the dielectric increments for some typical α,α -aminocarboxylic acids (Table I) suggests that the assumption of a constant value for their dipole moments would not be unreasonable. In Figure 2 we have therefore plotted values of δ vs. V_2 for the α -aminocarboxylic acids and it can be seen that there is a general dependence of these properties upon each other. However, no distinct linear relationship between these quantities can be deduced from the data presented and the scatter around a linear function is presumably due to both the differing shapes of these amino acids, and the different effects of their side chains on the structure of water. The majority of the compounds listed in Table I do not approximate to spheres, but to ellipsoids of varying size and hence of varying A_2 factors. This effect will probably outweigh any effects of the side chains upon the water structure.

TABLE III: Shape Factors, A_2 , and the Intercharge Distances Calculated from Dielectric Increments for Amino Acids and Betaines^a

Compd	R_K	R_{KF}	A_2^{\min}	R_B	A_2'	R_B^c	\bar{R}
1	3.56	2.56	0.270	2.98	0.240	3.25	
2	3.66	2.63	0.275	3.09	<i>b</i>	<i>b</i>	
3	3.62	2.60	0.310	2.77	0.260	3.25	
4	3.55	2.58	0.315	2.71	0.270	3.15	
5	3.58	2.58	0.340	2.56	0.274	3.09	
6	3.76	2.71	0.310	2.88	0.290	3.15	
7	3.79	2.74	0.310	2.90	0.280	3.25	
8	3.65	2.63	0.270	2.80	0.250	3.35	
9	3.49	2.39	0.280	2.74	0.260	3.01	
10	3.58	2.58	0.290	2.85	0.270	3.13	
11	3.66	2.56	0.290	2.84	0.275	3.08	
12	3.52	2.51	0.315	2.70	0.295	2.97	
13	9.05	6.22	0.115	10.30	<i>b</i>	<i>B</i>	
14	7.42	5.18	0.130	8.31			
15	7.35	5.15	0.130	8.30			
16	6.34	4.46	0.190	6.16			
17	6.25	4.39	0.190	6.11			
18	6.18	4.18	0.230	5.58	0.195	6.14	
19	3.72	2.75	0.285	3.06	<i>b</i>	<i>b</i>	
20	5.04	3.72	0.233	4.65			4.49
21	5.76	4.25	0.180	5.95			5.43
22	6.34	4.67	0.170	6.68			6.00
23	6.95	5.11	0.150	7.40			6.74
24	4.64	3.33	0.235	4.20	0.200	4.65	4.65
25	5.46	3.92	0.215	5.13	0.187	5.59	5.59
26	4.27	3.07	0.230	3.88	0.200	4.23	4.23
27	5.15	3.71	0.210	4.97	0.185	5.41	5.41
28	5.72	4.13	0.180	5.70	0.158	6.24	5.98
29	6.35	4.59	0.170	6.55	0.145	7.07	6.88
30	6.95	5.02	0.148	7.61	0.130	7.97	7.28
31	7.50	5.42	0.138	8.34	0.118	8.83	8.01
32	8.58	6.21	0.125	9.39	0.110	9.80	8.86
33	8.83	6.39	0.114	10.38	0.105	10.67	9.78

^a Compound numbering is as in Table I. ^b No hydration by dielectrically inactive water molecules assumed, i.e., the values of A_2' = A_2 and R_B^c = R_B .

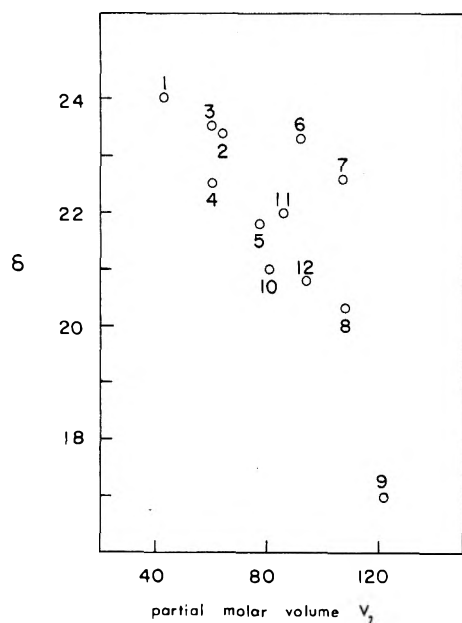


Figure 2. Dielectric increments of α -amino acids, δ , as a function of their partial molar volume, V_2 . The numbers correspond to compounds listed in Table I.

Intercharge Distances. As was noted above, the Kirkwood and Kirkwood-Fröhlich equations for the calculation of dipole

moments differ only by the inclusion of any enhancement due to the entire reaction field in the former. Therefore for solutes with the correlation factor g_2 equal to unity, the dipole moments of *spherical* molecules calculated using eq 4 ($\bar{\mu}_2^*$) are expected to be greater than the corresponding gas phase or "theoretical" dipole moments.

Dipole moments for these molecules calculated from eq 5 should thus give gas phase values, and hence intercharge distances in agreement with those calculated from known bond lengths, bond angles, etc., i.e., the molecular structure. However, for molecules whose shapes are nonspherical, e.g., ellipsoidal, then the Kirkwood-Fröhlich equation will give underestimated values of μ_2^* , and therefore of R .

In column 3 of Table III, R_{KF} values derived from dipole moments calculated using eq 5 are shown. Comparison of these R_{KF} values with the R_{\max} values of Table I shows that they are all less than their corresponding R_{\max} , as was predicted above for nonspherical zwitterions. As the R_{\max} values were calculated from the known molecular geometries, and the values of $(R_{\max} - R_{KF})$ for both rigid and "pseudorigid" molecules are of the same order as those for molecules whose charged groups are separated by a flexible chain, then the R_{KF} values would not give reliable estimates of intercharge distances. Thus these R_{KF} values should not be used to estimate the conformations of flexible-chain molecules.

Calculated intercharge distances obtained using eq 4 (R_K) are also shown in Table III (column 2), where it can be seen that the derived values for the α,α -aminocarboxylic acids are

considerably greater than their corresponding R_{\max} values (Table I). Assuming that these molecules may be considered spherical, then these derived values are also in accord with the predictions above. For molecules having fixed interchange distances of 4.4–6.4 Å Kirkwood's equation leads to R_K values in agreement with those calculated from bond length and angles. However, in the case of flexible zwitterions with maximum interchange distances (R_{\max}) in the above range, the derived R_K values are shorter than R_{\max} . Thus, although R_K values are not the best estimates of interchange distances, they do not support the idea that flexible chain molecules exist in their fully extended conformations.

The values of R calculated using eq 6 (R_B) are given in column 5 of Table III. Inspection of these values shows that, for rigid symmetrical betaines, R_B values are in very good agreement with R_{\max} , whereas those for rigid amino acids are slightly less than R_{\max} values.

Dielectric studies of aqueous solutions of electrolytes led Hasted to conclude that the molecules of water hydrating small positive ions are dielectrically inactive.^{21,22} Thus, in the treatment of dielectric data, hydrated cations should be considered as species having low dielectric constants. Hasted estimated²¹ that the unsubstituted ammonium ion is solvated by four, dielectrically inactive, water molecules, while the monoalkylammonium cations and β -alanine are solvated by two water molecules and tetraalkylammonium cations are unsolvated. He found that carboxyl groups were not solvated by irrotationally bound water molecules. Assuming that the $^+\text{NH}_3$ groups of all amino acids are similarly solvated by two molecules of dielectrically inactive water, then this will have a very significant effect upon the calculated dipole moments and hence interchange distances for these molecules.

If we consider that the amino group is hydrated by two molecules of water, each having a molar volume of 18 ml, then the molar volume of this hydrated species becomes V_2' ($= V_2 + 36$ ml). The major axis (a') of the ellipsoid circumscribing such a molecule is then *maximally* increased by the van der Waals radius of a water molecule. Thus, modified shape factors A_2' will be obtained, as shown in column 6 of Table III. Use of these A_2' values in eq 6 will then lead to modified values of the interchange distances, R_B^c , as shown in column 7 of Table III. These R_B^c values for rigid amino acids are generally in excellent agreement with the calculated R_{\max} values, although some variation is observed for the α -amino acids. In view of the asymmetry of the α -amino acids studied (Table I), and expected differences in the effects of the side chains on the structure of water (which have not been considered), the observed variations of R_B^c are acceptable.

Assuming that the hydration of the $^+\text{NH}_3$ group occurs via interaction with the oxygen atom of a water molecule it is conceivable that the maximum of three water molecules could be irrotationally bound to the alkylammonium ion and we have therefore examined the effect of changing hydration upon the calculated R_B^c values for glycine, 10-aminodecanoic acid, and 4-aminobicyclo[2.2.2]octanoic acid. It can be seen from the data presented in Table IV that the hydration number has only a minor effect upon R_B for 10-aminodecanoic acid, i.e., $R_B \approx R_B^c$, whereas values of R_B for the other amino acids of Table IV are considerably affected by hydration. This is especially true for glycine in which the relative volume change is very large.

The assumption of two irrotationally bound water molecules per $^+\text{NH}_3$ group leads to R_B^c values which are in closest agreement with R_{\max} , although the relative changes in R_B^c with varying number of such bound solvent molecules are

TABLE IV: The Effect of the Assumed Number of Water Molecules Hydrating the $^+\text{NH}_3$ Group on the Calculated Interchange Distance R_B^c for Selected Amino Acids

Compd	R_B	R_B^c No. of H ₂ O molecules		
		1	2	3
1	2.98	3.40	3.25	3.28
33	10.38	10.79	10.67	10.55
18	5.58	6.25	6.14	5.95

small. The good agreement between R_{\max} and R_B values for rigid betaines or R_B^c values for rigid amino acids suggests that Buckingham's theory, including hydration, provides a good interpretation of the large dielectric increments of polar molecules in polar solvents.

This agreement can be argued to justify the use of eq 6 to interpret the dielectric increments of flexible betaines and amino acids in terms of their conformations. A comparison of the values of R_B for betaines and R_B^c for amino acids (Table III) with their corresponding R_{\max} values (Table I) suggests that the dielectric increments of the flexible zwitterions are not compatible with their existence in fully extended conformations, in contrast to our previous suggestion.⁸ However, the calculation of R_B and R_B^c values depends upon values of A_2 and it was pointed out above that A_2^{\min} values, based upon fully extended chains, were used to derive R values. Hence these R values are, of necessity, maximum values. Furthermore, the hydration of the ammonium ions is assumed to increase the total volume of the ellipsoid containing the molecule, and to extend the major axis of the ellipsoid. Thus the values of R_B and R_B^c may not approximate real average molecular lengths and an alternative check on these derived values is desirable.

One can assume that for an ellipsoidal cavity the major axis a and the interchange distance within the molecule R can be related by $a = R + d$, where d depends on the size of the charged groups but is independent of chain length. Also, the shape factor for the ellipsoid A_2 can be approximated by a linear equation of the form

$$A_2 = -0.09 + 0.36 \frac{b}{a}$$

Then for known values of V_2 ($= \pi b^2 a / 6$), and d , the corresponding values of R (\bar{R}) can be found by iteration. These values of \bar{R} for flexible betaines and amino acids are listed in column 8 of Table III.

The values of \bar{R} for the amino acids with three or less $-\text{CH}_2-$ groups separating the charged functions suggest that these molecules exist in their fully extended conformation. However, the \bar{R} values for the longer chain amino acids and betaines become increasingly shorter than R_{\max} . While these final values of \bar{R} are also greater than R values corresponding to the average length of a molecule with a random coil conformation,^{3,4b} they are perfectly compatible with a restricted C-C bond rotation coil conformation.²³ With respect to the rotational barriers known for methylene groups²⁴ such a conformation seems to be the most realistic. The different \bar{R} values found for amino acids and betaines of the same chain length might be real, but more likely they reflect the imperfections of the theory.

Thus the interpretation of dielectric increment data for α, ω -amino acids in water suggests that these substances do

not exist in their most extended forms, as was previously proposed,⁸ but possess average interchange distances implying some slight coiling of the aliphatic chains.

Acknowledgment. We are grateful to the National Research Council of Canada and to the Faculty of Graduate Studies and Research, McGill University, for financial support.

References and Notes

- (1) J. Wyman, *Chem. Rev.*, **19**, 213 (1936).
- (2) J. G. Kirkwood, *J. Chem. Phys.*, **7**, 911 (1939).
- (3) E. J. Cohn and J. T. Edsall, "Proteins, Amino Acids and Peptides", Hafner, New York, N.Y., 1965.
- (4) (a) W. P. Connors and C. P. Smyth, *J. Am. Chem. Soc.*, **64**, 1872 (1942); (b) J. T. Edsall and J. Wyman, "Biophysical Chemistry", Vol. I, Academic Press, New York, N.Y., 1958, Chapter 6.
- (5) A. D. Buckingham, *Aust. J. Chem.*, **6**, 93 (1953).
- (6) L. Onsager, *J. Am. Chem. Soc.*, **58**, 1486 (1936).
- (7) A. D. Buckingham, *Aust. J. Chem.*, **6**, 323 (1953).
- (8) J. T. Edward, P. G. Farrell, and J. L. Job, *J. Am. Chem. Soc.*, **96**, 902 (1974).
- (9) J. T. Edward, P. G. Farrell, and J. L. Job, *J. Phys. Chem.*, **77**, 2191 (1973).
- (10) G. Némethy and H. A. Scheraga, *J. Chem. Phys.*, **36**, 3401 (1962).
- (11) G. Némethy and H. A. Scheraga, *J. Phys. Chem.*, **66**, 1773 (1962).
- (12) C. Tanford, "The Hydrophobic Effect: Formation of Micelles and Biological Membranes", Wiley, New York, N.Y., 1973.
- (13) J. B. Hasted, "Aqueous Dielectrics", Chapman and Hall, London, 1973.
- (14) (a) R. Willstätter, *Chem. Ber.*, **35**, 595 (1902); (b) J. L. Job, Thesis, McGill University, 1973.
- (15) H. Fröhlich, "Theory of Dielectrics", 2d ed, Oxford University Press, Oxford, 1958.
- (16) A. I. Vogel, *J. Chem. Soc.*, 1842 (1948).
- (17) J. T. Edward, *J. Chem. Educ.*, **47**, 261 (1970).
- (18) J. A. Osborn, *Phys. Rev.*, **62**, 351 (1945).
- (19) L. E. Sutton, *Chem. Soc., Spec. Publ.*, No 11 (1958).
- (20) H. S. Frank and M. W. Evans, *J. Chem. Phys.*, **13**, 507 (1945).
- (21) G. H. Haggis, J. B. Hasted, and T. J. Buchanan, *J. Chem. Phys.*, **20**, 1452 (1952).
- (22) J. B. Hasted and S. M. El Sabek, *Trans. Faraday Soc.*, **49**, 1003 (1953).
- (23) C. Tanford, "Physical Chemistry of Macromolecules", Wiley, New York, N.Y., 1961.
- (24) E. L. Eliel, N. L. Allinger, S. J. Angyal, and G. A. Morrison, "Conformational Analysis", Interscience, New York, N.Y., 1967.
- (25) J. C. W. Shephard and E. H. Grant, *Proc. R. Soc. London, Ser. A*, **307** 335 (1968).
- (26) In his paper Buckingham had taken $n_1^2 = 1.86$ thus obtaining $P_1^B = 182.6 \text{ cm}^3$.
- (27) For molecules having a dipole moment directed along their major axis, $0.333 > A_2 > 0$. $A_2 = 0.333$ corresponds to an axial ratio of $b/a = c/a = 1$, i.e., a sphere.

Allowance for Composition Dependence of Activity Coefficients in the Analysis of Sedimentation Equilibrium Results Obtained with Heterogeneously Associating Systems

L. W. Nichol*

Department of Physical Biochemistry, John Curtin School of Medical Research, Australian National University, Canberra, A.C.T. 2601, Australia

and D. J. Winzor

Department of Biochemistry, University of Queensland, St. Lucia, Queensland 4067, Australia (Received March 2, 1976)

An iterative procedure is described that permits analysis of sedimentation equilibrium distributions obtained with heterogeneously associating systems, account being taken of the dependence of each activity coefficient on the composition of the solution, which varies with radial distance. The procedure is illustrated with treatment of distributions simulated for a system of the type $A + B \rightleftharpoons C$, and comment is made on its applicability to systems involving higher order complexes.

Sedimentation equilibrium offers a potentially powerful approach to the study of a wide range of interacting systems involving heterogeneous association between dissimilar macromolecules. The analysis of such results is difficult because the composition of the solution and hence the activity coefficient γ_i of each species i varies with radial distance r . The purpose of this communication is to examine this problem and to present a simple method of analysis, which should prove useful in correlating a series of equilibrium experiments encompassing a wide range of composition variation.

General Theory

Consider the sedimentation equilibrium of the system $A + B \rightleftharpoons C$ where the following relationships pertain:

$$a_i(r_1) = a_i(r_2) \exp\{\phi_i M_i (r_1^2 - r_2^2)\} \quad (1a)$$

$$\phi_i = (1 - \bar{v}_i \rho) \omega^2 / 2RT \quad (1b)$$

$$K = \frac{a_C(r)}{a_A(r)a_B(r)} = \frac{c_C(r)}{c_A(r)c_B(r)} \frac{\gamma_C(r)}{\gamma_A(r)\gamma_B(r)} \quad (1c)$$

$a_i(r)$ denotes the activity of species i ($i = A, B, C$), characterized by molecular weight M_i and partial specific volume \bar{v}_i . It will be assumed that no volume change occurs on reaction so that K is independent of r and $\bar{v}_C = (M_A \bar{v}_A + M_B \bar{v}_B) / (M_A + M_B)$. The latter relation does not imply that all \bar{v}_i are identical but rather permits calculation of \bar{v}_C from measurements obtained from separate studies on the individual reactants. The composition dependence of the activity coefficients is given by

$$\gamma_A(r) = \exp \left\{ \alpha_{AA} \frac{c_A(r)}{M_A} + \alpha_{AB} \frac{c_B(r)}{M_B} + \alpha_{AC} \frac{c_C(r)}{M_C} \right\} \quad (2a)$$

$$\gamma_B(r) = \exp \left\{ \alpha_{BB} \frac{c_B(r)}{M_B} + \alpha_{AB} \frac{c_A(r)}{M_A} + \alpha_{BC} \frac{c_C(r)}{M_C} \right\} \quad (2b)$$

$$\gamma_C(r) = \exp \left\{ \alpha_{CC} \frac{c_C(r)}{M_C} + \alpha_{AC} \frac{c_A(r)}{M_A} + \alpha_{BC} \frac{c_B(r)}{M_B} \right\} \quad (2c)$$

where only terms involving second virial coefficients (denoted by α) have been retained: $c_i(r)/M_i$ is the molar concentration of species i , which has been substituted for the molal concentration. The expression for composition dependence of activity coefficients embodied in eq 2 is that used recently by Ogston and Winzor¹ and is formally identical with similar relations presented previously.²⁻⁴

It is possible, with the use of eq 1 and 2, to form a set of nonlinear simultaneous equations for the total concentration $\bar{c}(r)$, and to attempt a solution in terms of the nine unknowns (all c_i and α_{ij} values);⁵⁻⁷ but this puts unrealistic demands on experimental precision even though α_{AA} and α_{BB} may be determined from separate studies on the individual reactants. It is not surprising, therefore, that other suggested procedures of analysis have invoked certain simplifying assumptions; in particular, that $\gamma_C/(\gamma_A\gamma_B) = 1$ and that activity coefficients may be expressed in terms of constituent concentrations and a lesser number of nonideality coefficients.⁸ The former assumption may be shown from eq 2 not to have general validity, while the second leads to the experimental determination of quantities that are neither constants nor thermodynamically meaningful parameters.¹ The present work considers an alternative approach of assigning values to the six virial coefficients in eq 2 on the basis of molecular covolume and charge contributions. It too is not without criticism because of the various assumptions that are necessary for calculating covolumes, but seems to be a more realistic approach when the major aim is the determination of K , with account taken of the actual composition variation with radial distance.

In this work each species is considered as a rigid, impenetrable sphere, whereupon the covolume of species i and j is given by⁹

$$U_{ij} = \frac{4\pi N(r_i + r_j)^3}{3000} \quad (3)$$

where r_i and r_j are the radii of the hydrated species, which may be calculated either by standard procedures on the basis of anhydrous molecular weights, anhydrous partial specific volumes and appropriate degrees of hydration, or from the translational frictional coefficients (in the case of A and B).¹⁰ The corresponding virial coefficient α_{ij} is given by¹

$$\alpha_{ij} = U_{ij} + \frac{Z_i Z_j}{2I} \quad (4)$$

where Z_i and Z_j are the net charges on the respective species and I the ionic strength of the supporting univalent electrolyte. In relation to eq 4, values of α_{AA} and α_{BB} predicted from it may be compared with experimental values obtained from separate studies on the individual reactants. Such comparisons, together with other preliminary studies on A and B, may indicate ellipsoidal shapes for either or both of the reactants whereupon expressions alternative to eq 3 are available for the calculation of covolumes.^{1,11,12}

Simulation of Sedimentation Equilibrium Distributions

It is now possible to simulate a sedimentation equilibrium

distribution in terms of the total weight concentration $\bar{c}(r)$ as a function of radial distance, a form available to the experimenter from Rayleigh optics, provided it is assumed that the specific refractive increments of all species i are identical. This assumption was not invoked in other treatments¹³ and may indeed not prove to be a limiting assumption in the present analysis. In the first step, values are assigned to the activity of each species $a_i(r_m)$ at the meniscus, and eq 1a and 1b are employed to calculate the activity distribution of each species. In the second step, the values of $a_i(r)$ at each r are substituted for $c_i(r)$ in eq 2, together with appropriate molecular weights and the numerical values of the calculated virial coefficients, to yield a first approximation of each $\gamma_i(r)$. Division of $a_i(r)$ by this estimate of $\gamma_i(r)$ yields a first estimate of each $c_i(r)$, which may be substituted in eq 2 to yield a second estimate of $\gamma_i(r)$: division of the original $a_i(r)$ by this second estimate of $\gamma_i(r)$ gives an improved estimate of $c_i(r)$. It will be shown later that on iteration this procedure converges rapidly to yield constant $c_i(r)$ values at each r , which may then be summed to give $\bar{c}(r)$.

The results of such simulations are shown in Figure 1 for the parameters listed in the caption. In this connection the initial loading concentrations \bar{c}_A^0 and \bar{c}_B^0 were found by trapezoidal integration from meniscus to base of plots of $c_i(r)$ vs. r^2 to yield $2(Q_i)_{\text{cell}}/\theta h$, where $(Q_i)_{\text{cell}}$ is the amount of species i in the cell of thickness h and sector angle θ . Since $(Q_A)_{\text{total}}/(\theta h) = (Q_A)_{\text{cell}}/(\theta h) + M_A(Q_C)_{\text{cell}}/(M_C\theta h)$ and $\bar{c}_A^0 = 2(Q_A)_{\text{total}}/\{\theta h(r_b^2 - r_m^2)\}$, it follows that \bar{c}_A^0 may be calculated, with similar reasoning applying to the calculation of \bar{c}_B^0 .¹⁴ It is noted that a procedure has been described^{14,15} for the simulation of $\bar{c}(r)$ vs. r plots that utilizes directly \bar{c}_A^0 and \bar{c}_B^0 together with expressions for conservation of mass, but this applies only to *ideal* systems; it was for this reason that values of $a_i(r_m)$ were initially selected, and the loading concentrations deduced thereafter.

Two points in relation to Figure 1 merit comment. First, it is seen from Figure 1a that the total activity distribution is virtually identical with the total concentration distribution; indeed, a maximum difference of 0.007 g/l. at r_b was found, corresponding to an 8- μm fringe displacement. This implies that within experimental error of measurement, nonideality effects could be neglected in analyzing this distribution. On the other hand, in Figure 1b where $\bar{c}(r_b)$ is some tenfold greater than in Figure 1a, the difference between concentration and activity distributions over the entire range of r is quite pronounced, varying from 260 to 980 μm in terms of fringe displacement. Clearly, if the $\bar{c}(r)$ vs. r distributions shown in Figures 1a and 1b (both of which are realistic from the viewpoint of fringe density) are to be correlated, it is vital that nonideality effects be considered explicitly in relation to Figure 1b.

At first sight it may appear that only experiments designed to cover a low concentration range (where nonideality effects may be neglected) are required for the determination of K . However, in order to verify that a single equilibrium constant suffices to describe the interaction it is necessary to encompass a wide range of composition,¹⁶ and, therefore, we now turn to the correlation of the $\bar{c}(r)$ vs. r plots shown in Figure 1, viewed as "experimental" concentration distributions.

Interpretation of Experimental Sedimentation Equilibrium Distributions

From an experimentally determined distribution covering a low concentration range, typified in the present work by Figure 1a, it is possible to determine $a_A(r)$ (A being the species

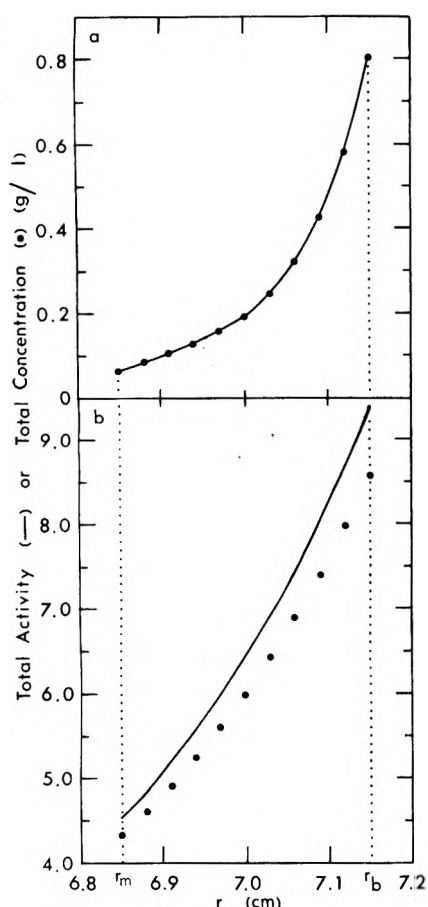


Figure 1. Simulated sedimentation equilibrium distributions for a system $A + B \rightleftharpoons C$ with $M_A = 15\,000$, $M_B = 45\,000$, $M_C = 60\,000$, $(1 - \bar{v}_i\rho) = 0.27$ for all species, and $K = 8.9$ l./g. Both experiments were visualized as being conducted with $T = 298.2^\circ\text{A}$, $r_m = 6.85$ cm, and $r_b = 7.15$ cm: (a) $\omega = 1.780 \times 10^3$ rad/s, $\bar{c}_A^0 = \bar{c}_B^0 = 0.135$ g/l.; (b) $\omega = 8.564 \times 10^2$ rad/s, $\bar{c}_A^0 = 3.129$ g/l., $\bar{c}_B^0 = 3.034$ g/l. The solid curves describe the total activity distributions for (a) $a_A(r_m) = 0.0625$ g/l., $a_B(r_m) = 0.009$ g/l., $a_C(r_m) = 0.005$ g/l.; and (b) $a_A(r_m) = 2.000$ g/l., $a_B(r_m) = 0.135$ g/l., $a_C(r_m) = 2.400$ g/l. Points denote the total weight-concentration distributions calculated from eq 2 and the following second virial coefficients (M^{-1}): $\alpha_{AA} = 145$, $\alpha_{BB} = 433$, $\alpha_{CC} = 578$, $\alpha_{AB} = 263$, $\alpha_{AC} = 313$, $\alpha_{BC} = 502$. These in turn were calculated from eq 3 and 4 on the basis of zero charge for all species and $r_A = 19.3$ Å, $r_B = 27.8$ Å, $r_C = 30.6$ Å.

with lowest $M_i(1 - \bar{v}_i\rho)$ by application of the $\Omega_A(r)$ function described by Nichol and co-workers.^{17,18} If the reasonable approximation is made that $a_A(r) = c_A(r)$ for this experiment, K follows from eq 17 of ref 18; implicit in this equation is the assumption that the system is ideal, which permits tractable formulation of the conservation of mass equations in terms of the initial loading concentrations \bar{c}_A^0 and \bar{c}_B^0 (known to the experimenter). A check on the value of K and on the negligible contribution of nonideality effects may be made by simulating the $\bar{c}(r)$ vs. r distribution^{14,15} and comparing it with the experimental pattern. In addition, since the simulation gives the distribution of each $c_i(r)$, it is possible to show from eq 2 that the values of $\ln \gamma_i(r)$ are, indeed, negligibly small.

We are now required to test the applicability of this single value of K to the distribution shown in Figure 1b. While application of the $\Omega_A(r)$ function again gives $a_A(r)$ at all radial distances,¹⁸ including r_m , it is no longer possible to assume corresponding values of $a_B(r_m)$ and $a_C(r_m)$, as was done in the construction of Figure 1b, nor to utilize the known values of \bar{c}_A^0 and \bar{c}_B^0 to estimate species concentrations at the menis-

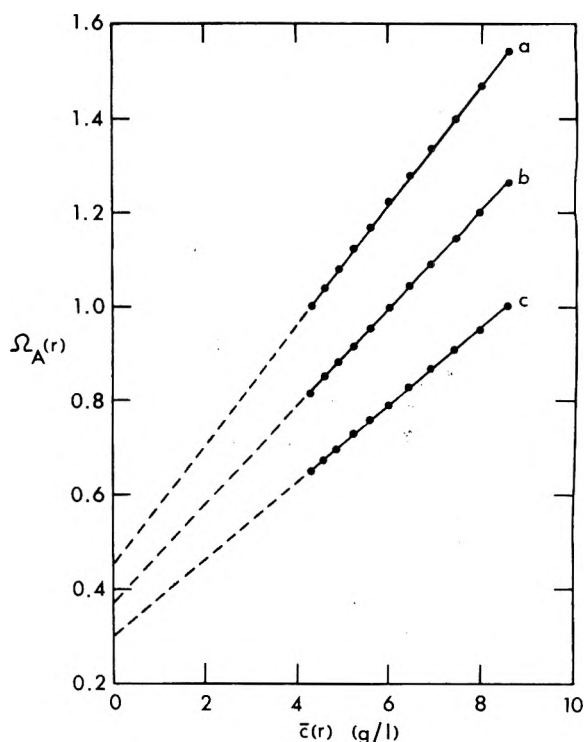


Figure 2. Plots of $\bar{c}(r)$ obtained from Figure 1b as functions of $\Omega_A(r) = \bar{c}(r) \exp\{\phi_A M_A (r_F^2 - r^2)\} / \bar{c}(r_F)$ for different reference positions: (a) $r_F = 6.85$ cm, $\bar{c}(r_F) = 4.320$ g/l.; (b) $r_F = 7.00$ cm, $\bar{c}(r_F) = 5.994$ g/l.; (c) $r_F = 7.15$ cm, $\bar{c}(r_F) = 8.576$ g/l.

cus.¹⁹ We can, however, select a value of $a_B(r_m)$ and, with the knowledge of $a_A(r_m)$ and K , calculate the corresponding value of $a_C(r_m)$. Equation 2 may now be applied iteratively as described above to yield the apparent $\bar{c}(r_m)$ based on the selected $a_B(r_m)$. Correct values of $a_B(r_m)$ and $a_C(r_m)$ are thereby located readily by continuing the selection until the experimentally observed value of $\bar{c}(r_m)$ is obtained. The complete activity distributions of A, B, and C may now be calculated using eq 1a and 1b, and be corrected to concentration distributions by the iterative procedure based on eq 2. Consistency between the two experiments on the basis of the assumed model and characteristic equilibrium constant K would be reflected by superposition of the calculated and experimental concentration distributions.

The feasibility of this approach will now be demonstrated. Figure 2 shows a plot of $\Omega_A(r)$ vs. $\bar{c}(r)$ derived from the concentration distribution shown in Figure 1b. Three $(\bar{c}(r_F), r_F)$ points were selected for the determination of $\Omega_A(r)$ values, whose extrapolated magnitudes at infinite dilution ($= a_A(r_F)/\bar{c}(r_F)$) led, via eq 1a, to estimates of 1.961, 1.970, and 2.000 g/l. for $a_A(r_m)$. Use of the average value of 1.976 g/l. for $a_A(r_m)$ and 8.9 l./g for K (the value obtained from Figure 1a) yielded values of 0.137 g/l. for $a_B(r_m)$ and 2.411 g/l. for $a_C(r_m)$. Table I summarizes values of $a_i(r)$ computed from these meniscus values, together with the corresponding $c_i(r)$ obtained by the iterative procedure based on eq 2. The last two columns of Table I compare the calculated and "experimental" $\bar{c}(r)$ values, the standard deviation obtained from the sums of squares of residuals over the entire range of r being equivalent to a fringe displacement of approximately 6 μm , an entirely satisfactory result. The remaining point of interest concerns the convergence of the iterative procedure, which is illustrated in Table II for r_b , where nonideality effects are most extreme. Clearly, the convergence is rapid and leads to final estimates

TABLE I: Analysis of the Sedimentation Equilibrium Distribution Shown in Figure 1b

r , cm	Species activities, g/l.			Species concn, g/l.			Total concn, g/l.	
	$a_A(r)$	$a_B(r)$	$a_C(r)$	$c_A(r)$	$c_B(r)$	$c_C(r)$	Calcd	Obsd
6.85	1.976	0.137	2.411	1.916	0.130	2.264	4.310	4.320
6.88	2.025	0.148	2.661	1.960	0.140	2.490	4.590	4.599
6.91	2.076	0.159	2.939	2.006	0.150	2.741	4.897	4.905
6.94	2.129	0.171	3.246	2.053	0.161	3.016	5.230	5.237
6.97	2.182	0.185	3.588	2.100	0.173	3.321	5.594	5.599
7.00	2.238	0.199	3.967	2.149	0.186	3.655	5.990	5.994
7.03	2.295	0.215	4.388	2.198	0.200	4.024	6.422	6.426
7.06	2.354	0.232	4.855	2.248	0.215	4.430	6.893	6.894
7.09	2.414	0.250	5.375	2.299	0.230	4.877	7.406	7.406
7.12	2.477	0.270	5.953	2.352	0.247	5.369	7.968	7.967
7.15	2.541	0.291	6.596	2.404	0.265	5.911	8.580	8.576

TABLE II: Convergence of the Iterative Procedure for Estimating Activity Coefficients^a

Activity Coeff	Estimates of $\gamma_i(r_b)$			
	First	Second	Third	Fourth
γ_A	1.062	1.057	1.057	1.057
γ_B	1.106	1.098	1.098	1.098
γ_C	1.127	1.115	1.116	1.116

^a Data refer to the cell base, where effects of nonideality are most pronounced.

of the activity coefficients which individually differ significantly from unity. It could, however, be noted that the ratio $\gamma_C/(\gamma_A\gamma_B)$ differs from unity by only 3.8%, a finding that lends some support to this basic assumption invoked in an earlier suggested procedure of analysis.⁸ This is particularly relevant since the present numerical example sets the second term of eq 4 equal to zero and thereby emphasizes the covolume contribution to nonideality. It has already been established²⁰ that in the reverse extreme ($U_{ij} \ll Z_i Z_j / 2I$), the assumption $\gamma_C/(\gamma_A\gamma_B) \sim 1$ is quite reasonable.

Systems with Higher Order Complexes

The analysis of sedimentation equilibrium distributions obtained with heterogeneously associating systems involving stoichiometries in addition to 1:1 is undeniably more complicated, and requires consideration of several models in relation to a series of sedimentation equilibrium distributions; but even in these cases the present approach offers advantage. In the first place, for any selected model it is a simple matter to write the array of expressions analogous to eq 2 expressing the composition dependence of activity coefficients of all postulated species, and to calculate reasonable estimates of the second virial coefficients; indeed, as the system becomes more complicated the need for so doing becomes more compelling. Secondly, such an array may readily be programmed to permit the iteration procedure to be executed by computer. Thirdly, the present method makes full use of ability to define the thermodynamic activity of the smallest species at each radial distance, independently of the model being examined.¹⁸

This means that evaluation of all $a_i(r_m)$ is still possible solely by examining a range of $a_B(r_m)$ in relation to the experimental $\bar{c}(r_m)$, even though several complexes and their respective association constants have been postulated. Fourthly, on the basis of the $a_i(r_m)$, plots of $\bar{c}(r)$ vs. r may readily be constructed for the various models and be compared directly with the experimental concentration distribution, a potentially more accurate comparison than is possible in procedures based on differentiation to yield molecular weight averages. These simulated $\bar{c}(r)$ vs. r plots will have taken into account the composition dependence of activity coefficients for each model examined, which is essential if a distinction is to be made between models on the basis of a series of sedimentation equilibrium experiments that are necessarily conducted over a wide range of composition. There is, however, no doubt that the analysis in terms of available experimental precision continues to be a difficult problem for systems containing a large number of complexes.

References and Notes

- (1) A. G. Ogston and D. J. Winzor, *J. Phys. Chem.*, **79**, 2496 (1975).
- (2) J. W. Williams, K. E. Van Holde, R. L. Baldwin, and H. Fujita, *Chem. Rev.*, **58**, 715 (1958).
- (3) H. Fujita, "Mathematical Theory of Sedimentation Analysis", Academic Press, New York, N.Y., 1962.
- (4) H. Fujita, "Foundation of Ultracentrifugal Analysis", Wiley-Interscience, New York, N.Y., 1975.
- (5) P. W. Chun and S. J. Kim, *J. Phys. Chem.*, **74**, 899 (1970).
- (6) R. H. Haschemeyer and W. F. Bowers, *Biochemistry*, **9**, 435 (1970).
- (7) D. C. Teller, *Methods Enzymol.*, **27**, 346 (1973).
- (8) E. T. Adams, Jr., A. H. Pekar, D. A. Soucek, L. H. Tang, G. Barlow, and J. L. Armstrong, *Biopolymers*, **7**, 5 (1969).
- (9) E. Edmond and A. G. Ogston, *Biochem. J.*, **109**, 569 (1968).
- (10) C. Tanford, "Physical Chemistry of Macromolecules", Wiley, New York, N.Y., 1961.
- (11) A. Isihara, *J. Chem. Phys.*, **18**, 1446 (1950).
- (12) L. W. Nichol, P. D. Jeffrey, and D. J. Winzor, *J. Phys. Chem.*, **80**, 648 (1976).
- (13) A. H. Pekar, P. J. Wan, and E. T. Adams, Jr., *Adv. Chem. Ser.*, **No. 125**, 260 (1973).
- (14) G. J. Howlett, P. D. Jeffrey, and L. W. Nichol, *J. Phys. Chem.*, **74**, 3607 (1970).
- (15) G. J. Howlett and L. W. Nichol, *J. Biol. Chem.*, **248**, 619 (1973).
- (16) G. J. Howlett, L. W. Nichol, and P. R. Andrews, *J. Phys. Chem.*, **77**, 2907 (1973).
- (17) B. K. Milthorpe, P. D. Jeffrey, and L. W. Nichol, *Biophys. Chem.*, **3**, 169 (1975).
- (18) L. W. Nichol, P. D. Jeffrey, and B. K. Milthorpe, *Biophys. Chem.*, in press.
- (19) G. J. Howlett, P. D. Jeffrey, and L. W. Nichol, *J. Phys. Chem.*, **76**, 777 (1972).
- (20) E. Braswell, *J. Phys. Chem.*, **72**, 2477 (1968).

Micellar and Nonmicellar Association of Antiacetylcholine Drugs in Aqueous Solution

D. Attwood

Pharmacy Department, University of Manchester, Manchester M13 9PL, England (Received January 19, 1976)

Light scattering methods have been used to determine the pattern of association of a series of antiacetylcholine drugs in aqueous solution. The intensity of the light scattered from solutions of propantheline bromide, methantheline bromide, and methixene hydrochloride increased continuously with concentration, with no significant inflection attributable to a critical micelle concentration. The scattering behavior of these compounds was not consistent with the mass action model of micellization. It could be adequately reproduced using a nonmicellar, stepwise association model in which the products of each stage of the association were present in solution in significant amounts, giving a highly polydisperse system. A micellar pattern of association was established for oxyphenonium bromide, tricyclamol chloride, glycopyrronium bromide, dicyclomine hydrochloride, and penthienate bromide. The micellar properties of these compounds have been determined. The mode of association has been related to the nature of the hydrophobic region of the molecule.

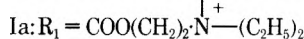
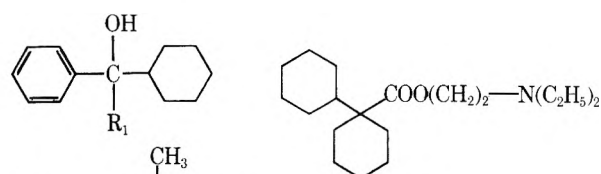
The influence of the nature of the hydrophobic group on the pattern of association of amphipathic molecules has recently been discussed.¹ It has been suggested that micellar aggregation is most readily achieved by molecules possessing flexible hydrocarbon chains which allow cooperativity of aggregation. Molecules with planar aromatic groups, which are roughly symmetrical with respect to their hydrophobicity, may associate by face-to-face stacking in a stepwise association pattern. A significant distinction between the two types of association is in the size distribution of the products of association. In micellar association there is a predominance of micelles of an energetically preferred size, while in the stepwise association model the products of association are generally multimers with a broad size distribution.

In previous studies of aggregation of drug molecules in aqueous solution we have shown that compounds with a diphenylmethane hydrophobic group associate in a micellar pattern.²⁻⁴ Diphenylmethane is nonplanar and rotation around the central C atom hinders any monomeric stacking. In contrast, some compounds with a hydrophobic region essentially composed of a single phenyl ring may aggregate by a stepwise association process when associated with a large counterion such as the maleate ion.^{5,6}

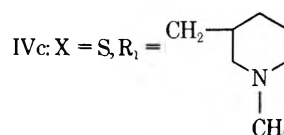
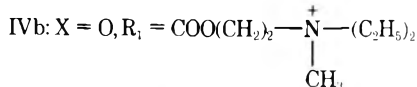
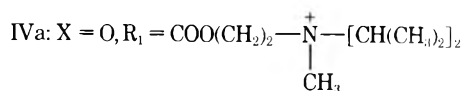
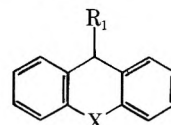
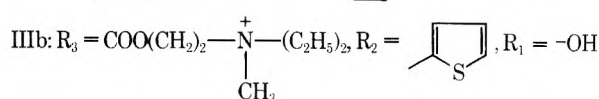
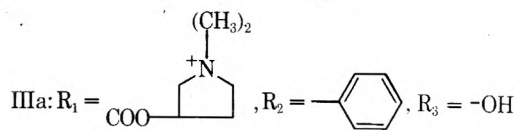
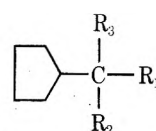
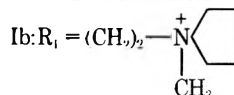
In the present study, the modes of association of a series of antiacetylcholine drugs have been determined by fitting the light scattering data using mass action and stepwise association models.

Experimental Section

Materials. The following compounds were used: oxyphenonium bromide (Ia) (Ciba Laboratories), tricyclamol chloride (Ib) (Lilly Research Centre), dicyclomine hydrochloride (II) (Richardson-Merrill Ltd.), glycopyrronium bromide (IIIa) (A. H. Robins and Co. Ltd.), penthienate bromide (IIIb) (Winthrop Laboratories), propantheline bromide (IVa) and methantheline bromide (IVb) (G. D. Searle and Co. Ltd.), methixene hydrochloride (IVc) (Wander Pharmaceuticals). With the exception of oxyphenonium bromide and methixene hydrochloride, the above compounds are subject to the purity requirements of either the British Pharmacopoeia or the United States National Formulary and, as such, contain not less than 98.0% of the specified compound. The remaining compounds were of equivalent purity according to information from the suppliers. All compounds were used as received.



II



Light scattering measurements were made at 303 K with a Fica 42000 photogoniometer (A.R.L. Ltd.) using a wavelength of 546 nm. Aqueous solutions were clarified by

ultrafiltration through 0.1- μm Milipore filters until the ratio of the light scattering at angles of 30 and 150° did not exceed 1.10. The refractive index increments (dn/dm) were measured at 546 nm using a differential refractometer. The following values (kg mol^{-1}) were obtained: oxyphenonium bromide (Ia) 0.0660, tricyclamol chloride (Ib) 0.0574, dicyclomine hydrochloride (II) 0.0516, glycopyrronium bromide (IIIa) 0.0616, penthienate bromide (IIIb) 0.0631, propantheline bromide (IVa) 0.0740, methantheline bromide (IVb) 0.0694, methixene hydrochloride (IVc) 0.0692.

Results

Light scattering results are presented in Figures 1, 2, and 3 as plots of scattering at 90°, S_{90} , as a function of molal concentration, m . All of the compounds studied showed some degree of aggregation, with scattering intensities in excess of those calculated for monomers. Two apparently different patterns of association were evident. The scattering curves of Ia, Ib, IIIa, and II (Figure 1) and IIIb (Figure 3) showed abrupt changes of slope over narrow, well-defined concentration regions. At concentrations below the critical concentration, the scattering of such compounds did not deviate significantly from that calculated for unassociated monomers. In contrast, IVa, IVb, and IVc (Figures 2 and 3) showed a continuous increase in scattering with no apparent discontinuity which could be attributed to a critical micelle concentration (cmc).

According to the mass action theory of micellization, the micellar equilibrium constant, K_m , may be approximated to

$$K_m = \frac{[M^{p+}]}{([X^-] - p[M^{p+}])^N [X^-]^{N-p}} \quad (1)$$

M^{p+} and X^- represent the micellar species and counterions, respectively, N is the micellar aggregation number, and p is the number of charges per micelle. The scattering intensities from micellar and monomeric species, designated $S_{90\text{mic}}$ and $S_{90\text{mon}}$, respectively, were calculated as described previously⁵ from equations proposed by Anacker and Westwell.⁷

$$K^1 m_{\text{mic}}/R_{90\text{mic}} = A + B m_{\text{mic}} \quad (2)$$

where $K^1 = 2\pi^2 n^2 (dn/dm)^2 V^0/L\lambda^4$; n is the refractive index of the solution; V^0 is the volume of solution containing 1 kg of water; L is the Avogadro's number; λ is the wavelength of incident light, and m_{mic} is the molality of the micellar species (in terms of monomeric units) as determined from eq 1. The second virial coefficient, B , was calculated from

$$B = pA[(1+p)N^{-1} - A](2m_{\text{mon}})^{-1} \quad (3)$$

where m_{mon} is the molality of monomer. The approximation $A = N^{-1}$ was made to simplify the calculations. $S_{90\text{mic}}$ was calculated from $R_{90\text{mic}}$ using the instrumental calibration constant. $S_{90\text{mon}}$ was estimated from eq 3 assuming a zero value of B . The total scattering intensity, S_{90} , was then a summation of $S_{90\text{mic}}$, $S_{90\text{mon}}$, and the intensity of the light scattered by the solvent.

Theoretical scattering curves were generated using eq 1–3 for a range of combinations of K_m , N , and p in an attempt to reproduce the experimental scattering curves and thereby distinguish micellar and nonmicellar aggregation patterns. The scattering behavior of all the compounds included in Figure 1 and also of penthienate bromide (Figure 3) could be adequately described using the mass action equations, confirming the micellar behavior of these compounds. The con-

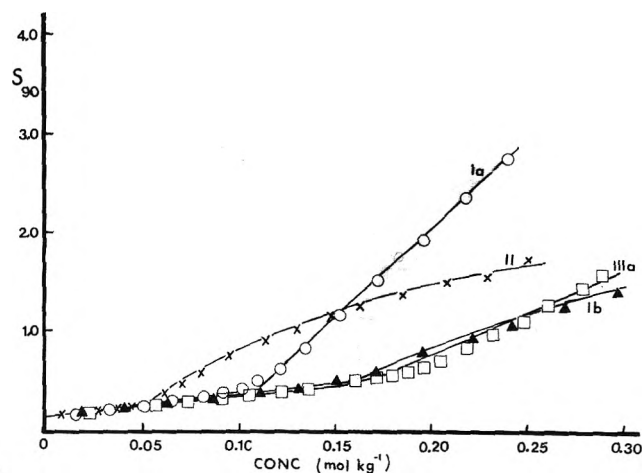


Figure 1. Variation of the scattering ratio, S_{90} , with concentration for (O) Ia, (X) II, (□) IIIa, and (▲) Ib. Continuous lines represent theoretical scattering as predicted by mass action equations using values of N , α , and K_m given in Table I.

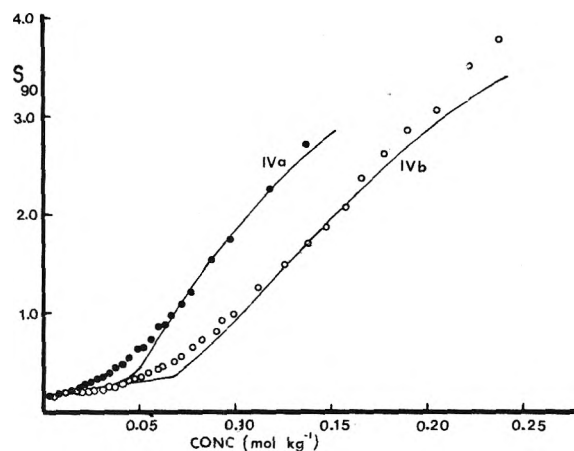


Figure 2. Concentration dependence of the scattering ratio, S_{90} , for (●) IVa and (○) IVb. Continuous lines represent theoretical scattering as predicted by mass action equations using $N = 13$, $\alpha = 0.2$, and $K_m = 10^{67}$ for IVa and $N = 10$, $\alpha = 0.2$, and $K_m = 10^{47}$ for IVb.

tinuous lines of these figures are those calculated using K_m , N , and $\alpha (= p/N)$ values shown in Table I. The standard free energies of micellization, ΔG_m , per mole of monomeric surfactant calculated from

$$\Delta G_m = -(RT/N) \ln K_m \quad (4)$$

are given in Table I. Despite extensive calculation using a wide range of combinations of the mass action parameters, it was not possible to generate the scattering curves of IVa, IVb, or IVc. The continuous lines of Figures 2 and 3 represent the best fit of data. In order to reproduce the appreciable scatter at high concentrations, high values of K_m and N were required (see legends to Figures 2 and 3) and such values produced abrupt inflections in the curves. The discrepancy between the experimental and calculated data in the region of these inflections was too great to be accounted for by experimental error. The ΔG_m values calculated from eq 4 using the best fit mass action parameters were -29.9 , -27.3 , and -34.8 kJ mol^{-1} for propantheline, methantheline, and methixene, respectively. These values are considerably higher than the free energy values calculated for the micellization of phenothiazine derivatives⁸ to which these molecules bear some resemblance.

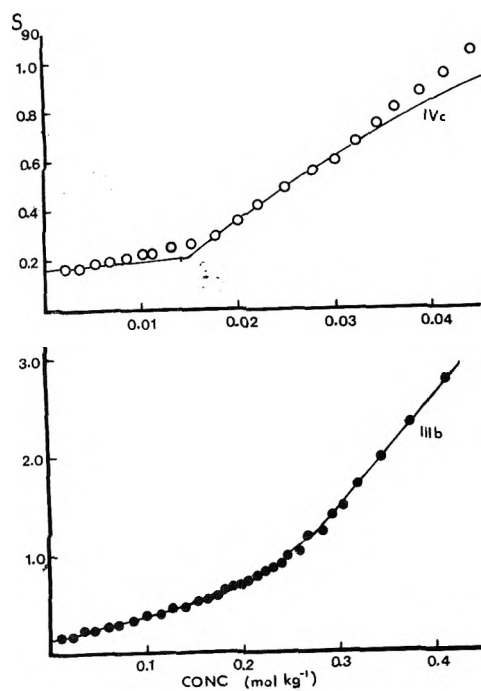


Figure 3. Concentration dependence of the scattering ratio, S_{90} , for (O) IVc and (●) IIIb. Continuous lines represent theoretical scattering as predicted by mass actions using $N = 14$, $\alpha = 0.2$, and $K_m = 10^{22}$ for IVc and $N = 6$, $\alpha = 0.2$, and $K_m = 5 \times 10^{21}$ for IIIb.

TABLE I: Micellar Properties of Antiacetylcholine Drugs

Compd	cmc, mol kg ⁻¹	N^a	α^a	K_m^a	ΔG_m^b , kJ mol ⁻¹
Ia	0.108	10.0	0.18	1×10^{44}	-25.5
Ib	0.150	5.7	0.26	5×10^{20}	-21.1
IIIa	0.189	5.4	0.16	5×10^{20}	-22.2
II	0.050	9.5	0.20	1×10^{48}	-29.3
IIIb	0.220	6.0	0.20	5×10^{21}	-21.0

^a Values giving best fit of experimental data using mass action equations. ^b Calculated using eq 4.

A model of association assuming the stepwise addition of monomers was used in an attempt to reproduce the apparently nonmicellar scattering behaviour of IVa and IVb and IVc. The analytical treatment was that of Steiner.⁹ This treatment does not necessitate the assumption of equal aggregation constants for each stage of the association, which is thought unlikely in aggregating systems in which small ionic aggregates are formed. It does, however, ignore the interactions between the charged aggregates, which become increasingly significant with increase in solution concentration. Stepwise equilibrium constants, K_N , were evaluated from eq 5 in a manner described previously.⁵

$$[(M_w/xM) - 1]/(xc/M) = 4K_2$$

$$+ 9K_2K_3(xc/M) \dots + N^2 \left(\prod_{N=2}^N K_N \right) (xc/M)^{N-2} \quad (5)$$

M_w and M are the apparent weight-average aggregate weights and monomer molecular weight respectively, c is the weight concentration (g dm⁻³), and N is the aggregation number. x is the weight fraction of compound existing as monomer, as determined from graphical integration of the light scattering data, according to

TABLE II: Stepwise Association Constants, Limiting Aggregation Numbers, and Free Energies of Association of Antiacetylcholine Drugs

Compd	Equilibrium constants, dm ³ mol ⁻¹				ΔG_m^a , kJ mol ⁻¹
	K_2	K_3	K_4	l	
IVb	2.8	33	4	12	-15.7
IVa	12.5	76	25	14	-18.0
IVc	50	149	67	>20	-20.3

^a Calculated using eq 7.

$$\ln x = \int_0^c [(M/M_w) - 1] d \ln c \quad (6)$$

Values of K_N are given in Table II. Because of the cumulative nature of the errors in the evaluation of K_N , only the lower K_N values are quoted. Error in K_N arising from a neglect of interactions between the charged aggregates is also least significant for these lower values. Application of eq 5 and 6 to the data for IVa and IVb suggested that the aggregates attained a limiting size, with a characteristic aggregation number, l . (See Table II.) It was not possible to determine a value of l for IVc even though K_N values up to $N = 20$ were evaluated.

The average free energy change per monomer, ΔG_m , for the formation of the N mer was calculated from¹

$$\Delta G_m = -(RT/N) \ln \left(\prod_2^l K_N \right) \quad (7)$$

values of ΔG_m (Table II) are in reasonable agreement with similar values calculated for several phenothiazine derivatives.⁸

Discussion

The effect which the structure of the hydrophobic group has on the mode of aggregation is clearly shown by the light scattering data presented here. The hydrophobic ring structures of IVa, IVb, and IVc are sufficiently planar and rigid to allow a stepwise stacking of monomers. The molecules are not symmetrical with respect to their charge distribution and it is probable that the monomers associate with their cationic head groups stacked in an alternate manner as has been suggested from NMR studies of the phenothiazines.¹⁰ The remaining compounds studied have flexible nonplanar hydrophobic regions and it is significant that these molecules associate in a micellar pattern.

The effect on the micellar properties of modifications of the chemical structure of the hydrophobic groups may be assessed by comparisons with previous studies⁴ on diphenylmethane derivatives with similar hydrophilic chains. The diphenylmethane derivative, lachesine chloride, was shown to dimerize with a cmc of 0.204 mol kg⁻¹. In Ia one of the phenyl rings is replaced with a cyclohexane ring, the rest of the molecule remaining unchanged. The effect of this replacement is to considerably increase the hydrophobicity, as evidenced by the lower cmc and higher aggregation number. Conversely, the replacement of a phenyl ring with a cyclopentane ring has little apparent effect on hydrophobicity; the diphenylmethane derivative, benzilium bromide (cmc = 0.143 mol kg⁻¹, $N = 4$), has similar properties to IIIa.

The greater hydrophobicity of the 2-diisopropylaminoethyl derivative of xanthine, IVa as compared with the 2-dieth-

ylaminoethyl derivative IVb, is reflected by the higher limiting aggregation size, the higher individual K_N values, and the increased free energy of association.

Acknowledgments. The author wishes to thank Lilly Research centre, Richardson-Merrill Ltd., A. H. Robins and Co. Ltd., Winthrop Laboratories, and G. D. Searle and Co. Ltd., for their generous gifts of drugs.

References and Notes

- (1) P. Mukerjee, *J. Pharm. Sci.*, **63**, 972 (1974).
- (2) D. Attwood, *J. Pharm. Pharmacol.*, **24**, 751 (1972).
- (3) D. Attwood and O. K. Udeala, *J. Pharm. Pharmacol.*, **26**, 854 (1974); **27**, 395 (1975).
- (4) D. Attwood, *J. Pharm. Pharmacol.*, **28**, 407 (1976).
- (5) D. Attwood and O. K. Udeala, *J. Phys. Chem.*, **79**, 889 (1975).
- (6) D. Attwood and O. K. Udeala, *J. Pharm. Sci.*, in press.
- (7) E. W. Anacker and A. E. Westwell, *J. Phys. Chem.*, **68**, 3490 (1964).
- (8) D. Attwood, A. T. Florence, and J. M. N. Gillan, *J. Pharm. Sci.*, **63**, 988 (1974).
- (9) R. F. Steiner, *Arch. Biochem. Biophys.*, **39**, 333 (1952).
- (10) A. T. Florence and R. T. Parfitt, *J. Phys. Chem.*, **75**, 3554 (1971).

Correlation between Melting Points of Alkanoic Acids and Krafft Points of Their Sodium Salts

Kōzō Shinoda,*

Department of Chemistry, Faculty of Engineering, Yokohama National University, Ooka-2, Minamiku, Yokohama, Japan

Yutaka Minegishi, and Haruhiko Arai

Household Goods Research Laboratories, Kao Soap Company Limited, Bunka-2 Sumidaku, Tokyo, Japan (Received April 26, 1976)

Publication costs assisted by Yokohama National University

In order to facilitate the use of longer chain surfactants which are more surface active, various ways of depressing the Krafft point have been studied. There is a close correlation between the melting points of alkanolic acids and the Krafft points of their sodium salts in water. Therefore, depressing the melting point also depresses the Krafft point and permits the use of long chain length surfactants at ordinary temperatures. Moderate branching of the lipophilic chain and the introduction of some groups, such as ethylene oxide, between the lipophilic chain and the hydrophilic group effectively depress the Krafft point as well as the melting point.

An ionic surfactant dissolves in water in a singly dispersed state up to the saturation concentration. Above this concentration a hydrated solid surfactant phase separates at temperatures below the Krafft point and micelles are formed above the Krafft point.¹ It is evident that the Krafft point is an important temperature above which hydrated solid surfactant melts and forms micelles, i.e., pseudophases in the liquid state.²⁻⁴ The solubility of ionic surfactants increases abruptly due to micellar dispersion, and solubilization of oily materials occurs above this temperature. Minimum surface tension values are not attained below the Krafft point, because the concentration of singly dispersed species is smaller than the critical micelle concentration. Hence, in most practical applications, the Krafft point of a surfactant has to be lower than the experimental temperature. The surface activity of surfactants increases rapidly with the hydrocarbon chain length.⁵ There exists also a rough parallelism between the Krafft points of soaps and the melting points of the corresponding acids.⁶ Therefore, it is very important to find surfactants whose Krafft points are low yet the hydrocarbon chains are long. The experimental determination of the Krafft point, however, requires solubility^{7,8} or electrical conductivity measurements⁹ of the saturated solution of the surfactant as a function of temperature. This process is time consuming. In order to estimate the Krafft point from some other more

easily accessible property of the surfactant the relationships between the melting points of alkanolic acids and the Krafft points of their sodium salts are plotted in Figure 1.

Experimental details will be published elsewhere along with other properties.¹⁰ It is evident from Figure 1 that the melting points of α -alkyl alkanolic acids are lower, and the Krafft points of their sodium salts are similarly lower, than the corresponding alkanolic acids and salts. The larger the side chain, the lower the melting and Krafft points. If the temperature at which a certain process has to be executed is 30 °C, the Krafft point has to be less than 29 °C or so. It is concluded from Figure 1 that the hydrocarbon chain length has to be 12 or less in the case of straight chain soap, 14 or less in the case of $R_{n-1}CH(CH_3)COONa$, but it can be as long as 19 in the case of $R_{n-1}CH(C_4H_9)COONa$. This means much more surface active substances can replace ordinary surfactants. Data on $C_{n-1}H_{2n-1}OCH_2COOH$ and their sodium salts are also shown in Figure 1.¹¹ The Krafft points of these salts were not as low as one might have expected from the melting points of $C_{n-1}H_{2n-1}OCH_2COOH$. Hence, the introduction of an oxygen atom into an alkanolic acid does not greatly depress the Krafft point. On the other hand, further introduction of ethylene oxide groups between the hydrocarbon chain and the polar group depresses the melting and Krafft points very much. The rough parallelism between the Krafft points and

TABLE I

Compd	Mp, °C	Kp, °C
$n\text{-C}_7\text{F}_{15}\text{COOH}$	56.4–57.9	20
$n\text{-C}_7\text{F}_{15}\text{COONa}$		8
$n\text{-C}_7\text{F}_{15}\text{COOK}$		25.6
$(\text{CF}_3)_2\text{CF}(\text{CF}_2)_4\text{COOH}$	13–14	Below 0
$(\text{CF}_3)_2\text{CF}(\text{CF}_2)_4\text{COONa}$		Below 0
$(\text{CF}_3)_2\text{CF}(\text{CF}_2)_4\text{COOK}$		Below 0
$n\text{-C}_6\text{F}_{13}\text{COOH}$	27	Below 0

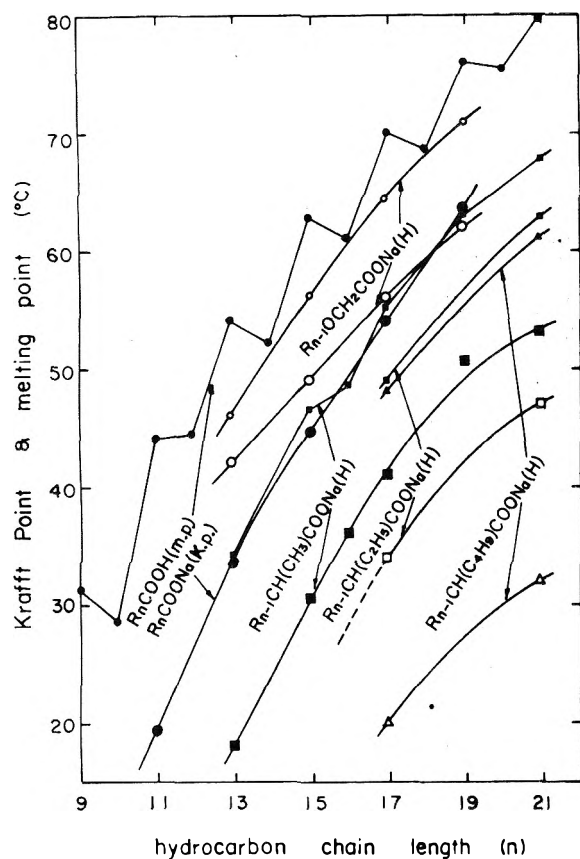


Figure 1. The effect of hydrocarbon chain length and the size of the side chain on the melting points of alkanolic acids and Krafft points (Kp) of their sodium salts: (●) mp of $R_n\text{COOH}$; (●) Kp of $R_n\text{COONa}$; (■) mp of $R_{n-1}\text{CH}(\text{CH}_3)\text{COOH}$; (■) Kp of $R_{n-1}\text{CH}(\text{CH}_3)\text{COONa}$; (□) mp of $R_{n-1}\text{CH}(\text{C}_2\text{H}_5)\text{COOH}$; (□) Kp of $R_{n-1}\text{CH}(\text{C}_2\text{H}_5)\text{COONa}$; (△) mp of $R_{n-1}\text{CH}(\text{C}_4\text{H}_9)\text{COOH}$; (△) Kp of $R_{n-1}\text{CH}(\text{C}_4\text{H}_9)\text{COONa}$; (○) mp of $R_{n-1}\text{OCH}_2\text{COOH}$; (○) Kp of $R_{n-1}\text{OCH}_2\text{COONa}$.

melting points of corresponding acids as a function of lypophilic chain length also holds in $\text{C}_n\text{F}_{2n+1}\text{COONa}(\text{H})$. The relation is shown in Figure 2.¹²

In the case of fluorinated compounds, the melting and Krafft points increase much faster with chain length (about 30–35 °C per $-\text{CF}_2-\text{CF}_2-$ group) and the differences between

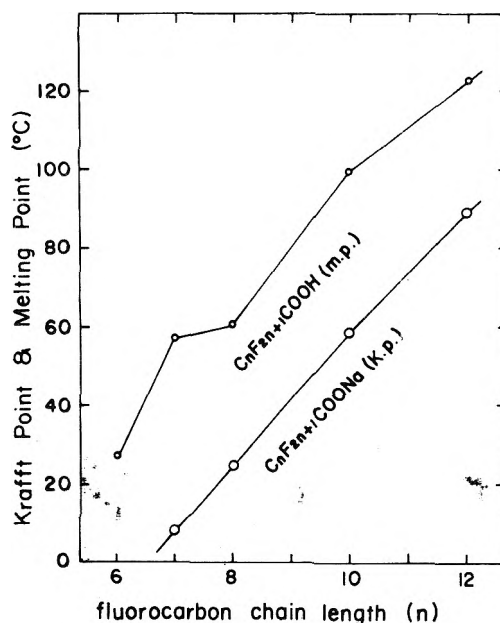


Figure 2. The relation between the melting points of perfluoroalkanoic acids and the Krafft points of their sodium salts.

the melting points and Krafft points were also larger (about 35–40 °C) than in paraffin chain compounds. As found above for paraffin chain compounds, branching leads to lower melting and Krafft points for fluorinated surfactants as well (see Table I).¹³

In conclusion, it was found that moderate branching of the hydrocarbon or fluorocarbon chain effectively depress the Krafft point and the melting point. Other means to depress the Krafft point include changing the kind of gegenions and introducing groups such as ethylene oxide in order to facilitate the use of longer chain surfactants.

References and Notes

- (1) K. Shinoda, T. Nakagawa, B. Tamamushi, and T. Isemura, "Colloidal Surfactants", Academic Press, New York, N.Y., 1963, pp 7, 8.
- (2) K. Shinoda and T. Soda, *J. Phys. Chem.*, **67**, 2072 (1963).
- (3) K. Shinoda, S. Hiruta, and K. Amaya, *J. Colloid Interface Sci.*, **21**, 102 (1966).
- (4) H. Nakayama, K. Shinoda, and E. Hutchinson, *J. Phys. Chem.*, **70**, 3502 (1966).
- (5) K. Shinoda and K. Mashio, *J. Phys. Chem.*, **64**, 54 (1960); ref 1, pp 79, 80.
- (6) F. Krafft, and H. Wiglow, *Berichte*, **28**, 2566 (1895).
- (7) R. C. Murray and G. S. Hartley, *Trans. Faraday Soc.*, **31**, 183 (1935).
- (8) N. K. Adam and K. G. A. Pankhurst, *Trans. Faraday Soc.*, **42**, 523 (1946).
- (9) O. Yoda, K. Meguro, T. Kondo, and T. Ino, *J. Chem. Soc. Jpn.*, **77**, 905 (1957) (in Japanese).
- (10) Y. Minegishi, K. Aigami, and H. Arai, *J. Oil Chem. Soc. Jpn.*, **24**, 237 (1975) (in Japanese).
- (11) M. Hato, K. Shinoda, and T. Miyagawa, *Bull. Chem. Soc. Jpn.*, in press.
- (12) H. Kunieda and K. Shinoda, to be submitted for publication.
- (13) K. Shinoda, M. Hato, and T. Hayashi, *J. Phys. Chem.*, **76**, 909 (1972).

Study of Metal Oxide Catalysts by Temperature Programmed Desorption.

1. Chemisorption of Oxygen on Nickel Oxide

Masakazu Iwamoto, Yukihiro Yoda, Makoto Egashira, and Tetsuro Seiyama*¹

Department of Materials Science and Technology, Faculty of Engineering, Kyushu University, Higashi-ku, Fukuoka, 812 Japan, and Department of Materials Science and Engineering, Faculty of Engineering, Nagasaki University, Nagasaki, 852 Japan (Received September 10, 1975; Revised Manuscript Received March 22, 1976)

Publication costs assisted by Kyushu University

The chemisorption of oxygen on nickel oxide was investigated over a wide range of temperature (0–600 °C) by means of the temperature programmed desorption (TPD) technique. At least four different states of adsorbed oxygen were indicated by the appearance of four TPD peaks, with peak maxima located at 30~40 (α), 320~360 (β), 420~450 (γ), and 520~550 °C (δ), respectively. Taking into account their adsorptive characteristics, the corresponding adsorbed species were tentatively assigned to O_2 (α), O_2^- (β), and O^- (γ and δ). Experimental facts that none of the β , γ , and δ oxygen retarded the chemisorption of the others suggested that these chemisorptions took place on different surface sites, while the chemisorption site for α was estimated to be common to β oxygen. The activation energies of adsorption for β and γ were 12.8 and 17.5 kcal/mol, respectively, and that of desorption for β was 23 kcal/mol. Adsorbed oxygen in various forms amounted altogether to ca. 3×10^{13} molecules/(cm² of NiO surface). The corresponding surface coverage was estimated to be ca. 4% with respect to surface nickel atoms, suggesting adsorptions on some sorts of surface defects. Discussions of these results are presented in relation to the oxidation power distribution of the surface excess oxygen, the oxygen isotopic exchange reaction, the binding energy of oxygen, etc.

Introduction

Catalytic oxidation is one of the most interesting reactions in heterogeneous catalysis. For an understanding of it, it would be very important to know the adsorption state of oxygen. For example, Boreskov et al.² pointed out that the catalytic activities of metal oxides for the complete oxidation or for the homomolecular oxygen isotopic exchange are closely related to the energies of metal–oxygen bonds of the oxides. This indicates that the rate-determining step for these reactions includes the rupture of the metal–oxygen bond, and suggests as well the significance of the experimental examination of interactions between oxygen and the catalyst surface. In addition, knowledge on the nature of the adsorbed oxygen and its adsorption mechanism would provide valuable criteria for catalyst conditioning.

Interactions between oxygen and metal oxides have been studied fairly extensively by a number of workers with techniques such as adsorption isotherm, adsorption kinetics, and ESR. Several types of adsorbed oxygen species have been proposed over various metal oxides, including O_2^- and O^- confirmed by ESR.³ The adsorption of oxygen, however, may in fact depend very sensitively on the nature and the preparation method of the oxides used. Therefore, we attempted to probe oxygen adsorption on various metal oxides systematically by means of the temperature programmed desorption (TPD) technique.

The TPD technique developed by Cvetanović and Amenomiya⁴ is a simple but very useful one to investigate interactions between a gas and a solid, and has been applied by several workers to studies of gas adsorption on metals or metal oxides.^{5,6} On the oxygen–metal oxide systems, however, few applications have been reported so far.

In the present paper, the chemisorption of oxygen on nickel oxide was investigated. Nickel oxide was chosen because it is a typical oxidation catalyst. As for the oxygen–NiO system,

Charman et al.⁷ suggested three or possibly four modes of oxygen adsorption on the basis of adsorption kinetics. Recently the existence of several modes of oxygen adsorption was in fact observed by means of the temperature programmed desorption technique by Gay.⁸ However, Gay's results were insufficient in terms of reproducibility and characterization for each mode of adsorption. From the viewpoint of nonstoichiometry, on the other hand, adsorbed oxygen on NiO may be regarded as surface excess oxygen, which is measurable with chemical techniques. Dereñ and Stoh⁹ measured, by means of modified Bunzen–Rupp and hydrazine methods, the excess oxygen content on NiO samples obtained by decomposition of nickel salts and showed that oxygen coverage was changeable with the method and condition of sample preparation. Uchijima et al.¹⁰ showed the distribution of oxidation power of excess oxygen on nickel oxide by the measurements using iodometric and hydrazine methods. These results obtained by chemical techniques are quite interesting, but the mode and nature of oxygen adsorption on NiO have remained almost unsolved due to the limitation of the methods. Considering that the various modes of oxygen adsorption are associated with different binding energies between oxygen and surface, it will be reasonably suggested that TPD is one of the best techniques for revealing the situation. The purpose of the present investigation is to establish the nature and occurrence of several modes of oxygen adsorption on NiO.

Experimental Section

In a preliminary experiment, we measured the temperature programmed desorption chromatograms of oxygen from commercial nickel oxide. However, it was revealed that (1) TPD chromatograms included water vapor as well as oxygen, and (2) the nickel oxide used was shown to contain trace amounts of Ni_2SiO_4 by x-ray diffraction. The present work was performed to the complete exclusion of such flaws.

Apparatus. The apparatus used for the TPD experiments is shown in Figure 1. It is in principle the same as that described in the literature.³ The reactor (R) was devised to minimize the dead volume and consisted of a quartz tube of 9.6 mm i.d. with a protective quartz tube of 8.0 mm o.d. with a thermocouple (TC₁) inserted inside. The detector was a conventional thermal conductivity cell with four tungsten filaments, G80-TCD of Yanagimoto Mfg. Co. Ltd. The temperature of catalyst was raised at uniform heating rates (from 5 to 30 °C/min) using a programming controller with a thyristor voltage regulator, and measured by a chromel–alumel thermocouple located on top of the catalyst bed. Uniform temperature increase was very important; otherwise the distortion of the chromatogram or even the appearance of false desorption peaks would occur. The temperature lag between the sample and the thermocouple was corrected using the results of preliminary heat transfer experiments. The correction value was, for example, 4 °C at a heating rate 20 °C/min under a gas flow rate 30 ml/min.

Materials. Commercial helium gas (above 99.995%, Air Product and Chemical) was used as a carrier. To remove trace amounts of moisture, it was passed through molecular sieve 5A at liquid nitrogen temperature. Commercial oxygen (above 99.8%) was also dried before use by liquefaction at liquid nitrogen temperature.

NiO samples were prepared by calcining nickel carbonate precipitated from a nickel nitrate solution with ammonium carbonate. Surface area and color of the samples obtained are summarized in Table I together with the calcination (or decomposition) conditions. The surface area was determined by the BET method. For TPD experiments, the powder was sieved and a fraction of 20~48 mesh was used.

Procedure. A fixed amount of NiO of ca. 1 ml (2.00 g for NiO-I-IV or 0.60 g for NiO-V) was loaded into the reactor. Before use, the oxide was evacuated for more than 2 h at the calcination (or decomposition) temperature (see Table I) until no more water was condensed in a liquid nitrogen trap connected to the reactor.

Oxygen adsorption prior to the TPD experiment was usually processed in two ways. In both ways, the NiO sample, after evacuation ($<10^{-5}$ Torr) for 1 h at the calcination temperature, was cooled to the desired temperatures and exposed to oxygen atmospheres (1~120 Torr) for a prescribed time. Subsequently, the sample was first degassed by evacuation for 1 h at the same temperature and then cooled to 0 °C in vacuo within 30 min (treatment A), or it was first cooled to 0 °C under an oxygen atmosphere at a constant cooling rate (10 °C/min), and then degassed for 1 h (treatment B). After these manipulations, the carrier gas was diverted to flow through the reactor at a rate of 30 ml/min. Programmed heating was started as soon as the recorder base line became stabilized. The heating rate was set at 20 °C/min unless specified otherwise. Gas desorption during heating was continuously monitored with a TCD and recorded as a TPD "chromatogram".

In all present experiments the desorbed gas was identified to be oxygen alone by gas chromatography and mass spectroscopy. The amount of desorbed oxygen was calculated from the peak area of the chromatogram.

Results

Desorption Chromatogram. It is expected that the TPD chromatogram varies with the conditions of calcination (or decomposition) and pretreatment of the oxide sample used, since those would affect the surface state of the oxide sensi-

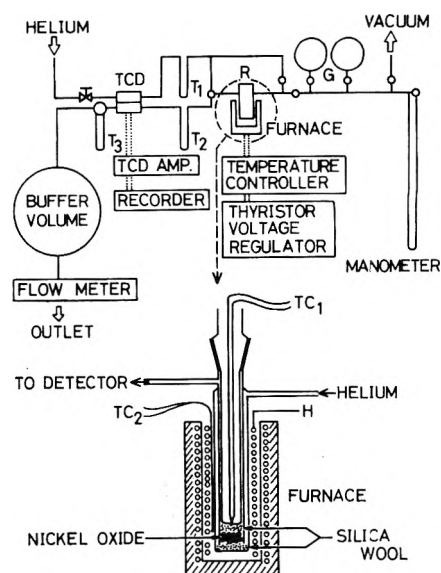


Figure 1. Apparatus for temperature programmed desorption: R, reaction vessel; G, gas reservoirs; T₁, T₂, T₃, traps; TC₁, thermocouple for recorder; TC₂, thermocouple for temperature controller; H, heater for temperature control.

TABLE I: Calcination Conditions and Properties of the NiO Samples Used

Catalyst	Calcination conditions			Surface Area, m ² /g	Color
	Temp, °C	Time, h	Atm		
NiO-I	400	5	Air	48.7	Black
NiO-II	500	5	Air	8.3	Dark gray
NiO-III	600	5	Air	4.6	Grayish green
NiO-IV	700	5	Air	2.9	Green
NiO-V	600	17	In vacuo	11.4	Yellowish green

tively. Therefore, this was first examined. The influence of the calcination temperature on the TPD chromatograms of oxygen is shown in Figure 2, where curves 1–5 were taken on five fresh samples calcined at various temperatures (NiO-I–V). As a pretreatment, the samples were exposed to 100 Torr of oxygen at 300 °C for 1 h after evacuation for 1 h at the calcination temperatures and cooled by treatment A. Clearly, the number of peak appearing in the TPD chromatograms as well as the respective peak area varies with the calcination condition. It is noticed, however, that the chromatograms consists of the combinations of three kinds of desorption peaks with the peak maxima located at 320~360, 420~450, and >520 °C, which are designated here as peaks β , γ , and δ , respectively. Peak α , to be shown later, denotes an additional peak observed around 30 °C in certain cases when oxygen is preadsorbed below 100 °C.

As shown in the figure, peak β is commonly observed over all the samples, though the peak area (amount of desorbed oxygen) differs largely with samples. The difference was mainly due to the variation in surface area, as indicated by the fact that the amounts of β -oxygen per surface area were 0.005, 0.008, 0.009, 0.006, and 0.008 ml/m² for NiO-I, -II, -III, -IV, and -V, respectively. On the other hand, peaks γ and δ are not always observed but are remarkable on the samples NiO-I, -II, and -V. This suggests that the adsorption sites on the NiO

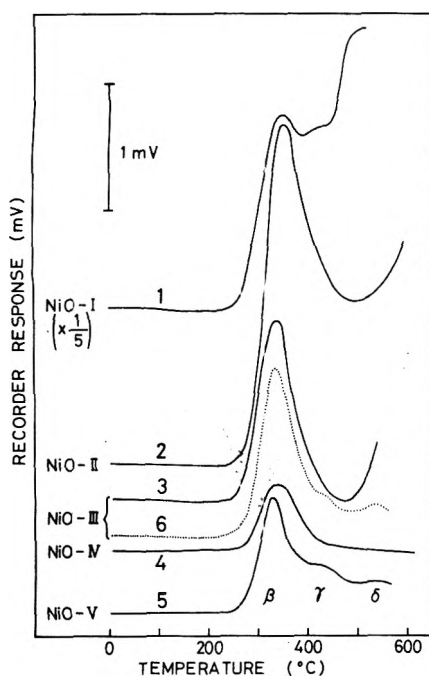


Figure 2. TPD chromatograms of oxygen from various NiO samples. Preadsorption of oxygen was carried out for 1 h at 300 °C and 100 Torr by treatment A. Curves 1–5 are chromatograms for NiO-I, -II, -III, -IV, and -V, respectively, obtained in the first run of TPD experiments. The fifth run on NiO-III gave curve 6 (see text).

surface responsible to these peaks are strongly affected by the sample quality or its preparation.

In addition, it should be mentioned that, when NiO samples freshly prepared by calcination in air were used, the TPD chromatograms underwent considerable changes with the repetition of the oxygen adsorption–desorption cycles. In the case of NiO-III the chromatogram changed gradually from curve 3 in Figure 2 with the repetition of exactly the same experiments and was finally “stabilized” after the fourth cycle as curve 6, which resembles curve 5 for NiO-V very well. Similar changes of the chromatograms were also observed for NiO-I and -II when the same cycles, i.e., evacuation at 600 °C, adsorption at 300 °C, and desorption up to 600 °C, were repeated. No such examination was made for NiO-IV because of the small surface area. In contrast, chromatograms for sample NiO-V prepared by decomposition in vacuo remained unchanged from curve 5 irrespective of the repetition of the cycles. These results are interesting, indicating that the adsorption sites for γ oxygen are created by evacuation at higher temperatures. The change or the stabilization of the samples with the repetitious treatments mentioned above is probably caused by evacuation at 600 °C. The analyses regarding its implications, especially in terms of the NiO surface character, are difficult at the present stage, however. With these facts in mind, only the samples NiO-V and “stabilized” NiO-III were used in the experiments hereafter.

Characterization of Desorption Peaks. In order to characterize the desorption peaks described above, the influence of the experimental conditions of the oxygen preadsorption on TPD chromatogram was examined. Figures 3 and 4 show the effect of the adsorption temperature when processed with treatments A and B, respectively. The dependence on the adsorption pressure is shown in Figure 5. Careful comparison of these chromatograms with each other affords the following

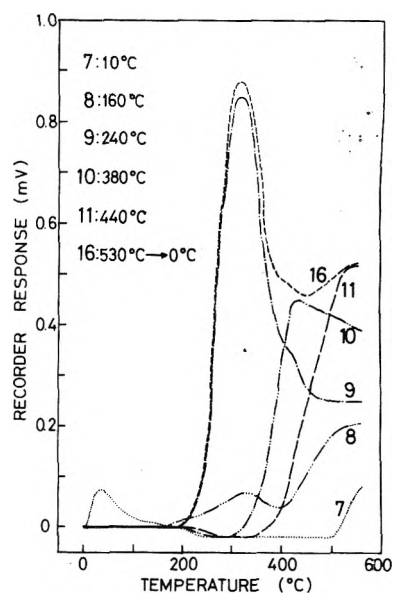


Figure 3. TPD chromatograms of oxygen from NiO-V after oxygen adsorption at various temperatures for 1 h at 120 Torr by treatment A. Dotted line (curve 16 of Figure 4) is also included for comparison.

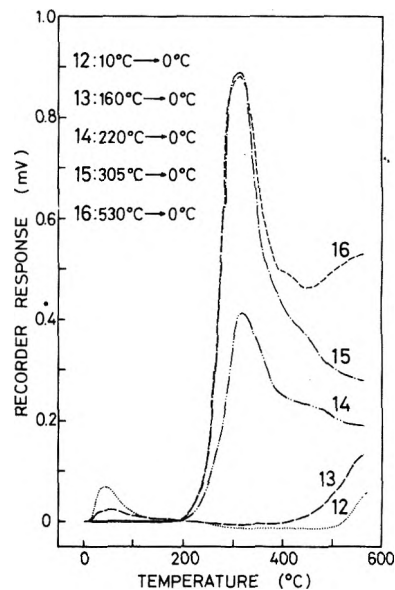


Figure 4. TPD chromatograms of oxygen from NiO-V after oxygen adsorption at various temperatures for 1 h at 40 Torr by treatment B.

information about the character of each desorption peak and the adsorbate involved.

(1) A new peak, α , appeared at 30–40 °C when oxygen was preadsorbed below 100 °C, as shown by curves 7, 12, and 13. Though α oxygen was removed by brief pumping at 120 °C, it is likely to be a chemisorbed species since no desorption resulted by evacuation for 1 h at 10 °C.

(2) Peak α is absent in curves 14–16 in spite of the exposure to oxygen at lower temperatures. Since these chromatograms show large desorption peaks of β and/or γ compared with curves 7, 12, and 13, it is suggested that the adsorption in α form is inhibited by the presence of the others. To further confirm this, it was examined whether NiO samples which had already preadsorbed β , γ , or δ oxygen could adsorb α oxygen additionally at 10 °C. As a result, α oxygen was adsorbed independently of γ or δ , but inhibited exclusively by β . Thus,

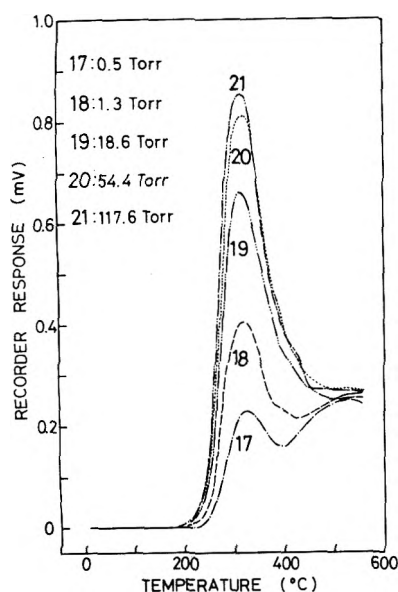


Figure 5. TPD chromatograms of oxygen from NiO-V after oxygen adsorption at various pressures for 1 h at 240 °C.

α oxygen interacts with β oxygen presumably by "sharing a common site".

(3) On the other hand, comparison of curve 16 with curves 9 and 10 suggests that the adsorption sites for β oxygen are different from those for γ and δ . This was supported by a series of TPD experiments. For instance, NiO samples which had preadsorbed δ oxygen by treatment A at 440 °C could adsorb β oxygen at 240 °C to the same amount as attained in the absence of δ . Similar result was also obtained between β and γ oxygen or γ and δ oxygen. Therefore, it may be stated that each of β , γ , and δ oxygen has specific adsorption sites of its own.

(4) The strength of the adsorption bonding should be in the order of $\alpha < \beta < \gamma < \delta$ oxygen in accordance with the sequence of desorption temperatures.

(5) Figure 5 shows that oxygen adsorption in δ form occurs easily and is saturated at the lowest oxygen pressure applied, while those in β and possibly γ forms are dependent upon oxygen pressure. It is also noted that the peak temperature of β peak is independent of the amount of β oxygen. This indicates the first-order desorption for the β peak as mentioned later.

(6) When NiO samples preevacuated at 600 °C for 1 h were treated in vacuo at 240 °C for 1 h, no desorption peak appeared in the TPD chromatogram. This excludes the possibility that the strongly bound oxygen species such as the excess lattice oxygen or any adsorbed surface oxygen unable to be desorbed below 600 °C transforms thermally into species of weaker adsorption bonds during the treatments.

(7) After δ oxygen was preadsorbed by treatment A at 440 °C, the sample was kept under evacuation for 1 h at 240 °C. Subsequent TPD chromatogram showed only the δ peak, indicating that no such transformation as $\delta \rightarrow \gamma$ or $\delta \rightarrow \beta$ occurred during the treatment. Similarly, it was assured that γ oxygen was inactive for the transformation to β at 240 °C.

Kinetics of Adsorption and Desorption. Kinetic data on oxygen adsorption were obtained under the condition of 240 °C and 120 Torr of oxygen pressure. After the adsorption treatment for a desired time the sample was briefly evacuated for 10 min at the same temperature, cooled to 0 °C in vacuo, and submitted to TPD measurement to determine the amount

of adsorbed oxygen vs. the adsorption time. It was confirmed that the desorption of oxygen during evacuation or cooling in this experiment was negligible. The results are shown in Figure 6. The amount of δ oxygen, which was approximately estimated from the peak area below 560 °C, is obviously underestimated to a considerable extent so that only qualitative discussions about it are permissible. The amounts of β and γ oxygen increase with time, attaining saturation value in 1 h, while δ becomes nearly saturated in the initial short period. This indicates that δ adsorption occurs far more rapidly than β or γ adsorption.

For β and γ adsorptions, the activation energies of adsorption (E_a) were estimated from the temperature dependence of the adsorption rates (Figure 7). Here, the adsorption rates were calculated approximately from the amounts of adsorption during an initial short period, 6 min. The values obtained were $E_a(\beta) = 12.8$ and $E_a(\gamma) = 17.5$ kcal/mol, respectively, for β and γ adsorptions. The latter coincides well with $E_a = 18$ kcal/mol reported by Winter¹¹ for oxygen adsorption on nickel oxide at 250~420 °C, though he made no distinction between β and γ oxygen.

The activation energy of desorption (E_d) was also determined. Essentially TPD chromatogram shows the progress of desorption as a function of temperature. When the sample temperature increases linearly with time and the desorption takes place from a homogeneous surface without appreciable readsorption, peak temperature (T_M) of a desorption peak is correlated with E_d and the heating rate (b) by the following equation.^{4,12}

For first-order desorption

$$2 \ln T_M - \ln b = \frac{E_d}{RT_M} + \ln \frac{E_d v_m}{Rk_0}$$

For second-order desorption

$$2 \ln T_M - \ln b = \frac{E_d}{RT_M} + \ln \frac{E_d v_m^2}{2Rk_0} - \ln v_m \theta_M$$

In these equations, v_m is the amount of the adsorbate at the full surface coverage, θ_M the surface coverage at peak maximum, and k_0 and R are constants. Thus, for first-order desorption we can obtain E_d from the plots of $(2 \ln T_M - \ln b)$ vs. $1/T_M$. Such an analysis was applied to the β peak. As shown in Table II, T_M increased with an increase in heating rate, while the amount of desorbed oxygen remained unchanged. The plotting gave a straight line in agreement with the above equation as shown in Figure 8. From the slope and the intercept, $E_d(\beta)$ and k_0/v_m were determined to be 23.7 kcal/mol and $2.09 \times 10^8 \text{ min}^{-1}$, respectively, for sample NiO-V. The corresponding values for stabilized NiO-III were 23.0 kcal/mol and $1.98 \times 10^8 \text{ min}^{-1}$. The agreement of the values between the two samples was excellent. The value for $E_d(\beta)$ is close to that obtained by Gay.⁸ The peak width calculated with these rate parameters by the method of Cveticanović et al.¹³ was 98 °C, which was consistent with the experimental value (ca. 100 °C). For the α , γ , or δ peaks no such analysis was made because the peak temperatures could not be measured with sufficient accuracy.

Discussion

Oxygen adsorbing (or desorbing) on NiO in the temperature range of 0–600 °C exhibited four characteristic peaks in the TPD chromatograms. Of these peaks, two (β and γ) are clearly evident whereas the remaining two (α and δ) are less evident being indicated by weak responses. Next concern would then

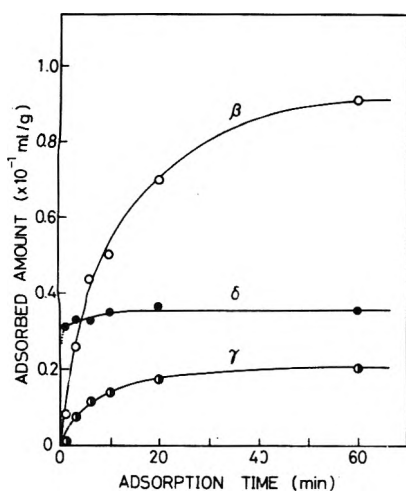


Figure 6. Time course of β , γ , and δ adsorptions.

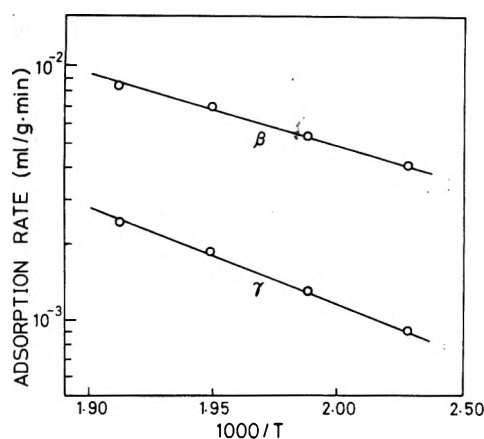


Figure 7. The Arrhenius plots of the rate for β and γ adsorptions (see text).

be on the corresponding adsorbed oxygen species and the adsorption sites for them.

To begin with, β type oxygen will be considered. It is well known^{6,13} that the peak temperature T_M of a desorption peak in the TPD chromatogram shifts to the higher side with a decrease in the amount of adsorbed gas in the following four cases: (1) the desorption rate is of second order, (2) the surface is energetically heterogeneous, (3) re-adsorption occurs significantly in the desorption process, (4) diffusion controls the TPD process. For β oxygen, none is the case since T_M is almost independent of adsorbed amounts, as shown in Figure 5. This suggests first-order desorption from an energetically homogeneous surface. In addition, the amount of β calculated from Figure 5 was found to follow the Langmuir isotherm of molecular adsorption

$$\frac{v}{v_m} = \frac{KP}{1 + KP}$$

where v is the adsorbed amount (ml STP/g) at an equilibrium partial pressure of oxygen P (Torr), v_m is the maximum adsorbed amount, and K is an equilibrium adsorption constant. v_m and K were determined to be 0.0918 ml (STP)/g of catalyst and 0.183 Torr⁻¹, respectively. From these two facts we tentatively assign β oxygen to be of a molecular type (probably O₂⁻).

The conclusion leads us to the estimation that α oxygen

TABLE II: Temperature Programmed Desorption of β Oxygen^a

b , °C/min	T_M , °C	V_d , ^b ml/g
10	320	0.0872
15	324	0.0922
20	338	0.0911
20	335	0.0909
25	340	0.0931
30	346	0.0910

^a Adsorptions of oxygen were carried out by treatment B at 530 °C and 40 Torr. ^b V_d is the amount of desorbed oxygen.

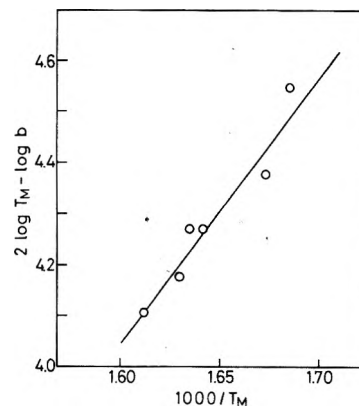


Figure 8. Application of eq 1 for β desorption from NiO-V.

should also be a molecular type (probably O₂), since α oxygen interacts with β oxygen probably by sharing common sites.

δ oxygen, the strongly and rapidly chemisorbed species in Figures 3–6, is the predominant species formed in the adsorption at room temperature. From the heat of formation of oxygen anions in gas phase, it is anticipated that O₂⁻ and O⁻ species would be rapidly formed while the formation of O²⁻ would be slower.^{14,15} In fact, several investigators have reported that oxygen is adsorbed as O⁻ on nickel oxide in the first place. Bierański and Najbar¹⁶ found, by determination of the mean electric charges acquired by an oxygen atom on the nickel oxide surface, that O⁻ was the predominant species in the irreversible adsorption at room temperature, and that at 150 °C only O⁻ was observed after a short period of adsorption. Robert et al.¹⁷ showed by means of XPS that a strongly chemisorbed oxygen (probably O⁻, 531.4 eV(O 1s)), different from the lattice oxygen (O²⁻, 529.2 eV(O 1s)), was formed by exposing nickel oxide to desiccated air. Taking these results into account, δ oxygen would be appropriately assigned to O⁻.

For γ adsorption, its occurrence is caused by the pretreatment of NiO in vacuo at higher temperatures as mentioned before. In this connection, very interesting is the fact reported by Winter¹⁸ that the activation energy of the isotopic exchange reaction of oxygen was smaller on nickel oxide outgassed at 520 °C than on one exposed to oxygen at 620–320 °C. On the basis of our observation, this fact is well interpreted as follows: on the latter sample the isotopic exchange proceeds with the participation of δ oxygen, while, on the former, γ oxygen which is the more labile species produced after the evacuation takes part in the reaction. Thus, we tentatively assign γ oxygen to O⁻ which is the same species as δ oxygen but is adsorbed on different surface sites. This assignment accounts for the fact

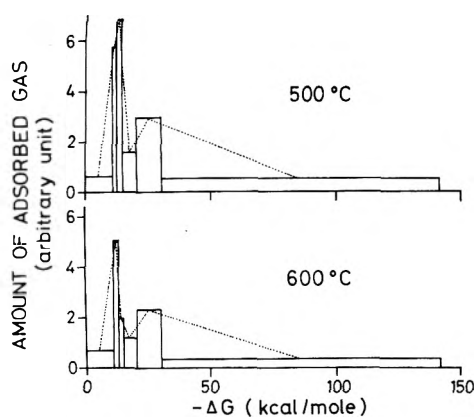


Figure 9. The amounts of the excess oxygen of NiO as a function of the free energy of adsorption ΔG . Numerical values indicated in the figure show the calcination temperatures of the samples.

that γ oxygen has a stronger adsorption bond than β , probably O_2^- .

In conclusion, we tentatively assign α and β oxygen to O_2 and O_2^- , respectively, probably on common surface sites, and γ and δ oxygen to O^- on different surface sites.

What kind of sites are then responsible to these adsorbed state? Dereń and Stoh⁹ have measured and reviewed the excess oxygen on the surface of and in the bulk nickel oxide. According to them, nickel oxide prepared by thermal decomposition in vacuo of nickel salts such as carbonate shows the exact stoichiometry ($Ni/O = 1/1$),^{16,19} while the oxide obtained by decomposition in air retains a significant amount of excess oxygen unable to be removed readily.^{7,9,20} It may then be suggested that surface nickel atoms uncovered by the excess oxygen act as the chemisorptive sites for oxygen. This, however, cannot give a quantitative explanation for our experimental results.

The number of surface nickel atoms on the (100), (110), or (111) plane of NiO is shown to be 1.15×10^{15} , 0.81×10^{15} , or 1.32×10^{15} atoms/cm², respectively. On the other hand, the amounts of β , γ , and δ oxygen obtained from curve 16, for example, are 1.82×10^{13} , 0.48×10^{13} , and 0.72×10^{13} molecules/cm² of NiO surface, respectively. The total number of the sites occupied by them is estimated to be 4.21×10^{13} sites/cm² on the basis of the above assignment, which corre-

sponds to surface coverage of ca. 4% with respect to surface nickel atoms. Consequently, it seems more reasonable to assume that oxygen is adsorbed onto surface defects such as oxygen vacancies, dislocations, edges, and corners.

Finally, it would be noteworthy that the TPD chromatogram of oxygen obtained in the present study is well correlated to the distribution of oxidation power of the surface excess oxygen on nickel oxide measured by Uchijima et al.¹⁰ Using their data on the samples calcined at 500~600 °C, the amount of surface excess oxygen is depicted vs. the free energy change of adsorption, $-\Delta G$, in Figure 9. Clearly, the distribution of the surface excess oxygen shows two maxima which correspond well to the desorption peaks of the TPD chromatograms measured after similar sample conditioning (Figure 2, curve 2 and 3). Taking into account that E_d is usually a monotonic function of T_M in TPD experiments, probably such a correlation suggests a sort of parallelism between ΔG and E_d for the adsorbed species involved.

Acknowledgment. The authors wish to express their gratitude to Dr. Noboru Yamazoe for helpful discussions.

References and Notes

- (1) Author to whom correspondence should be addressed at Kyushu University.
- (2) B. A. Sazonov, V. V. Popovskii, and G. K. Borekov, *Kinet. Katal.*, **9**, 312 (1968); F. Basolo and R. L. Burwell, Jr., "Catalysis Progress in Research", Plenum Press, New York, N.Y., 1973, p 91.
- (3) J. H. Lunsford, *Catal. Rev.*, **8**, 135 (1973).
- (4) Y. Amenomiya and R. J. Cvetanović, *J. Phys. Chem.*, **67**, 144, 2046, 2705 (1963).
- (5) Y. Amenomiya, J. H. B. Chenier, and R. J. Cvetanović, *Proc. Int. Congr. Catal.*, **3rd**, 1964, 2, 1135 (1965).
- (6) R. J. Cvetanović and Y. Amenomiya, *Catal. Rev.*, **6**, 21 (1972).
- (7) H. B. Charman, R. M. Dell, and S. S. Teale, *Trans. Faraday Soc.*, **59**, 453 (1963).
- (8) I. D. Gay, *J. Catal.*, **17**, 245 (1970).
- (9) J. Dereń and J. Stoh, *J. Catal.*, **18**, 249 (1970).
- (10) Y. Uchijima, M. Takahashi, and Y. Yoneda, *Bull. Chem. Soc. Jpn.*, **40**, 2767 (1967); *J. Catal.*, **9**, 403 (1967).
- (11) E. R. S. Winter, *J. Catal.*, **6**, 35 (1965).
- (12) J. L. Stakebake, *J. Phys. Chem.*, **77**, 581 (1973).
- (13) R. J. Cvetanović and Y. Amenomiya, *Adv. Catal.*, **17**, 103 (1967).
- (14) E. R. S. Winter, *Adv. Catal.*, **10**, 196 (1958).
- (15) M. M. Taqui Khan and A. E. Martell, "Homogeneous Catalysis by Metal Complexes", Academic Press, New York, N.Y., 1974, p 83.
- (16) A. Bieranski and M. Najbar, *J. Catal.*, **25**, 398 (1972).
- (17) T. Robert, M. Bartel, and G. Offergeid, *Surface Sci.*, **33**, 123 (1972).
- (18) E. R. S. Winter, *J. Chem. Soc.*, 2889 (1968).
- (19) A. Bieranski, J. Dereń, J. Haver, and J. Skiczynski, *Trans. Faraday Soc.*, **58**, 166 (1962).
- (20) S. J. Teichner et al., *Bull. Soc. Chim. Fr.*, 3244, 3251 (1967).

Infrared Studies of Reactions on Oxide Surfaces. 5. Lewis Acid Sites on Dehydroxylated Silica

B. A. Morrow* and I. A. Cody

Department of Chemistry, University of Ottawa, Ottawa, Ontario, K1N 6N5, Canada (Received March 5, 1976)

Publications costs assisted by the National Research Council of Canada

When silica is subjected to a vacuum degassing at about 600 °C two new infrared bands are observed at 908 and 888 cm^{-1} and the intensity of these bands increases with higher degassing temperature reaching a maximum at about 1200 °C. These bands are associated with the formation of a new active site on to which pyridine and trimethylamine can reversibly coordinate without dissociation of the site or of the adsorbate. It is suggested that a surface silicon atom of strained siloxane bridge is electron deficient thereby acting as a Lewis acid center. The nature and unusual chemical reactivity of this site are discussed in the following paper

We have previously shown¹ that when silica is subjected to a high temperature degassing under vacuum (400–1200 °C), new active sites are formed which are capable of acting as centers for the subsequent room temperature chemisorption of ammonia, methanol, or water (no chemisorption occurs at 20 °C without the vacuum degassing). The new site was associated with the appearance of two infrared bands at 888 and 908 cm^{-1} in the spectrum of degassed silica,² and the site was thought to be a strained siloxane bridge (Si–O–Si). Both the 908- and 888- cm^{-1} bands disappeared in unison when titrated with small doses of reactant (or with the boron halides²). In the present paper we report that these active sites are also capable of displaying typical Lewis acidic behavior following the adsorption of pyridine or trimethylamine whereby only one of the aforementioned infrared bands disappears. This is the first evidence for the presence of such sites on silica and as such may have considerable importance with respect to the mechanism of the rehydration of hydrophobic silicas.^{3,4} Preliminary details of the latter are discussed in the following paper which is concerned with the chemisorption of NH_3 , H_2O on such silicas, and further mechanistic details will follow in part 7.

Experimental Section

(This section applies to this and the following paper.)

The silica used in this work was Cab-O-Sil HS-5 and had a BET (N_2) surface area of 320 $\text{m}^2 \text{g}^{-1}$. The bulk powder was generally heated in a muffle furnace at 700 °C prior to disk pressing in order to oxidize any hydrocarbon impurities, although no differences were observed if this procedure was omitted. One inch diameter disks were pressed in a stainless steel die at a pressure of 1000 lb in.^{-2} for 2 s and the optical thickness was 10 or 40 mg cm^{-2} . The quartz cell has been described previously⁵ and NaCl windows were sealed with either Glyptal or with Tec Kits E-7 epoxy resin. Heating temperatures <1000 °C were measured with a chromel–alumel thermocouple which was imbedded in the external furnace area of the cell and do not necessarily reflect the real sample temperature. In order to produce a totally dehydroxylated silica, a temperature of about 1300 °C was employed, and, although generally not measured in each experiment, the heating current was adjusted on a trial and error basis so as to be just below a temperature which would cause collapse of the evacuated quartz cell.

The gaseous reactants used were exhaustively dried by repeatedly passing the vapor through tubes packed with P_2O_5 . Liquid reactants were generally dried by refluxing with LiAlH_4 or with CaH_2 .

Infrared spectra were recorded on a Perkin-Elmer Model 13G spectrometer utilizing spectral slit widths which were generally less than one half of the minimum $\nu_{1/2}$ of any observed band. Accurate calibration was obtained with reference to known bands of gas phase molecules mainly H_2O , NH_3 , HCl , DCl , and HBr .

Results

General Properties of Dehydroxylated Silica. Thin silica disks of Cab-O-Sil (10 mg cm^{-2}) totally absorb in the infrared between about 1350–750 cm^{-1} except for a “window” of partial transparency between 1000 and 850 cm^{-1} . Using untreated Cab-O-Sil (i.e., omitting the preheating step at 700 °C described above) the transmission increased with increasing temperature when the sample was degassed under vacuum, reaching a maximum at about 500–600 °C (Figure 1A–C). With higher temperatures, two strong bands started to appear at 908 and 888 cm^{-1} accompanied by a weak shoulder at about 940 cm^{-1} (Figure 1D and E), and the intensity of all three features increased in proportion to the temperature of degassing, reaching a maximum near 1200 °C (Figure 1F).

The surface of untreated silica has both free and hydrogen bonded hydroxyl groups and degassing up to about 500 °C removes most of those which hydrogen bond leaving a strong but relatively sharp band at 3748 cm^{-1} due to isolated SiOH groups.⁶ Therefore, the increase in transmission at 900 cm^{-1} during degassing up to 500 °C is due to a decrease in the number of H-bonded hydroxyls having low frequency bending modes which absorb in this region.^{7,8}

With a treated silica (i.e., one which had been preheated to 700 °C) the hydrogen bonded hydroxyls do not re-form on cooling to 20 °C and only the strong 3748- cm^{-1} band (with a slight low wave number tail) was observed in the $\nu(\text{OH})$ region. With these samples, the background at 900 cm^{-1} after degassing at any temperature within the range 20–460 °C was identical with that shown in Figure 1C, and with increasing temperatures the spectral changes were the same as in Figure 1D–F. As the temperature was increased from 600 to 1200 °C, the intensity of the 3748- cm^{-1} band progressively decreased until its peak absorbance was about 0.10 after 1200 °C corre-

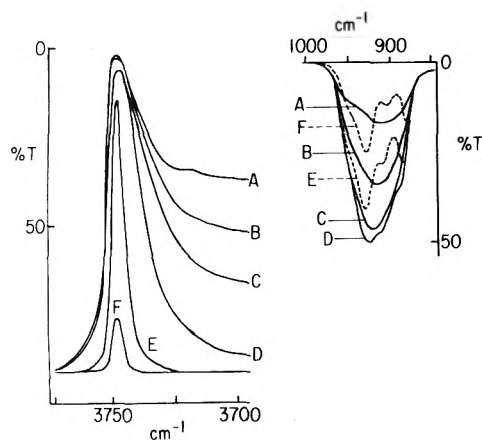


Figure 1. Background spectra of untreated silica (10 mg cm^{-2}) after degassing under vacuum: (A) 180°C ; (B) 300°C ; (C) 460°C ; (D) 675°C ; (E) 900°C ; (F) 1200°C .

sponding to the removal of about 95% of the isolated silanols. (Representative spectra are shown in the following paper, and in ref 2.) Heating from 1200 to about 1300°C (just below the softening point of the cell) caused no measurable increase in the intensity of the new features but did cause the total removal of the 3748-cm^{-1} band.

The new bands in the $1000\text{--}850\text{-cm}^{-1}$ spectral region are associated with the formation of a new active site when silica is degassed at temperatures above 400°C . This and the following paper are concerned with the reactivity of this site and identical results were obtained whether treated or untreated Cab-O-Sil was used. However, since it was desirable to oxidize hydrocarbon impurities before use, the preheat-treated silica was used most of the time.

Reactivity of the Sites with Lewis Bases. When 8 Torr of pyridine was allowed to adsorb at 20°C on to a silica sample which had been previously degassed at 250°C so as to remove physically adsorbed water, only the well-known⁹ infrared bands at 1595, 1487, and 1445 cm^{-1} due to hydrogen bonded pyridine were observed (Figure 2A) and these bands slowly disappeared following several hours evacuation at 20°C or after 1-h evacuation at 70°C . However, when a sample had been degassed for 3 h at 1100°C so as to cause the formation of the sharp bands at 888 and 908 cm^{-1} (Figure 3A), then additional bands were observed at 1620, 1490, and 1451 cm^{-1} following the admission of 8 Torr of pyridine (Figure 2B, marked with an asterisk) and the 888-cm^{-1} band disappeared leaving only the 908-cm^{-1} band which had shifted to 913 cm^{-1} (Figure 3B). (The weak shoulder near 940 cm^{-1} was only observed when the intensity at 908 and 888 cm^{-1} was large. None the less, it also disappeared in unison with the 888-cm^{-1} band and for convenience it will not be specifically referred to.) No further spectral changes occurred if the pyridine was left in the cell for up to 12 h. However, upon evacuation at 20°C for up to 10 h, all bands decreased in intensity, but the bands due to hydrogen bonded pyridine disappeared faster than the new set of bands, and after 1-h evacuation at 70°C , all high wave number bands disappeared and the 888-cm^{-1} band had reappeared more or less to its original intensity (Figures 3C and D).

In order to eliminate the possibility of hydrogen bonding with the surface SiOH groups a totally dehydroxylated silica was prepared by degassing at about 1250°C for 2 h. Following the admission of 8 Torr of pyridine, the spectrum shown in

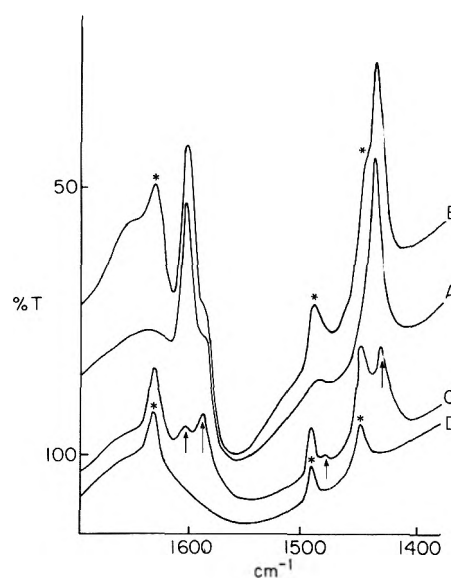


Figure 2. Spectra of adsorbed pyridine on silica which had been previously degassed at (A) 250°C , (B) 1100°C , and (C,D) 1250°C (totally dehydroxylated). Gaseous pyridine (8 Torr) was left in the cell for spectra A, B, and C. Spectrum D was obtained after 1-min evacuation of C. The %T scale refers to A.

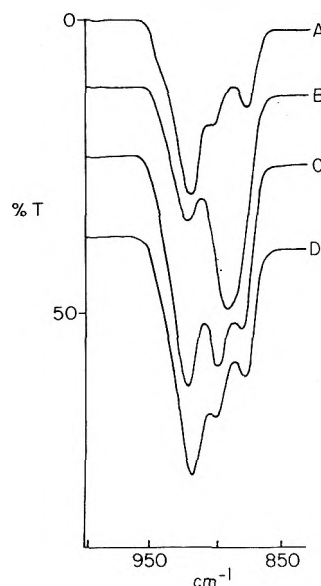


Figure 3. Spectra of silica (10 mg cm^{-2}) after (A) degassing at 1100°C , (B) after adsorption of 8 Torr of pyridine, (C) after evacuation at 20°C for 10 h, and (D) after evacuation at 70°C for 1 h. The %T scale refers to A.

Figure 2C was obtained which shows, in addition to the new set of bands described above, bands due to liquid like pyridine (marked with a vertical arrow), presumably physically adsorbed (these bands were identical with those observed in the spectrum of a thin film of liquid pyridine). The bands due to physically adsorbed pyridine disappeared after 1-min evacuation (Figure 2D) whereas the new set of bands slowly decreased in intensity as before after several hours evacuation, eventually disappearing when the intensity of the 888-cm^{-1} band was restored. The process could be repeated if pyridine was again added.

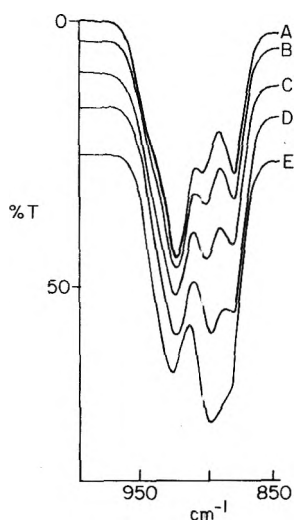
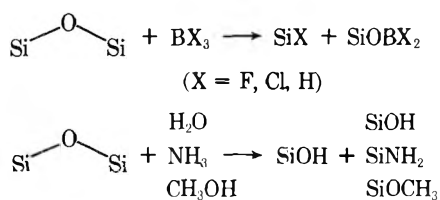


Figure 4. Spectrum of silica (10 mg cm^{-2}) after (A) degassing at 1100°C . Spectra B-E were recorded after the addition of successive micromole doses of gaseous trimethylamine. The %T scale refers to A.

The spectral changes which were observed in the $1000\text{--}850\text{-cm}^{-1}$ region with pyridine were also observed when trimethylamine was the adsorbate. Figure 4 shows a series of spectra which were observed when a dehydroxylated silica was "titrated" with successive micromole doses of the latter, and again, as the intensity of the 888-cm^{-1} band diminished, the 908-cm^{-1} band shifted to 913 cm^{-1} . Strong bands due to $\nu(\text{CH}_3)$ and $\delta(\text{CH}_3)$ modes were also observed (not shown). Degassing at 200°C was necessary in order to desorb trimethylamine and restore the intensity of the 888-cm^{-1} band.

Discussion

The infrared bands at 888 and 908 cm^{-1} have previously been shown to be correlated with the formation of a new active site on dehydroxylated silica.² Both infrared bands disappeared in unison when a degassed silica was titrated with micromole doses of BF_3 , BCl_3 , B_2H_6 , H_2O , NH_3 , or CH_3OH and new features were observed in other spectral regions which indicated that dissociative chemisorption had occurred.^{1,2} It had been assumed that the dehydroxylation process resulted in the formation of a strained siloxane bridge site which reacted with the above molecules as follows:



Spectroscopic evidence has conclusively shown that the above products were formed^{1,10} and that when SiOH was formed this differed from the normal silanol groups on silica in that the $\nu(\text{OH})$ mode of the chemically generated, SiOH was shifted 7 cm^{-1} to lower wave number. Further, a dissociative chemisorption appears to be always favored when the adsorbate molecule contains NH, OH, or BX bonds and further aspects of these and other reactions will be discussed in the following

paper. However, we stress that the above mechanism is only intended to represent the apparent stoichiometry since the "real" site may be considerably more complex.

The present results have shown that two typical Lewis bases which are not capable of reacting dissociatively with the active site none the less reversibly adsorb such that only one of the two strong bands in the $1000\text{--}850\text{-cm}^{-1}$ region disappears. Further, the in-plane ring deformation and CH deformation modes of pyridine ($1650\text{--}1300 \text{ cm}^{-1}$) are very sensitive to the surrounding environment and infrared spectroscopy has become a well-established technique for showing whether sites are present which can hydrogen bond, accept electron pairs (Lewis acid sites), or transfer protons (Bronsted acid sites).^{9,11} The new band positions and their relative intensities are clearly indicative of the presence of coordinated pyridine. Such clear evidence for the formation of a coordinate bond is not available in the case of trimethylamine but in view of the identical spectral behavior in the $1000\text{--}850\text{-cm}^{-1}$ spectral region we assume that this molecule has also adsorbed on a Lewis acid site.

The coordinate bond in either case is relatively weak in that the adsorbed species could be desorbed slowly with prolonged evacuation at 20°C or rapidly with mild heating at $100\text{--}150^\circ\text{C}$, thereby regenerating the active sites. At least 600°C is necessary to fully regenerate the sites when chemisorbed species are present. Moreover, additional experiments have shown that coordinated pyridine or trimethylamine could be readily displaced when H_2O or NH_3 was added, i.e., the 913-cm^{-1} band disappeared as chemisorption of H_2O or NH_3 proceeded accompanied by the disappearance of the high wave number bands of pyridine or Me_3N , and the resultant spectra of chemisorbed H_2O and NH_3 were the same as could be obtained when these molecules were added to an activated surface which displayed both of the 888- and 908-cm^{-1} bands.

The present results show that the three bands between $1000\text{--}850 \text{ cm}^{-1}$ which are associated with the formation of the active center cannot simply be related to a single adsorption site since two of the three bands disappear upon coordination whereas all three disappear when dissociative chemisorption takes place. Consequently, the real site is unlikely to be a simple symmetric single siloxane bridge as drawn previously; such a bridge is not expected to give rise to three bands in this spectral range since the symmetric and antisymmetric $\nu(\text{Si-O-Si})$ modes are usually widely separated (about 500 and 1050 cm^{-1}). Further, the presence of a coordinated species does not block the active center with respect to its ability to facilitate the dissociative chemisorption of H_2O or NH_3 .

In consideration of the above, it would appear that the 888-cm^{-1} band (and the shoulder at 940 cm^{-1}) is primarily associated with a Lewis acid center, possibly a trivalent electron deficient surface silicon atom, or to a silicon atom which is in a favorable geometric configuration so as to accept an extra pair of electrons in order to achieve greater than fourfold coordination.¹² The 908-cm^{-1} band would then be primarily associated with a reactive siloxane bridge or network which ruptures when dissociative chemisorption occurs.

At this stage it is not profitable to speculate further about the exact nature of this site without additional experimental investigation, some of which is given in the following paper. However, the present data obviously have some important ramifications with regard to the mechanism of the rehydration of hydrophobic silicas. Thus, Chuiko et al.¹³ have suggested from their simultaneous infrared and gravimetric study of the reactions of CH_3OH and of H_2O on hydrophobic silicas that a "coordinationally unsaturated silicon atom" plays a key role

in the rehydration and the present work provides the first direct proof that such centers exist.

Finally, we have briefly investigated whether some other potential electron-donating molecules (which do not contain NH or OH bonds) also capable of reacting in a similar manner and have found that no coordination occurred when PH_3 , CH_3CN , CO , NO , or NO_2 were added to a dehydroxylated silica.

Acknowledgment. We gratefully acknowledge financial support from the National Research Council of Canada and from Imperial Oil Ltd. B.A.M. also acknowledges the help provided by Dr. G. Somorjai and the staff at the University of California, Berkeley, where this manuscript was written while he was on sabbatical.

References and Notes

- (1) B. A. Morrow and I. A. Cody, *J. Phys. Chem.*, **79**, 761 (1975).
- (2) B. A. Morrow and A. Devi, *J. Chem. Soc., Faraday Trans. 1*, **68**, 403 (1972).
- (3) A. V. Volkov, A. V. Kiselev, and V. I. Lygin, *Russ. J. Phys. Chem.*, **48**, 703 (1974).
- (4) V. Ya. Davydov, A. V. Kiselev, V. A. Lokutsievskii, and V. I. Lygin, *Russ. J. Phys. Chem.*, **48**, 1342 (1974).
- (5) B. A. Morrow and P. Ramamurthy, *J. Phys. Chem.*, **77**, 3052 (1973).
- (6) A. V. Kiselev and V. I. Lygin, "Infrared Spectra of Surface Compounds", Wiley, New York, N.Y., 1975.
- (7) M. Hino and T. Sato, *Bull. Chem. Soc. Jpn.*, **44**, 33 (1971).
- (8) H. A. Benesi and A. C. Jones, *J. Phys. Chem.*, **63**, 179 (1959).
- (9) E. P. Parry, *J. Catal.*, **2**, 371 (1963).
- (10) B. A. Morrow, I. A. Cody, and L. S. M. Lee, *J. Phys. Chem.*, **79**, 2405 (1975).
- (11) Reference 6, pp 246-254.
- (12) Reference 6, p 162.
- (13) A. A. Chuiko, V. A. Sobolev, and V. A. Tertykh, *Ukr. Khim. Zh.*, **38**, 774 (1972) (in Russian).

Infrared Studies of Reactions on Oxide Surfaces. 6. Active Sites on Dehydroxylated Silica for the Chemisorption of Ammonia and Water

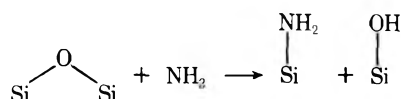
B. A. Morrow* and I. A. Cody

Department of Chemistry, University of Ottawa, Ottawa, Ontario, K1N 6N5, Canada (Received March 5, 1976)

Publication costs assisted by the National Research Council of Canada

When silica is subjected to a vacuum degassing at temperatures above 400 °C a new active site is generated which is capable of facilitating the dissociative chemisorption of NH_3 and H_2O . This site can also act as a Lewis acid center (see the preceding paper) and the simplest model for the site would be an unsymmetrical strained siloxane bridge in which one of the surface silicon atoms is electron deficient. The reaction stoichiometry indicates that a 1:1 mixture of SiNH_2 and SiOH is formed from NH_3 and that two SiOH groups are formed from H_2O . In all cases, the SiOH generated absorbs at 3741 cm^{-1} and normal isolated silanols (3748 cm^{-1}) are not generated. NH bond rupture also results when CH_3NH_2 or $(\text{CH}_3)_2\text{NH}$ reacts with the site and OH bond rupture when CH_3OH is used, and in each case the new SiOH species is formed. The number of sites generated increases with the degassing temperature reaching a maximum at about 1200 °C at which point the site concentration is estimated to be about $0.15/100\text{ \AA}^2$. The reaction products desorb upon degassing at 650 °C when the sites are regenerated and the sample is again active for chemisorption. The site does not react at 20 °C with CH_4 , C_2H_4 , HCN , CH_3CN , HCl , O_2 , H_2 , PH_3 , CCl_4 , or $\text{SiCl}(\text{CH}_3)_3$.

Several infrared investigations of the adsorption of ammonia on silica have been carried out but the most detailed recent study was by Blomfield and Little,¹ who cleared up a previous controversy by showing that trace quantities of chlorine were not necessary in order to facilitate chemisorption. However, in agreement with previous work,^{2,3} they found that chemisorption at 20 °C only occurred after the silica had previously been activated by a high temperature degassing under vacuum at temperatures greater than 400 °C and that a new chemisorbed species was formed which was attributed to SiNH_2 with $\nu(\text{NH})$ modes adsorbing at 3520 and 3450 cm^{-1} , and the HNH deformation mode at 1550 cm^{-1} . They suggested that the reaction center involved a strained siloxane bridge site, with the reaction proceeding as follows:



However, the spectroscopic evidence for this mechanism was ambiguous because (1) a surface SiONH_2 or coordinatively bonded NH_3 would also give rise to a similar set of spectral features in the stretching and deformation regions, and (2) there was a large background absorption at 3748 cm^{-1} due to the residual SiOH groups, so that the formation of SiOH above could not be confirmed.

In an earlier communication,⁴ we presented spectroscopic evidence for the formation of reactive siloxane bridge sites which are generated when silica is subject to high temperature degassing under vacuum. That study was concerned with the chemisorption of H_2O and NH_3 on such samples (no chemisorption at 20 °C occurred without the thermal degassing) and we showed that a new type of surface silanol group (SiOH) resulted from the reaction, absorbing near 3741 cm^{-1} .

In a subsequent publication⁵ (part 4 of this series) we showed that ammonia is also capable of chemisorbing on silica if the reaction was carried out at 650 °C, giving rise to an

identical set of infrared bands at 3540, 3452, and 1550 cm^{-1} . In addition, a new absorption was observed at 932 cm^{-1} , associated with the above bands, which, by means of observed isotopic shift data combined with force constant calculations, we were able to unambiguously assign to the SiN stretching mode of SiNH_2 .

In the preceding paper in this issue (part 5) we have shown that this site is also capable of acting as an electron pair acceptor (a Lewis acid site) in that pyridine and trimethylamine could reversibly coordinate with the site without disrupting it; i.e., the site was still active for the chemisorption of NH_3 and H_2O even in the presence of a coordinated species.

In the present paper, further details of the nature of this new reactive site and of the mode of the chemisorption of ammonia, water, and other related molecules are discussed.

Experimental Section

Experimental details are given in the preceding paper in this issue. The volume of the reaction cell used in this work was about 300 ml so that the addition of 1 Torr of a reactant gas at 20 $^\circ\text{C}$ corresponds to about 16 μmol .

Results

Chemisorption of NH_3 and H_2O . In agreement with previous work ammonia did not chemisorb on silica in the absence of a vacuum degassing treatment at high temperatures. However, the infrared spectrum shown in Figure 1A was obtained if 300 Torr of ammonia was allowed to react at 25 $^\circ\text{C}$ with a 200-mg silica sample (40 mg cm^{-2}) which had been degassed at 1100 $^\circ\text{C}$ for 5 h prior to cooling. The reaction time was about 5 min and the excess gas phase was evacuated until the pressure dropped to less than 10^{-4} Torr. Two new bands in the NH stretching region were observed at 3525 and 3447 cm^{-1} , accompanied by an additional band at 1550 cm^{-1} (not shown) and the sharp symmetrical band due to isolated surface SiOH groups at 3748 cm^{-1} had developed a shoulder to the low wave number side. When ammonia reacted with a sample which had only been degassed at 800 $^\circ\text{C}$ prior to reaction, a virtually identical profile was observed between 3600 and 3400 cm^{-1} and at 1500 cm^{-1} but the 3748- cm^{-1} band was so intense that the shoulder was not observed. None of the above spectral features altered following prolonged evacuation at temperatures up to 300 $^\circ\text{C}$.

By using less silica (10 mg cm^{-2}) and by increasing the degassing temperature to just below the softening point of the quartz cell it is possible to remove most of the residual surface silanol groups. The spectra shown in Figure 1B and 1C were obtained after 300 Torr of NH_3 had been allowed to react with a 10 mg cm^{-2} sample which had been degassed at about 1150 and 1200 $^\circ\text{C}$, respectively, and the low wave number shoulder near 3741 cm^{-1} now appears quite distinct. The spectrum shown in Figure 1D was obtained after about 5 μmol of NH_3 had been allowed to react with a fully deuterated 10 mg cm^{-2} silica which had been degassed at 1200 $^\circ\text{C}$. No SiOD/ NH_3 exchange occurred and the previously noted "shoulder" appeared as a symmetrical band at 3741 cm^{-1} , with a half-width of 12 cm^{-1} . The latter spectrum could also be obtained if 300 Torr of NH_3 reacted with a totally dehydroxylated silica.

Following chemisorption of ND_3 on a 1100 $^\circ\text{C}$ degassed deuterated silica ($\nu(\text{SiOD}) = 2763 \text{ cm}^{-1}$) the only bands observed were at 2634 and 2528 cm^{-1} , with relative intensities which were about the same as the 3525/3447 cm^{-1} pair shown in Figure 1, and a shoulder appeared to the low wave number side of the normal SiOD band near 2758 cm^{-1} . When an

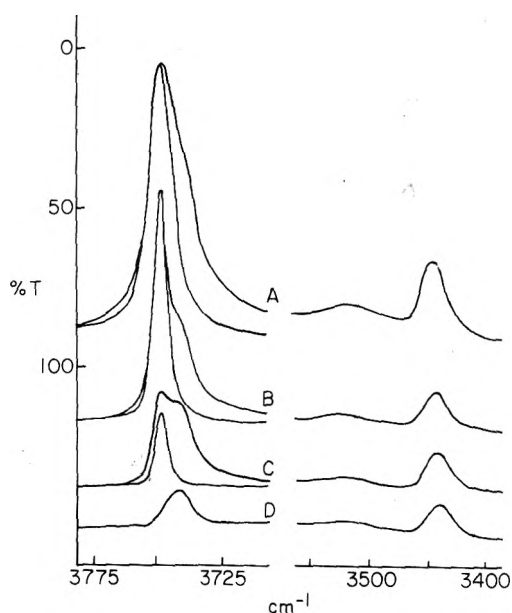


Figure 1. Infrared spectra of partially dehydroxylated silica after reaction with NH_3 at 20 $^\circ\text{C}$. Sample sizes and degassing temperatures were as follows: (A) 40 mg cm^{-2} , 1100 $^\circ\text{C}$; (B) 10 mg cm^{-2} , 1150 $^\circ\text{C}$; (C) 10 mg cm^{-2} , 1200 $^\circ\text{C}$; (D) 10 mg cm^{-2} , 1200 $^\circ\text{C}$, deuterated silica. The insert sharp band at 3748 cm^{-1} in A, B, and C shows the background spectrum due to isolated SiOH groups before reaction. The %T scale refers to A.

equimolar mixture of NH_3/ND_3 was similarly reacted strong sharp bands appeared at 3491, 2575, and 1390 cm^{-1} accompanied by the bands previously noted for NH_3 or ND_3 alone. The deuterium analogue of the 3741- cm^{-1} band appeared at 2758 cm^{-1} .

As noted in the preceding paper, a pair of strong bands at 888 and 908 cm^{-1} appeared in a "window" between 1000 and 850 cm^{-1} when thin silica samples (10 mg cm^{-2}) were heated at high temperatures ($>550 \text{ }^\circ\text{C}$) under vacuum. (There was also a weak shoulder near 940 cm^{-1} which was associated with the 888- cm^{-1} band. In what follows we will not specifically refer to this shoulder since its behavior was identical to that of the 888- cm^{-1} band.) The intensity of these bands increased with degassing temperature, reaching a maximum after degassing at about 1200 $^\circ\text{C}$. The 888/908 cm^{-1} bands disappeared immediately following the admission of 300 Torr of NH_3 to a degassed 10 mg cm^{-2} sample, and the intensities of the bands due to chemisorbed ammonia were approximately proportional to the intensity of the 888/908 cm^{-1} bands before reaction. The 888/908 cm^{-1} bands also disappeared instantaneously when water was used for the reaction in place of ammonia, in which case the only new spectral feature noted was the similar growth of a band near 3741 cm^{-1} . Further, the decrease in intensity of the 908/888 cm^{-1} bands was in proportion to the growth of the 3741- cm^{-1} band as was found by titrating a degassed sample with micromole doses of H_2O vapor. A series of spectra showing this effect is shown in Figure 2.

When 300 Torr of NH_3 was added, the spectrum in 1000–850- cm^{-1} region changed from that shown in Figure 2A (before reaction) to that in Figure 2F after reaction. The latter was similar to that shown in Figure 2E except for an additional broad shoulder near 932 cm^{-1} . This shifted to 882 cm^{-1} with ND_3 and bands appeared near 930 and 882 cm^{-1} with a 1:1 NH_3/ND_3 mixture. However, when a titration with micromole doses of NH_3 was carried out, a slightly different profile of

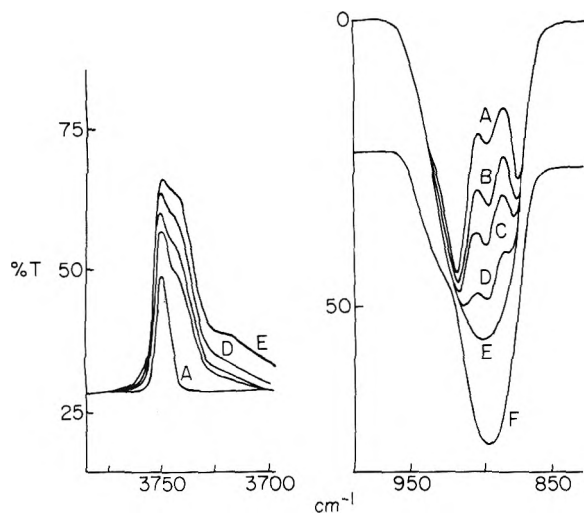


Figure 2. Background spectrum (A) of a 10 mg cm^{-2} silica disk after degassing at 1200°C , (B–D) after successive additions of about $1 \mu\text{mol}$ of H_2O vapor, (E) after addition of 5 Torr of H_2O for 5 min followed by evacuation for 5 min, (F) spectrum from 1000 to 850 cm^{-1} when 300 Torr of NH_3 had been added after A.

change with respect to the $908/888 \text{ cm}^{-1}$ bands was observed than was the case with water, the reaction rate appeared to be slower, but the end effect appeared to be the same as was the case with water. The nature of this effect, and the spectra, will be discussed in a subsequent paper. The important point, however, is that there was a one to one relationship between the disappearance of the $888/908 \text{ cm}^{-1}$ bands and the growth of the 3741-cm^{-1} band in the case of H_2O , and also of the $3741\text{-}, 3525\text{-}, 3447\text{-}, 1550\text{-},$ and 932-cm^{-1} bands in the case of NH_3 .

When a degassed deuterated silica was allowed to react with micromole doses of H_2O vapor, the 3741-cm^{-1} band appeared in isolation (i.e., without being overlapped by the 3748-cm^{-1} band) and had a half-width of 19 cm^{-1} (Figure 3B). However, its shape differed from that which was produced in the case of NH_3 in that it was somewhat flat-topped and there was a weak residual tail to low wave number. The corresponding band at 2758 cm^{-1} which appeared when D_2O was the reactant had a half-width of 16 cm^{-1} . When various mixtures of $\text{H}_2\text{O}/\text{D}_2\text{O}$ were added (varying from 1 to 9 each way), both the 3741- and 2758-cm^{-1} bands appeared with intensities reflecting the initial H/D ratio, and the half-widths and band shapes were identical with that observed using pure H_2O or D_2O .

When a micromole dose of water containing 98.7% oxygen-18 was added to a deuterated degassed silica, a broad band was observed centered at 3735 cm^{-1} with a half-width of about 30 cm^{-1} (Figure 3C). This band had prominent shoulders to high and low wave number of the central peak and could be "reconstructed" by summing two identical bands (such as observed for H_2^{16}O), one centered at 3741 cm^{-1} and the other at 3730 cm^{-1} (Figure 3D). The ^{18}O shift⁶ for the normal SiOH band at 3748 cm^{-1} is 11 cm^{-1} and the new band at 3741 cm^{-1} can be assigned to a new type of surface silanol species.

When methanol was added to a degassed silica, the $888/908 \text{ cm}^{-1}$ bands disappeared, an "ammonia type" SiOH band appeared at 3741 cm^{-1} ($\nu_{1/2} = 12 \text{ cm}^{-1}$) and infrared bands characteristic of SiOCH_3 groups were observed in the CH stretching region.⁷

Temperature Effects. As noted in the preceding paper, the $908/888 \text{ cm}^{-1}$ bands were just detectable as weak superimposed peaks on a steeply sloping background if the initial

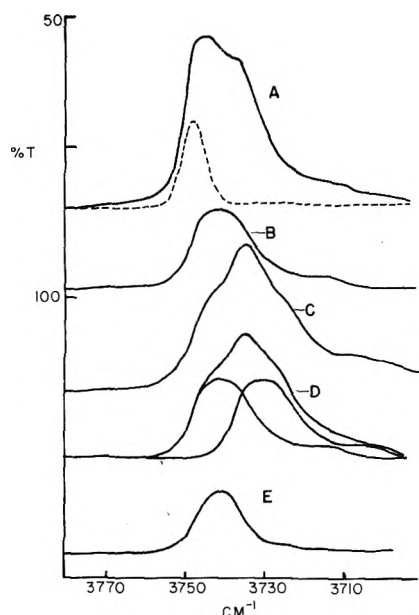


Figure 3. (A) Dashed line represents the residual 3748-cm^{-1} SiOH band on silica which had been degassed under vacuum at about 1100°C . The solid line represents the spectrum after admitting 10 Torr of H_2O at 20°C and evacuating. (B) After adding $5 \mu\text{mol}$ of H_2O to a degassed deuterated silica. (C) After adding H_2^{18}O to a degassed deuterated silica. (D) Taking two spectra as in B, displacing one by 11 cm^{-1} to 3730 cm^{-1} and summing the two. (E) After adding $5 \mu\text{mol}$ of NH_3 to a degassed deuterated silica. The %T scale refers to A.

degassing temperature was about 550°C . However, very weak bands due to chemisorbed NH_3 could be detected if the degassing temperature was 400°C using a 10 mg cm^{-2} sample, or 350°C using a 40 mg cm^{-2} sample. Therefore, we conclude that the number of active sites ($908/888 \text{ cm}^{-1}$ bands) for chemisorption of H_2O , CH_3OH , and NH_3 increases with the initial degassing temperature with a lower limit of about 400°C for the onset of site formation. The maximum number of sites could be generated with a temperature of about 1200°C . Furthermore, the time of heating did not appear to alter the number of sites generated once a given temperature was reached; in most experiments the sample was heated for about 1 h, but essentially the same results were obtained for up to 24-h heating.

When a dehydroxylated sample was allowed to react with sufficient H_2O or NH_3 so as to just cause the disappearance of the $908/888 \text{ cm}^{-1}$ bands, then prolonged evacuation at room temperature or up to 300°C did not alter the intensity of the 3741-cm^{-1} band or of the NH bands when present. However, above 300°C the intensity of the 3741-cm^{-1} band (and the NH bands) started to decrease (with no change in intensity of the normal SiOH band at 3748 cm^{-1} if present) accompanied by a parallel reappearance of the $908/888 \text{ cm}^{-1}$ bands. Again, temperature and not the time of heating was important, and when about 650°C was reached all bands due to chemisorbed H_2O or NH_3 had disappeared and the $908/888 \text{ cm}^{-1}$ bands were fully restored. This temperature of 650°C was independent of the initial activation temperature, as long as it was above 650°C and it applied to all subsequent regenerations. In summary, once a sample had been initially heated under vacuum, a much lower degassing temperature was required in order to reactivate the sample and obtain reproducible results.

When a high pressure (≥ 20 Torr) of NH_3 was used all of the bands due to chemisorbed ammonia appeared instantaneously.

During degassing at temperatures in the range from 300 to 650 °C all bands started to decrease in intensity and the 3525-cm⁻¹ band gradually shifted to 3540 cm⁻¹, the 3447-cm⁻¹ band shifted to 3452 cm⁻¹, while no shift was observed for the two low wave number bands. The 3525-cm⁻¹ band also decreased in intensity to a greater extent than the other bands. At 650 °C, the 908/888 cm⁻¹ bands had regained their original intensity whereas a very weak spectrum of chemisorbed NH₃ remained. The latter could only be removed by degassing up to 1000 °C and no further frequency shifts occurred while heating in the 650–1000 °C range.

Exchange Reactions. The isolated silanol groups of a nonactivated silica can be deuterated instantly with 10 Torr of gaseous D₂O or ND₃. On a partially dehydroxylated silica, exchange did not occur if the quantity of reactant added was less than that required to react with the active sites, i.e., chemisorption was preferred. However, if NH₃ or H₂O were added so as to consume all of the active sites such that both the 3748- and 3741-cm⁻¹ silanol bands were observed (as in Figure 1C), then both hydroxyls exchanged at an equal rate giving their deuterated analogues if successive small doses of D₂O or of ND₃ were added. In the case of chemisorbed NH₃, the NH bands did not exchange after the above.

If 10 Torr of HCl was added to a surface containing chemisorbed NH₃, the 3525-, 3447-, 1550-, and 932-cm⁻¹ bands immediately disappeared whereas the 3741-cm⁻¹ band was unaltered and a spectrum of NH₄Cl was detected.

Other Molecules. In view of the reactivity with the aforementioned molecules, several other molecules were allowed to react with degassed silica in order to see if similar spectral features were to be observed. No reaction took place (at 20 °C) with CH₄, C₂H₄, HCN, CH₃CN, HCl, O₂, H₂ (even at 700 °C for H₂), PH₃, CCl₄, and SiCl(CH₃)₃. However, a reaction did occur with CH₃NH₂ and (CH₃)₂NH and this will be discussed further below.

At no stage in the present study were any infrared bands observed between 2350 and 2000 cm⁻¹, which could be attributed to surface SiH species. Further, no band shifts (<3600 cm⁻¹) were detected when NH₃ was allowed to react with a 70% oxygen-18 exchanged silica.

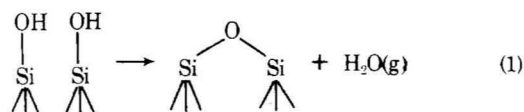
Discussion

The spectrum (Figure 1A) of ammonia chemisorbed at 20 °C on a 40 mg cm⁻² silica disk which had been heated to 1100 °C prior to reaction differs from that reported by Blomfield and Little in two ways: (1) The band positions in the 3500-cm⁻¹ region was slightly different (3525 cm⁻¹ vs. 3520 cm⁻¹, and 3447 cm⁻¹ vs. 3450 cm⁻¹), and (2) we observe a new SiOH band at 3741 cm⁻¹ which they were unable to observe because of overlapping by the strong 3748-cm⁻¹ band when lower degassing temperatures were employed. Upon degassing in the 300–600 °C temperature range Blomfield and Little also noted that the intensity of the 3525-cm⁻¹ band decreased more rapidly than that of the 3450-cm⁻¹ band while its peak maximum shifted to 3540 cm⁻¹ and we have noted that the 3447-cm⁻¹ band also shifted slightly to higher wave number. The origin of this effect is quite complex and will be discussed in a subsequent publication. The present paper is concerned solely with an attempt to characterize the nature of the active site responsible for the chemisorption of H₂O, NH₃, and CH₃OH.

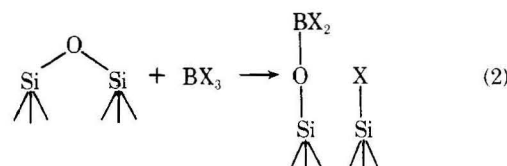
In a previous paper⁵ (part 4) we obtained the spectrum of a chemisorbed species which was formed when NH₃ was allowed to react with silica at 650 °C. Sharp intense bands were observed at 3540, 3452, 1550, and 932 cm⁻¹ which were as-

signed to a surface SiNH₂ species, and the 932-cm⁻¹ band was attributed to the Si–N stretching mode. The band positions and isotopic shifts are virtually the same in the present work so that we infer that surface SiNH₂ groups are present. (Complete spectra of all H/D isotopic species are shown in part 4.) We note that the initial NH stretching frequencies are slightly lower in the present work, but after degassing to 650 °C they have apparently shifted to the same values found in the earlier work. The nature of this shift will be discussed in a subsequent paper but in anticipation of that work, we believe that two types of surface SiNH₂ are formed by different mechanisms, and that only the “low frequency” type (3525/3447 cm⁻¹) involves a direct reaction with the active sites under discussion.

It has been recognized for some time⁸ that new reactive sites are produced when silica is subjected to high temperature vacuum degassing. (This is not to be confused with the so-called “active silica” produced by pyrolyzing methylated silica⁹.) These sites are generally assumed to be strained surface siloxane bridge sites produced during degassing where for example, two adjacent silanol groups might interact as follows to eliminate water:

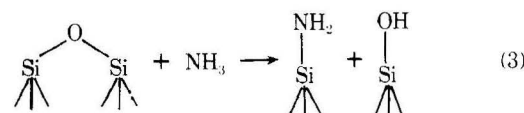


Such a mechanism would account for the observation that the number of SiOH groups decreases as the temperature of degassing increases and the number of reactive sites increases. Morrow and Devi⁶ first pointed out that new spectral changes (growth of bands at 888 and 908 cm⁻¹) occur in proportion to the decrease in the number of isolated surface SiOH groups and suggested that the latter mechanism was operative although they had no clear idea of why two new infrared bands should be produced. However, they showed that even in the absence of silanol groups, BF₃ and BCl₃ probably reacted with such sites as follows:



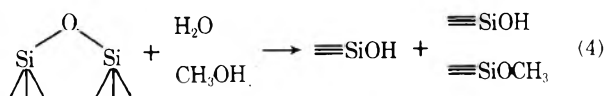
although direct spectroscopic evidence for the formation of SiX was not available, because of the expected low frequency of the $\nu(\text{SiX})$ mode. On the other hand, when diborane was the reactant, the formation of SiH was detected and the above mechanism involving BH₃ was assumed to be operative.

Blomfield and Little¹ have suggested that NH₃ reacts with these sites as follows:



However, they were not able to observe the formation of SiOH during this reaction because they did not dehydroxylate their sample sufficiently prior to reaction and their postulated mechanism was based on the assumption that the 3525/3450 cm⁻¹ bands were due to SiNH₂ and not, for example, due to SiONH₂ or to coordinately bonded NH₃. In the present work (and in part 4) we have conclusively shown that the disappearance of the infrared bands due to a new “active” site (888/908 cm⁻¹) is correlated with the growth of the bands due

to SiNH₂ and due to a new SiOH species (3741 cm⁻¹). Assuming a siloxane site, the reaction with water or methanol would be as follows:

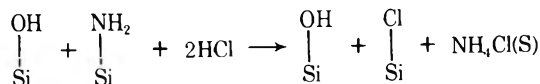


In the case of 99% H₂¹⁸O the expected pair of ν(OH) bands (Si¹⁶OH + Si¹⁸OH) of identical intensity separated by 11 cm⁻¹ was observed.

In other isotopic experiments, if equal doses of either ND₃ or of a 50% mixture of H₂O/D₂O were added to the same dehydroxylated sample (after a reproducible regenerative cycle had been achieved) then the anomalous SiOD band at 2758 cm⁻¹ had the same intensity in both cases. Assuming (3) and (4) then this shows that one SiNH₂ group is formed per new SiOH group. Thus, as was pointed out in the preceding paper, although the real site may be more complex than a simple siloxane bridge, perhaps involving polymers of siloxane bridges, eq 3 and 4 most simply represent the apparent stoichiometry.

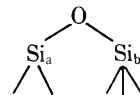
There has been much recent discussion¹⁰⁻¹² concerning the possible existence of geminal hydroxyl groups ≡Si(OH)₂ on silica and we have considered the possibility that the anomalous 3741-cm⁻¹ band might be due to such species. The unusually large breadth and shape of the 3741-cm⁻¹ band when H₂O was allowed to react might be due to weak coupling between the two OH units. However, since the band shape did not alter in mixed H/D isotope experiments, this hypothesis appears to be incorrect. We also do not think that radical sites (SiO· or Si·) are responsible, and no ESR signals have been detected from such degassed samples.

Structure of the Active Site. As noted in the preceding paper, when coordination occurs only the 888-cm⁻¹ band decreased in intensity whereas when chemisorption occurs both bands uniformly decreased in intensity. The active site apparently contains an electron deficient center and a siloxane bridge. Further, the 3741-cm⁻¹ SiOH band which is generated in the case of H₂O being the reactant was broader and somewhat flat-topped (Figure 3B) relative to that which was formed in the case of NH₃ (see Figure 3E) or with CH₃OH (not shown). In the latter cases the band shape more resembled a standard Lorentzian contour. On the other hand, the water type band contour could be more or less reconstructed if we assumed it was composed of two NH₃ type bands separated by 1-2 cm⁻¹. Physically, this could arise if the two SiOH groups generated by eq 4 were in slightly different environments. This difference could be due to structural effects, e.g., different positions of the Si atoms in the lattice, or due to bonding effects, e.g., an unsaturated valence shell or other unusual coordination, or to both of these. The unusual shape is not likely to be due to interactions (e.g., weak hydrogen bonding) between the two silanols because a similar interaction would be expected in the case of a SiOH being adjacent to a SiNH₂ group. Indeed, when the latter was allowed to react with HCl via the presumed reaction



no change in the 3741-cm⁻¹ band was detected. Thus, since the 3741-cm⁻¹ band always had the same Lorentzian type contour when the adjacent functional group was any of SiNH₂, SiCl, or SiOCH₃, we must assume that the two groups generated in eq 3 and 4 are far enough apart so as not to perturb one another.

The simplest possible model for the active site is one in which we assume that there is some structural or electronic difference associated with the two silicon atoms in a strained siloxane bridge. If we label these with subscripts a or b, and assume that Si_a also is the center responsible for the reversible coordination of a strong Lewis base, then the site emerges as



where Si_a is electron deficient. Reaction with NH₃ or CH₃OH is very specific in that the new SiOH is always formed at either Si_a or Si_b, whereas with H₂O we obtain both Si_aOH and Si_bOH which absorb at slightly different frequencies (1-2 cm⁻¹).

In this scheme, we must assume that the 888-cm⁻¹ band is primarily associated with a motion involving the a type silicon atom whereas the 908-cm⁻¹ band is due to the asymmetric ν(SiOSi) mode. Partial support for this comes from our earlier study of oxygen-18 exchanged silicas⁶ where we noted that the 908-cm⁻¹ band decreased in intensity whereas the 888-cm⁻¹ band apparently increased in intensity. This could arise if the 908-cm⁻¹ band shifted to 888 cm⁻¹ for ¹⁸O substitution whereas little or no shift resulted for the 888-cm⁻¹ band.

Further details of the nature of the new 3741-cm⁻¹ SiOH band can only be obtained by studying its reactivity with other probe molecules. However, we have noted that both the 3748- and the 3741-cm⁻¹ bands exchange at equal rates when micromole doses of D₂O are added and we have found that the 3741-cm⁻¹ band preferentially reacts with BCl₃. We do not know whether this can be attributed to steric factors or whether this reflects a difference in chemical reactivity and we anticipate extending our studies in this direction.

Number of Sites. It would be desirable to measure the volume of H₂O or NH₃ which reacted with the new sites as a function of degassing temperature, thereby facilitating a determination of the number of active sites. However, since (a) the quantities adsorbed are in the micromole range, (b) the cell has a large "dead" volume, and (c) we are not able to accurately determine the extent of physical adsorption on the cell walls, such a measurement was not possible. Nonetheless, if we assume that the relative band areas of the normal 3748-cm⁻¹ band and the new 3741-cm⁻¹ band reflect the relative proportions of the two types of SiOH, then when NH₃ is the reactant, the following ratio

$$\frac{\text{intensity 3748-cm}^{-1} \text{ band after degassing at } 800^\circ\text{C}}{\text{intensity 3741-cm}^{-1} \text{ band after degassing at } 1200^\circ\text{C and after reaction with NH}_3}$$

is approximately 10. That is, the number of new SiOH (3741 cm⁻¹) species is approximately 1/10 of the number of normal SiOH (3748 cm⁻¹) species on a fresh sample which had only been degassed at 800 °C, and this also therefore gives the ratio of the number of strained siloxane sites to original SiOH sites under these conditions. Therefore, since the number of normal isolated SiOH groups on a silica which has been degassed at 800 °C is known^{8,13,14} to be about (1.5 ± 0.2)/100 Å², the number of "active" sites after heating at 1200 °C would be about 0.15/100 Å².

Hair and Hertl¹³ have studied the rate of reaction of a number of chlorine containing compounds with the isolated hydroxyl groups on degassed silica (800 °C). In general, the reactions take the form MCl_x + ≡SiOH → SiCMCl_{x-1} + HCl and they found that, in most cases, an initial fast reaction (up to 10% of the total) took place, which did not follow the above

stoichiometry, a reaction which led to higher surface chlorine analyses than would be expected from the above. In the case of $\text{SiCl}(\text{CH}_3)_3$, they suggested that part of the fast reaction might be $\text{SiOH} + \text{SiCl}(\text{CH}_3)_3(\text{g}) \rightarrow \text{SiCl} + \text{Si}(\text{CH}_3)_3\text{OH}(\text{g})$ as evidenced by the rapid initial decrease in intensity of the SiOH band.

From this work, we could also suggest that a small contribution to the high chlorine values might arise from reactions of the type $\text{Si-O-Si} + \text{SiCl}(\text{CH}_3)_3(\text{g}) \rightarrow \text{SiO}(\text{CH}_3)_3 + \text{SiCl}$. Experimentally we found that ClSiMe_3 did not react at 20 °C with 800 °C degassed silica, but the reactive sites (908/888 cm^{-1}) disappeared and a rapid initial decrease in the intensity of the SiOH band was observed when ClSiMe_3 was allowed to react at 350 °C for 1 min. Thus, if there are 0.15 "sites"/100 Å² for degassing at 1200 °C, perhaps half this number for degassing at 800 °C, this would only provide 0.08 Cl atoms/100 Å² by this mechanism, whereas Hair and Hertl report 0.34 Cl/100 Å² for complete reaction of ClSiMe_3 with silica.¹³

Temperature Effects. It is known^{8,15} that the dehydroxylation of the isolated silanol groups depends on the degassing temperature and not on the time of degassing at a particular temperature. Therefore, the observation that the number of sites on a freshly prepared sample increased with degassing temperature was not unexpected. That these sites could be regenerated to the same concentration at a much lower temperature on subsequent degassing (after reaction of H_2O or NH_3) is probably related to the fact that only the desorption of neighboring species occurs in this case as opposed to the removal of isolated silanols during the original treatment. Another possible explanation might involve the migration of bulk hydroxyls to the surface in the case of a fresh sample, and these form new SiOH groups as others are removed. Hockey et al.¹⁴ have postulated such a mechanism for the hydrolysis of adsorbed chloro compounds during prolonged evacuation. If this were the case, then on a second degassing, such migration would be essentially nonexistent and stable sites could be generated at a much lower temperature.

The silica used in this work had been heated at 700 °C prior to pressing into disks in order to oxidize hydrocarbon impurities, and we had considered whether this operation itself might have led to the formation of "active sites" which became rehydrated during cooling in the laboratory atmosphere. However, all of the results discussed could be identically reproduced if the preheating operation was omitted. This was not unexpected since aerosil is produced at considerably higher temperatures during the flame hydrolysis of SiCl_4 . None the less the isolated SiOH band at 3748 cm^{-1} is smoothly asymmetric to the low wave number side¹¹ if the degassing temperature is 800 °C and *part* of this asymmetry may well be due the 3741- cm^{-1} band discussed above. However, this has never been previously detected as a distinct shoulder¹¹ regardless of the initial degassing temperature, and this asymmetry has usually been attributed to other effects. Once the silica is heated to above about 800 °C, the 3748- cm^{-1} band becomes totally symmetrical and indeed, only with such temperatures does its peak intensity also start to decrease appreciably.

Finally, it is important to consider the effect of changes in specific surface area on the number of active siloxane sites. Such measurements were not carried out in the present work, but it appears that the specific surface area does not decrease until the softening point of the quartz cell is reached, and we have noted that once this temperature has been achieved, the surface of the silica disks starts to exhibit a reflective luster characteristic of fused ceramics. Qualitatively, we have noted

that the concentration of siloxane sites (908/888 cm^{-1} bands) does not appreciably increase once the degassing temperature is increased beyond about 1200 °C, in spite of a dramatic decrease in the 3748- cm^{-1} band due to residual silanol groups.

Other Molecules. In order to determine whether a similar reaction would take place with other NH containing molecules and to see whether NH bond rupture would be the favored process, we reacted the methylamines with degassed silica.

In the case of methylamine, a single band at 3465 cm^{-1} was observed or at 2570 cm^{-1} from CD_3ND_2 , in both cases the new silanol band was observed and a complex profile due to $\nu(\text{CH})$ or $\nu(\text{CD})$ modes was observed near 2900 or 2200 cm^{-1} , respectively. The reaction products must therefore be $\text{SiNH}(\text{CH}_3)$ and SiOH . The chemisorption of dimethylamine gave no $\nu(\text{NH})$ bands but did give a 3741- cm^{-1} silanol band and a very complex $\nu(\text{CH})$ profile, indicating that the products were SiOH and $\text{SiN}(\text{CH}_3)_2$. The reaction with trimethylamine is described in the preceding paper.

It is very difficult to explain why the other molecules examined failed to react with the degassed silica. In many cases, reaction could possibly be ruled out using qualitative thermodynamic arguments. Apart from H_2 , we did not examine whether elevated temperatures would facilitate reaction, so that large activation energy barriers might also control the reaction. We do note, for example, that HCN readily reacts with silica at 800 °C, but not to an appreciable extent at lower temperatures; however, this reaction is much more complex in that three distinct surface CN containing species are formed.¹⁶

Concluding Remarks

Although the results presented in this and the preceding paper have shown that a site of unusual chemical activity can be generated when silica is degassed under vacuum at elevated temperatures we have avoided discussing the ramifications of these findings with respect to the mechanism of the rehydration of hydrophobic silica. The latter is still a somewhat controversial topic¹⁷⁻¹⁹ and we have indicated that the fine details of the reaction with NH_3 are quite complex. It is certainly true that both NH_3 and H_2O react via a secondary effect when high pressures or longer adsorption times are involved. For example, with a large dose of H_2O there is an additional band at 3720 cm^{-1} (Figure 2E) which is always accompanied by a broad band at 3520 cm^{-1} , and these features have been observed by others.^{17,18} A paper describing the mechanistic details of the primary and secondary reactions of NH_3 and H_2O is in preparation and will be submitted shortly. Finally, we note that as far back as 1958 McDonald²⁰ reported that a shoulder was formed at 3740 cm^{-1} during the initial stages of the rehydration of partially dehydroxylated silica which he suggested might be due to weakly hydrogen bonded SiOH groups. The present results show that their conclusion is probably incorrect and we have suggested what type of site is responsible for the generation of this spectral feature.

Acknowledgment. We gratefully acknowledge financial support from the National Research Council of Canada and from Imperial Oil Ltd. B.A.M. also acknowledges the help provided by Dr. G. Somorjai and the staff at the University of California, Berkeley, where this manuscript was written while he was on sabbatical.

References and Notes

- (1) G. A. Blomfield and L. H. Little, *Can. J. Chem.*, **51**, 1771 (1973).
- (2) J. B. Peri, *J. Phys. Chem.*, **70**, 2937 (1966).
- (3) L. Abrams and J. W. Sutherland, *J. Phys. Chem.*, **73**, 3160 (1969).

- (4) B. A. Morrow and I. A. Cody, *J. Phys. Chem.*, **79**, 761 (1975).
 (5) B. A. Morrow, I. A. Cody, and L. S. M. Lee, *J. Phys. Chem.*, **79**, 2405 (1975).
 (6) B. A. Morrow and A. Devi, *J. Chem. Soc., Faraday Trans. 1*, **68**, 403 (1972).
 (7) B. A. Morrow, *J. Chem. Soc., Faraday Trans. 1*, **70**, 1527 (1974).
 (8) A. V. Kiselev and V. I. Lygin, "Infrared Spectra of Surface Compounds", Wiley, New York, N.Y., 1975.
 (9) C. Morterra and M. J. D. Low, *Ann. N.Y. Acad. Sci.*, **220**, 135 (1973).
 (10) F. H. Van Cauwelaert, P. A. Jacobs, and J. B. Uytterhoevan, *J. Phys. Chem.*, **76**, 1434 (1972).
 (11) B. A. Morrow and I. A. Cody, *J. Phys. Chem.*, **77**, 1465 (1973).
 (12) M. L. Hair and W. Hertl, *J. Phys. Chem.*, **73**, 2372 (1969).
 (13) M. L. Hair and W. Hertl, *J. Phys. Chem.*, **77**, 2070 (1973); **73**, 2372 (1969).
 (14) C. G. Armistead, A. J. Tyler, F. H. Hambleton, S. A. Mitchell, and J. A. Hockey, *J. Phys. Chem.*, **73**, 3947 (1969).
 (15) J. A. Hockey and B. A. Pettrica, *Trans. Faraday Soc.*, **57**, 2247 (1961).
 (16) B. A. Morrow and I. A. Cody, *J. Chem. Soc., Faraday Trans. 1*, **71**, 1021 (1975).
 (17) A. V. Volkov, A. V. Kiselev, and V. I. Lygin, *Russ. J. Phys. Chem.*, **48**, 703 (1974).
 (18) A. A. Chuiko, V. A. Sobolev, and V. A. Tertykh, *Ukr. Khim. Zh.*, **38**, 774 (1972) (in Russian).
 (19) K. Klier, J. H. Shen, and A. C. Zettlemoyer, *J. Phys. Chem.*, **77**, 1458 (1973).
 (20) R. S. McDonald, *J. Phys. Chem.*, **62**, 1168 (1958).
 (21) G. J. Young, *J. Colloid Sci.*, **13**, 67 (1958).

Integrated Infrared Intensities and Effective Charges in Acetylene^{1a}

G. B. Mast^{1b} and W. T. King*

Metcalf Research Laboratory, Brown University, Providence, Rhode Island 02912 (Received April 5, 1976)

The integrated intensities of the fundamental bands of C₂H₂ and C₂D₂ were measured by the Wilson-Wells-Penner-Weber method. In C₂H₂, these intensities are $\Gamma(\Sigma_u) = 0.210 \text{ m}^2 \text{ mol}^{-1}$ and $\Gamma(\Pi_u) = 3.164 \text{ m}^2 \text{ mol}^{-1}$, and in C₂D₂, $\Gamma(\Sigma_u) = 0.164 \text{ m}^2 \text{ mol}^{-1}$ and $\Gamma(\Pi_u) = 2.030 \text{ m}^2 \text{ mol}^{-1}$. The effective hydrogen charge found by analyzing these data is $\xi_H = 0.404e$, a value that is more than twice as large as that found in other saturated and olefinic hydrocarbons.

Introduction

Recently, considerable interest has been shown in interpreting integrated infrared intensities in terms of atomic polar tensors² and atomic effective charges.³ Most attention has been devoted to accounting for the many systematic variations observed in these quantities,^{2a,3-6} and to the possibility of using these properties to predict infrared absorption intensities. This paper, to the contrary, is devoted to verifying the strikingly anomalous behavior reported for the effective charges in acetylene, in comparison to the equally striking systematic behavior of the effective charges in other hydrocarbons.³ New measurements of the integrated intensities of C₂H₂ and C₂D₂ are reported which, taken with the intensities reported by others,⁷⁻⁹ demonstrate that an anomalous value for the effective charges in acetylene is indeed genuine. In a subsequent paper the difference between the effective charges in acetylene and other hydrocarbons is rationalized by examining the differences in the electronic structure of the hydrocarbons.

The effective charge, ξ_{α} , of atom α in a molecule is defined by the relation³

$$\xi_{\alpha}^2 = (\nabla_{\alpha} \mathbf{P}) : (\nabla_{\alpha} \mathbf{P})' \quad (1)$$

In (1)

$$\nabla_{\alpha} \mathbf{P} = \begin{pmatrix} \partial P_x / \partial x_{\alpha} & \partial P_x / \partial y_{\alpha} & \partial P_x / \partial z_{\alpha} \\ \partial P_y / \partial x_{\alpha} & \partial P_y / \partial y_{\alpha} & \partial P_y / \partial z_{\alpha} \\ \partial P_z / \partial x_{\alpha} & \partial P_z / \partial y_{\alpha} & \partial P_z / \partial z_{\alpha} \end{pmatrix}$$

defines the polar tensor for atom α , and consists of the components of the molecular dipole moment, \mathbf{P} , differentiated with respect to the Cartesian coordinates of atom α , and the prime denotes transposition. The square of the effective

charge then is just the sum of squares of the elements of this tensor.

Experimentally, effective charges are determined from the frequency sum rule first derived by Crawford.¹⁰ Expressed here in a Cartesian coordinate representation, this sum rule takes the form³

$$\sum_{\alpha} \mu_{\alpha} \xi_{\alpha}^2 = (3/\pi N_A) [\sum_j \omega_j \Gamma_j + \Omega] \quad (2)$$

where μ_{α} denotes the reciprocal mass of atom α , Γ_j the integrated intensity of the j th normal mode with frequency ω_j , and Ω the so-called rotation term. The summations are carried over all atoms in the molecule and all normal modes. In (2) the integrated intensity is that defined by Crawford^{11,12}

$$\Gamma_j = (1/nl) \int \ln(I_0/I) d(\ln \omega) \quad (3)$$

in which I_0 and I represent, respectively, the radiation intensity incident upon and transmitted by a sample of molar concentration, n , and thickness l . The integration is carried out over the frequency interval covered by the j th absorption band. The rotation term in (2) is defined as

$$(\pi N_A/3)\Omega \equiv (P_y^2 + P_z^2)/I_{xx} + (P_z^2 + P_x^2)/I_{yy} + (P_x^2 + P_y^2)/I_{zz} \quad (4)$$

in which P_y , for instance, denotes the y component of the permanent molecular dipole moment and I_{xx} denotes a principle moment of inertia. In the hydrocarbons considered here, Ω is either zero or is small enough to neglect in (2).

The effective charges in (2) can be computed by solution of the system of linear equations generated by the intensity sums for a molecule of interest and its isotopic derivatives. The effective charges for the atoms in a molecule are not all independent, however, because the polar tensors, $\nabla_{\alpha} \mathbf{P}$, satisfy the relation^{2a}

$$\sum_{\alpha} \nabla_{\alpha} \mathbf{P} = 0 \quad (5)$$

expressing the translational invariance of the molecular dipole moment, \mathbf{P} .

The relationship between the effective charges defined by (1) such that (5) is also satisfied is a complicated one that depends upon the structure of the particular molecule examined.^{5,6} Person and Newton^{2a} observed, however, that to a rough approximation the effective charge of the carbon atoms in hydrocarbons were about equal to the sum of the effective charges of the hydrogen atoms to which they are bonded; that is

$$n_C \xi_C \approx n_H \xi_H \quad (6)$$

in which n_C and n_H equal the number of carbon and hydrogen atoms in the molecule. In accordance with eq 6, then, the intensity sum (2) for hydrocarbons depends only upon the property, ξ_H^2 , and the number of atoms in the molecule. Specifically, for a deuterated hydrocarbon (2) becomes, using (6)

$$\sum \omega_j \Gamma_j = (\pi N_A / 3) F(n_H, n_D, n_C) \xi_H^2 \quad (7)$$

where

$$F(n_H, n_D, n_C) = \mu_H n_H + \mu_D n_D + \mu_C (n_H + n_D)^2 / n_C$$

The graph of eq 7 for a number of hydrocarbons and their deuterium substituted derivatives is shown in Figure 1. One of the more remarkable features of this graph is that, to a very good approximation, most of the hydrocarbons lie along a common line that passes through the origin. This implies that the correlation between carbon and hydrogen effective charges in (6) is indeed a good one, and, what is more, that the effective charge, ξ_H , has the same value in this diverse set of hydrocarbons. The intensity sums for the methanes clearly do not fall along the regression line common to the other hydrocarbons, but along a line essentially parallel to it. This, in turn, implies that the effective charge, ξ_H , in methane is the same as in the other hydrocarbons, but that its carbon effective charge is not that given by (6).

The intensity sums for the acetylenes are clearly exceptional. Although it is possible that the line connecting the C_2H_2 and C_2D_2 intensities might pass within experimental error of the origin as implied by (7), the effective charge, ξ_H , in acetylene is apparently markedly different from that in the other saturated and unsaturated hydrocarbons considered. Before speculating upon reasons for this exceptional behavior, however, it seems prudent to first determine if it is real, and not due to experimental error.

This is the purpose of this paper. The integrated intensities of the fundamental bands in C_2H_2 and C_2D_2 were determined using the Wilson–Wells–Penner–Weber method.^{13–15} It was found that the sums of intensities were even higher than those previously reported in the literature.^{7–9}

Experimental Section

In the Wilson–Wells–Penner–Weber method, the integrated intensity of an absorption band is found by determining the limiting slope, Γ , of a Beer's law graph of the integrated absorption, Bpl , plotted against the "optical thickness", pressure times path length (or some other convenient concentration–length unit)

$$\int \ln(I_0/I)(1/\omega) d\omega \equiv Bpl = \Gamma \cdot (pl) + \Delta \cdot (pl)^2 + \dots \quad (8)$$

In order to obtain accurate values for the integrated absorp-

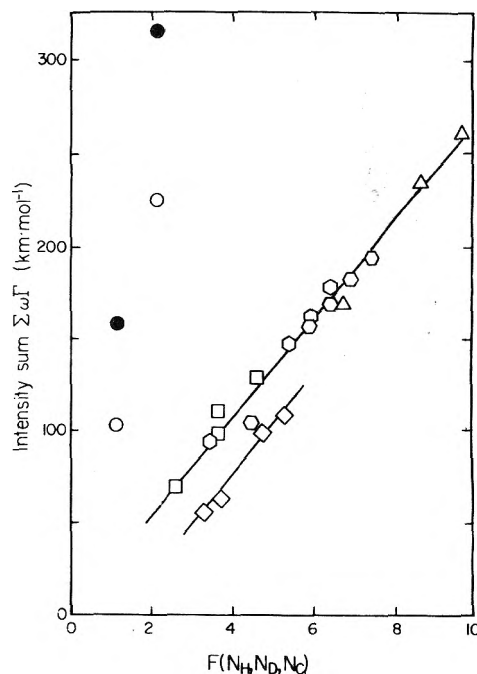


Figure 1. Sum of Integrated intensities for various molecules determined using eq 7: (●) deuterioacetylenes, this work; (○) deuterioacetylenes; (○) deuteriobenzenes; (◇) deuterioethanes; (□) deuterioethylenes; (◇) deuteriomethanes, see ref 3 and references therein; (Δ) deuteriopropanes, ref 22.

tion, it is usually necessary to pressure broaden the lines in the rotation–vibration band system. Because pressure-induced absorption, $\Delta \cdot (pl)^2 + \dots$ in (8), is usually negligible except at exceptionally high pressures, an experimental test that integrated intensities determined by this method are free of instrumental error is that the graph of (8) be linear and pass through the origin.¹⁵ Thus, to obtain good results by this method requires that the composition and pressures of the gases studied are known precisely, that the infrared cell used to contain the gases is leak-free at high pressures over the course of an experiment, and that the spectrometer used for the intensity measurements has good photometric accuracy.

The C_2H_2 gas used in these measurements was Matheson CP grade, and was found to be sufficiently pure by the method described below that further treatment was unnecessary. The C_2D_2 gas, however, was prepared by the reaction of calcium carbide and D_2O . To minimize contamination with hydrogen-containing impurities, the calcium carbide was baked in vacuo for about 8 h at 930 K, before its reaction with D_2O . The deuterioacetylene produced by this reaction was passed through an acetone–dry ice trap to remove any D_2O vapor before storage.

The purity of the gases was determined by mass spectrometry. Using the methods described by Mohler et al.^{16,17} it was found that the deuterioacetylene sample contained 95.1–96.2% C_2D_2 , with C_2HD as the only significant impurity.

The acetylenes absorb infrared radiation strongly, particularly in the Q branches of their bending modes. To obtain reliable values for the integrated intensity of the Q-branches using (8), precisely known acetylene pressures, in the 60–500-Pa¹⁸ range, were required. For this purpose a U-tube manometer similar to the one described by Meyer and Wade¹⁹ was constructed. The difference in mercury levels in the arms of the manometer was measured by a micrometer where

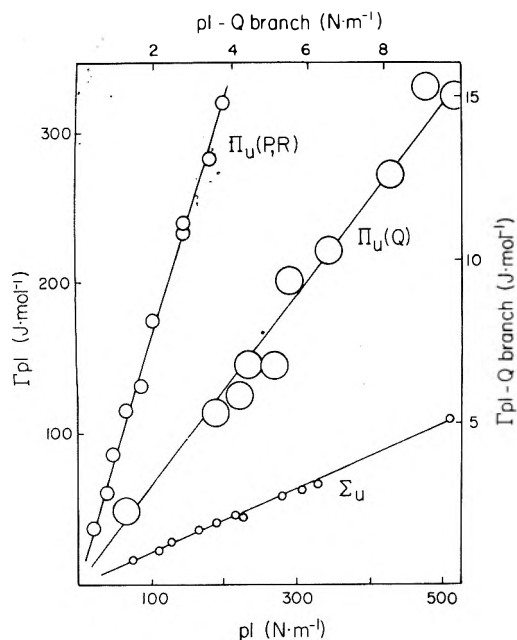


Figure 2. Beers law graph for the integrated intensities of C_2H_2 .

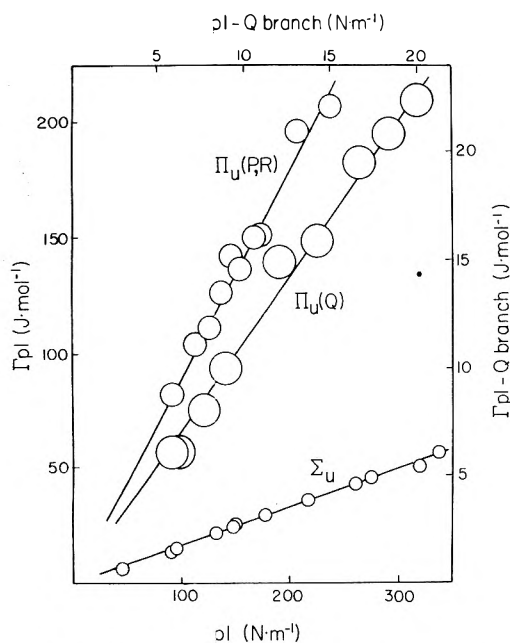


Figure 3. Beers law graphs for the integrated intensities of C_2D_2 .

contact with the mercury surfaces was sensed electrically. Acetylene pressures in the 60–500-Pa range were readily measured with a precision of about 1 Pa, using this device. For pressure measurements in the 500–27 000-Pa range, also covered in this experiment, a cathetometer with a precision of about 15 Pa was used to measure the differences in the mercury levels in an ordinary large-bore U-tube monometer.

Preliminary experiments revealed that the spectral lines in the rotation-vibration bands of acetylene were adequately pressure broadened by helium gas at pressures of 4.8–6.9 MPa. The integrated absorption was independent of helium pressure in this range, for a fixed partial pressure of acetylene, and, for variable acetylene pressures, Beer's law graphs of inte-

grated intensity against acetylene pressure were obtained that were linear and passed through the origin. In all measurements used to determine intensities, a constant He pressure of 6.89 MPa was used. The infrared absorption cell used for these measurements has been described previously.²⁰ It had a length, l in (8), of 20.70 mm and was fitted with KBr windows.

A Perkin-Elmer Model 301 spectrometer operated in the single-beam mode was used to determine the intensities. The spectrometer was equipped with 240, 101, and 40 lines/mm gratings, and was calibrated using the 435.8-nm blue line of mercury. The photometric accuracy was determined by inserting rotating sectors of known transmission into the sample compartment of the spectrometer, and found to be accurate to about $\pm 0.8\%$ in the single beam mode.

The acetylenes, C_2H_2 and C_2D_2 , each exhibit only two fundamental absorption bands, an asymmetrical stretching mode (Σ_u) and a bending mode (Π_u). The Beer's law graphs obtained by plotting the absorption, Bpl , against pl are shown in Figures 2 and 3. Because of its high intensity, the integrated absorption of the Q branch in the Π_u modes was determined separately from that in the P and R branches.

Each point in the Beer's law plot was obtained by integrating the quantity $(1/\omega) \ln(I_0/I)$, averaged over duplicate measurements at the same acetylene pressure. Significant difference between any pair of repeated measurements was attributed to cell leakage during the course of the experiment, or to instrumental error. The few measurements for which such differences were found were rejected. The integrated absorption in (3) was obtained by numerical integration using Simpson's rule. The frequency interval, $\Delta\omega$, was chosen such that the error of numerical integration was less than that due to photometric accuracy.

Results and Discussion

The integrated intensities of the fundamental bands of C_2H_2 and C_2D_2 were obtained by a least-squares analysis of the data displayed in Figures 2 and 3. Two models were assumed. In the first (calcd I) it was assumed that these data satisfy the experimental criterion given in the preceding section; that is

$$Bpl = \Gamma \cdot pl \quad (9)$$

In the second (calcd II), it was assumed that this criterion was not satisfied, and, instead, the data were represented by

$$Bpl = \Gamma \cdot pl + A \quad (10)$$

Here, a significant value for the intercept A is assumed to indicate systematic error in the intensity measurements.

The results of these two analyses are summarized in Table I. Possibly significant values for the intercept A in (10) were found in two cases, for the Σ_u band, and the Q branch of the Π_u band of C_2D_2 . Assuming that repeated experiments would yield a normally distributed set of values for these intercepts, with the estimated population parameters listed in Table I, then based upon Students' t -statistic,²¹ there is only about a 10% chance that the averaged graph of (10) for these two bands would pass through the origin. Comparing the intensities and their estimated standard errors found in both calculations, however, suggests that the risk of drawing an erroneous conclusion from these measurements does not hang upon the assumption that these data satisfy the experimental criterion. Consequently, the intensities found from (9) in calcd I are reported as our experimental results.

There is one other test of the accuracy of the intensities.

TABLE I: Fundamental Band Intensities in C₂H₂ and C₂D₂

	ω , K	Calcd I Γ , m ² mol ⁻¹	Calcd II	
			Γ , m ² mol ⁻¹	A, J mol ⁻¹
ν_5 (P, R)		1.613 (0.020) ^a	1.585 (0.042)	0.290 (0.372)
ν_5 (Q)		1.551 (0.038)	1.619 (0.098)	-0.035 (0.046)
ν_5 (C ₂ H ₂)	766.8	3.164 (0.043) ^b	3.204 (0.011) ^b	
ν_3 (C ₂ H ₂)	3390.9	0.210 (0.002)	0.211 (0.005)	-0.020 (0.088)
ν_5 (P, R)		0.895 (0.014)	0.896 (0.056)	-0.014 (0.067)
ν_5 (Q)		1.135 (0.018)	1.185 (0.045)	-0.054 (0.044)
ν_5 (C ₂ D ₂)	555.4	2.030 (0.023) ^b	2.081 (0.072) ^b	
ν_3 (C ₂ D ₂)	2502.8	0.164 (0.002)	0.169 (0.003)	-0.095 (0.054)

^a Standard error shown in parentheses. ^b Sum of intensities for the P, Q, R branches.

TABLE II: Comparison of the Intensities Reported for the Fundamental Bands of C₂H₂ and C₂D₂ and the Isotope Sum Rule

	$\Gamma(\omega_3)$, m ² mol ⁻¹	$\Gamma(\omega_5)$, m ² mol ⁻¹	Ref
C ₂ H ₂	0.210 (0.002)	3.164 (0.043)	This work
	0.214 (0.004)	2.310 (0.090)	7
	0.215 (0.011)	2.351 (0.047)	8
	0.203 (0.020)	2.339 (0.468)	9
C ₂ D ₂	0.164 (0.002)	2.030 (0.023)	This work
	0.122 (0.020)	1.272 (0.095)	8

F sum rule	C ₂ H ₂ C ₂ D ₂		Error, ^a	Ref
			%	
$\Gamma(\omega_3)/\omega_3$ (m ³ mol ⁻¹) × 10 ⁶	0.619	0.655	5.7	This work
$\Gamma(\omega_5)/\omega_5$ (m ³ mol ⁻¹) × 10 ⁴	0.413	0.365	12.3	
$\Gamma(\omega_3)/\omega_3$ (m ³ mol ⁻¹) × 10 ⁶	0.599	0.487	20.6	8
$\Gamma(\omega_5)/\omega_5$ (m ³ mol ⁻¹) × 10 ⁴	0.305	0.229	28.5	

^a The percent error is defined as 200 [(Γ/ω)_a - (Γ/ω)_b]/[(Γ/ω)_a + (Γ/ω)_b], where a and b refer to the two isotopes.

TABLE III: Effecting Charges for the Hydrogen Atoms and Carbon Atoms in Acetylene and Other Hydrocarbons

	ξ_H^a (obsd)	ξ_C (obsd)	ξ_C (eq 6)	Ref
C ₂ H ₂	0.404 ^b		0.404	This work
C ₂ H ₂	0.321 ^b		0.321	8
C ₂ H ₄	0.178	0.242	0.356	3
C ₆ H ₆	0.167	0.171	0.167	3
C ₂ H ₆	0.176	0.388	0.528	3
C ₃ H ₈	0.181	0.210	0.428	22
CH ₄	0.167 ^b		0.668	3

^a The charges are given in units of the electronic charge. ^b The value found for $\xi_C = 0$, see text.

Applied to the symmetrical acetylenes, Crawford's F-sum rule¹⁰ states that the quantities $\Gamma(\omega_i)/\omega_i$ for C₂H₂ and C₂D₂ are equal. The results of the F-sum rule tests are given in Table II. Although the intensities measured here do not satisfy the conditions of the F-sum rule exactly, they are in better agreement with it than the only other reported intensities, those of Eggers et al.,⁸ included in Table II, for which a similar comparison is possible.

The intensities reported here are compared in Table II with other studies in which the intensities of both infrared active fundamentals were measured. Good agreement is seen for the

intensities of the Σ_u stretching mode determined here and in all of the earlier studies listed. The intensities for the Π_u bending mode found here, however, is in serious disagreement with these earlier studies. Although it is usually difficult to account for the differences between the intensities reported from different laboratories, one comment seems pertinent. Repeating the experimental conditions used by Eggers et al.⁸ and Varanashi and Bangaru⁷ we found that rotation lines were clearly discernible within the pressure-broadened rotation-vibration systems at the total cell pressures they reported, which were lower than those used here. These lines were particularly pronounced in the Π_u band. It is possible, then, that the disagreement noted in Table II might be due to inadequate pressure broadening in these two earlier studies, perhaps compounded with difficulties in determining accurate intensities in the Q branch regions in all studies, including this one.

The effective charges, ξ_H , derived from the intensities reported in Table I are given in Table III and compared with those in the other hydrocarbons considered in Figure 1. These were computed by solution of (2). Where data for more than two isotopes were available, the effective charges were found by least-squares adjustment. Unfortunately, negative values for ξ_C^2 were obtained for acetylene, $-0.009e^2$ using our data, or $-0.3e^2$ using the data in ref 7. Because the hydrogen term in (2) is dominant in determining the intensity sums, only relatively small experimental error is sufficient to yield meaningless values for ξ_C^2 .³ In these cases, it was assumed that $\xi_C^2 = 0$, and it is anticipated that such an assumption does not alter the computed values of ξ_H^2 significantly. Although none of the derived values of ξ_C are at all precise, they are included in Table III, where possible and are compared with the values estimated by eq 6.

Conclusions

The intensity measurements reported here support the observation that the effective charge for hydrogen, ξ_H , in acetylene is indeed anomalous. The hydrogen charges in saturated, aromatic, and olefinic hydrocarbons has been found to be essentially constant, differing from one another by less than 10%. The hydrogen charge in acetylene, on the other hand, is more than twice as large as the averaged value in these other hydrocarbons. In a subsequent paper the dependence of effective charges upon electronic structure is analyzed and it is shown that the relationship of the effective charges in the hydrocarbons can be rationalized.

Acknowledgment. We wish to express our gratitude to Dr. R. Rysnik Gaughan for her work on the initial stages of this research.

References and Notes

- (1) (a) Based on a thesis presented by G. B. Mast in partial fulfillment of the requirements for the degree of Doctor of Philosophy, Brown University, June, 1976. (b) Present address: Department of Chemistry, Oregon State University, Corvallis, Ore.
- (2) (a) W. B. Person and J. H. Newton, *J. Chem. Phys.*, **61**, 1040 (1974); (b) J. F. Biarge, J. Herranz, and J. Morcillo, *An. R. Soc. Espan. Fis. Quim. (Madrid)*, **A57**, 81 (1961).
- (3) W. T. King, G. B. Mast, and P. P. Blanchette, *J. Chem. Phys.*, **56**, 4440 (1972); **58**, 1272 (1973).
- (4) A. B. M. S. Bassi and R. E. Bruns, *J. Chem. Phys.*, **62**, 3235 (1975).
- (5) W. B. Person, S. K. Rudys, and J. H. Newton, *J. Phys. Chem.*, **79**, 2525 (1975).
- (6) J. H. Newton and W. B. Person, *J. Chem. Phys.*, **64**, 3036 (1976).
- (7) P. Varanashi and B. R. P. Bangaru, *J. Quant. Spectrosc. Radiat. Transfer*, **14**, 839 (1974).
- (8) D. F. Eggers, I. C. Hisatsune, and L. Van Alten, *J. Phys. Chem.*, **59**, 1124 (1955).
- (9) R. L. Kelly, R. Rollefson, and B. Schurin, *J. Chem. Phys.*, **19**, 1595 (1951).
- (10) B. L. Crawford, Jr., *J. Chem. Phys.*, **20**, 977 (1952).
- (11) B. L. Crawford, Jr., *J. Chem. Phys.*, **29**, 1042 (1958).
- (12) I. M. Mills and D. H. Whiffen, *J. Chem. Phys.*, **30**, 1619 (1959).
- (13) A. J. Wells and E. B. Wilson, Jr., *J. Chem. Phys.*, **9**, 659 (1941); **14**, 578 (1946).
- (14) S. S. Penner and D. Weber, *J. Chem. Phys.*, **19**, 807, 817 (1951).
- (15) J. Overend, M. J. Youngquist, E. C. Curtis, and B. L. Crawford, Jr., *J. Chem. Phys.*, **30**, 532 (1959).
- (16) F. L. Mohler, V. H. Dibeler, L. Williamson, and H. Dean, *J. Res. Natl. Bur. Stand.*, **48**, 188 (1952).
- (17) P. Kusch, A. Hustrulid, and J. T. Tote, *Phys. Rev.*, **52**, 843 (1937).
- (18) Either the International System of Units (SI) or the Natural (Atomic) system of units are used exclusively in this paper. In SI units, 1 Torr \approx 133 Pascals.
- (19) D. E. Meyer and W. H. Wade, *Rev. Sci. Instrum.*, **33**, 1283 (1962).
- (20) I. W. Levin and W. T. King, *J. Chem. Phys.*, **37**, 1375 (1962); **39**, 241 (1963).
- (21) See, for instance, N. Arley and K. R. Buch, "Probability and Statistics", Wiley, New York, N.Y., 1950.
- (22) S. Kondo and S. Saeki, *Spectrochim. Acta, Part A*, **29**, 735 (1973).

Charge Transfer Band of the Benzyl Radical-Halide Ion Formed by Dissociative Electron Attachment to Benzyl Halides in a Rigid Organic Matrix

Masahiro Irie, Masaaki Shimizu, and Hiroshi Yoshida*

Faculty of Engineering, Hokkaido University, Kita-ku, Sapporo 060, Japan (Received January 15, 1976)

Publication costs assisted by Hokkaido University

In order to elucidate the anomalous features previously reported on electronic spectra of the benzyl radical generated from benzyl chloride, the spectra were studied by the fluorescence spectrophotometric method for benzyl radicals generated from benzyl fluoride, chloride, bromide, and iodide in a 3-methylhexane matrix by either uv or γ irradiation at 77 K. When benzyl radicals were generated by dissociative electron attachment to the benzyl halides in the γ -irradiated matrix, the halide ions close to the benzyl radicals were found to cause a red-shift of the spectra of the radicals, a change in the vibrational structure (especially an increase in the 0-0 band intensity of the fluorescence spectrum), and also the appearance of CT bands due to complexes between the halide ion and the benzyl radical at 265, 362, 413 and 500 nm for F^- , Cl^- , Br^- , and I^- , respectively. The dependence of the CT transition energy upon the halide ions agrees well with that expected from the ionization energy of the donors (the electron affinity of the halogen atoms) and the solvation energy of the halide ions in the matrix. For the benzyl radical from benzyl chloride, the effects of the chloride ion were found to be much less in 2-methyltetrahydrofuran matrix, and could not be observed at all in an ethanol matrix. Halide ions also caused a decrease in the fluorescence lifetime of the benzyl radical.

Introduction

The benzyl radical is one of the conjugated π radicals most extensively studied. It has attracted interest and attention from both experimental¹⁻⁸ and theoretical points of view.⁹⁻¹⁴ Photolysis and radiolysis of benzyl derivatives such as benzyl chloride are efficient ways of generating benzyl radicals either in the gas phase or in condensed media. Electric discharge in the gas phase also yields the benzyl radical. The electronic spectra of the benzyl radicals thus formed have been studied extensively. It is now well established that electronic transitions in the benzyl radical give rise to absorption in visible, near-uv, and far-uv regions (the absorption in the visible region is very weak, so that it is detected only as an excitation spectrum of the benzyl radical fluorescence) as well as fluorescence in the visible region. These absorption bands are, after some conflicting arguments, now assigned to the elec-

tronic transitions, $1^2A_2-1^2B_2$, $2^2A_2-1^2B_2$, and $4^2B_2-1^2B_2$, respectively.^{5,7,8,10-13} The last transition is sometimes assigned to $3^2B_2-1^2B_2$, because excitation to the lower 2^2B_2 excited states has not been evidenced experimentally.

By irradiating the rigid matrix containing benzyl chloride with ionizing radiations, the benzyl radical is generated through dissociative electron attachment to benzyl chloride.¹⁵⁻¹⁷ Thereby a chloride ion is expected to locate close to the benzyl radical and to affect the electronic spectra of the radical. Actually Gallivan and Hamill observed a difference in the wavelength of near-uv absorption maximum between benzyl radicals radiolytically generated from several benzyl derivatives in a rigid hydrocarbon matrix, and suggested the effect of the counterpart ions on the benzyl spectrum.¹⁶ Later Brocklehurst and Savadatti studied this effect by observing the isothermal change of the near-uv absorption spectrum of the benzyl radical radiolytically generated from benzyl chlo-

ride in a hydrocarbon matrix, and they attributed the change to the gradual escape of the chloride ion from the cage.¹⁸ We also studied, by means of the fluorescence spectrophotometric method, anomalous features of the electronic spectra of the benzyl radical generated from benzyl chloride by the dissociative electron attachment. The results, which were briefly communicated,¹⁹ indicated evidently the intermolecular interaction between the benzyl radical and the chloride ion in the matrix. Similar results were obtained also for α -methylbenzyl radical from (chloroethyl)benzenes.²⁰ The interaction between radicals and anion seems to occur generally as a transient state in the dissociative electron attachment reaction in the rigid matrix irradiated by ionizing radiations.

The interaction between hydrocarbon radicals and halide ions seems to be interesting not only from the radiation chemical point of view (to elucidate basically an electron scavenge reaction in matrices) but also from the viewpoint of molecular spectroscopy. The interaction between radiolytically generated methyl radicals and halide ions was evidenced also by means of the electron spin resonance method.^{21,22} Recently the charge transfer absorption bands due to phenyl radical-halide ion complexes were found by irradiating the ethanol matrix containing halobenzenes at 4 K.²³ However, experimental results on the interaction between radicals and ions are still limited. In order to obtain further information on this interaction, we extended here our previous spectroscopic study on the radiolysis of benzyl chloride in rigid matrices to other benzyl halides (fluoride, bromide, and iodide). The benzyl radical gives a prototype for studying the interaction between radicals and ions, because its electronic spectra can be readily observed by the sensitive fluorescence spectrophotometric method even when it is generated at low concentration in rigid matrices irradiated by ionizing radiations.^{19,20}

Experimental Section

Commercial benzyl fluoride (BzF), benzyl chloride (BzCl), and benzyl bromide (BzBr) were used after being purified by distillation. Benzyl iodide (BzI) was synthesized from BzBr and KI. 3-Methylhexane (3MHx) and isopentane were shaken with concentrated sulfuric acid and then with a mixture of concentrated sulfuric acid and nitric acid, washed with distilled water, fractionally distilled twice, dried with calcium hydride, and distilled in vacuo into a sodium-potassium mirrored vessel several times until the mirror was no longer damaged. 2-Methyltetrahydrofuran (MTHF) was fractionally distilled three times from sodium and distilled in vacuo into a sodium-potassium mirrored vessel several times. Ethanol (EtOH) was distilled twice before use.

The solution of benzyl halides (mostly 0.1 mol %) was prepared in vacuo (less than 10^{-5} Torr), sealed in quartz tubes (4 mm i.d.) and frozen in liquid nitrogen into the glassy state. The samples were irradiated with ^{60}Co γ rays to a dose of about 0.3 Mrad at a dose rate of 1.0 Mrad/h or photolyzed with uv light (wavelength longer than 290 nm) from a high-pressure Hg lamp (500 W) through a water filter of 5 cm path length at 77 K and then subjected to measurements. Emission and excitation spectra of the irradiated samples were recorded with a recording fluorescence spectrophotometer (Hitachi, Model MPF-2A) equipped with a Xe lamp as an excitation source with a resolution of 2.0 nm (full-width at half-height) or less. The fluorescence lifetime was measured by exciting with the second harmonics (347 nm) of a Q-switched ruby laser with a pulse duration of 20 ns by means of the experimental facilities previously used for the measurement of transient

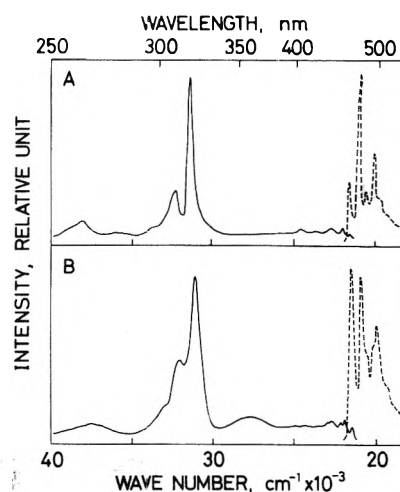


Figure 1. Excitation and emission spectra of benzyl radicals generated in a 3-methylhexane matrix at 77 K by (A) uv or (B) γ irradiation of the matrix containing benzyl chloride. Spectral intensity was not corrected.

absorption and described elsewhere.²⁴ The lifetime was examined at several wavelength between 470 and 500 nm.

Results and Discussion

Effect of Chloride Ion on Benzyl Spectra. Photolysis of BzCl in 3MHx glassy matrix gives emission and excitation spectra as shown in Figure 1A. The emission spectrum was observed in the visible region, whereas the excitation spectrum consists of three bands in the visible (around 460 nm), near-uv (around 320 nm), and far-uv (around 260 nm) regions. These spectra are essentially the same as those of the benzyl radicals reported previously.^{5,25} The spectral shape of the emission and excitation was found to be independent of the excitation wavelength and the monitored wavelength, respectively.

Benzyl radicals generated by γ irradiation in the 3MHx matrix give the spectra shown in Figure 1B. They are very similar to those of the photolytically generated benzyl radical mentioned above and to those of the radiolytically generated benzyl radicals so far reported.¹⁵⁻¹⁷ Examining the spectra carefully, however, one may notice features of the spectra dependent on the method of generating benzyl radicals, as briefly reported in the previous communication.¹⁹ First, all of the spectra (three excitation spectra and the emission one as well) are more or less red-shifted. Secondly, the relative intensity of vibration bands changes as noticed especially in the emission spectrum: the 0-0 band of the emission is weak for the photolytically generated benzyl radical because of the partially forbidden nature of the $1^2A_2 \rightarrow 1^2B_2$ transition,^{9-11,26-28} whereas it is very intense for the radiolytically generated benzyl radical. The intensity ratio of the 0-0 band to the second vibration band gives a measure of the spectral shape and it will be used as a "distortion factor" hereafter. Finally, the radiolytically generated benzyl radical shows a novel excitation spectrum around 360 nm, which is very broad and indicates no structure. This excitation spectrum cannot be due to some radiation-formed products but is influenced by the benzyl radical, because the emission spectrum recorded by exciting at 360 nm is really that of the benzyl radical as shown by the dashed line in Figure 1B. In addition, it was found that the half-width of the 0-0 band in the emission spectra was broader for the radiolytically generated benzyl radical than for the photolytically generated one.

Observed spectral features are summarized in Table I,

TABLE I: Spectra of Benzyl Radicals Generated from Benzyl Chloride in Various Organic Glassy Matrices at 77 K

Matrix	Generation method	Excitation spectra, nm (cm ⁻¹)				Emission spectrum	
		Far-uv ^a	Near-uv ^b	Visible ^b	New band	Wavelength, nm (cm ⁻¹)	Distortion factor ^c
3MHx	Uv	259.3 (38 570)	319.3 (31 320)	462.2 (21 640)		462.5 (21 620)	0.30
	γ	269.6 (37 090)	322.2 (31 040)	464.7 (21 520)	362 (27 600)	465.5 (21 480)	1.13
MTHF	Uv	264.5 (37 810)	320.9 (31 160)	462.2 (21 640)		463.0 (21 600)	0.42
	γ	267.5 (37 380)	322.4 (31 020)	463.2 (21 590)		463.5 (21 570)	0.50
Ethanol	Uv	260.3 (38 420)	319.3 (31 320)	462.2 (21 640)		461.8 (21 650)	0.39
	γ	262.8 (38 050)	319.3 (31 320)	462.2 (21 640)		461.8 (21 650)	0.39

^a Wavelength for the spectral peak. ^b Wavelength for the 0-0 transition. ^c Intensity ratio of the 0-0 transition line to the second vibronic line. The value for uv-generated benzyl radicals is thought to be inherent to "free" benzyl radicals in particular matrices.

which indicates clearly the red shift of the spectra for the radiolytically generated benzyl radical in the 3MHx matrix. Since the far-uv spectra show no resolved structure, the wavelength corresponding to the spectral peak is indicated in Table I. Therefore, the difference in the wavelength of the far-uv spectrum between benzyl radicals generated in different ways includes both the shift of wavelength and the change in spectral shape. Table I also shows features of the spectra of benzyl radicals in MTHF and EtOH matrices. In the former matrix, the red shift and the change in the vibration band structure (indicated by the distortion factor) are observed for the radiolytically generated benzyl radical, though less remarkably than in the 3MHx matrix. However, the novel spectrum around 360 nm is no longer observed in the MTHF matrix. In the EtOH matrix, the spectra of the radiolytically generated benzyl radical are identical with those of the photolytically generated one. No difference was observed at all in the wavelengths, the vibration band structure, and the width of the vibration band. The novel spectrum was not observed at all in the EtOH matrix.

The benzyl radical is formed by the photolysis of BzCl by the homolytic cleavage of the C-Cl bond, so that the benzyl radical has a neutral chlorine atom as a counterpart in its vicinity. On the other hand, the formation of the benzyl radical in the γ -irradiated matrices is brought about by the dissociative electron attachment to BzCl.^{16,17} It is very plausible that a chloride ion formed by the electron attachment reaction, $\text{BzCl} + e^- \rightarrow \text{Bz}\cdot + \text{Cl}^-$, exists close to the benzyl radical in rigid matrices. The observed difference in the spectra of the benzyl radical between photolysis and radiolysis is attributed to the intermolecular interaction between the benzyl radical and the chloride ion in the latter case. The effect of the charged entity, Cl^- , is expected to be less pronounced in the more polar matrix because of solvation of the chloride ion, and this was found to be the case as shown in Table I.

An alternative interpretation for the difference between photolysis and radiolysis might be that the α -chlorobenzyl radical is formed by hydrogen abstraction from BzCl in the γ -irradiated 3MHx matrix along with the benzyl radical. Since the spectra are almost the same for both radicals,¹⁸ the observed spectral shift and distortion would be attributed to overlapping of the spectra of these two radicals. However, this interpretation can give no reason for the presence of the novel spectrum, because the α -chlorobenzyl radical has no absorption around 360 nm. It has been known also that the benzyl

radical is almost exclusively formed from BzCl in γ -irradiated matrices.^{16,18}

The effect of a counterpart anion on the radiolytically generated benzyl radical was previously indicated by observing the dependence of the wavelength of the absorption maximum around 320 nm upon the variety of the anion.¹⁶ The present results reveal that the shift of the spectra accompanies the distortion of the vibration band structure as well as the appearance of the novel spectrum. The spectrum is too weak to be observed by absorption measurements. This may be the reason why it has not been reported yet. The interaction between a methyl radical and a counterpart anion was found by observing the effect of the anion on the electron spin resonance spectrum of the methyl radical generated by dissociative electron attachment in γ -irradiated solid matrices.^{21,22,29} In the present investigation, however, the dependence of the electron spin resonance spectrum of the benzyl radical on the counterpart halide ions could not be evidenced partly because of the poor resolution of the hyperfine lines of the spectrum of the benzyl radical and also because of an intense underlying spectrum of solvent radicals.

The dependence of the effect of the chloride ion on the solvent polarity was examined also by changing the composition of the 3MHx-MTHF mixed matrix, as shown in Figure 2. By increasing the matrix polarity (by increasing the MTHF fraction), the near-uv excitation spectrum of the radiolytically generated benzyl radical shifts to the blue side rapidly at low MTHF fractions and then gradually at high fractions. Concomitantly, the distortion factor also changes from the value observed in pure 3MHx matrix to that in pure MTHF matrix. It changes continuously and no evidence was obtained that the two emission spectra, characteristic to the 3MHx and MTHF matrices, are overlapping in the mixed matrix.

Figure 3 shows the change of the emission spectrum of the benzyl radical generated radiolytically in the 3MHx-isopentane mixed matrix (50:50 in volume) as a function of time after γ irradiation. The intensity of the 0-0 band decreases gradually. This indicates the decrease in the distortion factor and, therefore, the decrease in the interaction between the benzyl radical and the chloride ion. The decreasing interaction may indicate the gradual separation of the ion from the radical due to the softness of the mixed matrix at 77 K. The half-width of the 0-0 band increases once and then decreases toward the final value of 270 cm⁻¹, which is the half-width observed for the "free" benzyl radical generated photolytically in the 3MHx

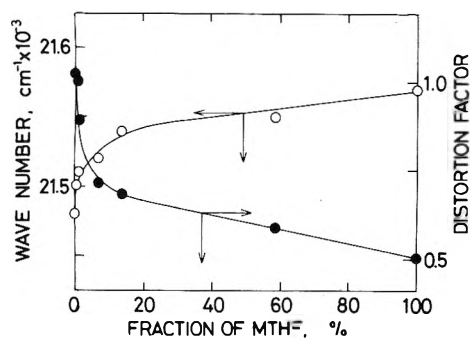


Figure 2. Dependence of (O) the transition energy and (●) the vibrational structure (distortion factor) of the emission spectrum of the benzyl radical upon the polarity (composition) of the mixed matrix of 3-methylhexane and 2-methyltetrahydrofuran at 77 K. The benzyl radical was generated from benzyl chloride by γ irradiation.

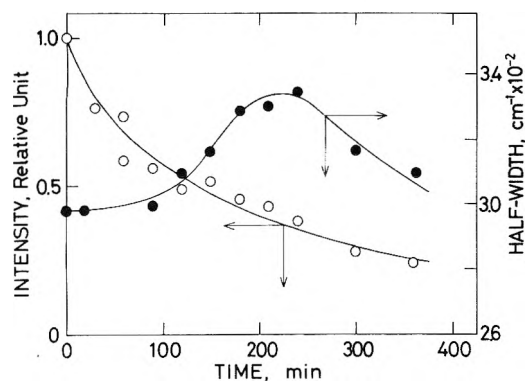


Figure 3. The intensity (O) and the width (●) of the 0-0 band of emission spectrum of the benzyl radical generated from benzyl chloride in the γ -irradiated mixed matrix of 3-methylhexane and isopentane (50:50 by volume) at 77 K as a function of time after γ irradiation. The final value of the half-width was 270 cm^{-1} .

matrix. The observed maximum of the half-width may have been caused by the overlapping of the spectra corresponding to various extent of benzyl radical-chloride ion separation, as reported previously.¹⁸

Charge Transfer Band of Halide Ion-Benzyl Radical Complexes. In order to elucidate the nature of the novel spectrum observed around 360 nm for the benzyl radical generated from BzCl, the emission and excitation spectra were studied also for benzyl radicals generated from other benzyl halides in γ -irradiated 3MHx, where the effect of the counterpart anion was most prominent. Figure 4 shows the visible excitation spectra as well as the emission spectra of benzyl radicals. The benzyl radical from BzBr shows a swelling in the shorter wavelength region (360–430 nm) of the visible excitation spectrum. This is a feature distinctive for the radical generated radiolytically from BzBr, because the swelling is not observed for neither of the benzyl radicals generated radiolytically from other benzyl halides (see Figure 4) nor the benzyl radical generated photolytically from BzBr. It strongly suggested that a broad structureless spectrum underlies the normal visible excitation spectrum of the benzyl radical, as shown by the dotted line in Figure 4.

For the benzyl radical generated from BzI, the novel spectrum is red-shifted much more and lies around 500 nm. It is observed at a transition energy lower than that of the visible excitation spectrum of the benzyl radical, as shown by a dotted line in Figure 4. Accordingly, the lowest excited state of the benzyl radical cannot be the fluorescent state, but the emission is observed as a structureless broad spectrum by exciting ei-

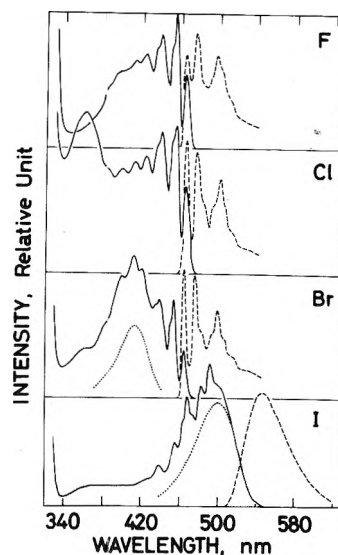


Figure 4. Emission (dashed lines) and excitation (solid lines) spectra in visible and near-uv regions of the benzyl radicals generated from benzyl fluoride, chloride, bromide, and iodide in γ -irradiated 3-methylhexane matrix at 77 K. The dotted lines indicate the assumed curves of the CT band. Spectral intensity was not corrected.

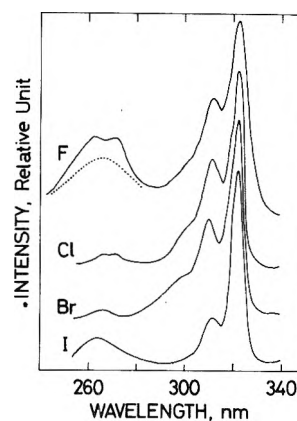


Figure 5. Excitation spectra in far-uv region of the benzyl radicals generated from benzyl fluoride, chloride, bromide, and iodide in γ -irradiated 3-methylhexane matrix at 77 K. The dotted line indicates the assumed curve of the CT band due to the complex between the fluoride ion and the benzyl radical.

ther at the spectra of the benzyl radical or at the novel broad excitation spectrum. The emission spectrum is very probably a mirror image of the novel excitation spectrum for the benzyl radical-iodide ion complex.

At wavelengths longer than 340 nm, no indication of a broad structureless spectrum was obtained for the benzyl radical generated from BzF, as shown in Figure 4. However, the far-uv excitation spectrum of this benzyl radical was found to be exceptionally intense in comparison with that of the benzyl radical from other sources, as shown in Figure 5. This suggests that the novel spectrum is blue-shifted to around 265 nm for the benzyl radical from BzF.

The above results seem to indicate that the appearance of a broad structureless spectrum is a general feature of the benzyl radical generated by dissociative electron attachment to benzyl halides in a nonpolar rigid matrix. We suggested previously two possible interpretations of the broad spectrum around 360 nm observed for the benzyl radical generated radiolytically from BzCl.¹⁹ One is that the spectrum is due to the $2^2B_2 \leftarrow 1^2B_2$ transition which has not yet been observed. The

chloride ion close to the benzyl radical might cause a shift of the spectrum, so that it might become isolated from the intense near-uv excitation spectrum and be observed clearly. An alternative interpretation is that the broad spectrum might be a charge transfer (CT) band of the chloride ion–benzyl radical complex. According to the present results that the wavelength of the broad spectrum is strongly dependent on the halide ions and it shifts from 265 to 500 nm, the former interpretation is excluded, because the $2^2B_2-1^2B_2$ transition is not believed shifted so much as a result of the effect of halide ions.

The novel spectrum shows, irrespective of its transition energy, a broad structureless shape very similar to that of the CT band of a number of electron donor–acceptor complexes. In the present case, the benzyl radical has a large electron affinity of 0.91 eV³⁰ and is thought to act as an electron acceptor. For the presumed electron donor–acceptor complex between the halide ion and the benzyl radical, the energy of its CT transition is approximately given by the relationship

$$h\nu = IP(X^-) - EA(Bz\cdot) + E_s(Bz\cdot - X^-) - E_s(Bz^- - X^-) \quad (1)$$

where IP represents the ionization energy, EA the electron affinity, and E_s the solvation energy in the matrix. The ionization energy of halide ions is given by the electron affinity of corresponding halogen atoms: 3.40, 3.61, 3.36, and 3.06 eV for F, Cl, Br, and I, respectively.³¹ Solvation energy of the ground state complex, $E_s(Bz\cdot - X^-)$, is approximately given by the solvation energy of the halide ion

$$E_s(X^-) = \frac{e^2}{2r} \left(1 - \frac{1}{D}\right) \quad (2)$$

where r refers to the ionic radius (1.16, 1.64, 1.80, and 2.05 Å for F⁻, Cl⁻, Br⁻, and I⁻, respectively³²) and D is the dielectric constant of the 3MHx matrix at 77 K ($D = 2.0$ ³³). Since EA(Bz \cdot) and $E_s(Bz\cdot - X^-)$ are regarded as identical for all halide ions, a linear relationship is expected between the observed transition energy of the CT band and the calculated sum of $IP(X^-) + E_s(X^-)$. It was really observed with a slope of unity as shown in Figure 6, though the datum for BzF was somewhat scattered. This indicates that the novel spectra of the benzyl radicals generated by dissociative electron attachment to benzyl halides are well interpreted on the basis of eq 1 and are attributed to the CT band of complexes between a halide ion and a benzyl radical.

The broad structureless spectrum was also studied for substituted benzyl radicals generated from *p*-methylbenzyl chloride and 3,4-dimethylbenzyl chloride in the γ -irradiated 3MHx matrix. The spectrum was observed to shift as a result of methyl substitution, as shown by arrows in Figure 7. The electron affinity of methyl substituted benzyl radicals has not yet been determined. However, it is believed to depend on methyl substitution, since the electron affinity of nitrobenzene was reported to change if a ring hydrogen was substituted by a methyl group.³⁴ The observed shift of the broad spectrum shown in Figure 7 supports that it is due to the CT transition and its transition energy is dependent on the electron affinity of the acceptors (benzyl radicals) as predicted by eq 1.

Because of a large energy separation of 0.942 eV between the $2^2P_{3/2}$ and $2^2P_{1/2}$ states of atomic iodine due to the spin–orbit interaction, the excited CT state of the iodide ion–benzyl radical complex is expected to comprise two levels, so that the CT band is expected to show two peaks as observed for the ionic intermediate formed from iodobenzene in the EtOH matrix γ irradiated at 4 K.²³ The spin–orbit interaction energy

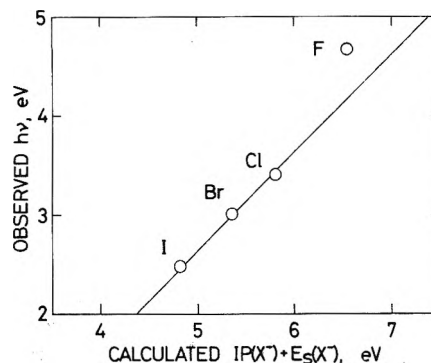


Figure 6. The dependence of the observed transition energy of the CT band upon the calculated sum of the ionization energy of halide ions (the electron affinity of halogen atoms) and their solvation energy in the 3-methylhexane matrix at 77 K. The line indicates the expected slope of unity.

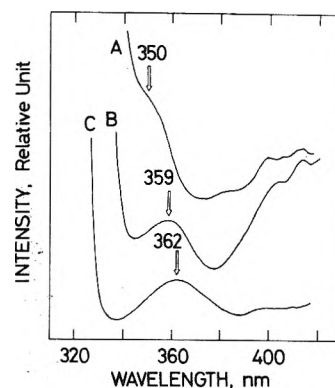


Figure 7. Excitation spectra of (A) the *p*-methylbenzyl radical from methylbenzyl chloride, (B) the 2,4-dimethylbenzyl radical from dimethylbenzyl chloride, and (C) the benzyl radical from benzyl chloride, generated in γ -irradiated 3-methylhexane matrix at 77 K. The arrows indicate the broad structureless spectra due to the CT transition in the complex between the chloride ion and the radicals.

predicts that another peak of the CT band may, if any, be located at 360 nm. As a matter of fact, a shoulder of the spectral curve was observed at this wavelength as shown in Figure 4 (I), but it is too weak to make sure if it is due to the CT transition or not. A weak peak at about 360 nm in Figure 4 (Br) may also be attributable to the smaller spin–orbit interaction, 0.456 eV, in atomic bromine, which is expected to broaden the CT band of the bromide ion–benzyl radical complex.

Red-Shift of Near-Uv and Visible Spectra of the Benzyl Radical. Observed spectral parameters are summarized in Table II for benzyl radicals generated by the dissociative electron attachment to benzyl halides in the 3MHx matrix. In addition to the appearance of the CT band, halide ions associated with benzyl radicals apparently cause the red-shift of the near-uv and visible (both excitation and emission) spectra of benzyl radicals, to which extent depends on the halide ions. The transition energy of the near-uv and visible spectra is found to increase with decreasing ionic radius of the halide ions and to be linearly dependent on the inverse of the ionic radius as shown in Figure 8. The extrapolation of the linear dependence to the infinite radius agrees well with the transition energy in the benzyl radical photolytically generated from BzCl (the benzyl radical free from the effect of the halide ion) for both the spectra. The slope of the linear dependence for the near-uv spectra is about twice as large as that for the visible one. The shift of the far-uv spectrum could not

TABLE II: Spectra of Benzyl Radicals Generated from Different Sources by γ Irradiation in a 3-Methylhexane Glassy Matrix at 77 K

Source	Excitation spectra, nm (cm^{-1})			Emission spectrum	
	Near-uv ^a	Visible ^a	New band	Wavelength, nm (cm^{-1})	Distortion factor ^b
BzF	323.5 (30 910)	466.0 (21 460)	265 (37 700)	466.9 (21 420)	0.81
BzCl	322.2 (31 040)	464.7 (21 520)	362 (27 600)	465.5 (21 480)	1.13
BzBr	321.9 (31 070)	464.3 (21 540)	413 (24 200)	465.2 (21 470)	0.97
BzI	321.6 (31 090)	503 ^c (19 900)	500 (20 000)	548 (18 200)	

^a Wavelength for the 0-0 transition. ^b Intensity ratio of the 0-0 transition line to the second vibronic line. ^c The 0-0 transition line of the emission spectrum is not observed clearly. See text.

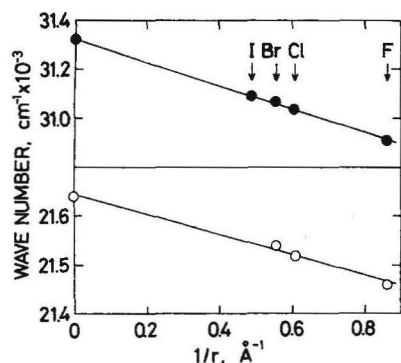


Figure 8. The dependence of the transition energy of (O) the emission spectrum and (●) the near-uv excitation spectrum of the benzyl radicals generated from benzyl halides in γ -irradiated 3-methylhexane matrix at 77 K upon the reciprocal of the ionic radius of the halide ions. The data for $1/r = 0$ indicate the values for the benzyl radical generated by the photolysis of benzyl chloride in the matrix.

be determined because of its unresolved vibration band structure.

The above-mentioned effect of halide ions on the spectra of benzyl radicals seems to be very similar to the effect of counteraction on the absorption spectra of anions such as the fluorenyl carbanion in the tight ion-pair state.³⁵ If one assumes that the halide ion locates close to the atom where the electron density is high in the ground electronic state of benzyl radical, the negative charge of halide ion makes the ground state less stable. A redistribution of electrons occurs on excitation of the benzyl radical, but the halide ion associated with the benzyl radical cannot readjust its position. Consequently, the excited state is more stabilized by the halide ion than the ground state, and the spectra of benzyl radical are red-shifted. As pointed out by Warhurst et al. for the counteraction effect on the absorption spectra of anions,³⁶ the perturbation of the molecular orbital levels of the benzyl radical due to the field of the halide ion depends, as an approximation, on the electrostatic interaction energy and is proportional to the reciprocal of the interdistance between the radical and the ion. If one takes the ionic radius as a measure of the interdistance,³⁵ the magnitude of the red-shift is expected to be proportional to the inverse of the ionic radius. The infinite radius eventually gives the absence of the halide ion in the vicinity of the benzyl radical.

Electron density distribution of π electrons in the benzyl radical in its ground and excited states was calculated by the CI methods in different approximations by Kruglyak and

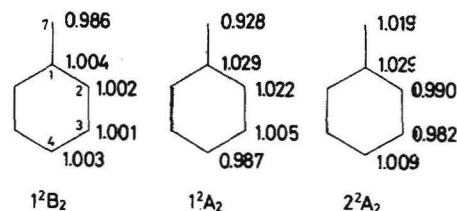


Figure 9. Electron density distributions in the benzyl radical at its 1^2B_2 ground, 1^2A_2 excited, and 2^2A_2 excited states calculated by Kruglyak and Mozdor (ref 12) in the π -electron approximation by the CI method on open shell SCF orbitals.

Mozdor.¹² The calculated results depended on the approximations used, but typical results shown in Figure 9 give a general trend of the calculated electron density distributions. The electron density at the methylene carbon (position 7) decreases considerably upon excitation of the benzyl radical to the 1^2A_2 state. If one assumes that the halide ion does not escape far from its original position when the benzyl halide undergoes dissociative electron attachment, the halide ion locates in the vicinity of the methylene carbon and destabilizes the ground state more than the excited state. Thus the transient pairing of the benzyl radical with the halide ion, frozen in the rigid matrix, interprets qualitatively the red-shift of the visible excitation and emission spectra of the benzyl radical.

However, the electron density at position 7 is higher for the 2^2A_2 state than for the ground 1^2B_2 state. This calculated results predict a considerable blue-shift of the near-uv excitation spectrum caused by the nearby halide ion, and contradict with the observed red-shift. Examining simply the electron densities of the 1^2A_2 and 2^2A_2 states of the benzyl radical (see Figure 9), one can find no location of the halide ion which seems to predict the red-shift of both the visible and near-uv spectra simultaneously. More rigorous treatments of the ion-radical interaction is needed in order to interpret quantitatively the red-shift of both the spectra due to the 1^2A_2 - 1^2B_2 and 2^2A_2 - 1^2B_2 transitions.^{5,7,8,12} It may also be important to know if the maximum position of the near-uv spectrum really corresponds to the 0-0 band of the latter transition as presumed in the study of the effect of methyl substitution on the electronic structure of benzyl-type radicals.³⁷

Fluorescence Lifetime of Benzyl Radicals. The first doublet-doublet electronic transition of the benzy. radical has been theoretically suggested to have a forbidden character, though it is allowed by the symmetry selection rule.⁹⁻¹⁴ Experimentally the forbidden character is indicated by the weak

TABLE III: Fluorescence Lifetime of Benzyl Radicals Generated from Different Sources in Different Ways when Excited by the Light of 347 nm from a Pulsed Ruby Laser at 77 K

Source	Matrix	Generation method	Distortion factor	Fluorescence lifetime, ns
BzCl	3MHx	Uv	0.30	1180
BzCl	3MHx	γ	1.13	770
BzBr	3MHx	γ	0.97	910
BzCl	MTHF	γ	0.50	1160
Toluene	EtOH	Uv		1500 ^a
Toluene	3MP	Uv		1450 ^a

^a Reference 27.

visible excitation spectrum. In accordance with the predicted forbidden nature, the fluorescence lifetime of the benzyl radical and its derivatives generated photolytically in rigid matrices were found to be long.²⁶⁻²⁸ The interaction between the halide ion and the benzyl radical, when generated radiolytically, was expected to be indicated not only by the shape of the electronic spectra but also by the effect of the former on the fluorescence lifetime of the latter.

The observed lifetime are shown in Table III. The benzyl radicals generated from BzCl either photolytically in the nonpolar matrix or radiolytically in the MTHF matrix show lifetimes as long as 1.2 μ s, which is somewhat shorter than that reported previously for benzyl radicals in the absence of halide ions.^{27,28} The long lifetimes are consistent with the fact that those benzyl radicals show neither the CT band nor the red-shift of their excitation spectra (for the benzyl radical generated by γ rays in the MTHF matrix, the red-shift was observed but very slightly). On the other hand, the lifetime was found to be much shorter for the benzyl radical generated radiolytically from BzCl in the nonpolar matrix, for which the effect of the chloride ion was indicated by the electronic spectra of the benzyl radical itself and the CT band as well. The effect of bromide ion on the lifetime was smaller than that of the chloride ion. This is also consistent with the magnitude of the ion-radical interaction as shown in Figures 6 and 8.

It was suggested that the fluorescence lifetime of the benzyl radical contained both radiative and radiationless contributions.²⁷ No definite mechanism can be given at the moment for the decrease in the fluorescence lifetime under the effect of the halide ions. However, the increase in the intensity of the 0-0 emission band in the presence of halide ion (see Figure 1) seems to indicate that the halide ion associated with the benzyl radical enhances not only the radiationless pathway but also the radiative one.

Conclusions

When benzyl radicals are generated by dissociative electron attachment to benzyl halides in a γ -irradiated nonpolar matrix, the benzyl radicals are exerted under the effect of a halide ion which is formed as a counterpart of reaction products and cannot escape from the benzyl radical because of the rigidity of the matrix. The interaction between the benzyl radical and the halide ion is indicated by the red-shift of the electronic spectra of the benzyl radical, the change in their vibration band structure, the decrease in the fluorescence lifetime of the benzyl radical, and the appearance of a CT band due to the halide ion-benzyl radical complex. As far as the present au-

thors know, no CT band has not yet been reported for a complex between the neutral free radical and ion except the band observed by Namiki, who could not, however, identify the structure of the free radical.²³

The observed transition energy of the CT band agrees well with that predicted by the ionization energy and the solvation energy of fluoride, chloride, bromide, and iodide as electron donors. However, the red-shift of the spectra is only partly but not totally rationalized by the simple Coulombic field effect of the halide ion on the molecular orbital levels of the benzyl radical. Informations about the location of the halide ion seems to be crucial for the further elucidation of the interaction between the halide ion and the benzyl radical, for example, by the symmetry considerations from the detailed analysis of the vibration band structure and from the polarization measurements, which could not be made successfully in the present investigation.

Acknowledgment. The authors are indebted to Professor Hiroshi Kato of Nagoya University for his valuable suggestions on the theoretical aspects of molecular orbital treatments, and to Professor Noboru Mataga and his group for giving us an opportunity to use the experimental laser flash photolysis facilities.

References and Notes

- (1) H. Schüler, L. Reinbeck, and R. Koberle, *Z. Naturforsch. A*, **7**, 421 (1952).
- (2) H. Schüler and J. Kusjakow, *Spectrochim. Acta*, **17**, 356 (1961).
- (3) G. Porter and E. Strachan, *Spectrochim. Acta*, **12**, 299 (1958).
- (4) G. Porter and B. Ward, *J. Chim. Phys.*, **61**, 1517 (1964).
- (5) L. Grajcar and S. Leach, *J. Chim. Phys.*, **61**, 1523 (1964).
- (6) L. Watmann-Grajcar, *J. Chim. Phys.*, **66**, 1023 (1972).
- (7) C. Cossart-Magos and S. Leach, *J. Chem. Phys.*, **56**, 1534 (1972).
- (8) (a) D. M. Friedlich and A. C. Albrecht, *J. Chem. Phys.*, **58**, 4766 (1973); (b) D. M. Friedlich and A. C. Albrecht, *Chem. Phys.*, **6**, 366 (1974).
- (9) H. C. Longuet-Higgins and J. A. Pople, *Proc. Phys. Soc. London, Ser. A*, **68**, 591 (1955).
- (10) W. A. Bingel, *Z. Naturforsch. A*, **10**, 462 (1955).
- (11) Y. Mori, *Bull. Chem. Soc. Jpn.*, **34**, 1031, 1035 (1961).
- (12) Y. A. Kruglyak and E. V. Mozdor, *Theor. Chim. Acta*, **15**, 365, 374 (1969).
- (13) J. Baudet and M. Suard, *J. Chim. Phys.*, **67**, 1088 (1972).
- (14) P. Jorgensen and J. Bellum, *Mol. Phys.*, **26**, 725 (1973).
- (15) B. Brocklehurst, G. Porter, and M. I. Savadatti, *Trans. Faraday Soc.*, **60**, 2017 (1964).
- (16) J. B. Gallivan and W. H. Hamill, *Trans. Faraday Soc.*, **61**, 1960 (1965).
- (17) T. Higashimura, A. Namiki, M. Noda, and H. Hase, *J. Phys. Chem.*, **76**, 3744 (1972).
- (18) B. Brocklehurst and M. I. Savadatti, *Nature (London)*, **212**, 1231 (1966).
- (19) M. Irie, M. Shimizu, and H. Yoshida, *Chem. Phys. Lett.*, **25**, 102 (1974).
- (20) T. Saito and H. Yoshida, *Bull. Chem. Soc. Jpn.*, **47**, 3167 (1974).
- (21) E. D. Sprague and F. Williams, *J. Chem. Phys.*, **54**, 5425 (1971).
- (22) S. P. Mishra and M. C. R. Symons, *J. Chem. Soc. Perkin Trans. 2*, 391 (1973).
- (23) A. Namiki, *J. Chem. Phys.*, **62**, 990 (1975).
- (24) H. Masuhara, M. Shimada, N. Tsujino, and N. Mataga, *Bull. Chem. Soc. Jpn.*, **44**, 3310 (1971).
- (25) P. M. Johnson and A. C. Albrecht, *J. Chem. Phys.*, **48**, 851 (1968).
- (26) T. Okamura, K. Obi, and I. Tanaka, *Chem. Phys. Lett.*, **20**, 90 (1973).
- (27) J. D. Lapos and V. Morrison, *Chem. Phys. Lett.*, **28**, 270 (1974).
- (28) A. Bromberg, D. M. Fridlich, and A. C. Albrecht, *Chem. Phys.*, **6**, 353 (1974).
- (29) Y. J. Chang, K. Nishikida, and F. Williams, *J. Phys. Chem.*, **78**, 1882 (1974).
- (30) "Handbook of Chemistry and Physics", 48th ed, Chemical Rubber Co., Cleveland, Ohio, 1968, p E68.
- (31) R. S. Berry and C. W. Reimann, *J. Chem. Phys.*, **38**, 1540 (1963).
- (32) B. S. Gourary and F. J. Adrian, *Solid State Phys.*, **1K**, 127 (1960).
- (33) L. Kevan, *Adv. Radiat. Chem.*, **4**, 188 (1974).
- (34) B. Dale, R. Foster, and D. L. Hammick, *J. Chem. Soc.*, 3986 (1954).
- (35) J. Smid, "Ions and Ion Pairs in Organic Reactions", Vol. 1, M. Szwarc, Ed., Wiley-Interscience, New York, N.Y., 1972, p 85.
- (36) H. V. Cater, B. J. McClelland, and E. Warhurst, *Trans. Faraday Soc.*, **56**, 455 (1960).
- (37) C. Branciard-Larcher, E. Migirdicyan, and J. Baudet, *Chem. Phys.*, **2**, 95 (1973).

An Electron Paramagnetic Resonance Study of the H_2S_2^- Radical on Magnesium Oxide

M. J. Lin and J. H. Lunsford*

Department of Chemistry, Texas A&M University, College Station, Texas 77843 (Received January 30, 1976)

Publication costs assisted by the Environmental Protection Agency

The paramagnetic ion H_2S_2^- was formed by allowing H_2S molecules at -78°C to react with trapped electrons on MgO. Two forms of H_2S_2^- ($\text{HSS}'\text{H}'^-$) were identified by their EPR spectra. Species A is characterized by $g_\perp = 2.015$ and $g_\parallel = 2.003$ with $a^{\text{H}}(\text{A}) = 9.4$ G, $a^{\text{H}}(\text{A}) = 6.6$ G and $a_\perp^{\text{S}}(\text{A}) \approx a_\parallel^{\text{S}}(\text{A}) \approx -2$ G, $a_\parallel^{\text{S}}(\text{A}) = 61$ G, $a_\parallel^{\text{S}}(\text{A}) = 41$ G; whereas, species B is characterized by $g_{\text{iso}}(\text{B}) = 2.009$ with $a_{\text{iso}}^{\text{H}}(\text{B}) = 9.4$ G, $a_{\text{iso}}^{\text{H}}(\text{B}) = 6.6$ G and $a_{\text{iso}}^{\text{S}}(\text{B}) = 13$ G, $a_{\text{iso}}^{\text{S}}(\text{B}) = 9$ G. Species A was more stable and dominated the spectrum upon irradiation at -196°C following the reaction of H_2S with trapped electrons at the surface. Species B was highly mobile. The spin density of the unpaired electron was predominantly localized in the $3p$ orbitals of the two nonequivalent sulfur atoms of the H_2S_2^- radical.

Introduction

A radical attributed to H_2S^- was first studied by Bennett, Mile, and Thomas,¹ who observed an EPR spectrum after impinging gaseous sodium or potassium and hydrogen sulfide on a rotating cryostat at -196°C . The assignment of the radical having $g_\parallel = 2.0023$ and $g_\perp = 2.0164$ was based on the hyperfine interaction with two equivalent protons ($a_\parallel = a_\perp = 7.7$ G). Weak satellite lines attributed to the hyperfine splitting of the ^{33}S in natural abundance were observed when D_2S was used to form the radical. Bennett et al. pointed out that the principal values of the g tensors for their radical were similar to those observed for negative ions containing two sulfur atoms;^{2,3} however, no mention was made of the possibility that the radical may be H_2S_2^- .

In reviewing the assignment of Bennett et al., Symons⁴ noted that considerable s character would be expected for H_2S^- ions and that a very large isotropic proton hyperfine coupling constant should be apparent in the spectrum. Possible alternatives included H_2S^+ , H_2S_2^- , H_2S_2^+ , or more complex polysulfide radicals.

In this work we have presented evidence for the formation of the H_2S_2^- radical by allowing H_2S neutral molecules at -78°C to react with MgO which contained trapped electrons. Sulfur-33 hyperfine lines together with hydrogen and deuterium hyperfine lines have been used to identify the molecule and to establish its electronic structure. Interpretation of the EPR spectra also provides evidence that H_2S_2^- is a better description of the radical earlier assigned as H_2S^- .

Experimental Section

The method for the preparation of the magnesium oxide samples used in these experiments has been described elsewhere.⁵ Approximately 50 mg of magnesium oxide pellets were degassed at 300°C for 2 h and at 500°C for 1 h under vacuum. The final pressure in the vacuum system was less than 5×10^{-5} Torr. Trapped electrons (S centers) on the surface of MgO were produced by irradiating the MgO in the presence of hydrogen for 10 h at 25°C with a 254-nm uv lamp. The color of the sample changed from white to blue upon irradiation. Subsequent to irradiation the H_2 was pumped off, and in a typical experiment a small amount (~ 18 mg/g of MgO) of H_2S was frozen at the top of the sample which was maintained at -196°C in a 4-mm fused-quartz tube. The sample was briefly warmed to -78°C by placing the tube in a dry ice-acetone

mixture and then rapidly cooled to -196°C , at which temperature the EPR spectra were recorded. In an alternate procedure the H_2S was first adsorbed and the sample was irradiated at -196°C .

The EPR spectra of the resulting paramagnetic species were recorded using a Varian E-6S X-band spectrometer. The g values in the spectra were determined relative to the DPPH (2,2-diphenyl-1-picrylhydrazyl) line which has $g = 2.0036$. The estimated error in the g values is ± 0.001 ; the estimated error in the a values is ± 0.5 G for the isotropic lines and ± 1 G for the anisotropic spectra.

The H_2S and D_2S gases were obtained from commercial sources. Isotopically enriched sulfur was purchased from Oak Ridge National Laboratory. Sulfur-33 enriched H_2S was prepared by allowing 5 mg of sulfur containing either 25.5% or 59.2% ^{33}S to react with an excess of pure hydrogen in a sealed reactor at 300°C for 10 h. The unreacted hydrogen was removed by the freeze-pump technique prior to adsorption.

Results

Upon warming the sample tube containing frozen H_2S and MgO with S centers to -78°C the color of the sample changed from blue to white, indicating that a surface reaction had occurred. The EPR spectrum, shown in Figure 1a, can best be understood in terms of two species, A and B. Species A is characterized by $g_\perp(\text{A}) = 2.015$ and $g_\parallel(\text{A}) = 2.003$ with two nonequivalent protons having $a_\perp^{\text{H}}(\text{A}) = a_\parallel^{\text{H}}(\text{A}) = 9.4$ G and $a_\perp^{\text{H}}(\text{A}) = a_\parallel^{\text{H}}(\text{A}) = 6.6$ G. The spectrum of species B is isotropic, and is characterized by $g_{\text{iso}}(\text{B}) = 2.009$ with $a_{\text{iso}}^{\text{H}}(\text{B}) = 9.4$ G and $a_{\text{iso}}^{\text{H}}(\text{B}) = 6.6$ G. The simulated spectrum, using these parameters and a concentration ratio of $A/B = 5.7$, is given in Figure 1b. The agreement between the simulated and experimental spectrum is reasonably good; however, a similar simulated spectrum could also be obtained by assuming two equivalent protons with $a^{\text{H}} = 8.0$ G. The reasons for choosing the two nonequivalent proton splitting will become evident when the ^{33}S hyperfine splitting is discussed.

The relative intensities of A and B may be altered by changing the mode of formation. When the sample was irradiated at -196°C following the adsorption of H_2S on S centers, the color became yellow and species A dominated the spectrum, as depicted in Figure 2a. Here the hydrogen hyperfine lines in the parallel direction become more evident,

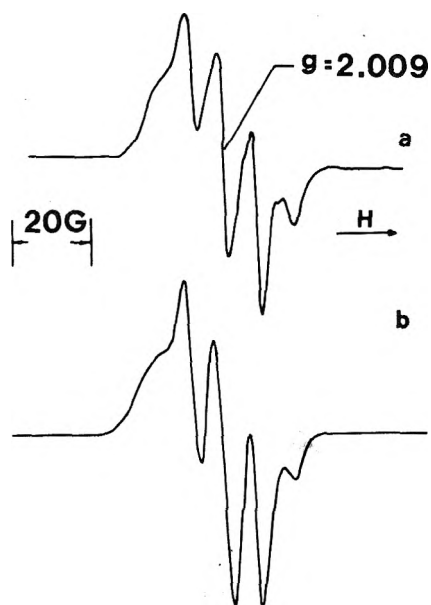


Figure 1. EPR spectra of H_2S_2^- obtained by allowing H_2S to react with trapped electrons on MgO at -78°C : (a) experimental spectrum; (b) simulated spectrum using a mixing ratio $A/B = 5.7$.

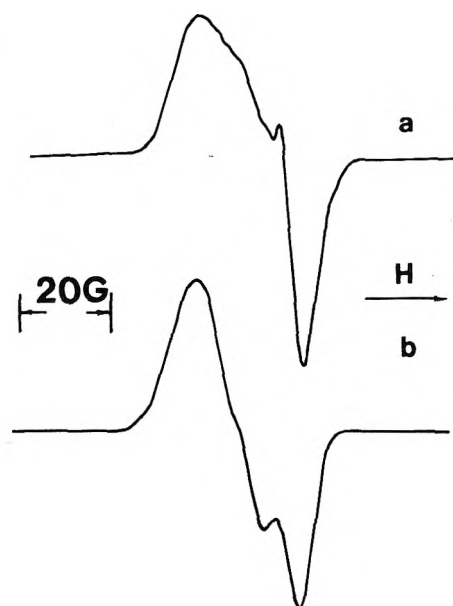


Figure 3. EPR spectra of D_2S_2^- obtained by allowing D_2S to react with trapped electrons on MgO at -78°C : (a) experimental spectrum; (b) simulated spectrum using a mixing ratio $A/B = 19$.

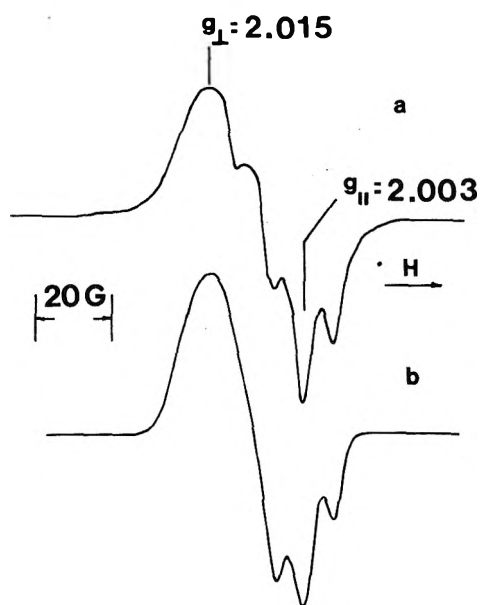


Figure 2. EPR spectra of $\text{H}_2\text{S}_2^-(A)$ obtained by irradiating the H_2S adsorbed on MgO at -196°C for 10 min: (a) experimental spectrum; (b) simulated spectrum.

although some of the isotropic spectrum is still observed. The simulated spectrum of only species A is shown in Figure 2b. Upon warming the sample to 25°C the color changed to white and no paramagnetic species was observed.

In a similar experiment D_2S was used, and the resulting EPR spectrum shown in Figure 3a is satisfactorily simulated in Figure 3b, using the same g values as described earlier and a concentration ratio $A/B = 19$. The two nonequivalent deuterium hyperfine splittings used in the simulation were 1.4 and 1.0 G, which are the expected values based on the magnetic moments of hydrogen and deuterium. The deuterium hyperfine splitting is not resolved in the spectrum.

When H_2S enriched to 25.5% in sulfur-33 was adsorbed on MgO containing S centers, the EPR spectrum revealed ad-

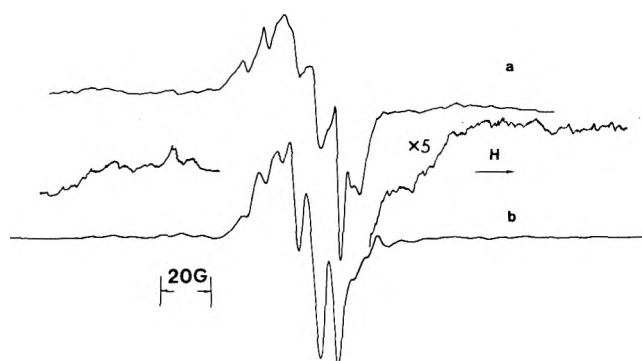


Figure 4. EPR spectra of $\text{H}_2^{33}\text{S}_2^-(B)$ obtained by allowing 25.5% ^{33}S -enriched H_2S to react with trapped electrons on MgO at -78°C : (a) experimental spectrum; (b) simulated spectrum.

ditional hyperfine lines as depicted in Figure 4a. Upon irradiation at 254 nm for 10 min the relative intensity of species B was greatly reduced; whereas, two sets of quartet lines having splitting constants 61 and 41 G, centered on g_{II} of species A, became apparent. These additional hyperfine lines became much more obvious when H_2S enriched to 59.2% in sulfur-33 was used (Figure 5a). In an attempt to analyze the experimental spectra by simulation, statistical percentages for sulfur-33 isotope combinations in the ion having two nonequivalent sulfur atoms were calculated, as listed in Table I. From the isotope combinations for 25.5% ^{33}S the spectrum of Figure 4b was simulated using the previous g values and hydrogen splitting constants with $|a_{\perp}^S(A)| = |a_{\perp}^{S'}(A)| = 2$ G, $|a_{\parallel}^S(A)| = 61$ G, $|a_{\parallel}^{S'}(A)| = 41$ G, $|a_{\text{iso}}^S(B)| = 13$ G, $|a_{\text{iso}}^{S'}(B)| = 9$ G, and a concentration ratio of $A/B = 5.7$. In Figure 5b the simulated spectrum of species A is depicted for the $\text{HSS}'\text{H}'^-$ ion enriched to 59.2% ^{33}S .

Discussion

The g values obtained for species A are in reasonably good agreement with those reported by Bennett et al.¹ for the spectrum assigned to the H_2S^- radical. Contrary to their as-

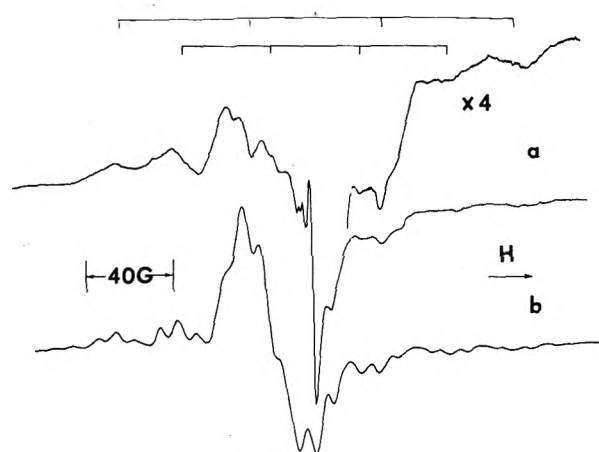


Figure 5. EPR spectra of $\text{H}_2^{33}\text{S}_2^-$ (A) obtained by irradiating 59.2% ^{33}S -enriched H_2S adsorbed on MgO at -196°C for 10 min: (a) experimental spectrum; (b) simulated spectrum.

TABLE I: Statistical Percentages for Sulfur-33 Isotope Combinations in H_2S_2^-

	59.2% ^{33}S	25.5% ^{33}S
HSS'H $^-$	16.6	55.5
H ^{33}S S'H $^-$	24.2	19.0
HS ^{33}S 'H $^-$	24.2	19.0
H ^{33}S ^{33}S 'H $^-$	35.0	6.5

signment it is believed that the hyperfine structure of hydrogen is derived from two nonequivalent hydrogen atoms for both species A and B. This assignment is based more on the observation of nonequivalent sulfur hyperfine splitting than on our actual ability to distinguish between equivalent and nonequivalent hydrogen atoms. The small, isotropic values of the hydrogen hyperfine constants suggest that the primary interaction is due to spin polarization by an unpaired electron which is almost totally on other atoms. As pointed out by Symons, the H_2S^- radical is expected to have large isotropic proton coupling constants, thus it is probable that none of the spectra are due to H_2S^- . The weak ^{33}S hyperfine lines which Bennett et al.¹ observed as having $a^{\text{S}} = 60 \pm 2$ G are probably the same as those observed in this study with $a_{\parallel}^{\text{S}}(\text{A}) = 61$ G.

The ^{33}S hyperfine structure, on the other hand, indicates that species A, and perhaps species B, contain two nonequivalent sulfur atoms. The two nonequivalent sulfur atoms ($I = 3/2$) give rise to two sets of four hyperfine lines each, as indicated in Figure 5. Each of these hyperfine lines is further split by the two nonequivalent hydrogen atoms. The experimental spectrum agrees well with the simulated spectrum of the proposed HSS'H $^-$ molecule. This agreement is considerably better than that obtained by assuming equivalent sulfur atoms.

The situation is not so clear with respect to species B since there is a large overlapping of hyperfine lines in the EPR spectrum. Better agreement between the experimental and simulated spectra is obtained using the model H_2S_2^- , rather than H_2S^- . It is proposed that the isotropic spectrum is the result of ion motion on the surface in three dimensions. Two dimensional motion has been previously noted for SO_3^- and S_3^- on magnesium oxide.^{6,7} The values $a_{\text{iso}}^{\text{S}}(\text{B}) = 13$ G and $a_{\text{iso}}^{\text{S}}(\text{B}) = 9$ G are somewhat less than the 19 and 12 G calculated from $a_{\perp}^{\text{S}}(\text{A}) = a_{\perp}^{\text{S}}(\text{A}) = -2$ G, $a_{\parallel}^{\text{S}}(\text{A}) = 61$ G, and

$a_{\parallel}^{\text{S}}(\text{A}) = 41$ G. A change in hybridization may be attributed to the formation of H_2S_2^- at different sites on the MgO surface. The calculated value of $g_{\text{iso}}(\text{A}) = 2.011$ is reasonably close to that observed for species B.

Since the sulfur atom has low-lying 3d orbitals, the energy levels for the 3p and 3d orbitals may be close; thus either a σ_{3d} bonding orbital or a σ_{3p}^* antibonding orbital may accommodate the unpaired electron. Consideration for the occupancy of the unpaired electron in the two possible molecular orbitals has been given by Akasaka et al.^{3,8} in their study of the radicals [R-CH $_2$ -S-S-CH $_2$ -R] obtained by γ irradiation of L-cystine dihydrochloride. Using their experimental g tensor they found an energy splitting between the ground and the first excited state which was much too large when an occupancy of the σ_{3d} orbital was assumed. Therefore, the unpaired electron probably occupies the σ_{3p}^* antibonding orbital. A similar conclusion can be drawn for H_2S_2^- (A) since the ion has a similar magnitude of g -tensor shift. Furthermore, the observation that $g_{\perp} > g_e$ and $g_{\parallel} \sim g_e$ for H_2S_2^- (A) is consistent with the calculated g values for the occupancy of σ_{3p}^* .

In the simplest description the σ_{3p}^* orbital can be expressed as

$$\sigma_{3p}^* = \frac{1}{\sqrt{2}} (3p_{x1} - 3p_{x2}) \quad (1)$$

where the subscripts 1 and 2 refer to the two sulfur atoms. The experimental hyperfine tensor may be resolved into its isotropic and anisotropic components:

$$\begin{bmatrix} -2 & & \\ & -2 & \\ & & 61 \end{bmatrix} = 19 + \begin{bmatrix} -21 & & \\ & -21 & \\ & & 42 \end{bmatrix} \quad (2)$$

and

$$\begin{bmatrix} -2 & & \\ & -2 & \\ & & 41 \end{bmatrix} = 12 + \begin{bmatrix} -14 & & \\ & -14 & \\ & & 28 \end{bmatrix} \quad (3)$$

Using a theoretical value of 970 G for the isotropic interaction in a pure 3s orbital⁹ and 59 G for 2β in a pure 3p orbital¹⁰ [$2\beta = \frac{4}{5}\gamma_e\gamma_s\langle r^{-3} \rangle_{3p}$] one obtains spin densities of 3% for the 3s orbitals and 119% for the 3p orbitals on the two sulfur atoms. A calculated spin density in excess of 100% is not unreasonable in view of the uncertainties in the experimental hyperfine constants and the theoretical value of 2β . The predominant 3p character estimated from the spin density agrees well with the anion model in which the unpaired electron is localized in the antibonding σ_{3p}^* orbital between the two sulfur atoms.

The mode of formation of the radicals via the transfer of electrons from the surface to the adsorbed H_2S confirms that the observed species are anions. When H_2S is adsorbed on the S centers of MgO, the H_2S^- ion may be formed initially. This ion may then react with a neutral H_2S molecule, forming H_2S_2^- and H_2 . Subsequent irradiation undoubtedly leads to the photolysis of H_2S and other reactions which may result in additional H_2S_2^- and elemental sulfur. The nonequivalency of the two sulfur and two hydrogen atoms may be generated from the effect of the surface environment. A similar situation exists when the superoxide ion is formed in a Y-type zeolite or on the surface of molybdenum oxide supported on silica gel.¹¹ The reason for the high mobility experienced by part of the H_2S_2^- molecules is not understood at this time.

Acknowledgment. This project has been financed with funds from the Environmental Protection Agency under Grant No. R 801136.

References and Notes

- (1) J. E. Bennett, B. Mile, and A. Thomas, *Chem. Commun.*, **7**, 182 (1966).
- (2) F. K. Truby, *J. Chem. Phys.*, **40**, 2768 (1964).
- (3) K. Akasaka, S. Ohnishi, T. Suita, and I. Nitta, *J. Chem. Phys.*, **40**, 3110 (1964).
- (4) M. C. R. Symons, *Adv. Chem. Ser.*, No. **82**, 1 (1968).
- (5) M. J. Lin and J. H. Lunsford, *J. Phys. Chem.*, **79**, 892 (1975).
- (6) Y. Ben Taarit and J. H. Lunsford, *J. Phys. Chem.*, **77**, 1365 (1973).
- (7) J. H. Lunsford and D. P. Johnson, *J. Chem. Phys.*, **58**, 2079 (1973).
- (8) K. Akasaka, S. Kominami, and H. Hatano, *J. Phys. Chem.*, **75**, 3746 (1971).
- (9) G. W. Chantry, A. Horsefield, J. R. Morton, J. R. Rowlands, and D. H. Whiffen, *Mol. Phys.*, **5**, 233 (1962).
- (10) K. P. Dinse and K. Möbius, *Z. Naturforsch. A*, **23**, 695 (1968).
- (11) Y. Ben Taarit and J. H. Lunsford, *J. Phys. Chem.*, **77**, 780 (1973).

Pulse Radiolysis and Electron Spin Resonance Studies of Nitroaromatic Radical Anions. Optical Absorption Spectra, Kinetics, and One-Electron Redox Potentials¹

P. Neta,*

Radiation Research Laboratories and Department of Chemistry, Mellon Institute of Science, Carnegie-Mellon University, Pittsburgh, Pennsylvania 15213

M. G. Simic,² and M. Z. Hoffman*

Department of Chemistry, Boston University, Boston, Massachusetts 02215 (Received April 5, 1976)

Publication costs assisted by the U.S. Energy Research and Development Administration

Nitrobenzoic acids, dinitrobenzenes, and di- and trinitrobenzoic acids were reduced by e_{aq}^- and by the CO_2^- and $(CH_3)_2\dot{C}OH$ radicals in irradiated aqueous solutions. The rate constants for reduction by the latter radicals were found to be close to $10^9 M^{-1} s^{-1}$ in most cases, with some substituent effects noted. The radical anions produced exhibit intense ($\epsilon \sim 10^4 M^{-1} cm^{-1}$) absorption spectra peaking around 300 nm, except for *p*-dinitro derivatives which are shifted to the 400-nm region. They protonate with pK_a 2–3 to produce radicals which absorb at lower wavelengths and which decay considerably more rapidly. One-electron redox potentials for the nitro compounds were determined using the electron transfer reactions between their radical anions and duroquinone and observing the kinetics of these reactions and the equilibrium concentrations of all components. The potentials were found to vary from -0.433 V for *m*-nitrobenzoic acid to -0.257 V for *p*-dinitrobenzene. The radical anions have also been observed by ESR and the assignment of hyperfine constants was usually straightforward. The nitro group nitrogen hyperfine constants were correlated with the redox potentials. The mononitro derivatives were found to follow a previous correlation of various nitroaromatic and nitroheterocyclic compounds, while the dinitro derivatives yield a similar linear correlation but with a different slope. The reason for this difference is discussed. Considerations of the present results and previous studies on intramolecular electron transfer in nitrobenzoatopentaamminecobalt(III) complexes show that the redox potential is of lesser importance in determining the rate of this transfer. The important factor appears to be the spin density on the carbon bearing the carboxyl group, which when higher provides a better channel for the electrons to be transferred from the nitro anion group to the cobalt center.

Introduction

Because of their relative ease of being reduced, nitroaromatic and nitroheterocyclic compounds find use as efficient radiosensitizers³ and one-electron acceptors.^{4,5} Sensitization of cells to radiation damage by these compounds has been related to the electron affinity of the sensitizer,⁶ while the sensitizing efficiency has been related to the one-electron reduction potential.^{7–9} A method for measuring thermodynamic one-electron redox potentials of nitro compounds has been fully established (cf. ref 7 and references therein). In this work, we have determined the reduction potentials of a series of dinitrobenzenes and nitrobenzoic acids using the technique of pulse radiolysis. The rate constants for the reduction of

the compounds by reducing radicals, such as CO_2^- and $(CH_3)_2\dot{C}OH$, and the spectral, kinetics, acid–base, and ESR parameters of the resulting radical anions have also been evaluated.

A knowledge of the spin density distribution in the radical anions of the nitrobenzoic acids and their redox potentials is of consequence to the interpretation of ligand-to-metal intramolecular electron transfer observed in the one-electron reduction of cobalt(III) complexes containing nitrobenzoato ligands.^{10,11} Specifically, the reduction of *o*-, *m*-, or *p*-nitrobenzoatopentaamminecobalt(III) results in the formation of coordinated radical species which decay via first-order unimolecular kinetics (with $k = 4.0 \times 10^5$, 1.5×10^2 , and $2.6 \times 10^3 s^{-1}$, respectively)^{10,11} to form Co^{2+} .

Experimental Section

The nitro compounds were obtained from Aldrich Chemical Co. and from Eastman Organic and were used without further purification. Isopropyl and *tert*-butyl alcohols were Baker Analyzed reagents. Aqueous solutions were buffered with Baker Analyzed sodium phosphates and were deoxygenated by the bubbling of pure nitrogen or argon. In some cases, the solutions were saturated with N_2O (2.5×10^{-2} M at 1 atm partial pressure).

The optical spectra and kinetics parameters were obtained at the U.S. Army Natick Research and Development Command using the Febetron 705 pulse radiolysis apparatus.¹² Determinations of one-electron redox potentials were carried out at Carnegie-Mellon University using the method described by Meisel and Neta⁷ and the computerized pulse radiolysis system first described by Patterson and Lilie¹³ and lately modified to allow more detailed examination of reaction kinetics. The ESR experiments were also performed at Carnegie-Mellon University using the in situ steady-state radiolysis-ESR technique described by Eiben and Fessenden.¹⁴ Both of the latter experiments utilized 2.8-MeV electrons from a Van de Graaff accelerator operated in the submicrosecond pulse or dc mode.

Results and Discussion

The radiolytic decomposition of liquid water yields e_{aq}^- (2.8), OH (2.8), and H (0.6) as the reactive radicals, where the values in parentheses are the G values of each species (G = number of radicals generated per 100 eV of energy absorbed). In the presence of N_2O , e_{aq}^- is converted to OH ($k = 8.6 \times 10^9$ $M^{-1} s^{-1}$),¹⁵ in acidic solution, e_{aq}^- is converted to H ($k = 2.2 \times 10^{10}$ $M^{-1} s^{-1}$).¹⁵ Hydroxyl radicals and H atoms react rapidly with HCO_2^- and $(CH_3)_2CHOH$ to form CO_2^- and $(CH_3)_2\dot{C}OH$ radicals. Thus, from the choice of OH and H scavengers, a system containing essentially a single reactive radical with $G = 6.2$ can be established. This radical reacts rapidly and stoichiometrically with the nitroaromatic solute to produce a reduced species with $G = 6.2$. From a knowledge of the radiation dose absorbed in the pulse and the G value, the concentration of the reduced nitroaromatic compound can be established, permitting evaluation of the extinction coefficient and decay kinetics of the optically absorbing species.

Reduction of Nitrobenzoic Acids and Dinitrobenzenes and Spectra of Intermediates. The reaction of CO_2^- and $(CH_3)_2\dot{C}OH$ radicals with the anionic forms of the nitrobenzoic acids at pH 7.0 generated the absorption spectra of the reduced radical species in good agreement with absorption spectra of nitroaromatic radical anions in MTHF glasses at 77 K.¹⁶ The same spectra were observed for a given substrate irrespective of the reducing radical used. At pH 0.8, the reaction of $(CH_3)_2\dot{C}OH$ with the nitroaromatic compounds produced somewhat different radical absorption spectra (Figures 1 and 2); the variation of the spectra as a function of pH gave rise to a "titration curve" from which the pK_a of the radical was derived. The rate constants for the reactions of the nitroaromatic compounds with the reducing radicals were determined from the pseudo-first-order formation of the optical absorption of the reduced species. The rate constants of the reduction reactions, the spectral characteristics of the nitroaromatic radical anions, and their pK_a values are given in Table I. At pH 0.8, the compounds reacted with $(CH_3)_2\dot{C}OH$ radicals with rate constants within 20–30% of those obtained at pH 7.0.

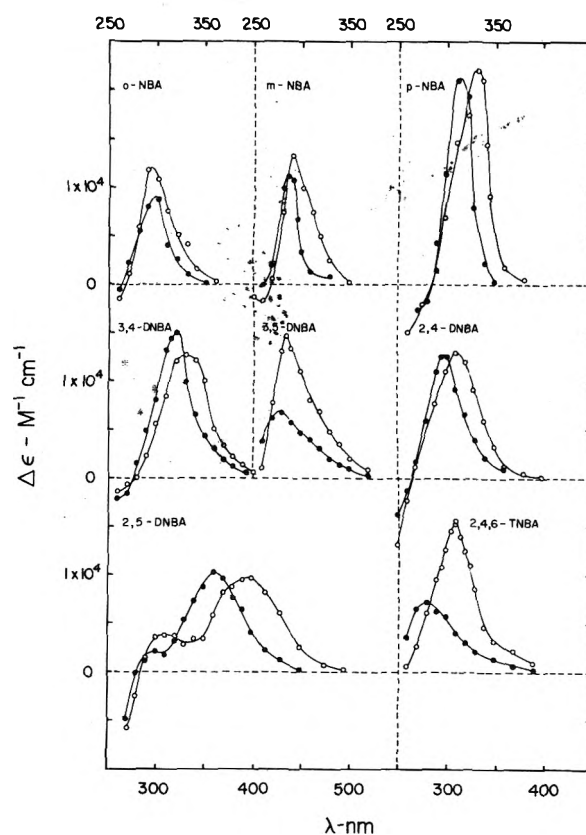


Figure 1. Transient optical absorption spectra of electron adducts to nitrobenzoic acids (NBA), dinitrobenzoic acids (DNBA), and trinitrobenzoic acid (TNBA), observed in irradiated (0.5–2 krad) aqueous solutions containing 5×10^{-5} M of the parent acid and 1 M *i*-PrOH; open circles, radical anions at pH 7.0; solid circles, protonated radicals at pH 0.8.

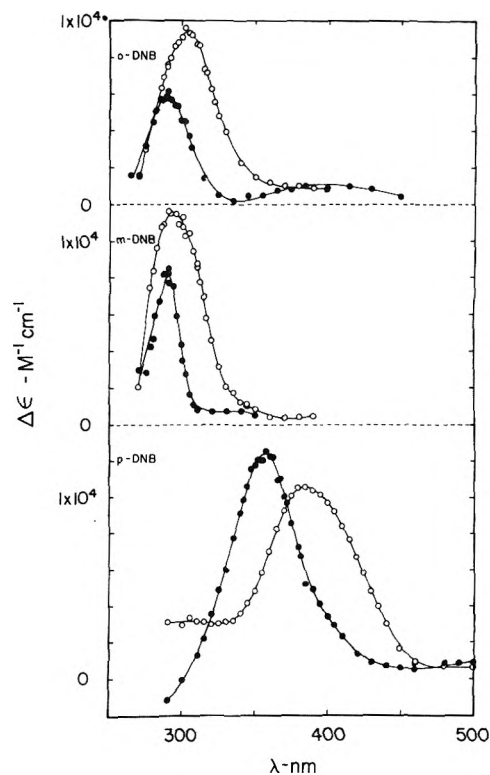


Figure 2. Transient optical absorption spectra of dinitrobenzene radical anions (pH 7, open circles) and of their protonated forms (pH 0, solid circles) in aqueous solutions.

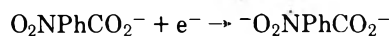
TABLE I. Rate of Reduction of Nitro Compounds and Spectra, Decay Rates, and Dissociation Constants of the Radicals Produced

Solute	Rate constant, $a M^{-1} s^{-1}$, for reduction by		Radical anion observed at pH 7			Radical observed at pH 0.8			pK_a of radical ^c
	CO_2^-	$(CH_3)_2COH$	λ_{max} , nm	ϵ_{max}^b , $M^{-1} cm^{-1}$	Decay rate constant k , $M^{-1} s^{-1}$	λ_{max} , nm	ϵ_{max}^b , $M^{-1} cm^{-1}$	Decay rate constant k , $M^{-1} s^{-1}$	
<i>o</i> -Nitrobenzoic acid	2.4×10^8	5.4×10^8	293	1.6×10^4	7.0×10^4	293	1.1×10^4	1.4×10^8	2.6
<i>m</i> -Nitrobenzoic acid	6.3×10^8	9.0×10^8	290	1.6×10^4	1.3×10^5	285	1.4×10^4	6.4×10^8	3.0
<i>p</i> -Nitrobenzoic acid	8.0×10^8	2.1×10^9	328	2.2×10^4	2.8×10^5	315	2.3×10^4	4.6×10^8	2.8
<i>o</i> -Dinitrobenzene	<i>d</i>	2.9×10^9	303	1.1×10^4	2.4×10^6	290	8.5×10^3	7.2×10^8	2.2
<i>m</i> -Dinitrobenzene	<i>d</i>	3.6×10^9	292	1.3×10^4	8.0×10^6	290	1.0×10^4	2.4×10^8	2.4
<i>p</i> -Dinitrobenzene	<i>d</i>	3.2×10^9	385	1.1×10^4	3.3×10^8	357	1.2×10^4	2.9×10^8	2.1
3,4-Dinitrobenzoic acid	1.8×10^9	3.2×10^9	330	1.4×10^4	5.6×10^5	315	1.7×10^4	6.8×10^8	$\sim 2e$
3,5-Dinitrobenzoic acid	2.5×10^9	3.1×10^9	285	1.5×10^4	6.4×10^5	265	8.7×10^3	2.8×10^8	2.2
2,4-Dinitrobenzoic acid	1.8×10^9	2.9×10^9	310	1.6×10^4	<i>f</i>	295	1.5×10^4	6.4×10^8	2.2
2,5-Dinitrobenzoic acid	1.9×10^9	3.3×10^9	400	1.0×10^4	1.5×10^7	360	1.1×10^4	3.4×10^8	2.1
2,4,6-Trinitrobenzoic acid	3.4×10^9	3.9×10^9	310	1.8×10^4	2.2×10^5	260	1.4×10^4	2.5×10^8	2.0

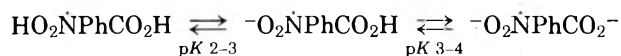
^a Measured at pH 7 using N_2O saturated solutions of the nitro compound and excess formate or 2-propanol. ^b Corrected for solute depletion. ^c Estimated accuracy ± 0.2 . ^d Could not be determined because of difficulties in dissolving the dinitrobenzenes in water without alcohol. ^e pK_a of nitro group likely overlaps with that of carboxyl group. ^f Decay of transient absorption was kinetically of mixed order.

The dinitro and trinitro derivatives react with CO_2^- with $k \sim 2-3 \times 10^9 M^{-1} s^{-1}$ and with $(CH_3)_2COH$ with $k \sim 3 \times 10^9 M^{-1} s^{-1}$ without any meaningful differences between isomers, the values being close to the diffusion-controlled limit. On the other hand, the mononitro compounds react somewhat more slowly with the para derivative being the most reactive with both radicals. The meta and ortho derivatives are less reactive in that order. The lower reactivity of the meta isomer is most probably related to its lower reduction potential (vide infra); in the case of the ortho, some additional effect may be exerted by the neighboring carboxylate group, possibly through steric or electrostatic repulsion.

Inasmuch as reduction of a nitro compound results in the radical having substantial spin density on the nitro group, albeit dependent upon the presence of electron-donating and -withdrawing groups on the ring, it is appropriate to assume that in neutral solution the nitrobenzoate radicals exist as 2-charged species.



The radicals would also be expected to be highly stabilized due to delocalization of spin throughout the aromatic system. Their second-order decay rates, probably representing disproportionation reactions, are quite low with $k \sim 10^5 M^{-1} s^{-1}$. (The radical from 2,4-dinitrobenzoate did not show purely second-order decay.) The two radicals which contain two nitro groups para to each other show considerably higher decay rate constants owing probably to a greater delocalization of the negative charge. At pH 0.8, the radicals are most probably protonated at both the carboxylate and nitro anion groups. A previous study¹⁷ on the reduction of nitrobenzene showed the pK_a value for the nitro anion group to be in the region 2-3. The pK_a value for the carboxylate group would be expected to be somewhat higher than that for the parent molecule due to the additional negative charge, as has been found in previous studies.¹⁸⁻²⁰ The second-order decay rates of the radicals at pH 0.8 are $>10^8 M^{-1} s^{-1}$ reflecting their uncharged nature in acidic solution and decreased resonance stabilization.



The spectral parameters of the radicals depend on the isomeric structure and the state of protonation of the radical. The transient absorption maxima shift to higher wavelengths in the order nitrobenzene < *m*-nitrobenzoic acid < *o*-nitrobenzoic acid < *p*-nitrobenzoic acid for the radical anions and their protonated forms. This order can be explained in terms of the increased resonance interaction of the substituents with the ring as a function of position. In the dinitro compounds (Figures 1 and 2 and Table I) it is clear that the relative position of the two nitro groups is a governing factor and the wavelength of the absorption maxima again increase in the order meta < ortho < para. In the two compounds where the nitro groups are meta to each other (3,5- and 2,4-dinitrobenzoic acid), the position of the carboxyl group is also effective in shifting the maximum. With all the variations in λ_{max} for the transients, no significant changes in ϵ_{max} are observed. The protonated forms of the radicals show absorption maxima at shorter wavelengths than the deprotonated forms but approximately the same ϵ_{max} values. This is in keeping with the reduction of the extent of resonance upon protonation of the substituents.

The pK_a values of the radicals were obtained by measuring the transient absorption under equilibrium conditions as a function of pH at an appropriate wavelength where the

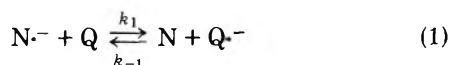
TABLE II: Equilibrium Constants, One-Electron Redox Potentials, and Rate Constants for $N^- + DQ \xrightleftharpoons[k_{-1}]{k_1} N + DQ^-$

No.	Nitro compound	k_1 , $M^{-1} s^{-1}$	k_{-1} , $M^{-1} s^{-1}$	k_1/k_{-1}	K from concn	E_7^1 , V
1	<i>o</i> -Nitrobenzoic acid	3.0×10^8	3×10^5	1000	950	-0.412
2	<i>m</i> -Nitrobenzoic acid	1.1×10^9	4.5×10^5	2400	2200	-0.433
3	<i>p</i> -Nitrobenzoic acid	7.2×10^8	1.8×10^6	400	550	-0.396
4	<i>o</i> -Dinitrobenzene	3.4×10^8	6.3×10^7	5.4	7.66	-0.287
5	<i>m</i> -Dinitrobenzene	1.1×10^9	1.3×10^7	85	73.8	-0.345
6	<i>p</i> -Dinitrobenzene	1.1×10^9	7.3×10^8	1.5	2.37	-0.257
7	3,4-Dinitrobenzoic acid	<i>a</i>			4.12	-0.271
8	3,5-Dinitrobenzoic acid	1.1×10^9	1.8×10^7	62	71.5	-0.344
9	2,4-Dinitrobenzoic acid	6.3×10^8	8.3×10^6	76	73.4	-0.345
10	2,5-Dinitrobenzoic acid	<i>a</i>			4.26	-0.272

^a Change of absorption with time was not sufficiently large to allow the determination of the rate constants.

spectral difference between the protonated and deprotonated forms was a maximum. Because of the large spin density on the nitro group compared to that on the carboxyl group, it is assumed that the chromophore resulting in optical absorption is the nitro group (protonated or deprotonated) with little contribution from the carboxylate group (protonated or deprotonated), i.e., spectral changes due to protonation of the carboxyl group are expected to be considerably smaller than those resulting from the protonation of the free radical site. Therefore, the pK_a values given in Table I are taken to be those of the nitro radical group. Effect of the carboxylate group can be ruled out on the basis of a comparison of the dinitrobenzoates to the dinitrobenzenes.

One-Electron Redox Potentials. The measurement of one-electron reduction potentials⁷ consists of the determination of the equilibrium constant K for



where N represents the nitro compound, Q is a reference quinone for which the one-electron potential E^1 is known, and N^- and Q^- are their respective radical anions. The concentrations of all components are determined under equilibrium conditions and are used to derive K and ΔE .

The one-electron reduction potentials of the nitrobenzoates and dinitrobenzenes at pH 7.0 were determined by reference to duroquinone using the method described in detail previously.⁷ Solutions containing varying concentrations of the nitro compound and duroquinone, and excess 2-propanol, were pulse irradiated and the change of absorption followed at 445 nm, the maximum of the durosemiquinone absorption. The nitro radical anions have a low absorbance at this wavelength but a correction was applied, if necessary. In all cases, an initial absorption was observed immediately after the pulse, followed by an increase resulting from electron transfer from the nitro aromatic radical anion to the duroquinone, up to a plateau which represents the equilibrium conditions achieved before any appreciable decay of the radicals took place. Except for two cases (3,4- and 2,5-dinitrobenzoate), the change in absorption with time was sufficiently large to allow the evaluation of both k_1 and k_{-1} as described previously.⁷

The results summarized in Table II show that all the nitro radical anions studied undergo electron transfer to duroquinone with rate constants (k_1) of $3\text{--}11 \times 10^8 M^{-1} s^{-1}$, with k_{-1} varying over three orders of magnitude. In most cases, the equilibrium constant, K , calculated from the solute and radical concentrations at equilibrium, is more accurate than that calculated from k_1/k_{-1} . However, Table II shows that the agreement between the two sets of results is very good and

represents less than ± 5 mV in the redox potential. The E_7^1 values in Table II have been calculated from the concentrations and using E_7^1 for duroquinone, -0.235 V.⁷

A comparison of the potentials in Table II and the value reported⁷ for nitrobenzene (-0.486 V) shows that the presence of the carboxylate group makes the potential considerably less negative; its effect is in the order meta < ortho < para, the same order of effect found in the optical absorption maxima. The addition of a nitro group to nitrobenzene has a stronger effect than the carboxylate group but the isomeric order of the effect is the same. The results for the dinitrobenzoates show that the relative positions of the two nitro groups are far more important than the position of the carboxylate group in determining the redox potential. Correlation of these potentials with spin distribution is given below.

Electron Spin Resonance Studies. The ESR spectra of the nitroaromatic radical anions have been recorded using the *in situ* radiolysis steady-state ESR technique¹⁴ and the parameters are summarized in Table III. The assignments of hyperfine constants in the mononitrobenzoate radicals are straightforward and follow previous assignments for nitrobenzene and its derivatives.¹⁴ Hyperfine constants for the dinitrobenzene radical anions can be also assigned easily and are in good agreement with previously reported results obtained by a different method.²¹ It should be noted that while both *o*- and *p*-dinitrobenzene anions have two equivalent nitrogens, the ortho isomer showed a strong alternating line widths effect while the spectrum of the para isomer gave little indication of such an effect. This difference can be rationalized by the dynamical model of Rieger and Fraenkel²² if it is assumed that steric effects in the ortho isomer cause an instantaneous twist of one of the nitro groups. In contrast, the meta isomer has inequivalent nitrogens and can be simply treated as a substituted nitrobenzene radical anion, with parameters very similar to those observed, for example, for the meta carboxy derivative (see Table III). Despite this localization of the radical site, caused by the strongly polar solvation, some electron exchange does take place to cause line widths alternation similar to that observed previously.²¹ The same type of line width effect was also evident in the spectra of all dinitrobenzoate radical anions.

The structure of radicals derived from the dinitrobenzoates and their hyperfine constants are also given in Table III. It is seen that the nitro groups of both *o*- and *p*-dinitrobenzene become inequivalent upon the introduction of a carboxyl group on the ring. This is of course expected and the assignments do not present any difficulty. The assignments for the other two dinitrobenzoate radicals are easily made by comparison with the parameters for the *m*-dinitrobenzene anion.

TABLE III: ESR Parameters of Nitroaromatic Radical Anions^a

Radical	a^N	a^H	g factor
	13.85	<i>o</i> 3.29 <i>m</i> 1.12; 1.18 <i>p</i> 3.55	2.00453
	14.03	<i>o</i> 3.38 (2) <i>m</i> 1.13 <i>p</i> 3.61	2.00449
	13.02	<i>o</i> 3.35 (2) <i>m</i> 1.14 (2)	2.00458
	5.83 (2)	3,6 1.00 (2) 4,5 1.20 (2)	2.00466
	13.12 0.26	2,6 3.42 (2) 5 1.12 4 3.68	2.00451
	4.66 (2)	1.09 (4)	2.00485
	8.70 1.86	6 2.31 3,5 0.42; 0.13	2.00470
	12.86 0.26	2,6 3.42 (2) 4 3.69	2.00449
	12.70 0.24	2,6 3.46; 3.37 5 1.13	2.00458
	8.88 0.24	2,6 2.67 (2) 5 0.48	2.00486
	11.85	2,6 3.46 (2)	2.00452

^a Determined in irradiated aqueous solutions containing $1-5 \times 10^{-4}$ M of the nitro compounds, 0.1 M 2-propanol, 2 mM phosphate buffer at pH 7, and deoxygenated by bubbling with pure nitrogen. The hyperfine constants a are given in gauss and are accurate to ± 0.03 G. The g factors were determined relative to the signal from the silica cell¹⁴ and are accurate to ± 0.00005 . Second-order corrections have been made.

The radical from 3,5-dinitrobenzoate has also been reported previously²¹ and the splittings are in good agreement with the present measurements. The spectrum recorded with the

trinitrobenzoate showed the presence of only one nitrogen and two equivalent protons and must be assigned as in Table III. The other two nitrogens probably have hyperfine constants of ≤ 0.1 G.

The g factor also shows variation with isomeric structure. In each series the g factor increases in going from meta to ortho to para, the same order as that of the decrease in nitrogen hyperfine constants. Again the effect of an additional nitro group on nitrobenzene and of its position is far greater than that of the carboxyl group.

Correlation of Redox Potentials with Hyperfine Constants. In the previous paper on the one-electron redox potentials of nitroaromatic and nitroheterocyclic compounds,⁷ an inverse linear correlation between these potentials and the nitrogen hyperfine constant $a_{\text{NO}_2}^N$ of the corresponding radical anion has been presented. It was argued that a decrease in $a_{\text{NO}_2}^N$ means greater stabilization of the radical and, therefore, a more positive potential for the reduction of the parent compound. The results obtained in the present study for the three nitrobenzoate anions are found to fit quite well with the previous correlation;⁷ the results for 2,4- and 3,5-dinitrobenzoate also fall close to the same line (Figure 3). However, the dinitrobenzenes and the 2,5- and 3,4-dinitrobenzoate do not give quantitative agreement with these other results showing a linear relationship with a different slope; the qualitative order is as expected. In considering this type of correlation for the nitro compounds, it must be remembered that the simple plot of E_7^1 vs. $a_{\text{NO}_2}^N$ is based on the assumption that $a_{\text{NO}_2}^N$ represents the spin density on the nitro group and indicates the portion of the spin density that is on the ring. This assumption is correct to a first approximation if the internal spin distribution within the nitro group remains constant. This approximation may not hold for the dinitro derivatives, especially the para isomer, if strong solvation by the polar water molecules changes the spin distribution within the nitro group. In this connection, it should be noted that $a_{\text{NO}_2}^N$ in water is greater than that in acetonitrile by a factor of 1.4 for nitrobenzene and m -dinitrobenzene, 1.8 for o -, and 2.7 for p -dinitrobenzene.²³ Moreover, molecular orbital calculations²² also show that the spin on the oxygen increases at the expense of the spin on the nitrogen for the radical anions derived from nitrobenzene $< o- < p$ -dinitrobenzene. A straight line can be drawn through the data for the dinitrobenzenes using double the value of $a_{\text{NO}_2}^N$ for the ortho and para derivatives. The results for all four dinitrobenzoates fit the same line quite well. The slope is only 0.025 as compared with 0.054 for the mononitro derivatives.⁷

In using ESR data for the estimation of redox potentials, caution must be taken in accounting for effects which cause a change in $a_{\text{NO}_2}^N$ unrelated to the change in spin density on the ring. Substituents which attract a considerable spin density may also cause deviations from the linear correlation. However, if a closely related group of compounds is examined and the differences in potential are very small, then the ESR results can be employed to discover variations in E^1 within the experimental error of their actual determination.

Intramolecular Electron Transfer. The nitrobenzoate radical anions are rather good reducing agents accounting for the efficiency of intramolecular electron transfer when coordinated to a Co(III) center.^{10,11} If one assumes that the redox potentials of the radical anions are the same when free or coordinated, it is clear that the rate constants for intramolecular electron transfer cannot be directly correlated to the potentials. Instead, the factor of 10 difference in rate constants between the m - and p -nitrobenzoate complexes is probably

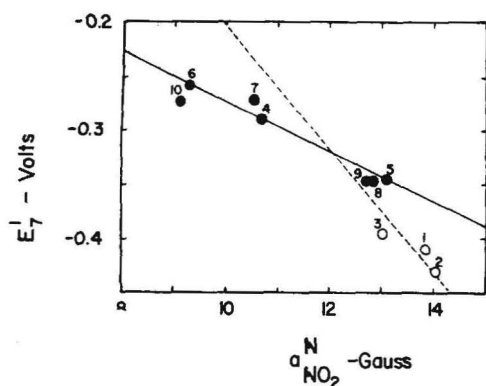


Figure 3. Correlation of one-electron redox potentials E_7^1 with nitrogen hyperfine constants $a_{\text{NO}_2}^{\text{N}}$. Numbers relate to number of compounds in Table II. For the values of $a_{\text{NO}_2}^{\text{N}}$ used see Table III and text. The dashed line is the line drawn in ref 7 and fits the mononitrobenzoates (open circles). The dinitro derivatives (solid circle) are correlated by the solid line.

the result of the difference in spin density distribution. The carbon para to the nitro group bears a considerable spin density (~15%) while the meta carbon has a negligible amount. Therefore, in the *p*-nitrobenzoate complex, a channel is provided for the electron to be transferred to the metal center; in the *m*-nitrobenzoate complex, such channeling is limited. The 100-fold faster electron transfer rate in the ortho isomer probably arises from overlap of the nitro and carboxylate orbitals providing an efficient pathway to the metal center. The spin densities on the coordinated radical appear to establish the trends and correlation with the intramolecular rates for other nitroaromatic carboxylate complexes will be discussed in a separate publication.²⁴

References and Notes

- (1) Supported in part by the U.S. Energy Research and Development Administration and in part by the National Science Foundation through Grant No. MPS 73-05025.
- (2) Visiting Professor, Boston University, 1975. Permanent address: Food Engineering Laboratory, U.S. Army NRDC, Natick, Mass. 01760.
- (3) G. E. Adams, J. C. Asquith, D. L. Dewey, J. L. Foster, B. D. Michael, and R. L. Willson, *Int. J. Radiat. Biol.*, **19**, 575 (1971).
- (4) K.-D. Asmus and A. Henglein, *Ber. Bunsenges. Phys. Chem.*, **68**, 348 (1964).
- (5) K.-D. Asmus, A. Henglein, M. Ebert, and J. P. Keene, *Ber. Bunsenges. Phys. Chem.*, **68**, 657 (1964).
- (6) G. E. Adams and M. S. Cooke, *Int. J. Radiat. Biol.*, **15**, 457 (1969).
- (7) D. Meisel and P. Neta, *J. Am. Chem. Soc.*, **97**, 5198 (1975).
- (8) G. E. Adams, I. R. Flockhart, C. E. Smithen, I. J. Stratford, P. Wardman, and M. E. Watts, *Radiat. Res.*, in press.
- (9) M. Simic and E. L. Powers, *Int. J. Radiat. Biol.*, **26**, 87 (1974).
- (10) M. Z. Hoffman and M. Simic, *J. Am. Chem. Soc.*, **94**, 1757 (1972).
- (11) M. Z. Hoffman and M. Simic, Proceedings of the XIV International Conference on Coordination Chemistry, Toronto, Canada, June 1972, p 501.
- (12) M. Simic, P. Neta, and E. Hayon, *J. Phys. Chem.*, **73**, 3794 (1969).
- (13) L. K. Patterson and J. Lilie, *Int. J. Radiat. Phys. Chem.*, **5**, 129 (1974).
- (14) K. Eiben and R. W. Fessenden, *J. Phys. Chem.*, **75**, 1186 (1971).
- (15) M. Anbar, M. Bambenek, and A. B. Ross, *Natl. Stand. Ref. Data Ser., Natl. Bur. Stand.*, No. 43 (1972).
- (16) T. Shida and S. Iwata, *J. Phys. Chem.*, **75**, 2591 (1971).
- (17) W. Grünbein, A. Fojtik, and A. Henglein, *Z. Naturforsch. B*, **24**, 1336 (1969).
- (18) M. Simic and M. Z. Hoffman, *J. Phys. Chem.*, **76**, 1398 (1972).
- (19) C. L. Greenstock, I. Dunlop, and P. Neta, *J. Phys. Chem.*, **77**, 1187 (1973).
- (20) For compilation of pK values see E. Hayon and M. Simic, *Acc. Chem. Res.*, **7**, 114 (1974); P. Neta, *Adv. Phys. Org. Chem.*, **12**, 223 (1975).
- (21) W. E. Griffith, C. J. W. Gutch, G. F. Langster, J. Myatt, and P. F. Todd, *J. Chem. Soc. B*, 785 (1968).
- (22) P. H. Rieger and G. K. Fraenkel, *J. Chem. Phys.*, **39**, 609 (1963).
- (23) From a comparison of the present results or of those reported in ref 15 with the results in CH_3CN reported by A. H. Maki and D. H. Geske, *J. Chem. Phys.*, **33**, 825 (1960).
- (24) M. G. Simic, M. Z. Hoffman, and N. V. Brezniak, manuscript in preparation.

The Internal Chemical Shift—A Key to Bonding in Aromatic Molecules. 2. Substituent Effects on the Carbon-13 Magnetic Resonance Spectra of the 1,4-Disubstituted Benzenes¹

D. W. Beistel* and W. Dan Edwards

Department of Chemistry, University of Missouri—Rolla, Rolla, Missouri 65401 (Received March 26, 1976)

Carbon-13 magnetic resonance shifts were determined for six families of 1,4-disubstituted benzenes. Linear least-squares correlations between the internal shifts of the families suggest an additivity relationship for ¹³C substituent effects at all four nonidentical ring carbons and at the α position when one of the substituents has a central carbon. The correlation of ¹H and ¹³C shifts for these compounds is also linear, implying that the additivity relationships derived in a previous ¹H study can be generalized to ¹³C.

Introduction

The ¹³C spectra of many aromatic substances have been reported in recent years. Except for early investigations by Lauterbur,²⁻⁶ Spiess and Schneider,⁷ and Savitsky⁸ little attention was paid the substituted benzenes before 1965. Perhaps the need to characterize more complex systems

prompted that neglect. In any case Dhimi and Stothers⁹⁻¹¹ and Grant et al.¹² were among the few later investigators who showed any marked interest in the substituted benzenes.

The studies of Grant and co-workers¹² suggested a possible theoretical model for ¹³C shifts. The shift was attributed to contributions from the π -charge density, ΔQ_π , the σ -charge

TABLE I: ^{13}C Shifts of the 4-Z-Substituted Nitrobenzenes (in ppm) Relative to TMS

Z	$\text{C}_1(\text{Z})$	$\text{C}_2(\text{Z})$	$\text{C}_3(\text{NO}_2)$	$\text{C}_4(\text{NO}_2)$	$\Delta_{\text{C}_{23}}$
NMe ₂	154.09	110.08	125.83	135.75	-15.75
OMe	164.52	113.93	125.67	141.39	-12.0
F	160.99	115.79	125.99	144.29	-9.92
	171.23	116.75	126.39		
Me	145.79	129.64	123.29	146.07	6.35
Et	151.83	128.45	123.49	146.19	5.16
<i>t</i> -Bu	158.65	126.03	123.17	145.79	2.86
Cl	141.15	129.44	124.80	146.43	4.64
Br	129.71	132.46	124.80	146.87	7.66
I	102.38	138.45	124.68	147.62	13.77
COOMe	135.40	130.60	123.45	150.48	7.15
CH=O	140.0	130.36	124.21	151.07	6.15
CN	116.67	133.33	124.17	150.0	9.16
COCl	137.94	132.10	123.89	151.47	8.21

TABLE II: ^{13}C Shifts of the 4-Z-Substituted Benzonitriles (in ppm) Relative to TMS

Z	$\text{C}_2(\text{CN})$ $\text{C}-\text{N}$	$\text{C}_1(\text{Z})$	$\text{C}_2(\text{Z})$	$\text{C}_3(\text{CN})$	$\text{C}_4(\text{CN})$ $\text{C}=\text{N}$	$\Delta_{\text{C}_{23}}$
NMe ₂	97.22	150.34	111.31	133.14	120.48	-21.83
NH ₂	99.76	150.44	114.29	133.57	120.04	-19.28
OMe	103.85	162.7	114.68	133.77	119.01	-19.09
OH	102.98	160.12	116.39	134.17	119.0	-17.78
Me	109.29	143.49	129.64	131.83	118.93	-2.19
H	112.46	132.58	128.97	131.98	118.65	-3.01
Cl	110.75	139.40	129.52	133.17	117.70	-3.65
Br	111.27	127.78	133.17	132.46	117.78	0.71
I	111.71	100.00	138.29	132.94	117.86	5.35
COMe	116.23	139.84	128.53	132.30	117.70	[3.77]
NO ₂	118.29	150.0	124.17	133.33	116.67	[9.16]

density, ΔQ_π , and the mobile bond order, ΔP , by the empirical relation

$$\delta_{^{13}\text{C}} = 100\Delta Q_\pi + 67\Delta Q_\sigma - 76\Delta P \quad (1)$$

Equation 1 predicted the ^{13}C shift relative to benzene to a sufficient accuracy that later refinements¹³ have not been published. The Schneider model for the shifts of aromatic protons^{14,15}

$$\delta = k\Delta\rho \quad (2)$$

related changes in π -charge density at carbon, $\Delta\rho$, to the shift, δ , of the attached proton. Unlike the Grant model, no theoretical basis was used to derive the latter and all other contributions were combined in k .

Several difficulties plague these shift models. The data bases used in their construction were slight and disorganized, and some anomalous substituent effects were required. A recent report¹⁶ summarizes the differences one notes between the conclusions drawn from preliminary ^1H shift studies and the fruits of an exhaustive approach and a current paper¹⁷ summarizes some theoretical considerations. Similar thoroughness should be required for a proper analysis of the ^{13}C shifts of these compounds if the results are to be useful to theoreticians and to students of higher aromatic compounds.

Experimental Section

The ^{13}C shift measurements were made at 25.2 Mhz with a Varian XL-100 high-resolution spectrometer and peripherals. The typical spectrum was obtained on a sample of the purified benzene in DCCl_3 (~100 mg/3 ml) in a 12-mm tube

using TMS as the internal standard. Proton and noise decoupling were employed and all accumulations were obtained by standard pulse delay techniques.¹⁸ Assignments were based on spin coupling measurements, relaxation times, and relative peak intensities. Sample sources and purification techniques have been reported elsewhere.^{16,19}

Computer graphics were run on a Texas Instruments Model 980A computer equipped with JEOL 10 bit DAC's and a Tektronics Model 604 oscilloscope at a resolution of 1024 channels. Linear least-squares analyses of the data were performed on an IBM 370/168 computer as well as the TI 980A. A detailed description of these systems is contained in a recent ACS Symposium Monograph.²⁰

Results and Discussion

The ^{13}C shifts for the 4-substituted nitrobenzenes and benzonitriles are summarized in Tables I and II. Those data, together with the shifts of other 4-substituted benzenes (see Tables III and VI), give a consistent picture for substituent interactions.

Figure 1 is an example of the linear relationships found between the internal shifts, $\Delta_{\text{C}_{23}}$, of the families of 1,4-disubstituted benzenes. A listing of the calculated slopes and intercepts for the correlations is given in Table VII. Obviously the additivity relationships that were suggested for the ^1H internal shifts¹⁶ must apply to their ^{13}C counterparts because the substituents again seem well behaved.

One can use these internal shift correlations together with the data in Tables I-VI to predict the shifts of other members of a family. For example, if one required the internal shift for 4-fluorobenzonitrile he could insert the shift of -16.53 ppm for 4-fluorobenzoic acid (see Table III) into the equation,

TABLE III: ^{13}C Shifts for the 4-Z-Substituted Benzoic Acids (in ppm) Relative to TMS

Z	COOH	C ₁ (Z)	C ₂ (Z)	C ₃ (COOH)	C ₄ (COOH)	$\Delta_{\text{C}_{23}}$
NMe ₂	167.26	152.82	110.56	130.67	116.79	-20.11
NH ₂	167.14	152.82	112.34	130.95	116.71	-18.61
OMe	166.71	162.54	113.53	131.07	122.82	-17.54
F	169.64	166.15	115.83	132.10	127.38	-16.53
		159.72	114.96	131.75	127.26	
H	172.42	133.65	128.33	130.12	129.29	-1.79
Br	166.31	126.63	131.39	129.82	131.03	1.57
I	166.55	100.79	137.30	130.79	130.12	6.51

TABLE IV: ^{13}C Shifts for the 4-Z-Substituted Acetophenones (in ppm) Relative to TMS

Z	COMe	C ₁ (Z)	C ₂ (Z)	C ₃ (COMe)	C ₄ (COMe)	$\Delta_{\text{C}_{23}}$
NH ₂	196.27	151.31	113.45	130.60	127.34	-17.15
OMe	196.35	163.33	113.61	130.44	130.28	-16.83
F	196.07	170.67	115.95	130.99	133.61	-15.28
		160.56	115.08	130.60	133.53	
H	197.18	132.82	128.10	128.33	136.98	-0.23
Cl	196.39	139.33	129.52	128.73	135.32	0.79
Br	196.47	135.71	131.67	129.60	128.02	2.07
CN	196.15	117.70	132.30	128.53	139.84	3.77
I	196.71	100.83	137.62	129.44	136.19	8.88

TABLE V: ^{13}C Shifts of the 4-Z-Substituted Benzoyl Chlorides (in ppm) Relative to TMS

Z	COCl	C ₁ (Z)	C ₂ (Z)	C ₃ (COCl)	C ₄ (COCl)	$\Delta_{\text{C}_{23}}$
NH ₂	167.02	150.91	113.61	131.43	119.25	-17.82
OH	166.39	165.52	114.37	133.85	125.04	-19.48
<i>i</i> -Pr	167.58	157.14	126.94	131.55	130.71	-4.61
Cl	166.47	141.98	129.53	132.34	131.35	-2.81
I	166.55	100.83	137.30	130.79	130.04	6.51
NO ₂	166.75	151.47	123.89	132.10	137.94	8.21

TABLE VI: ^{13}C Shifts of the 4-Z-Substituted Benzaldehydes (in ppm) Relative to TMS

Z	CH=O	C ₁ (Z)	C ₂ (Z)	C ₃ (CHO)	C ₄ (CHO)	$\Delta_{\text{C}_{23}}$
NMe ₂	189.72	154.17	110.91	131.71	125.12	-20.8
OH	190.79	161.27	115.83	132.30	129.88	-16.5
Me	192.18	138.73	127.80	129.80	133.37	-2.0
<i>i</i> -Pr	191.63	155.99	126.94	129.80	134.48	-2.86
Cl	190.40	140.67	129.29	130.67	134.64	-1.38
I	190.91	102.58	138.25	130.60	135.52	7.65
NO ₂	189.96	151.07	124.21	130.36	140.0	6.15

$\Delta_{\text{F,CN}} = 0.990\Delta_{\text{F,COOH}} + 0.893$ (see Table VII) and obtain a predicted value for $\Delta_{\text{F,CN}} = -15.47$ ppm. Similar calculations for shifts known in both families suggest an uncertainty of less than 2 ppm in the estimates of large negative shifts such as this and 0.5 ppm for the smaller, positive shifts. The approximate error is about 10% for most estimates. Considering the relative magnitudes of ^{13}C shifts an uncertainty of that magnitude is small enough to make line assignments when it is used in conjunction with intensity data from the FT output of the spectrometer.

Similar correlations were found between the $\Delta_{\text{C}_1-\text{C}_3}$ (and their $\Delta_{\text{C}_2-\text{C}_4}$ reciprocals) for these series (see Table VIII). These correlations of internal shifts at alternate carbons are quite good in all cases, suggesting an additivity of substituent effects even at C₁ and C₄.

Tables II-VI contain the ^{13}C shifts for sites external to the skeleton of the ring. The shifts for these α -carbons on 4 substitution parallel the trends at C₂ and are consistent with observations reported for other external nuclei such as ^{19}F in

substituted fluorobenzenes^{21,22} and ^{11}B in the benzenboronic acids.²³ One observes a threefold increase in the magnitude of the shift induced at the α -carbon of the benzonitriles over that induced at an α -boron (see Figure 2). The ^{13}C shift ranges for the other families are much smaller however, spanning only 2 ppm in the benzaldehyde family.

When one plots the internal shifts between the families of 1,4-disubstituted benzenes that are reported here against those of a previous ^1H NMR study,¹⁶ he notes some very interesting and distinctive relationships. Take Figure 3 for example. The substituents seem to fall into two sets when $\Delta_{(\text{C}_2-\text{C}_3)}$ is plotted against $\delta_{(\text{H}_2-\text{H}_3)}$. That is, two parallel lines correlate the substituents and the jump from one set to the other is equal in every case to the internal proton shift of the parent compound in the family. One set of substituents correlates directly while the other set correlates with its corresponding relative internal proton chemical shift.

In the previous paper¹⁶ the shift additivity relationship for ring protons suggested that the internal shifts due to the ref-

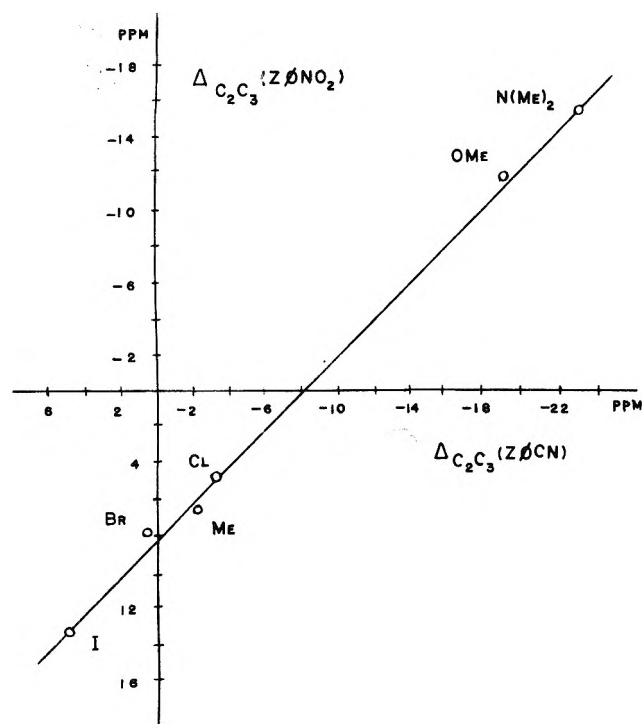


Figure 1. Internal ($\Delta_{C_2-C_3}$) shift correlation for the 4-substituted nitrobenzenes vs. the 4-substituted benzonitriles.

TABLE VII: Internal ^{13}C Shift Correlations (C_2-C_3) between Families of 1,4-Disubstituted Benzenes

Groups	Slope	Intercept	Corr coeff
$\text{NO}_2\text{-CN}$	0.931	-7.73	0.999
$\text{NO}_2\text{-COOH}$	0.914	-6.78	0.998
$\text{NO}_2\text{-CHO}$	0.955	-5.59	0.986
$\text{NO}_2\text{-COCH}_3$	0.985	-5.40	0.998
CN-COCl	1.008	+0.264	0.993
CN-COOH	0.990	+0.893	0.999
CN-CHO	0.952	+0.585	0.987
CN-COCH_3	1.038	+2.840	0.999
COCl-CHO	0.879	+0.746	0.992
COOH-H	1.084	+1.77	0.994
CN-H	1.130	+2.67	0.996
$\text{NO}_2\text{-H}$	1.158	-5.81	0.995

TABLE VIII: Internal Shift Correlations (C_1-C_3) between Families of 1,4-Disubstituted Benzenes

Groups	Slope	Intercept	Corr coeff
CHO-CN	1.029	-4.382	0.999
COOH-CN	0.9803	-3.143	0.995
$\text{NO}_2\text{-CN}$	1.016	-10.43	0.999
$\text{NO}_2\text{-COCH}_3$	1.013	-6.807	0.996
COOH-COCH_3	0.955	1.475	0.995
H-COCH_3	0.895	4.845	0.999
H-NO_2	0.906	11.03	0.995
H-CN	0.935	0.715	0.997

erence substituent were subtracted out of the relative internal shift. If so the correlation of substituents on the lower line in Figure 2 might infer that the ^{13}C internal shifts for that set of substituents were perturbed by the reference substituent while the ^1H shifts were not, relative to ^{13}C . Also, the slopes

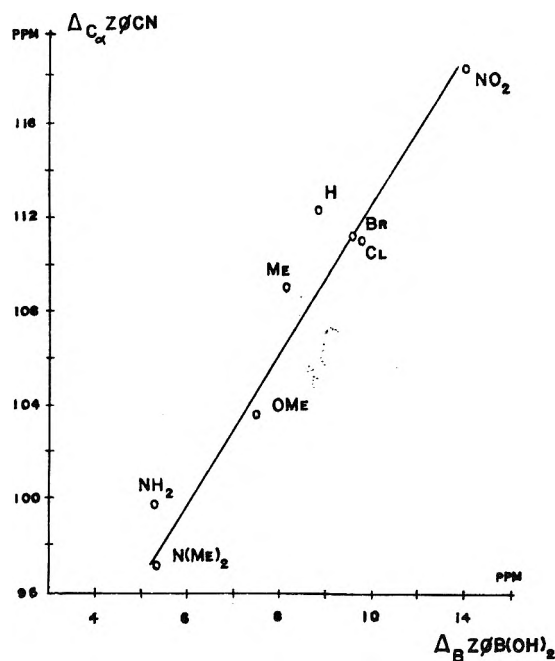


Figure 2. Correlation of the α -carbon shifts of a series of 4-substituted benzonitriles vs. the ^{11}B shifts of the 4-substituted benzenboronic acids.

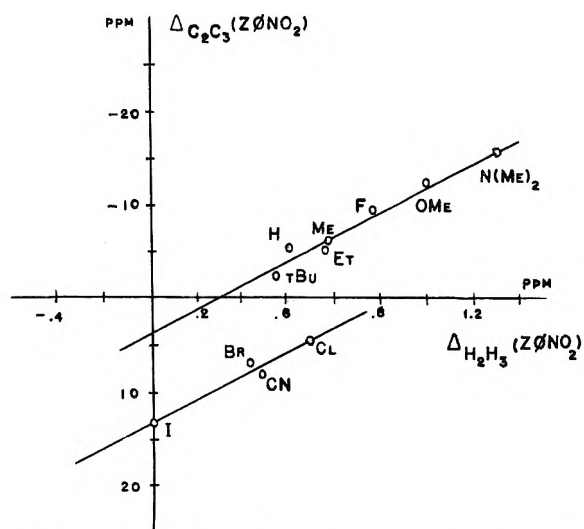


Figure 3. Internal ($\Delta_{C_2-C_3}$) shifts vs. internal ($\delta_{\text{H}_2-\text{H}_3}$) shifts of the 4-substituted nitrobenzenes.

for the other families of shifts should be equal and they are nearly identical for the benzonitriles and benzoic acids, differing only slightly for the nitrobenzenes. Apparently an interaction term does not subtract out in the latter series.

On close inspection an additional factor must be considered when analyzing these data. When one considers the shift relationships using computer graphics, it becomes obvious that both the ^{13}C and ^1H internal shifts always can be scaled to an interval of 0 to π . The transition from one parallel line to the other always comes at $\pi/2$ in the interval regardless of the substituent that falls there. That is, the proton shift range is 0 to 1.51 ppm for the nitrobenzenes, -0.46 to 0.77 ppm for the benzonitriles, and 0.17 to 1.08 ppm for the benzoic acids. The median values ($\pi/2$) are 0.75, 0.15, and 0.49, respectively, and the divergence occurs for each series at about those shifts. Further, when one makes a similar scaling of the ^{13}C shifts for

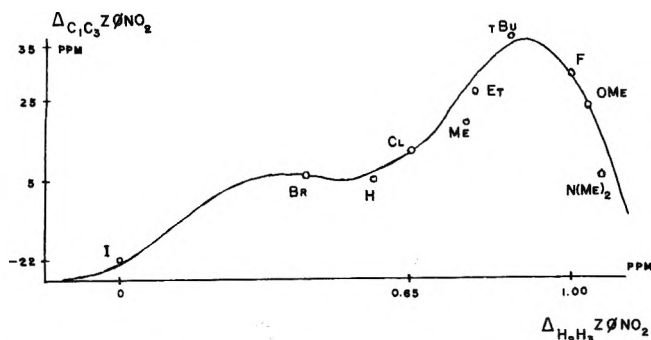


Figure 4. Internal ($\Delta_{C_1-C_3}$) shifts vs. the internal ($\delta_{H_2-H_3}$) shifts of the 4-substituted nitrobenzenes. The shape function is $-\sum_{k=1}^4 (-1)^k (2/k) \sin kx$.

these three series the respective median positions of 6.99, -6.34, and -6.80 ppm also seem to represent the points of divergence. These positions correspond to a shift of less than *t*-Bu but greater (more negative) than Cl for the nitrobenzene series, less than OH but greater than H for the benzonitrile series, and less than H but greater than Br for the benzoic acid series. So the absolute electronic properties of the substituent itself do not seem to be a factor of import.

When one examines the relationships between $\Delta_{C_1-C_3}$ and $\delta_{H_2-H_3}$ the scope of this proposed angular relationship becomes even clearer. Figure 4 was obtained by a computer graphics analysis of the fit of the Euler-Fourier²⁴ series

$$-\sum_{n=1}^k (-1)^n \left(\frac{2}{k}\right) \sin nx$$

to the data. This series gives $y = mx$ as k becomes infinite and the series is finite over the interval, $-\pi < x < \pi$.²⁵ For these data sets an excellent fit is obtained when $k = 4$ and other expansions in k are entirely unsuitable.

The Laplace solution²⁶ for differential equations of the form, $\nabla^2 \phi(x, y) = 0$, is a sine series similar to this. The differential equations can be used to describe field gradients within a two-dimensional frame which result in distortions in the z direction. There $y = b$ and $x = a$ at the boundaries where ϕ vanishes and $\phi_n = \sinh [n\pi(b - y)/a] \sin (n\pi x/a)$ reduces to $\phi_n = \sin (n\pi x/a)$ when $(b/a) = 0.28$. Noting that $\nu_0(^{13}\text{C})/\nu_0(^1\text{H}) = 0.25$, we may be observing the effects of a frequency boundary on the magnetic gradients.

Perhaps it is not surprising that one sees a possible angular dependence in data such as these. After all the empirical equation²⁷

$$H_i = \frac{2\pi\nu_0}{\gamma(1 - \sigma_i)}$$

contains a shielding term, $(1 - \sigma_i)$, suggestive of the range of a cosine function. Also, the well-known " τ " scale of Roberts implies that an entire family of hydrocarbons is bounded within a shift interval of 0 to 10. That interval might well be 0 to 3π . To find parallels among the shifts induced by moieties on the various nuclei to which they can be bonded, we may only need to scale the total absolute shift ranges for each type of nucleus, C, P, B, Sn, etc., to an interval in $n\pi$. A thorough examination of these possible theoretical implications is underway at the present time. If correctly interpreted they could

provide a model from which the now empirical shift equations can be derived.

It has been shown that the substituents induce well-behaved ^{13}C and ^1H chemical shifts in the 1,4-disubstituted benzenes. By well behaved one means that shift additivity prevails at C and H sites throughout the benzenoid system and any substituent interactions are of minor importance. Substituents capable of π conjugation do not seem to interact with their electronic environment in that mode because their influence on the ring current is negligible.¹⁶ In addition the correlation of α -C and α -B magnetic resonance shifts, a most sensitive test of either π conjugation or polarization effects, almost certainly negates that mechanism.

The 1,4 substitution was chosen to minimize any steric interactions so that inductive and conjugation effects could be isolated and examined. According to these ^1H and ^{13}C shift studies it would seem that conjugation effects are negligible and only inductive interactions play a significant role. Further the shift additivity and proportional decrease in shift at the 2, 3, and 4 positions suggests that the inductive influences are transmitted through the σ bonds. If so, the mathematical models proposed by Grant and others can be simplified considerably.

Acknowledgments. We wish to thank Drs. Charles Wilkins, David Theonnes, and Thomas Brunner, Department of Chemistry, University of Nebraska—Lincoln, for the outstanding spectral services they provided. We also thank the Committee of Deans, UMR, for their support of this project.

References and Notes

- (1) Presented in part at the 167th National Meeting of the American Chemical Society, Los Angeles, Calif., April, 1974.
- (2) P. C. Lauterbur, *Ann. N.Y. Acad. Sci.*, **70**, 841 (1958).
- (3) (a) P. C. Lauterbur, *J. Am. Chem. Soc.*, **83**, 1838 (1961); (b) *ibid.*, **83**, 1856 (1961).
- (4) P. C. Lauterbur, *J. Chem. Phys.*, **38**, 1406 (1963).
- (5) P. C. Lauterbur, *J. Chem. Phys.*, **38**, 1415 (1963).
- (6) P. C. Lauterbur, *J. Chem. Phys.*, **38**, 1432 (1963).
- (7) H. Spiesscke and W. G. Schneider, *J. Chem. Phys.*, **35**, 731 (1961).
- (8) G. B. Savitsky, *J. Chem. Phys.*, **67**, 2723 (1963).
- (9) K. S. Dhami and J. B. Stothers, *Can. J. Chem.*, **43**, 479 (1965).
- (10) K. S. Dhami and J. B. Stothers, *Can. J. Chem.*, **43**, 498 (1965).
- (11) K. S. Dhami and J. B. Stothers, *Can. J. Chem.*, **43**, 510 (1965).
- (12) T. D. Alger, D. M. Grant, and E. G. Paul, *J. Am. Chem. Soc.*, **88**, 5397 (1966).
- (13) C. L. Wilkins and D. J. Thoennis, private communication.
- (14) I. C. Smith and W. G. Schneider, *Can. J. Chem.*, **39**, 1158 (1961).
- (15) T. Schaefer and W. G. Schneider, *Can. J. Chem.*, **41**, 966 (1963).
- (16) D. W. Beistel, H. E. Chen, and P. J. Fryatt, *J. Am. Chem. Soc.*, **95**, 5455 (1973).
- (17) D. W. Beistel and W. D. Edwards, *J. Am. Chem. Soc.*, to be submitted for publication.
- (18) T. C. Farrar and E. D. Becker, "Pulse and Fourier Transform NMR", Academic Press, New York, N.Y., 1971.
- (19) H. E. Chen, Ph.D. Thesis, University of Missouri—Rolla, June, 1972.
- (20) P. Lykos, *ACS Symp. Ser.*, **19**, Chapter 8 (1975).
- (21) H. S. Gutowsky, D. W. McCall, B. R. McGarvey, and L. H. Meyer, *J. Am. Chem. Soc.*, **74**, 4809 (1952).
- (22) R. W. Taft, *J. Am. Chem. Soc.*, **79**, 1045 (1957).
- (23) H. C. Beachell and D. W. Beistel, *Inorg. Chem.*, **3**, 102E (1964).
- (24) W. Kauzmann, "Quantum Chemistry", Academic Press, New York, N.Y., 1957, p 32.
- (25) I. S. Sokolnikoff and R. M. Redheffer, "Mathematics of Physics and Modern Engineering", McGraw-Hill, New York, N.Y., 1958, pp 175–178.
- (26) W. Band, "Introduction to Mathematical Physics", Van Nostrand, Princeton, N.J., 1959, pp 176–178.
- (27) E. D. Becker, "High Resolution NMR", Academic Press, New York, N.Y., 1969, pp 61, 62.

Sedimentation Coefficient and X-Ray Scattering of a Double-Helical Model for Deoxyribonucleic Acid

J. García de la Torre and Arturo Horta*

Departamento de Química Física, Facultad de Química, Universidad Complutense, Madrid-3, Spain (Received December 29, 1975)

Publication costs assisted by Fondo Nacional para el Desarrollo de la Investigación Científica, Spain

A double-helical model is proposed to calculate solution properties of short fragments ($10^4 < M < 10^6$) of linear, double-stranded DNA. The model, which is based on the Watson-Crick structure, replaces the nucleotides by touching spheres, in order to allow for the calculation of hydrodynamic properties. The radius of the helix acts as an adjustable parameter. Using this model, we calculate sedimentation coefficients and x-ray scattering intensities. Comparison with experimental x-ray diagrams shows that the model contains enough structural details to reproduce the data at low and at high scattering angles. The more idealized models (cylinder, etc.) fail to reproduce these diagrams. The results for sedimentation are compared with experimental data compiled for DNA samples of $M < 10^6$. The external radius of the helix, obtained from this comparison, is 15.0 Å, somewhat higher than the one predicted by a cylinder model.

I. Introduction

Idealized models, such as the freely jointed chain,¹ the wormlike chain,² the bead and spring model,^{3,4} etc., and several modifications of them, have been widely used to interpret macromolecular solution properties. These models represent, in an approximate way, the longitudinal contour of the macromolecular chain, but do not take into account its cross-sectional thickness. Substitution of the actual chain by an infinitely thin model is a particularly poor approximation in the case of DNA, because of the very complicated cross-sectional structure of this macromolecule. To get an improved representation of DNA, several finite-thickness models, having various geometries, have been proposed. The most frequently used geometries are the touching spheres model (TSM) and the cylinder model (CM).⁵ They represent macromolecular thickness by means of the cross-sectional radius of the model, which is considered as an adjustable parameter. However, values obtained for the radius, by comparison with experimental data, depend strongly on the theory used. The wide range of values summarized by Triebel et al.,⁶ for the hydrodynamic diameter of DNA, is evidence of this circumstance.

In all of these theories, the double helical shape of native DNA is substituted by a simpler shape. The values obtained for the radius vary with the theory, because, among other factors, the cross section is represented in them by different idealizations of the actual geometry. Of course, the most correct procedure would be to obtain the radius for the actual double-helical structure of DNA, without substituting it by a more idealized one. This is, precisely, the purpose of this work. We represent the DNA molecule by means of a double-helical model (DHM) whose features are detailed in section II.

Molecular weights, M , of intact DNA samples are too high for the details of the cross section to be relevant, and the simpler models are, therefore, adequate to describe the properties of these samples. However, there is an intermediate region of M ($10^4 < M < 10^6$) where the usual macromolecular solution properties (hydrodynamic, scattering, etc.) are still useful, and, at the same time, where the thickness to contour length becomes appreciable in the chain. In the present paper, we analyze the influence of the double-helical

structure on solution properties of DNA's belonging to this molecular region. Even in this interval, some properties are insensitive to the helical shape. For example, we have shown in a previous work⁷ that a double-helical model with elements having three different polarizabilities gives almost the same intensity of polarized scattered light as the much simpler model of an anisotropic rod with only two polarizabilities.

However there are, also, solution properties which are sensitive to the details of the cross-sectional structure. The sedimentation coefficient, S , can be cited as an example. Its experimental determination has been used to calculate the thickness of the DNA molecule. S is typical in giving different values for the radius, depending on the theoretical model used. For this reason, we emphasize here the applicability of our DHM to the interpretation of this property.

Because of the high stiffness of the double-stranded chain, DNA samples in the region $10^4 < M < 10^6$ exhibit a rigid or slightly bending configuration. The flexibility of the DNA chain is, thus, not the main problem in our work. For this reason, our DHM is rigid and makes use of the double helical structure of DNA.

In order to calculate S , we have to introduce some arbitrary assumption about the frictional elements constituting the chain, because present-day hydrodynamic theories do not allow for an atomic scale description of this property. According to these theories, each one of the frictional elements has to be regarded as an equivalent unit that encloses several atoms of the molecule and which interacts with a solvent continuum. In view of this limitation, we choose the nucleotides of the DNA molecule as frictional units and assume that they behave, hydrodynamically, like spheres. The DHM is, then, a double helix of touching spheres having as many spheres as there are nucleotides in the molecule.

In this model we leave only one adjustable parameter to be determined by comparison with sedimentation data: the radius of the helix. Some other dimensions of the double-stranded helix could be used as adjustable parameters if required (for example, the pitch). However, in the nonhelical models (TSM, CM)⁵ only the radius can be defined as a measure of the cross section. Therefore, this same quantity has to be used as parameter in our DHM, in order to arrive at a clear-cut comparison between the different models.

Substitution of nucleotides by spheres makes our model somewhat idealized. Before using it to analyze sedimentation data, we have to find out what degree of arbitrariness is introduced by it in the description of the DNA structure. To this end, in section III we use our model to interpret the results of a solution property which is much more sensitive to the structural details of the molecular cross section than S : the intensity of x-ray scattering (XS) for DNA in water.

Several authors have reported low angle x-ray scattering (LAXS) of DNA solutions.⁸⁻¹² This technique gives the cross-sectional radius of gyration of the molecule, but it yields no information about other structural details. Kirste and Oberthür¹³ and Bram and Beeman¹² using Cu $K\alpha$ radiation of 1.54 Å have recorded wide angle x-ray scattering diagrams (WAXS) of DNA solutions. For angles above 50 mradian, these diagrams show a region of maxima and minima which, as pointed out by these authors, originate in the periodicities of the helical structure. By comparing the theoretical XS behavior of our model with the experimental diagrams, in section III we prove that the structural details detected in XS are adequately described by the DHM. Hence, no arbitrariness is expected to vitiate its use to determine the cross-sectional hydrodynamic radius of the DNA molecule.

After this confirmation, we proceed, in section IV, to calculate the sedimentation coefficient of the DHM and to compare it with existing experimental results corresponding to DNA fragments. Kirkwood's formula^{14,15} is followed in the calculation of S . Although this formula has been criticized by several authors,¹⁶ Yamakawa et al.¹⁷⁻¹⁹ have shown that it is sufficiently correct when the molecules are rigid and highly symmetrical, such that they can be modeled as an array of beads. This should be the case with the DNA fragments.

II. Models for DNA

The DHM proposed in this work is represented in Figure 1. It has 20 spherical units per turn of double helix, and the pitch in each strand is taken as 34 Å. These are the values characterizing the B form of DNA, which is the one existing in aqueous solutions. The radius of the helix is A , and is taken as an adjustable parameter. Deviations with respect to the axially symmetric double helix arise from minute structural details, such as the different nature of the bases paired. These deviations are taken into account in the model by means of a phase-shift between strands, ψ , defined as shown in Figure 1.

Properties depending on inter-unit distances can be calculated from a knowledge of the Cartesian coordinates of the units. For the i th one, these are:

$$\begin{aligned}x_i &= A \cos(t_i + \omega) \\y_i &= A \sin(t_i + \omega) \\z_i &= (34/2\pi)t_i\end{aligned}\quad (1)$$

t_i being

$$t_i = 0.2\pi \text{int} [(i-1)/2] \quad i = 1, 2, \dots, N \quad (2)$$

where $\text{int}(\)$ means the integer part function and N is the total number of elements constituting the macromolecular chain. $\omega = 0$ in the odd-numbered helix and $\omega = \pi - \psi$ in the even-numbered one. The units are tangent spheres, with diameter d_e . The external or effective radius, r , of the DHM is, then, given by

$$r = A + d_e/2 \quad (3a)$$

with

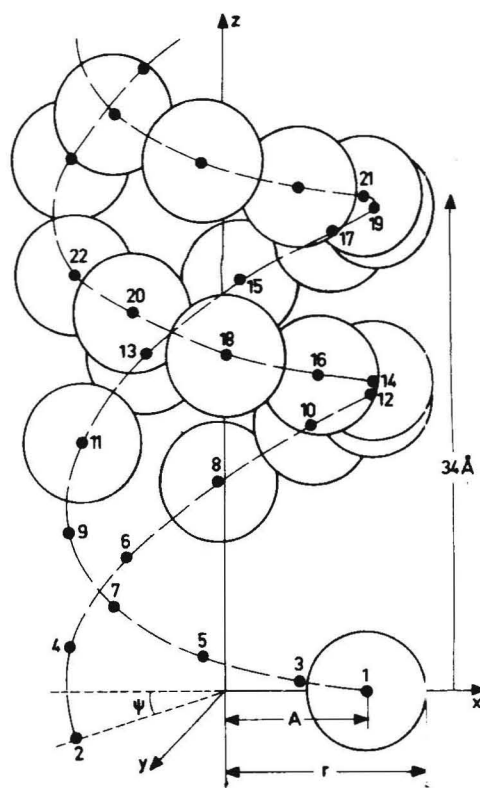


Figure 1. Double helical model (DHM) for DNA. The black circles (●) show the centers of the units. The numbering corresponds to the subscripts of eq 1 and 2 in the text. The position of the spherical units is shown on the upper part only.

$$d_e = \left[2 \left(1 - \cos \frac{\pi}{5} \right) A^2 + 3.4^2 \right]^{1/2} \quad (3b)$$

Besides the DHM, we are going to study, in detail, the two simpler models, which are of wider use for DNA: the TSM and the CM. The TSM is defined as a linear array of tangent spheres, and the CM as a continuous distribution of elements covering the surface (or the full volume) of a cylinder. In those models, the thickness parameter is the radius of the spheres (TSM) or the radius of the cylinder (CM), respectively. The equivalent counterpart of these radii, in our DHM, is r (eq 3).

The number of spherical units (in DHM and TSM), or the contour length, L (in CM), can be related to the molecular weight of the DNA fragments by means of M_L , the mass per unit length of the chain. X-ray scattering,^{8,12} light-scattering,^{20,21} and hydrodynamic studies²² give $M_L = 195$ dalton/Å for B-DNA. To represent the slight flexibility of the higher molecular weight fragments we are going to use, in section IV, the wormlike chain.² We assume that its corresponding stiffness parameter, the statistical segment length λ^{-1} , is close to $\lambda^{-1} = 1300$ Å for DNA.²¹⁻²⁶

III. X-Ray Scattering

The scattering form factor, P , expresses the intensity of radiation scattered by a molecular entity, as a function of angle, θ . It depends on the distances, r_{ij} , between pairs of scattering elements in the molecule through

$$P(\theta) = \sum_{i=1}^N \sum_{j=1}^N f_i(\theta) f_j(\theta) \frac{\sin hr_{ij}}{hr_{ij}} \bigg/ \sum_{i=1}^N \sum_{j=1}^N f_i(0) f_j(0) \quad (4)$$

Equation 4 applies to polyatomic molecules and to molecular

models as well. $f_i(\theta)$ are the scattering amplitudes of the atoms, or of the scattering elements, at angle θ , and h is

$$h = (4\pi/\lambda') \sin(\theta/2) \quad (5)$$

with λ' denoting wavelength. For a macromolecular chain, composed of identical elements, eq 4 may be rewritten as

$$P(\theta) = P_e(\theta)P_c(\theta) \quad (6)$$

where $P_e(\theta) = f^2(\theta)$, is the form factor of the elements, and $P_c(\theta)$ is the contribution of the chain configuration:

$$P_c(\theta) = \frac{1}{N^2} \sum_{i=1}^N \sum_{j=1}^N \frac{\sin hr_{ij}}{hr_{ij}} \quad (7)$$

In the case of the DHM, P_c can be obtained from eq 1 and 2, and P_e is the form factor of a sphere, given by

$$P_e(\theta) = [3(\sin u - u \cos u)/u^3]^2 \quad (8a)$$

with

$$u = hd_e/2 \quad (8b)$$

In the case of DNA, substitution of the actual P_e , corresponding to a nucleotide, by eq 8, valid for spheres, could be an oversimplification. For this reason, in XS we have developed two versions of the DHM: in the first one, we have used eq 8 for P_e , while, in the second one, we have calculated P_e in detail by using the atomic coordinates reported by Arnott et al.,^{27,28} for B-DNA, and the atomic scattering factors, $f_i(\theta)$ of Hanson et al.²⁹ The results are plotted in Figure 2; the insertion in this figure corresponds to the Guinier plot,³⁰ from which we obtain $R_{ge}^2 = 14.4 \text{ \AA}^2$, for the squared radius of gyration of the nucleotide. Throughout this calculation we have supposed the same probability for base pairs A-T and G-C. Deviations from equimolar composition affect the results very little.³¹

Equation 6 is also valid for the TSM. In such a model, P_c is given by

$$P_c(\theta) = N_e^{-1} + 2 N_e^{-2} \sum_{k=1}^{N_e-1} (N_e - k) \sin(2rkh)/(2rkh) \quad (9)$$

and P_e , again by eq 8. N_e is the number of elements (spheres) constituting the chain.

Mittelbach and Porod³² have studied XS by straight hollow cylinders in which the radial electronic density vanishes up to r_{inn} and is constant between r_{inn} and the external radius of the cylinder, r . Their equations are ($v = r_{inn}/r$):

$$P(\theta) = \int_0^{\pi/2} \left\{ \frac{1}{1-v^2} \frac{2}{hr \sin \alpha} [J_1(hr \sin \alpha) - v J_1(hrv \sin \alpha)] \right\}^2 \left[\frac{\sin(hL \cos \alpha/2)}{hL \cos \alpha/2} \right]^2 \sin \alpha \, d\alpha \quad (10)$$

for $v \neq 1$, and

$$P(\theta) = \int_0^{\pi/2} J_0^2(hr \sin \alpha) \left[\frac{\sin(hL \cos \alpha/2)}{hL \cos \alpha/2} \right]^2 \sin \alpha \, d\alpha \quad (11)$$

for $v = 1$. L is the contour length and J_0, J_1 , the Bessel functions of order 0 and 1, respectively.

Light scattering and x-ray scattering intensities have been calculated by Burchard and Kajiwara³³ for the TSM and by Koyama³⁴ for the CM. In both of these studies, attention was mainly focused on the characterization of chain stiffness, however, and not on molecular thickness.

(a) *Low Angle X-Ray Scattering*. Porod and Kratky^{35,36}

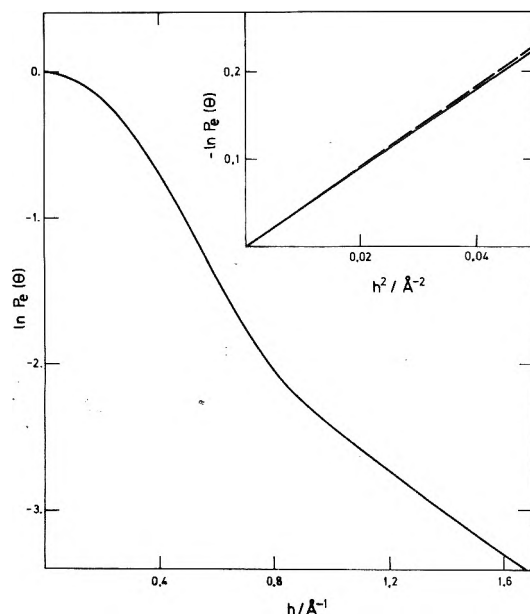


Figure 2. Form factor of a nucleotide, averaged over base composition. The insert is the low-angle Guinier plot, which gives 14.4 \AA^2 for the squared radius of gyration.

have shown that the cross-sectional radius of gyration, R_{gt} , of a long rodlike structure can be obtained from scattering data. R_{gt} is defined with respect to the macromolecular axis. In the range $R_{gt}^{-1} > h \gg L^{-1}$, $P(\theta)$ can be approximated by

$$\ln [hP(\theta)] = \ln I_0 - h^2 R_{gt}^2/2 \quad (12)$$

where I_0 is a constant, independent of chain configuration. Equation 12 has been applied by Kratky⁸ and by Luzzati et al.⁹⁻¹¹ to interpret LAXS of DNA. The results obtained by these authors, for R_{gt} , are close to the mean value $R_{gt} = 8.3 \text{ \AA}$.

For the theoretical models, R_{gt} can be written as a function of the adjustable parameter. In the case of a DHM composed of pointlike scattering units, R_{gt} would be equal to A . If the scattering units are represented as finite structures (spheres or actual nucleotides), then $R_{gt}^2 = A^2 + 3R_{ge}^2/2$, with R_{ge} being the radius of gyration of a unit. For nucleotides, $R_{ge}^2 = 14.4 \text{ \AA}^2$, as already stated. For spheres, $R_{ge}^2 = 3d_e^2/20$. R_{ge} does not depend on the phase shift, ψ , of the DHM.

For the hollow CM, R_{gt} is given by

$$R_{gt}^2 = \int_{r_{inn}}^r 2\pi t^3 dt / \int_{r_{inn}}^r 2\pi t dt = r^2(1+v^2)/2 \quad (13)$$

For the TSM, R_{gt} depends on the radius of the spheres, r , through $R_{gt}^2 = 2r^2/5$.

By comparison between these theoretical results of R_{gt} and the experimental value, we determine, for each model, the parameters used to characterize the thickness of the DNA molecule. The results thus obtained are shown in Table I. They will be discussed later on.

The experimental determination of R_{gt} , from $P(\theta)$, relies on the validity of the Porod and Kratky approximation,^{35,36} contained in eq 12. For the models here discussed, we have checked its range of validity by comparing eq 12 with the exact $P(\theta)$. Our results show that, for these rodlike models, when $L \approx 1500 \text{ \AA}$ and $r \approx 10 \text{ \AA}$, $\ln [hP(\theta)]$ is practically linear with h^2 , in the range $0.005 < h^2 (\text{\AA}^{-2}) < 0.04$. This is, approximately, the range defined by the values determined experimentally for R_{gt} in the case of DNA.⁸⁻¹¹

TABLE I: Parameters Obtained for the Different DNA Models by Comparison with X-Ray Scattering Data

Model	Wide angle		ψ
	Low angle $r, \text{\AA}$	$r, \text{\AA}$	
TSM	13.1	7.9	
CM			
$\nu = 0$	11.7	10.0	
0.3	11.2	9.2	
0.5	10.5	8.3	
1.0	8.3	6.4	
DHM			
Spherical elements	10.6 ($A = 7.7$)	10.4 ($A = 7.5$)	60°
Nucleotides	10.6 ($A = 7.7$)	11.0 ($A = 8.0$)	58°

(b) *Wide Angle X-Ray Scattering.* Kirste and Oberthür¹³ and Bram and Beeman¹² found that the XS diagrams of DNA show a series of maxima and minima for $h > 0.30 \text{\AA}^{-1}$. They are due to the periodicities of the double helix. The first minimum of intensity occurs at $h = 0.38 \text{\AA}^{-1}$ and is attributed to interference within a given transversal plane of the molecule. The following maxima and minima, occurring at higher h , correspond to interference between different planes. Bram and Beeman found four minima and three maxima (Figure 3 in ref 12). Their diagram is more detailed than the one reported by Kirste and Oberthür. In both papers the h values of the first maxima and minima are very similar.

By comparison of these maxima and minima with the theoretical $P(\theta)$ of the models we determine the values of the adjustable parameters in this region of WAXS.

The behavior predicted by the TSM shows the poorest agreement with experiment, as expected. In this model, $P_e(\theta)$ (eq 8) overshadows $P_c(\theta)$ (eq 9) and the behavior is almost entirely that of a sphere. The CM allows for a better representation of the diagrams. In this model, the minimum at $h = 0.38 \text{\AA}^{-1}$ can be reproduced using several pairs of values of the two parameters r and ν . In Figure 3 we show several $P(\theta)$'s having a minimum at 0.38\AA^{-1} and corresponding to different values of ν . It can be seen that the other maxima and minima are better reproduced when $\nu = 0$ (thick cylinder) than when $\nu \neq 0$.

In the case of the DHM, the intensity of XS at wide angles depends on N , A , and ψ . For given A and ψ , we have calculated $P(\theta)$ at various N between 20 and 1000. From the results obtained we may conclude that the location of the maxima and minima is independent of N (this also occurs in the CM when L is varied). This confirms that the short distances of the cross-sectional structure are the ones determining these maxima and minima.

The scattering units of the DHM cannot be considered as pointlike centers because the $P(\theta)$ calculated under this assumption is in conflict with the experimental diagram. With pointlike scatterers the only contribution to $P(\theta)$ comes from the helical structure (eq 7) and this tends asymptotically to $1/N$, for sufficiently high h . The experimental intensity, on the other hand, decreases monotonously as h grows. This problem is resolved introducing the form factor of the units, P_e . The location of some maxima and minima depends, very slightly, on the units being represented by spheres or by the actual nucleotides, because $P_e(\theta)$ has a different gradient in each case. The first minimum at 0.38\AA^{-1} is not changed, however.

The results obtained with the DHM, using spheres as scattering units, are shown in Figure 4. $P(\theta)$ is plotted for

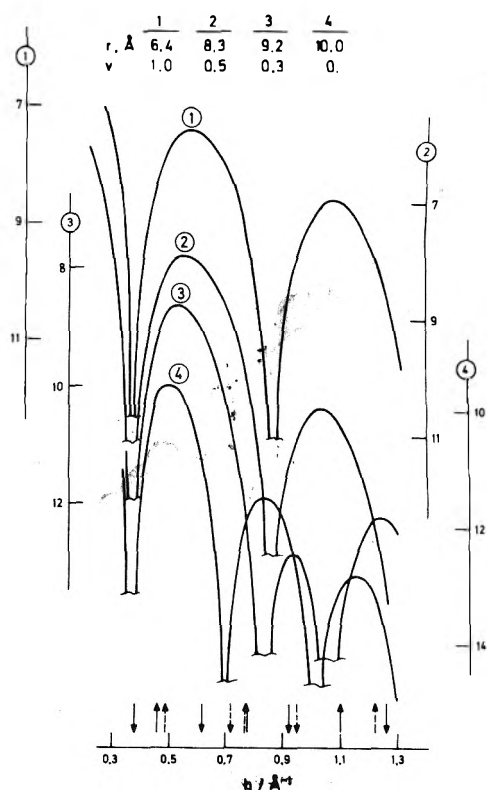


Figure 3. Form factor for cylinders with $L = 1500 \text{\AA}$. The vertical axis is $-\ln P(\theta)$. The parameters for each curve are indicated. Arrows pointing up and down show the location of the experimental maxima and minima, respectively; continuous arrows are for the Bram and Beeman's data,¹² and discontinuous ones, for Kirste and Oberthür's data.¹³

several values of A and ψ producing the first minimum at 0.38\AA^{-1} . The results obtained using the actual nucleotides as scattering units, are very similar to the ones shown in the figure.

A summary of the model-fitting results obtained in the two angular regions studied (LAXS and WAXS) is given in Table I. It can be seen that the two versions of the DHM (spheres or actual nucleotides) yield very similar results for the radius in both angular regions. In WAXS, the values of the adjustable parameters of the CM and of the DHM are chosen to reproduce the position of the first minimum and of the first maximum. The relative intensities of these two extrema agree well with the experimental ones only in the case of the DHM.

IV. Sedimentation Coefficient

(a) *Calculation.* The sedimentation coefficient of a macromolecule can be calculated according to the well-known Kirkwood¹⁵ equation:

$$S = \frac{M_0(1 - \bar{\nu}\rho)}{3\pi\eta_0\beta} \left[1 + \frac{\beta}{2N} \sum_{i=1}^N \sum_{\substack{j=1 \\ i \neq j}}^N \langle r_{ij}^{-1} \rangle \right] \quad (14)$$

where $\bar{\nu}$ is the macromolecular partial specific volume, ρ the solution density, η_0 the solvent viscosity, M_0 the molecular weight of the frictional units, and β their Stokes diameter. r_{ij} denotes the distance between frictional units i and j , and the angular brackets denote configurational average. For a rigid structure only one configuration exists.

Equation 14 applied to the TSM gives, when $L \gg r$

$$S_r = \frac{M_L(1 - \bar{\nu}\rho)}{3\pi\eta_0} \left[\ln \left(\frac{L}{2r} \right) + C_E \right] \quad (15)$$

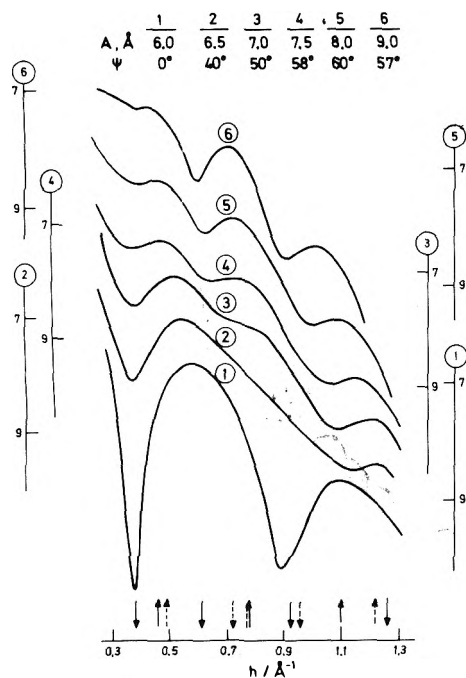


Figure 4. Form factor of the DHM with spherical units. The curves correspond to the values indicated for the parameters. The meaning of the vertical axis and of the arrows is the same as in Figure 3.

C_E being Euler's constant. In this equation and in the following ones, the subscript r denotes that S corresponds to a rigid model.

For B-DNA in 0.2 M NaCl solution, $\bar{v}\rho = 0.556$ and $\eta_0 = 0.01$ P, so that $M_L(1 - \bar{v}\rho)/3\pi\eta_0 = 1.525$ S. Replacing L by M , in eq 15 ($M = LM_L$), we finally obtain

$$S_r = 1.525 \ln M - a \quad (16)$$

$$a = 1.525 \ln r + Q \quad (17)$$

Q being a constant. If the double sum of eq 14 is approximated by a continuous integral, following Riseman and Kirkwood's^{37,38} procedure, then C_E vanishes in eq 15. The value of Q varies from one version of the TSM to the other.

In the CM, a continuous distribution of frictional elements covers uniformly the surface of the cylinder. When $L \gg r$, eq 16 and 17 are also valid for this model. There are several versions of it. The first one, due to Burgers,³⁹ was refined by Broersma⁴⁰ who treated end effects more rigorously. Bloomfield et al.⁴¹ have applied their shell model to the cylindrical shape. The most recent version of the CM is that of Yamakawa and Fujii.²⁶ Also, the model of Tchen⁴² is included here because the cylinder can be considered as a limiting case of a prolate ellipsoid. The values of Q , corresponding to each of these theories, are collected in Table II.

In our DHM, each nucleotide constitutes a frictional unit. Its Stokes diameter is taken equal to the sphere diameter of eq 3 ($\beta = d_e$). The increase in contour length per unit is 1.7 Å in DNA. Applying eq 14 to the DHM of DNA reads:

$$S_r = \frac{1.7M_L(1 - \bar{v}\rho)}{3\pi\eta_0 d_e} \left[1 + \frac{d_e}{2N} \sum_{i=1}^N \sum_{j=1}^N r_{ij}^{-1} \right] \quad (18)$$

where the r_{ij} 's are easily calculated from eq 1 and 2.

We have computed eq 18, extending the sums up to $N = 1000$, for various A , from 6 to 16 Å, and various ψ , from 0 to 90°. Some of the values thus obtained for S_r are plotted, vs. $\ln M$, in Figure 5. All the curves show the same trend, reaching

TABLE II: Values of the Constant Q (Eq 16) and of the Cross-Sectional Parameters Fitted for the Models

Theory	Ref	Model	Q , S	r , Å
Tchen	42	Ellipsoid	8.046	16.3
Burgers	39	CM	8.214	14.6
Kirkwood ^a	15	TSM	8.218	14.5
Bloomfield et al.	41	CM	8.501	12.1
Yamakawa-Fujii	26	CM	8.509	12.0
Broersma	40	CM	8.519	11.9
Riseman-Kirkwood	37, 38	TSM	9.098	8.2
This work		DHM	15.0 ($A = 11.2$)	$\frac{11.2}{\psi^*}$

^a Values calculated by exact summation (eq 14) of Kirkwood's formula.

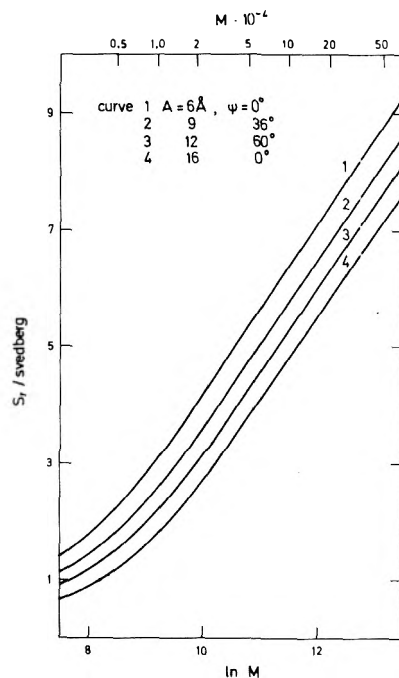


Figure 5. Sedimentation coefficient of the DHM, computed according to eq 1, 2, and 18.

a region where S_r varies linearly with $\ln M$, at high enough M . The slope and intercept of this asymptotically valid linear law can be obtained by extrapolation to $1/M \rightarrow 0$. The values extrapolated for the slope lie in the range 1.525–1.529. The fluctuations are very likely due to numerical inaccuracy. The slope of S_r vs. $\ln M$ has, then, the same value in the DHM as in the TSM and the CM. In other words, eq 16 holds also for the DHM.

Some of the extrapolations ($1/M \rightarrow 0$) which lead to the intercept, $-a$, of eq 16, are plotted in Figure 6. A least-squares fit with a second degree polynomial has been used to help in this extrapolation. Its accuracy has been checked by superimposing on the extrapolation curves the values calculated for $N = 2000$ (full circles of Figure 6). The resulting asymptotic values of a are collected in Table III. They show a much slower variation with ψ than with A . In view of this circumstance, we have discarded ψ as variable, in computing S_r , and have fixed its value at $\psi = 0^\circ$, corresponding to the axially symmetric double helix.

Figure 7 shows the variation of a with the cross-sectional radius ($\ln r$) for all the theories described above. In the case

TABLE III: Values of a , the Asymptotic Intercept of Eq 16, for the DHM

$A, \text{\AA}$	$\psi = 0^\circ$	36°	60°	72°	90°
6	11.28	11.25	11.22	11.15	11.11
7	11.52	11.50	11.46	11.40	11.37
8	11.74	11.71	11.67	11.63	11.59
9	11.94	11.91	11.87	11.83	11.80
10	12.12	12.10	12.07	12.03	11.99
11	12.28	12.26	12.23	12.20	12.16
12	12.42	12.40	12.37	12.34	12.31
13	12.55	12.54	12.51	12.48	12.45
14	12.67	12.66	12.64	12.60	12.58
16	12.88	12.87			

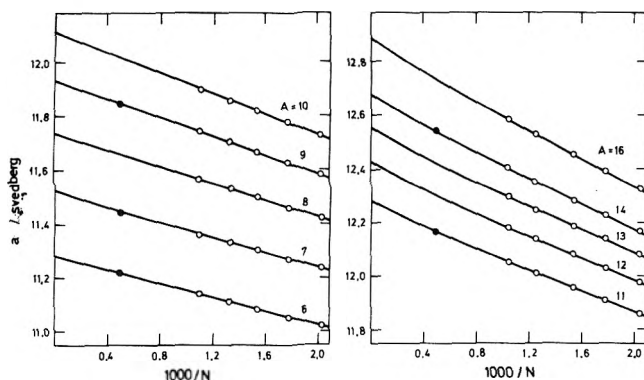


Figure 6. Extrapolations of the asymptotic intercept of S vs. $\ln M$, calculated with the DHM ($\psi = 0^\circ$). Open circles (O) correspond to discrete values below $N = 1000$. Continuous line is the extrapolating second-degree polynomial. Black circles (●) correspond to $N = 2000$ and have been superimposed to check the accuracy of the extrapolations.

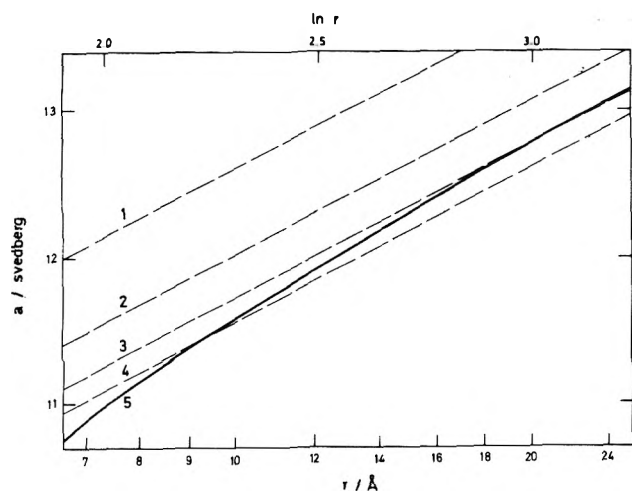


Figure 7. Asymptotic intercept of S vs. $\ln M$ for different theories: (1) Riseman-Kirkwood;^{37,38} (2) Yamakawa-Fujii,²⁶ Broersma,⁴⁰ and Bloomfield et al.;⁴¹ (3) Burgers³⁹ and Kirkwood¹⁵ (see footnote of Table II); (4) Tchen;⁴² (5) DHM (this work).

of the theories using the TSM or the CM, the curves correspond to eq 17, and, in the case of the DHM, to the data in column $\psi = 0^\circ$ of Table III. We can see from this plot that the DHM does not follow eq 17, presumably because the Stokes diameter of the units composing the model depend on the helical radius, A .

(b) *Comparison with Experimental Data.* The experimental values of S and M used to compare theory and ex-

periment are the ones reported in the literature⁴³⁻⁵⁰ for DNA fragments, in the range considered in our study. Values reported prior to 1965 have been reviewed by Eigner and Doty.⁵¹ The data attributed to Prunell and Bernardi represent the tabulation of their empirical equation⁴⁹ $S = 0.1345 M^{0.320}$, valid for $M = 2 \times 10^4 - 3 \times 10^5$.

For molecular weights above $M \simeq 2.5 \times 10^5$, the DNA molecule deviates from a perfect rodlike configuration and the influence of chain flexibility becomes important. Hearst and Stockmayer⁵² have used the TSM and Yamakawa and Fujii²⁶ the CM to calculate sedimentation coefficients of semiflexible macromolecules. The equations given in these two theories can be written in the form

$$S = S_r + S_c \quad (19)$$

where S_r represents the rodlike limit of S , defined as

$$S_r = \lim_{\lambda^{-1} \rightarrow \infty} S \quad (20)$$

and S_c is the correction arising from chain flexibility. S_c depends on r . In the limit $r \rightarrow 0$, both theories predict

$$S_c = \frac{M_L(1 - \bar{v}\rho)}{3\pi\eta_0} [c_1\lambda L + c_2(\lambda L)^2 + c_3(\lambda L)^3] \quad (21)$$

The coefficients are $c_1 = 0.166$, $c_2 = 0.020$, $c_3 = -0.002$, in the theory of Hearst and Stockmayer, and $c_1 = 0.167$, $c_2 = 0.019$, $c_3 = -0.002$, in the theory of Yamakawa and Fujii.

For nonvanishing r , the dependence of S_c on r has a different form in the two theories mentioned. However, for the values of λ^{-1} , L , and r , characteristic of low molecular weight DNA, we have found that the values calculated for S_c according to the theories of Hearst and Stockmayer and Yamakawa and Fujii differ from those calculated according to eq 21 (with either set of coefficients) by less than 0.1 S . Therefore, we may conclude that the flexibility correction is, in our case, practically independent of the cross-sectional structure. This implies that, for DNA samples below $M \simeq 10^6$, we may combine eq 16, 19, and 21, to evaluate the S corresponding to the TSM, CM, and DHM.

As a first step in our analysis of the experimental data we subtract, from each empirical value of S , the flexibility correction, S_c , corresponding to its molecular weight (eq 21). The resulting $S - S_c$ values are plotted in Figure 8. These $S - S_c$ values are fitted to eq 16 by a least-squares procedure. The two points with $\ln M < 10.5$ have not been considered in this fit because, for them, r/L has a relatively large value and eq 16 may be not obeyed.

The result obtained for a by this method is $a = 12.31 S$ (see Figure 8). With this experimental value of a we enter in Figure 7 and determine, by interpolation, the value of r corresponding to each model. The r values thus obtained are collected in Table II.

V. Discussion

The first conclusion we may draw from the analysis of x-ray diagrams, carried out on section III, is that our DHM allows for an accurate description of the experimental results, while the nonhelical models lead to a much poorer description of the XS data. The most important advantage of our model, with respect to the nonhelical ones, is its ability to determine the cross-sectional radius of the molecule. The values deduced for r from LAXS and from WAXS are concordant in the case of the DHM, but they are not in the case of the other models. The results summarized in Table I evidence that the nonhelical models do not determine a unique radius, since the value ob-

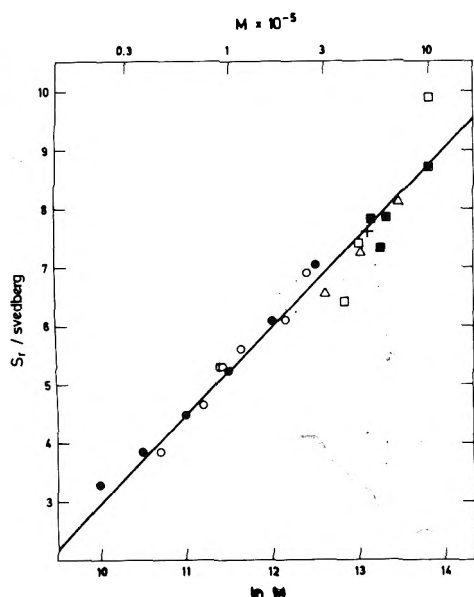


Figure 8. Values of S_r for DNA samples below 10^6 daltons. Experimental data are from: Doty et al.⁴³ (Δ), Watanabe et al.^{44,45} (\blacksquare), Pivec et al.⁴⁶ (\square), Eisenberg-Cohen^{47,48} (+), Prunell-Bernardi⁴⁹ (\bullet), and Record et al.⁵ (O). The line represents the least-squares fit: $S_r = 1.525 \ln M - 12.31$.

tained for this quantity depends on the angular region considered. This ambiguity is resolved by using the DHM.

In addition to this, the DHM is capable of detecting the lack of axial symmetry of the DNA molecule. This is seen in Figures 3 and 4. In Figure 3 the minima for the CM (having C_∞ symmetry) are extremely deep. In Figure 4 the minima for the DHM are more pronounced when $\psi = 0^\circ$ than when $\psi \neq 0^\circ$. Since the observed minima are shallow, we may conclude that they reflect a lack of axial symmetry in the molecule (due to the nonsymmetric position of the paired bases). This justifies our introduction of a phase shift in the DHM. It also proves that the WAXS region contains information about the molecular structure which is not present in the LAXS region.

The parameter ψ can be regarded as meaningful at the molecular level, because the phase shift between helices is in qualitative agreement with the shape usually attributed to the B form of DNA. According to such a shape, the DNA-B molecule has wide and narrow grooves with approximate widths of 20 and 14 Å, respectively.⁵³ When we use our DHM to calculate the grooves corresponding to $\psi = 58^\circ$ (value taken from Table I), we get 22.5 and 11.5 Å, respectively. The agreement is, thus, not quantitative. The discrepancy may arise from the inaccuracies associated with the fit of the WAXS diagrams, as well as from the model itself.

The second important conclusion obtained from the analysis of XS is that the two versions of our DHM (spheres and actual nucleotides) lead to practically identical values of A and ψ (Table I). This implies that the version which uses spheres as units of the macromolecular chain (the one that is useful to calculate hydrodynamic properties) constitutes a good approximation to the actual structure of DNA in solution. In view of this result, we may be confident that the interpretation of S by means of the DHM, contained on section IV, should be essentially correct. The value obtained with this model for the radius can be regarded as more realistic than the values obtained with the other models, since the DHM may be regarded as less idealized than the nonhelical ones.

Comparison between the values contained in Tables I and II indicates that the radius deduced from sedimentation is

considerably larger than the radius deduced from XS in all models studied. This result has to be attributed to the existence of a hydration shell covering the DNA molecule in solution. Frictional forces between solvent and macromolecule act on the surface of this hydration shell and determine, for the radius, a value somewhat larger than the one corresponding to the naked molecule. The DNA structure corresponds, approximately, to $r \approx 10$ Å, the distance from the phosphate group to the molecular axis. The contribution of the hydration shell to XS intensities is weak compared to the one arising from the macromolecule itself. Therefore, the value detected in XS for r should be about 10 Å. With the DHM we obtain $r = 10.4$ – 10.6 Å, close to it.

By comparing this value with the one obtained (with the same model) for the hydrodynamic radius, $r = 15.0$ Å, we estimate a thickness of 4.5 Å for the hydration shell. This corresponds to the fixation of about two or three layers of water.^{54–56} It can be argued against this result that the DHM is a porous structure that permits the solvent to pass through the double chains. The large hydrodynamic radius obtained ($r = 15$ Å) should then be attributed not entirely to hydration. According to this criticism, a better estimate of hydration would be to combine the radius obtained from XS using our DHM and the hydrodynamic radius obtained using the less porous CM ($r = 12.0$ Å). The hydration shell estimated in such a way is 1.5 Å, which corresponds to about a monolayer of water. However, the porosity of the DHM is mainly geometric and its influence on the sedimentation coefficient might be quite small. We base our speculation on the idea that hydrodynamic interaction is strong in the interior of the double chains and should block very effectively the passage of solvent through them.

We have obtained the value of r by analyzing experimental data corresponding to the molecular weight region $M = 2 \times 10^4$ – 1×10^6 (Figure 8). The nonlinearity of S vs. $\ln M$ has been attributed to chain flexibility. For the values of r and L in this region, we have seen that the flexibility correction does not depend on the model chosen to represent the cross-sectional structure. Namely, Yamakawa and Fujii's theory (wormlike CM) and Hearst and Stockmayer's theory (wormlike TSM) yield similar results. Therefore, it is not necessary to include chain flexibility rigorously in the DHM.

In a recent paper, Record et al.⁵⁰ have studied low molecular weight DNA in a region similar to the one here considered by us. They show that a single set of chain parameters, λ^{-1} and r , are good to describe sedimentation coefficients for both high ($M > 10^6$) and low ($M < 10^6$) molecular weights. They use Yamakawa and Fujii's theory and find $\lambda^{-1} = 1300$ Å, $r = 12.5$ Å. The value of r obtained by us, using the CM model (Yamakawa and Fujii's theory) and the same λ^{-1} , is $r = 12.0$ Å very close to the one obtained by Record et al. Our result for the CM agrees, then, with the conclusion drawn by these authors. Furthermore, our result for the TSM agrees with it. We have obtained $r = 14.8$ Å, for the TSM (Kirkwood's theory), which lies intermediate between the values derived by Hearst and Stockmayer⁵² and by Gray et al.,⁵⁷ in the high M region.

Acknowledgment. We are grateful to Professor Victor A. Bloomfield and to the Journal reviewers for very helpful comments on the original manuscript. J.G.T. acknowledges the award of a Fellowship by the Ministerio de Educación y Ciencia.

References and Notes

- (1) P. J. Flory, "Statistical Mechanics of Chain Molecules", Interscience, New York, N.Y., 1969, pp 16–19, 313–325.

- (2) O. Kratky and G. Porod, *Recl. Trav. Chim. Pays-Bas*, **68**, 1106 (1949).
 (3) P. E. Rouse, *J. Chem. Phys.*, **21**, 1272 (1953).
 (4) B. H. Zimm, *J. Chem. Phys.*, **24**, 269 (1956).
 (5) A recent discussion of TSM and CM geometries applied to DNA may be found in ref 26.
 (6) H. Triebel, K. E. Reinert, and J. Strassburger, *Biopolymers*, **10**, 2619 (1971).
 (7) J. Garcia de la Torre and A. Horta, to be submitted for publication.
 (8) O. Kratky, *Prog. Biophys. Mol. Biol.*, **13**, 107 (1963).
 (9) V. Luzzati, A. Nicolaieff, and F. Masson, *J. Mol. Biol.*, **3**, 185 (1961).
 (10) V. Luzzati, D. Luzzati, and F. Masson, *J. Mol. Biol.*, **5**, 365 (1962).
 (11) V. Luzzati, F. Masson, A. Mathis, and P. Saludjian, *Biopolymers*, **5**, 491 (1967).
 (12) S. Bram and W. W. Beeman, *J. Mol. Biol.*, **55**, 311 (1971).
 (13) R. G. Kirste and R. C. Oberthür, *Makromol. Chem.*, **127**, 301 (1969).
 (14) J. G. Kirkwood, *Recl. Trav. Chim. Pays-Bas*, **68**, 649 (1949).
 (15) J. G. Kirkwood, *J. Polym. Sci.*, **12**, 1 (1954).
 (16) R. Zwanzig, J. Keifer, and G. H. Weiss, *Proc. Natl. Acad. Sci. U.S.A.*, **60**, 381 (1968).
 (17) H. Yamakawa and G. Tanaka, *J. Chem. Phys.*, **57**, 1537 (1972).
 (18) H. Yamakawa and J. Yamaki, *J. Chem. Phys.*, **57**, 1542 (1972).
 (19) H. Yamakawa and J. Yamaki, *J. Chem. Phys.*, **58**, 2049 (1973).
 (20) Y. Mauss, J. Chambron, M. Daune, and H. Benoit, *J. Mol. Biol.*, **27**, 579 (1967).
 (21) H. Yamakawa and M. Fujii, *Macromolecules*, **7**, 649 (1974).
 (22) H. Yamakawa and M. Fujii, *Macromolecules*, **7**, 128 (1974).
 (23) C. W. Schmid, F. P. Rinehart, and J. E. Hearst, *Biopolymers*, **10**, 883 (1971).
 (24) J. Garcia de la Torre, J. J. Freire, and A. Horta, *Biopolymers*, **14**, 1327 (1975).
 (25) J. B. Hays, M. E. Magar, and B. H. Zimm, *Biopolymers*, **8**, 531 (1969).
 (26) H. Yamakawa and M. Fujii, *Macromolecules*, **6**, 407 (1973).
 (27) S. Arnott, S. D. Dover, and A. J. Wonacott, *Acta Crystallogr., Sect. B*, **25**, 2192 (1969).
 (28) S. Arnott, *Prog. Biophys. Mol. Biol.*, **22**, 179 (1971).
 (29) H. P. Hanson, F. Herman, J. D. Lea, and S. Skillman, *Acta Crystallogr.*, **17**, 1040 (1964).
 (30) A. Guinier, *Ann. Phys.*, **12**, 161 (1930).
 (31) J. Garcia de la Torre, Ph.D. Thesis, Madrid, 1975.
 (32) P. Mittelbach and G. Porod, *Acta Phys. Austriaca*, **14**, 405 (1961).
 (33) W. Burchard and K. Kajiwara, *Proc. R. Soc. London, Ser. A*, **316**, 185 (1970).
 (34) R. Koyama, *J. Phys. Soc. Jpn.*, **36**, 1409 (1974).
 (35) G. Porod, *Acta Phys. Austriaca*, **2**, 255 (1948).
 (36) O. Kratky and G. Porod, *Acta Phys. Austriaca*, **2**, 133 (1948).
 (37) J. Riseman and J. G. Kirkwood, *J. Chem. Phys.*, **18**, 512 (1950).
 (38) J. Riseman and J. G. Kirkwood, "Rheology", Academic Press, New York, N.Y., 1956, p 495.
 (39) J. M. Burgers, "Second Report on Viscosity and Plasticity of the Amsterdam Academy of Sciences", Nordemann, New York, N.Y., 1938, Chapter 3.
 (40) S. Broersma, *J. Chem. Phys.*, **32**, 1632 (1960).
 (41) V. A. Bloomfield, W. O. Dalton, and K. E. Van Holde, *Biopolymers*, **5**, 135 (1967).
 (42) C. M. Tchen, *J. Appl. Phys.*, **25**, 463 (1954).
 (43) P. Doty, B. McGill, and S. A. Rice, *Proc. Natl. Acad. Sci. U.S.A.*, **44**, 432 (1958).
 (44) K. Kawade and I. Watanabe, *Biochim. Biophys. Acta*, **19**, 513 (1956).
 (45) K. Iso and I. Watanabe, *Nippon Kagaku Zasshi*, **78**, 1268 (1957).
 (46) L. Pivec, S. Zadrazil, J. Sponar, and Z. Sormova, *Collect. Czech. Chem. Commun.*, **30**, 3928 (1965).
 (47) G. Cohen and H. Eisenberg, *Biopolymers*, **8**, 45 (1969).
 (48) H. Eisenberg, *Biopolymers*, **8**, 545 (1969).
 (49) A. Prunell and G. Bernardi, *J. Biol. Chem.*, **248**, 3433 (1973).
 (50) M. T. Record, C. P. Woodbury, and R. B. Inman, *Biopolymers*, **14**, 393 (1975).
 (51) J. Eigner and P. Doty, *J. Mol. Biol.*, **12**, 549 (1965).
 (52) J. E. Hearst and W. H. Stockmayer, *J. Chem. Phys.*, **37**, 1425 (1962).
 (53) K. C. Holmes and D. M. Blow, "The Use of X-Ray Diffraction in the Study of Proteins and Nucleic Acid Structures", Wiley, New York, N.Y., 1965.
 (54) P. Sharp and V. A. Bloomfield, *J. Chem. Phys.*, **48**, 2149 (1968).
 (55) V. A. Bloomfield, *Macromol. Rev.*, **3**, 225 (1968).
 (56) M. B. Tunis and J. E. Hearst, *Biopolymers*, **6**, 1325 (1968).
 (57) H. B. Gray, V. A. Bloomfield, and J. E. Hearst, *Biopolymers*, **14**, 393 (1975).

A Peroxy Isomer of Nitrogen Dioxide¹

H. F. Schaefer, III,

University of California at Berkeley, Department of Chemistry, Berkeley, California 94720

C. F. Bender, and J. H. Richardson*

University of California, Lawrence Livermore Laboratory, Livermore, California 94550 (Received April 9, 1976)

Publication costs assisted by the University of California

Ab initio SCF calculations on the relative stability of a peroxy isomer of NO₂, compared with the normal C_{2v} isomer, coupled with the experimental bond strength in the normal isomer suggest that a peroxy isomer is stable. Implications to photodetachment experiments are discussed.

Recent photodetachment experiments have demonstrated the existence of an anomalous nitrite ion.² Photodetachment of an electron from NO₂⁻ was observed to occur at energies significantly less than the electron affinity of NO₂. Three possible explanations were suggested for this unexpected observation:

(1) The "normal" C_{2v} isomer of NO₂⁻ (\tilde{X}^1A_1) might have been vibrationally excited. Photodetachment at wavelengths greater than the adiabatic electron affinity would then be expected, similar to the appearance of hot bands in conventional absorption spectroscopy. This explanation was eliminated because there is no evidence to suggest that a sufficiently high vibrational temperature (5000 K) was present in either of the apparatus used to generate nitrite ions.

(2) An excited metastable triplet state of NO₂⁻. The lowest reported³ triplet state of NO₂⁻ (3B_1) is at best marginally stable with respect to autodetachment to NO₂ + e⁻.^{2a} Furthermore, it is unlikely that such a metastable species could be produced copiously from a hot cathode plasma ion source^{2b} or be contained in an ion cyclotron resonance cell for several seconds.^{2a}

(3) A peroxy isomer of NO₂⁻. Such an ion would be structurally similar and isoelectronic to NO₃.⁴ Furthermore, its photodetachment spectrum might be expected to be similar to a perturbed oxygen ion, which is consistent with the threshold and cross section near threshold. Finally, an anomalous, energetic form of NO₂⁻ was observed in cluster ion reactions of NO; similar reactions with NO₂ resulted in the

TABLE I: Geometries and Energies for C_{2v} and Peroxy Isomers of NO_2^- and NO_2^a

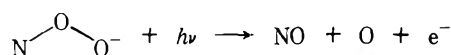
Property	NO_2				
	C_{2v}	Peroxy		NO_2^-	
		I^2A'	I^2A''	C_{2v}	Peroxy
$r(\text{N-O})$	1.20	1.16	1.23	1.264	1.245
$r(\text{O-O})$		1.90	1.49		1.493
θ , deg	135	122	115	117.0	118.5
E , hartrees	-203.9474	-203.8820	-203.8563	-204.0336	-203.9161
E , eV	0.0	1.78	2.48	0.0	3.20

^a Bond distances are in Å. Data for NO_2^- is taken from ref 6.

formation of a peroxy nitrate ion,⁵ and it is suggested that the anomalous form of NO_2^- was also a peroxy isomer.

To further substantiate the existence of a peroxy isomer of NO_2^- , ab initio SCF calculations were performed⁶ (the results of these calculations are reproduced in Table I). A peroxy form of NO_2^- was found to have a well-defined minimum in the potential energy surface. Symmetry restrictions and energy limitations prohibit interconversion of the peroxy isomer to the normal C_{2v} isomer via a ring intermediate. This prediction is also consistent with the experimental observation of two distinct, apparently noninterconverting ions of m/e 46.

Photodetachment of an electron generally does not result in subsequent dissociation; hence, photodetachment of the peroxy isomer of NO_2^- might be expected to result in formation of a peroxy isomer of NO_2 . It has been suggested² that in this case the photodetachment process results in dissociation, i.e.



Consequently, to investigate this hypothesis, a theoretical study of the relative stability of the peroxy isomer of NO_2 was undertaken. Further motivation was provided by the paramount importance of the presence and chemistry of nitrogen oxides in the atmosphere. While obviously not a major, long-lived species, the presence of a peroxy isomer of NO_2 in trace amounts or as an energetic intermediate would have major significance in atmospheric chemical reaction mechanisms and modeling.⁷ This paper presents the results of ab initio self-consistent-field calculations of a peroxy isomer of NO_2 .

Atom-optimized primitive Gaussian basis sets⁸ of size (9s 5p) were centered on the N and O nuclei. This primitive basis set was contracted to (4s 2p), providing a double ζ quality basis set.⁹

The peroxy isomer of NO_2 has only a plane of symmetry (point group C_s). The following configurations were investigated:

$$1a'^2 2a'^2 3a'^2 4a'^2 5a'^2 6a'^2 7a'^2 8a'^2 1a''^2 9a''^2 2a''^2 10a' \quad (I^2A')$$

$$1a'^2 2a'^2 3a'^2 4a'^2 5a'^2 6a'^2 7a'^2 8a'^2 1a''^2 9a''^2 2a''^2 10a'^2 \quad (II^2A'')$$

$$1a'^2 2a'^2 3a'^2 4a'^2 5a'^2 6a'^2 7a'^2 8a'^2 1a''^2 9a''^2 2a''^2 3a'' \quad (III^2A'')$$

$$1a'^2 2a'^2 3a'^2 4a'^2 5a'^2 6a'^2 7a'^2 8a'^2 1a''^2 9a''^2 2a''^2 10a' 11a' \quad (IV'')$$

This first configuration, I^2A' , corresponding to the most stable bound state, was observed to have a rather shallow minimum with respect to the O-O bond length (the N-O bond length is very similar to that of NO (1.151 Å)¹⁰). The depth of this well, ca. 0.008 hartree or 1700 cm^{-1} , is insufficient to prevent the molecule from dissociating at room temperature. However, this well depth can be estimated more reliably from semiempirical considerations (vide infra).

The second configuration studied, II^2A'' , corresponds to promotion of an electron from the π to σ framework. This configuration appears very tightly bound, presumably because it cannot dissociate in the single configuration approximation to ground state NO + O. It is interesting to note that the geometry of this configuration is very similar to that of the peroxy ion (Table I). The last two configurations studied did not exhibit any minimum with respect to the O-O bond length; each had an angular minimum corresponding to a linear geometry.

Simple SCF calculations do not reliably predict dissociation energies due to the restriction of having doubly occupied orbitals.¹¹ The results for the C_{2v} isomer are also included in Table I, and agree with similar calculations¹² done at the experimental geometry. Other basis sets and contraction schemes, including the use of polarization functions (d orbitals), have also been used and compared.^{12,13} The double ζ basis set used here was found to yield reliable predictions for equilibrium parameters and simple electronic expectation values, although dissociation energies are poorly estimated. However, by combining the energy difference (1.78 eV) between the C_{2v} isomer of NO_2 and the peroxy isomer (I^2A') with the accepted¹⁴ ON-O bond dissociation energy for the C_{2v} isomer (3.11 eV), the NO-O dissociation energy for the peroxy isomer can be estimated. Our resulting estimate for the NO-O dissociation energy is 1.33 eV. This estimate is likely to be accurate because of the electronic similarity between the two isomers¹³ and the success of SCF calculations in predicting geometries and relative differences near potential energy minima. Finally, it is interesting to note that even in the SCF approximation NO_2 is predicted to have a positive electron affinity.

The remaining question is whether photodetachment of the peroxy isomer of NO_2^- is accompanied by concomitant dissociation of the neutral fragment. This question cannot be irrefutably answered without knowing the complete energy surface. For comparison, the vertical detachment energy of the C_{2v} isomer exceeds the adiabatic electron affinity by only 0.4 eV, and there is a substantial geometry change in that process also.^{2a} Our results certainly suggest the possibility that NOO is a stable species and may play a role in atmospheric chemistry. Further calculations are being performed with a more extensive basis set (d orbitals) and the inclusion of significant configuration interaction (CI). These results will be presented in a subsequent article.

References and Notes

- (1) This work was performed under the auspices of the United States Energy Research and Development Administration under Contract No. W-7405-Eng-48.
- (2) (a) J. H. Richardson, L. M. Stephenson, and J. I. Brauman, *Chem. Phys. Lett.*,

- 25, 318 (1974); (b) E. Herbst, T. A. Patterson, and W. C. Lineberger, *J. Chem. Phys.*, **61**, 1300 (1974).
- (3) R. M. Hochstrasser and A. P. Marchetti, *J. Chem. Phys.*, **50**, 1727 (1969).
- (4) R. R. Sardzewski and W. B. Fox, Jr., *J. Am. Chem. Soc.*, **96**, 304 (1974).
- (5) (a) N. G. Adams, D. K. Bohme, D. B. Dunkin, F. C. Fehsenfeld, and E. E. Ferguson, *J. Chem. Phys.*, **52**, 3133 (1970); (b) E. E. Ferguson, D. B. Dunkin, and F. C. Fehsenfeld, *ibid.*, **57**, 1459 (1972).
- (6) P. K. Pearson, H. F. Schaefer, III, J. H. Richardson, L. M. Stephenson, and J. I. Brauman, *J. Am. Chem. Soc.*, **96**, 6778 (1974).
- (7) For an example of the importance of nitrogen oxides in the atmosphere, see G. Brasseur and M. Nicolet, *Planet. Space Sci.*, **21**, 939 (1973).
- (8) S. Huzinaga, *J. Chem. Phys.*, **42**, 1293 (1965).
- (9) T. H. Dunning, *J. Chem. Phys.*, **53**, 2823 (1970).
- (10) G. Herzberg, "Spectra of Diatomic Molecules", Van Nostrand-Reinhold, New York, N.Y., 1950.
- (11) H. F. Schaefer, "The Electronic Structure of Atoms and Molecules", Addison-Wesley, Reading, Mass., 1972.
- (12) S. Rothenberg and H. F. Schaefer, *Mol. Phys.*, **21**, 317 (1971).
- (13) G. D. Gillispie, A. U. Khan, A. C. Wahl, R. P. Hosteny, and M. Krauss, *J. Chem. Phys.*, **63**, 3425 (1975).
- (14) G. Herzberg, "Electronic Spectra of Polyatomic Molecules", Van Nostrand-Reinhold, New York, N.Y., 1966.

Theoretical Calculation of Strong Complex Formation by the HO₂ Radical: HO₂·H₂O and HO₂·NH₃^{1a}

E. J. Hamilton, Jr.,^{*1b} and C. A. Naleway

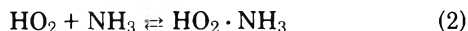
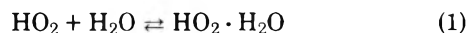
Chemistry Division, Argonne National Laboratory, Argonne, Illinois 60439 (Received February 20, 1976)

Publication costs assisted by Argonne National Laboratory

Exploratory ab initio calculations using a minimal basis set support the existence of the HO₂·H₂O and HO₂·NH₃ complexes, as proposed earlier by experiment. For the minimum energy configurations having HO₂ as the H donor within a linear H-bond structure, electronic stabilization energies of 9.1 and 12.0 kcal/mol are calculated for HO₂·H₂O and HO₂·NH₃, respectively, compared with 5.3 kcal/mol for (H₂O)₂. Values of ΔH° and ΔS° for the complex formations are estimated and found consistent with available experimental data. A plausible model is proposed to explain the reactivity of these complexes. These calculations indicate that in the troposphere a significant fraction of the HO₂ is complexed with H₂O.

Introduction

Recent experiments in this laboratory² have revealed that the observed rate of the atmospherically important^{3,4} self-reaction of HO₂ in the gas phase is increased by up to a factor of ≈2.5 (at ≈298 K) in the presence of a few Torr of H₂O or NH₃. Various considerations have led to the inference that this phenomenon is due to the formation of 1:1 complexes



which are more reactive than uncomplexed HO₂ toward a second uncomplexed HO₂ radical.⁵ Based on a kinetic model for this system, a preliminary equilibrium constant for (2) of $K_P \approx 95$ (based on a $P^\circ = 1$ atm standard state) at ≈298 K has been derived from the data.⁵ In connection with this proposed explanation of the data, ab initio calculations on hydrogen-bonded HO₂·H₂O and HO₂·NH₃ complexes have been carried out and equilibrium thermodynamic parameters for (1) and (2) estimated.

Ab Initio Calculations

In the Hartree-Fock calculations reported here, a minimal Gaussian basis set [3s 1p/1s] expansion was employed. The primitive basis consisted of a (10s 5p) expansion on the oxygen and nitrogen sites, while a (5s) expansion was used on the hydrogens. This primitive basis set is of essentially atomic double- ζ quality. The contraction scheme, composed from a

concatenation of Whitten's⁶ s-type orbitals with Huzinaga's⁷ p-orbital set, has been outlined in detail earlier.⁸ An effective Slater exponent of $\zeta = 1.2$ for all hydrogen orbitals was found to be near optimum for each monomer. This basis set is equivalent to that employed in previous studies of hydrogen bonding in the molecular series HF, H₂O, and NH₃.⁹ This basis set expansion yields a stabilization energy in good agreement with experiment (see next section) for the closed-shell (H₂O)₂ system,^{9,10} although the approximate character of this basis expansion dictates that this agreement is partially due to a cancellation of errors. It has been the authors' premise that agreement such as that found earlier could be extended to complexes between an uncharged radical and a neutral polar molecule wherein the open shell system is primarily removed from the region of H bonding.

Essentially experimental monomer geometries were held rigid for all calculations. The geometry used for the water monomer has an O-H bond length of 0.957 Å and an H-O-H angle of 104.52°. The ammonia geometry has an N-H bond length of 1.012 Å and an H-N-H angle of 106.7°. The HO₂ geometry¹¹ has an O-O bond length of 1.34 Å, an O-H bond length of 0.96 Å, and an O-O-H angle of 100.0°. Self-consistent field molecular orbital calculations were performed following Roothaan's formalism for open-shell systems¹⁴ using the MOLE LCAO-MO program package. The SCF energies for the H₂O, NH₃, and HO₂ monomers were calculated as -75.976 221 3, -56.142 436 9, and -150.101 432 0 hartrees, respectively.

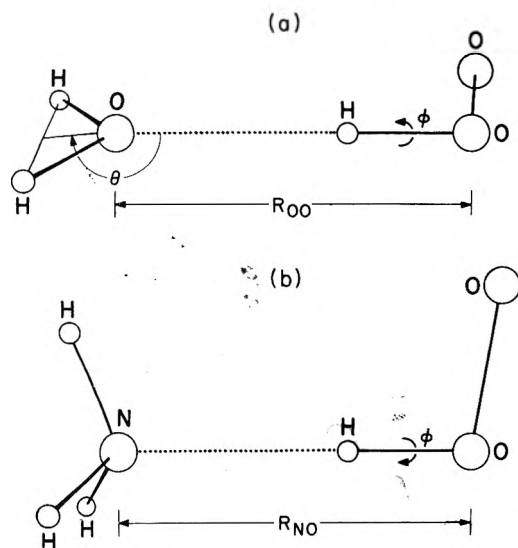


Figure 1. Calculated minimum energy geometries.¹⁸ (a) $\text{HO}_2\cdot\text{H}_2\text{O}$: $R_{\text{OO}} = 5.246$ bohr, $\theta = 176^\circ$, $\phi = 90^\circ$. (Note that when $\phi = 0$ or 180° , the HO_2 plane contains the C_2 axis of H_2O for all values of θ .) (b) $\text{HO}_2\cdot\text{NH}_3$: $R_{\text{NO}} = 5.196$ bohr, $\phi = 0^\circ$. (The HO_2 plane contains one N-H bond.)

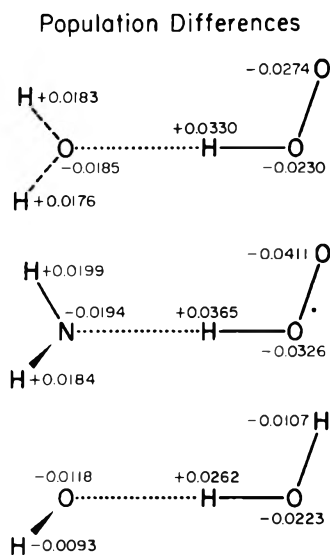


Figure 2. Population analysis¹⁵ for equilibrium configurations. These difference maps correspond to changes in charge distribution upon complexing. For comparison, $(\text{H}_2\text{O})_2$ at the same basis set level is included. [Note that in both the $\text{HO}_2\cdot\text{NH}_3$ and $(\text{H}_2\text{O})_2$ representations, one H atom of the proton acceptor is hidden.]

The Mulliken¹⁵ atomic charges on the monomer atoms were calculated as: $\text{HO}_2\text{—H}$, +0.43, O(central), -0.37, O(end), -0.06; $\text{H}_2\text{O—H}$, +0.36, O, -0.73; $\text{NH}_3\text{—H}$, +0.30, N, -0.91. Using such calculated Mulliken¹⁵ atomic charges, Kollman and Allen^{9,16} have found that for hydrogen-bonded complexes involving first-row hydrides, greater stabilization energy was correlated with greater positive charge on the atom in the proton donor and with greater negative charge on the heteroatom in the proton acceptor. Thus, for $\text{HO}_2\cdot\text{H}_2\text{O}$ and $\text{HO}_2\cdot\text{NH}_3$, the most stable structures should have HO_2 as the proton donor. This conclusion is also experimentally supported by the equality of the extinction coefficients at 230 nm for HO_2 and the complexes.^{2,5,17}

A potential energy surface search was carried out for each complex to obtain the equilibrium configuration, within the

TABLE I

$\text{HO}_2\cdot\text{H}_2\text{O}$ Geometric Search			
R_{OO} , bohr	θ , deg	ϕ , deg	$\Delta E^\circ_{\text{elec}}$, kcal mol ⁻¹
5.386	120	0	-6.76
5.386	125	0	-7.18
5.386	130	0	-7.55
5.386	135	0	-7.84
5.386	145	0	-8.30
5.386	155	0	-8.60
5.386	180	0	-8.84
5.386	185	0	-8.81
4.786	180	0	-7.15
4.986	180	0	-8.36
5.186	180	0	-8.92
5.246	180	0	-8.95
5.386	180	0	-8.84 ^a
5.586	180	0	-8.48
5.246	165	0	-8.90
5.246	170	0	-8.94
5.246	175	0	-8.96
5.246	180	0	-8.95 ^a
5.246	185	0	-8.92
5.246	175	180	-8.92 ^a
5.246	175	150	-8.80
5.246	175	135	-8.91
5.246	175	120	-8.89
5.246	175	100	-8.93
5.246	175	90	-9.07
5.246	175	80	-8.94
5.246	175	60	-8.91
5.246	175	45	-8.94
5.246	175	30	-8.84
5.246	175	0	-8.96 ^a
$\text{HO}_2\cdot\text{NH}_3$ Geometric Search			
R_{NO} , bohr	ϕ , deg	$\Delta E^\circ_{\text{elec}}$, kcal mol ⁻¹	
4.946	0	-11.30	
5.046	0	-11.74	
5.196	0	-11.96	
5.246	0	-11.95	
5.446	0	-11.58	
5.646	0	-10.99	
5.196	0	-11.96 ^a	
5.196	20	-11.86	
5.196	40	-11.86	
5.196	60	-11.83	

^a Duplication of equivalent geometries in this table is done as an aid to the reader.

restriction of a linear hydrogen-bond structure with HO_2 as the H donor; for $\text{HO}_2\cdot\text{H}_2\text{O}$, there was the additional restriction that the linear H-bond axis be contained in the σ_v plane of the H_2O that is perpendicular to the H_2O molecular plane; for $\text{HO}_2\cdot\text{NH}_3$, there was the additional restriction of collinearity of the C_3 axis of NH_3 and the linear H-bond axis. Optimization of the $\text{HO}_2\cdot\text{H}_2\text{O}$ complex required the variation of one intermolecular distance (R_{OO}) and two intermolecular angles (θ and ϕ), while for the $\text{HO}_2\cdot\text{NH}_3$ structure this required the variation of one intermolecular distance (R_{NO}) and one rotational angle (ϕ) about the H bond. These coordinate representations are defined in Figure 1.

For each complex, a geometry of lowest computed energy was obtained by successive variation of the above intermo-

TABLE II: Calculated ΔH° Contributions at 298.16 K (kcal mol⁻¹)

Reaction	$\Delta E^\circ_{\text{vib}}$		$\Delta E^\circ_{\text{elec}}$	ΔH° (calcd) ^f	ΔH° (exptl)
	intra-molec	6 intermolec			
3	-0.150 ^a	4.2 (3) ^b	-5.27 ^d	-3.6	-3.8 ^g
1		4.05 ^c	-9.07 ^e	-7.4	
2		4.05 ^c	-11.96 ^e	-10.3	

^a From frequencies in an N₂ matrix from ref 23. ^b An estimate based on the results of several theoretical calculations; see text. ^c Approximated as equal to $\Delta E^\circ_{\text{vib}}$ for (3). ^d From ref 10. ^e This work. ^f From (4). ^g From ref 30 and 31; see text.

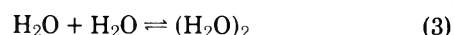
lecular coordinates as shown in Table I. A minimum geometry for the HO₂-H₂O complex was found (interpolated) at $R_{\text{OO}} = 5.246$ bohr, $\theta = 176^\circ$, and $\phi = 90^\circ$ with a stabilization energy ($\equiv \Delta E^\circ_{\text{elec}}$) of -9.07 kcal/mol,¹⁹ while the optimized geometry for the HO₂-NH₃ complex was calculated to be $R_{\text{NO}} = 5.196$ bohr, $\phi = 0^\circ$, with $\Delta E^\circ_{\text{elec}} = -11.96$ kcal/mol.

Considerable electronic relaxation (relative to the monomers) is evident from examination of the electronic structure of the complex. As a means of illustrating the extent of this electronic migration, a Mulliken population difference analysis¹⁵ is shown in Figure 2 for the two optimized complex configurations. A further analysis of the wave functions associated with the complexes indicates that the electron density of the unpaired electron remains primarily localized on the terminal oxygen of HO₂,²⁰ thus supporting our initial premise.

The restraints of a minimal basis set were examined in relation to a pair of calculations performed on the HO₂-H₂O system using a somewhat larger (split-out) basis [5s 2p/2s]. The results of these two calculations at $R_{\text{OO}} = 5.246$ bohr, $\theta = 175^\circ$, and $\phi = 90$ and 0° yielded stabilization energies of -11.86 and -11.76 kcal/mol, respectively. These higher stabilization energies (by 2.8 kcal/mol) are consistent with the basis set characteristics observed with (H₂O)₂, for which extension of the basis set as described above increased the stabilization energy from -5.3 to -7.5 kcal/mol.¹⁰ This suggests comparable reliability for the minimal basis set results on HO₂-H₂O and (H₂O)₂.

Estimation of ΔH° and ΔS°

In this section, ΔH° and ΔS° (units are per mole of complex) at 298.16 K are estimated for (1), (2), and the reaction



Separation of ΔE° into translational, rotational, vibrational, and electronic components leads to²¹

$$\begin{aligned} \Delta H^\circ &= \Delta E^\circ + \Delta(PV) = \Delta E^\circ_{\text{trans}} + \Delta E^\circ_{\text{rot}} + \Delta E^\circ_{\text{vib}} \\ &+ \Delta E^\circ_{\text{elec}} + \Delta(PV) = -4RT + \Delta E^\circ_{\text{vib}} + \Delta E^\circ_{\text{elec}} \\ &= -2.370 \text{ kcal mol}^{-1} + \Delta E^\circ_{\text{vib}} + \Delta E^\circ_{\text{elec}} \quad (4) \end{aligned}$$

for (1)–(3), where $RT/2$ has been allotted to each degree of translational and rotational freedom. The $\Delta E^\circ_{\text{elec}}$ values were calculated above for the HO₂ complexes and in ref 10 for (H₂O)₂. Within the harmonic oscillator approximation, each normal vibration (ν_i) will contribute²²

$$h\nu_i [1/2 + (e^{h\nu_i/RT} - 1)^{-1}] \geq RT \quad (5)$$

to the internal energy. Of the $3n - 6$ vibrational modes in each complex, six "intermolecular" modes are expected to be low frequency due to relative motion of the two entire component molecules; the remaining $3n - 12$ ("intramolecular") frequencies should be similar to the equal number of vibrational frequencies of the two isolated component molecules. Separating $\Delta E^\circ_{\text{vib}}$ in this manner, $\Delta E^\circ_{\text{vib}} = \Delta E^\circ_{\text{intra}} + \Delta E^\circ_{6 \text{ inter}}$. From the fundamental frequencies observed for H₂O and (H₂O)₂ in an N₂ matrix,²³ $\Delta E^\circ_{\text{intra}}$ is approximately -0.150 kcal mol⁻¹ for (3). The intermolecular normal mode frequencies of (H₂O)₂ have not been experimentally determined but have been theoretically predicted from several ab initio and empirical potentials.^{24–27} These predictions lead to values of $\Delta E^\circ_{6 \text{ inter}}$ for (3) in the range 4.0–5.1 kcal mol⁻¹ (the classical, lower limit is $6RT = 3.555$ kcal mol⁻¹);²⁸ from consideration of the reliabilities of the various theoretical treatments based upon the accuracy of prediction of other (H₂O)₂ properties,²⁵ we estimate $\Delta E^\circ_{6 \text{ inter}} = 4.2(3)$ kcal mol⁻¹ in Table II. For both (1) and (2), $\Delta E^\circ_{\text{vib}}$ is set equal to that for (3), which should be reasonable approximations;²⁹ the ΔH° values then calculated from (4) are listed in Table II. For (3), ΔH° (calcd) is consistent with the value ΔH° (exptl) = -3.8 kcal/mol obtained in two recent studies^{30,31} (which assumed ΔH° constant over the temperature ranges 423–673³⁰ and 285–400 K³¹).

Separation of the translational, rotational (external), vibrational, and electronic contributions to the total entropy gives²²

$$S^\circ_{\text{tot}} = S^\circ_{\text{trans}} + S^\circ_{\text{rot}} + S^\circ_{\text{vib}} + S^\circ_{\text{elec}} \quad (6)$$

In the rigid rotor and harmonic oscillator approximations,

TABLE III: Calculated Entropies^a at 298.16 K (cal mol⁻¹ K⁻¹)

	S°_{vib}				S°_{elec}	S°_{tot} (calcd) ^k	S°_{tot} (exptl)
	S°_{trans}	S°_{rot} ^b	intramolec	6 intermolec			
H ₂ O	34.611	10.453	0.008 ^d	0	0	45.072	45.11 ^l
NH ₃	34.443	11.433	0.128 ^d	0	0	46.004	46.01 ^l
HO ₂	36.416	16.868	0.082 ^c	0	1.377	54.743	
(H ₂ O) ₂	36.677	21.227 ^c	0.015 ^f	12.5 (20) ^h	0	70.4	69.6, ^m 72.2 ⁿ
HO ₂ -H ₂ O	37.714	23.607	0.090 ^g	12.5 ⁱ	1.377	75.3	
HO ₂ -NH ₃	37.656	23.624	0.210 ^g	11.7 ^j	1.377	74.6	

^a Gaseous standard state, $P = 1$ atm. ^b From geometries used or determined in this work. ^c From geometry measured in ref 32. ^d From the fundamental frequencies given in ref 33. ^e From the fundamental frequencies given in ref 34. ^f Assuming frequencies shifted from those of H₂O by the same shifts as observed in an N₂ matrix (ref 23). ^g Approximated as equal to the sum of the corresponding values for the two separate molecules. ^h An estimate based on the results of several theoretical calculations; see text. ⁱ Approximated as equal to the corresponding quantity for (H₂O)₂. ^j Approximated as equal to the corresponding quantity for (H₂O)₂ minus $R(\ln 3 - \ln 2)$; see text. ^k From (6). ^l From ref 35. ^m From ref 30. ⁿ From ref 31.

standard formulas are available for the above contributions,²² and the calculated results for the species involved in (1)–(3) are shown in Table III. As with $\Delta E^{\circ}_{\text{vib}}$ above, $S^{\circ}_{\text{vib}} = S^{\circ}_{\text{intra}} + S^{\circ}_{6\text{inter}}$. For the complexes, the $S^{\circ}_{6\text{inter}}$ are large and uncertain. The various theoretical predictions^{25–27} of the six intermolecular vibrations for $(\text{H}_2\text{O})_2$ lead to values of $S^{\circ}_{6\text{inter}}$ in the range 8.4–14.0 cal mol⁻¹ K⁻¹,²⁸ as above for the internal energy, we estimate $S^{\circ}_{6\text{inter}} = 12.5(20)$ cal mol⁻¹ K⁻¹ in Table III. $S^{\circ}_{6\text{inter}}$ for $\text{HO}_2\cdot\text{H}_2\text{O}$ is approximated also as 12.5 cal mol⁻¹ K⁻¹, while for $\text{HO}_2\cdot\text{NH}_3$ this figure is reduced by $R(\ln 3 - \ln 2)$ because of the increased effective symmetry of the internal rotation (about the H-bond axis) motion which is probably occurring in these complexes.²⁹ As shown in Table III, the calculated total entropies of H_2O and NH_3 are in excellent agreement with experiment, while for $(\text{H}_2\text{O})_2$ the calculated value is consistent with the two experimental measurements.^{30,31}

The above calculations give for (2) at 298.16 K the value $\Delta G^{\circ} = -2.5$ kcal mol⁻¹, while the preliminary experimental value for the equilibrium constant mentioned earlier corresponds to $\Delta G^{\circ} = -2.7$ kcal mol⁻¹. This small disagreement is certainly less than the uncertainty one would associate with the theoretical value. Nevertheless, the apparent accuracy of the theoretical calculations for (2) and (3) suggests that the results for (1), for which experimental thermodynamic data are as yet unavailable, are reliable. We note, then, the atmospherically relevant prediction of this work that at 298.16 K and 100% relative humidity ($p_{\text{H}_2\text{O}} = 23.76$ Torr), approximately 3.5% of the HO_2 is calculated to be complexed with H_2O .

Discussion and Conclusions

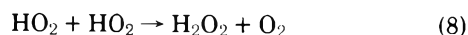
The theoretical results reported here constitute strong, independent support for the explanation of reported² and concurrent⁵ experimental results in terms of $\text{HO}_2\cdot\text{H}_2\text{O}$ and $\text{HO}_2\cdot\text{NH}_3$ complexes, since the experimental evidence for these complexes is quite indirect. Specifically, the calculated and experimental values of ΔG° at ≈ 298 K for (2) agreed closely; also, a greater stability of $\text{HO}_2\cdot\text{NH}_3$ than $\text{HO}_2\cdot\text{H}_2\text{O}$, which is experimentally suggested by a larger NH_3 than H_2O effect on the reaction rate, is calculated in this work.

From this work, it is strongly indicated that at temperatures and humidities relevant to the troposphere, a significant fraction of the HO_2 is complexed with H_2O . This substantially affects the rate of the HO_2 self-reaction,^{2,5} which is a very important chain termination process in the troposphere.^{3,4} The $\text{HO}_2\cdot\text{H}_2\text{O}$ species, which will likely exhibit reactivity different from HO_2 in other reactions as well, must be included in a complete model of the lower atmosphere.

In the calculated geometries of $\text{HO}_2\cdot\text{H}_2\text{O}$ and $\text{HO}_2\cdot\text{NH}_3$, the H of the HO_2 is hydrogen bonded. Thus, due to steric hindrance, the reaction probability for transfer of this H atom would be expected to be reduced. Yet, as stated in the Introduction, it has been inferred from experiment⁵ that the reactions



are faster than the reaction



We speculate that this is because the steric hindrance to the transfer of the H atom of one HO_2 is outweighed by the following effect: relative to the situation for (8), a reactant encounter in (7) should hold two HO_2 radicals in close proximity

for a longer time (due to enhanced hydrogen-bonding possibilities), during which a reactive orientation of the two HO_2 may be realized. This speculation is supported by the calculated electron migration in going from the monomers to the complexes (Figure 2), which would seem to favor further hydrogen bonding, and by the very low barrier to rotation about the hydrogen bond in each complex (Table I), suggesting some flexibility in the reactant encounter pairs of (7).

Acknowledgment. We thank A. C. Wahl for his active interest and support of this program. We are also grateful to L. L. Shipman for pointing out several references and for constructive criticism of our original manuscript, to C. D. Jonah for providing a moment of inertia program, to M. E. Schwartz for his assistance in establishing the MOLE program package at Argonne, and to J. M. Williams for use of his ORTEP-based plotting system.

References and Notes

- (1) (a) Based on work performed under the auspices of the U.S. Energy Research and Development Administration. (b) Present address: Research Staff, Ford Motor Company, Dearborn, Mich. 48121.
- (2) E. J. Hamilton, Jr., *J. Chem. Phys.*, **63**, 3682 (1975).
- (3) J. G. Calvert and R. D. McQuigg, *Int. J. Chem. Kinet.*, **7** (Symp. 1), 113 (1975).
- (4) H. Levy II, *Adv. Photochem.*, **9**, 369 (1974).
- (5) E. J. Hamilton, Jr. and R. R. Lii, to be submitted for publication.
- (6) J. L. Whitten, *J. Chem. Phys.*, **44**, 359 (1966).
- (7) S. Huzinaga, *J. Chem. Phys.*, **42**, 1293 (1965).
- (8) M. E. Schwartz, *Chem. Phys. Lett.*, **6**, 631 (1970).
- (9) P. A. Kollman and L. C. Allen, *J. Am. Chem. Soc.*, **93**, 4991 (1971).
- (10) P. A. Kollman and L. C. Allen, *J. Chem. Phys.*, **51**, 3286 (1969).
- (11) The O–O bond length was taken from ref 12; the graph in ref 13 was then used to obtain the two other parameters.
- (12) H. E. Hunziker and H. R. Wendt, *J. Chem. Phys.*, **60**, 4622 (1974).
- (13) J. T. Hougen, H. E. Radford, K. M. Evenson, and C. J. Howard, *J. Mol. Spectrosc.*, **56**, 210 (1975).
- (14) C. C. J. Roothaan, *Rev. Mod. Phys.*, **32**, 179 (1960).
- (15) R. S. Mulliken, *J. Chem. Phys.*, **23**, 1833 (1955).
- (16) P. Kollman, J. McKelvey, A. Johansson, and S. Rothenberg, *J. Am. Chem. Soc.*, **97**, 955 (1975).
- (17) This observation suggests that the complexing site in HO_2 is not at the chromophore (the O end of the radical).
- (18) From ORTEP plots (C. K. Johnson, ORNL).
- (19) A few calculations on the "inverse" hydrogen bond structure H_2O (donor)– HO_2 (acceptor), where the terminal oxygen of HO_2 is involved in H bonding, showed only marginal electronic stabilization of the order of 1.0 kcal mol⁻¹.
- (20) The Mulliken atomic population associated with the open-shell orbital of HO_2 changed by less than 1% upon complexation.
- (21) L. J. Schaad, "Theory of the Hydrogen Bond", in "Hydrogen Bonding", M. D. Joesten and L. J. Schaad, Ed., Marcel Dekker, New York, N.Y., 1974, p 88.
- (22) G. N. Lewis and M. Randall (revised by K. S. Pitzer and L. Brewer), "Thermodynamics", 2nd ed, McGraw-Hill, New York, N.Y., 1961, Chapter 27.
- (23) A. J. Tursi and E. R. Nixon, *J. Chem. Phys.*, **52**, 1521 (1970).
- (24) The present work does not include calculation of intermolecular force constants because of the excessive computer time required and because of the sensitivity of results to the basis set (ref 26).
- (25) J. C. Owicki, L. L. Shipman, and H. A. Scheraga, *J. Phys. Chem.*, **79**, 1794 (1975).
- (26) L. A. Curtiss and J. A. Pople, *J. Mol. Spectrosc.*, **55**, 1 (1975).
- (27) C. Braun and H. Leidecker, *J. Chem. Phys.*, **61**, 3104 (1974).
- (28) As Owicki et al. have discussed for $(\text{H}_2\text{O})_2$,²⁵ the harmonic oscillator model is expected to be only a crude representation of reality for the six intermolecular vibrations—by not taking into account vibrational anharmonicities and the low barriers to interconversion among isoenergetic minima, this model should underestimate the stability of $(\text{H}_2\text{O})_2$ in the calculation of both the enthalpy and the entropy.
- (29) In support of these approximations, we note the opposite signs of two major effects on the six intermolecular frequencies (ν_i) in going from $(\text{H}_2\text{O})_2$ to $\text{HO}_2\cdot\text{H}_2\text{O}$ and $\text{HO}_2\cdot\text{NH}_3$: the increased electronic interactions should give generally increased force constants and higher ν_i , while the change in proton donor from H_2O to HO_2 should give generally increased effective masses and lower ν_i .
- (30) G. S. Kell and G. E. McLaurin, *J. Chem. Phys.*, **51**, 4345 (1969).
- (31) F. T. Greene, J. Beachey, and T. A. Milne, U.S. Office of Saline Water, Research and Development Progress Report, No. 772 (1972).
- (32) T. R. Dyke and J. S. Muentner, *J. Chem. Phys.*, **60**, 2929 (1974).
- (33) D. R. Stull and H. Prophet, 2d ed *Natl. Std. Ref. Data Ser., Natl. Bur. Stand., No. 37*, (1971).
- (34) T. T. Paukert and H. S. Johnston, *J. Chem. Phys.*, **56**, 2824 (1972).
- (35) R. C. Weast, Ed., "Handbook of Chemistry and Physics", 56th ed, The Chemical Rubber Co., Cleveland, Ohio, 1975.

Tracer Diffusion Coefficients of Counterions in Homo- and Heteroionic Poly(styrenesulfonate) Resins

R. Fernández-Prini*

Sector Electroquímica Aplicada, INTI, Libertad 1235, Buenos Aires, Argentina

and Mario Philipp

Departamento de Bioquímica, Centro de Investigación del IPN, México, D.F. (Received March 16, 1976)

The tracer diffusion coefficients of Na^+ and Ba^{2+} ions in especially synthesized poly(styrenesulfonate) resins with 2.3% cross linking were determined at 25 °C. These data were employed to evaluate the various contributions to the ionic mobilities in such media, i.e. tortuosity effect and electrostatic interactions. Yasuda's equation is found to describe adequately the tortuosity effect in the range 0.1–0.8 of the resin volume fraction (V_p). It is concluded that electrostatic interactions are important even at large V_p , but the value of the acting electrostatic potential surrounding the charged chains is different from that calculated with theories of dilute polyelectrolyte solutions. The probable mechanism of transport of ions in resins is also discussed in terms of the values found for the activation energies for ionic transport.

Introduction

The transport of small mobile particles through polymeric materials bearing fixed charges is of importance in a variety of processes which are related to the permeability of synthetic or natural membranes as well as to the kinetics of ion exchange. In the past, it was common to interpret thermodynamic and transport properties of ion-exchange resins in terms of those of concentrated electrolyte solutions. However, it is now generally accepted that polyelectrolyte solutions are the correct homogeneous analogues of the resin systems.^{1–4} Solutions of linear polyelectrolytes are in every way similar to the corresponding cross-linked resins at the same concentration of fixed charges; a difference, however, exists in that the resins cannot be indefinitely "diluted" with solvent because it is impossible to stretch the chemical bonds linking two polymeric chains beyond a certain limit, thus the "infinite dilution limit" cannot be experimentally achieved in cross-linked resins.

The transport of small ions in dilute polyelectrolyte solutions is governed by the strong electrostatic interactions between the polymeric chains and the mobile counterions and coions. According to Manning⁵ and to Katchalsky and co-workers,⁶ these electrostatic interactions depend mainly on the distance between adjacent charges along the backbone, and very little on the concentration of the polyelectrolyte. On the other hand, when the concentration of macromolecules is sufficiently high, the displacements of the mobile species, which always occur through the regions containing water in the macroionic solution, will be hampered by the polymeric chains. This situation has the effect of lengthening the real path of the moving particles which travel through the macromolecular medium. This tortuosity effect⁷ is fundamentally related to the volume fraction of resin, V_p .

Thus, it may be said quite generally that the tracer diffusion coefficients of ions (D_i) in resins or polyelectrolyte solutions may be expressed for all V_p by

$$D_i = D_i^{(el)} f(V_p) \quad (1)$$

where

$$D_i^{(el)} = D_i^0 g(\Phi)/z_i \quad (2)$$

and $f(V_p)$ represents the tortuosity effect, Φ is the reduced electrostatic potential, z_i is the charge of the moving ion, and D_i^0 denotes the tracer diffusion coefficient of ion i in pure water which is proportional to the absolute mobility of the ion.

The present work reports measurements of tracer diffusion coefficients in homo- and heteroionic poly(styrenesulfonate) resins. The results were employed in order to clarify the nature of the various terms appearing in eq 1 and 2 and evaluate their general applicability.

Experimental Section

Preparation of the Resin Strips. The poly(styrenesulfonate) resin strips employed in the present work were synthesized from styrene (PASA S.A.) using divinylbenzene (Fluka technical grade) as the cross-linking agent. The styrene was washed with 5% NaOH and then distilled under reduced pressure (0.1 Torr) to eliminate any residual polymerization inhibitor. The precise content of divinylbenzene in the commercial product, which also contained ethylvinylbenzene and diethylbenzene, was established by vapor phase chromatography.

The polymerization was carried out⁸ in such a way that the final resin was in the form of thin strips of 200 μm thickness. A mixture of the monomers with 15% of toluene and 0.66% of azobis(isobutyronitrile) was prepared in a large test tube. A number of glass slides separated from each other by thin glass plates was tightly tied together and immersed in the reaction mixture. The glass slides had to be scrupulously clean to enable the preparation of smooth homogeneous strips. The test tube was sealed and the polymerization proceeded for successive periods of 24 h at 40, 70, and 100 °C.

The strips obtained were sulfonated at 100 °C in concentrated H_2SO_4 containing 0.2% Ag_2SO_4 as a catalyst. The sulfonation proceeded for a time which depended on the degree of cross linking of the resin; the end of the sulfonation occurred when the resins did not swell any more and their surfaces appeared smooth. In order to avoid a destructive osmotic shock when the sulfonated resins were immersed in water, it was necessary to equilibrate them successively in a series of H_2SO_4 solutions of decreasing concentration. All the syn-

TABLE I

V_p	$10^7 D_i / \text{cm}^2 \text{ s}^{-1}$									
	Na ⁺	Ba ²⁺	Na ⁺	Ba ²⁺	Na ⁺	Ba ²⁺	Na ⁺	Ba ²⁺	Na ⁺	Ba ²⁺
0.785	0.303									
0.724		0.0107							0.0851	0.00262
0.686	1.36	0.0399	0.880	0.209	0.678		0.594	0.0156	0.482	0.0217
0.659	2.21									
0.630	3.82	0.259	2.87	0.152	2.08	0.109	1.78	0.0906	2.49	0.238
0.582	8.52	0.747	5.64	0.421	3.89	0.268	3.39	0.255	5.56	0.527
0.558	9.96	1.15	7.60		5.03		4.22		7.67	0.681
$X_{\text{Ba}^{2+}}$		0.00		0.20		0.50		0.80		1.00

thesized resins were subjected to various cycles of ion exchange with HCl, NaCl, and BaCl₂ before being employed.

The exchange capacity of the resins resulted between 96 and 100% of the calculated theoretical capacity for poly(styrenesulfonate) resins. Electron-scan microscopy of the material obtained showed the resins were very smooth and homogeneous if the samples for microscopy were carefully dried; otherwise when the solvent desorbed abruptly from the strips, it damaged severely the surface of the resin.

Various strips were completely exchanged with ²²NaCl and then they were cut in small pieces which were found to have the same radioactivity per unit length; this showed that the resin strips had a constant thickness throughout their entire length.

Water Absorption Isotherms. The resin strips were isopiastically equilibrated inside a vacuum desiccator containing either saturated electrolyte solutions or solutions of sulfuric acid of such concentrations that the desired relative humidity could be obtained. The desiccators were provided with electromechanical devices that enabled stirring of the solutions from the outside of the thermostat when necessary. The isopiastic equilibration required between 5 and 7 days to be completed; all determinations were made in duplicate. The water content of the resins at each relative humidity was determined gravimetrically; the weight of dry resin was obtained after drying for 48 h at 120 °C.

Heteroionic Resins. They were obtained by equilibrating the resins with a solution containing a mixture of NaCl and BaCl₂ in a variable ratio. The ionic composition of the resin was established by exchanging the cations with HCl and by subsequent determination of the sodium content by flame photometry.

Tracer Diffusion Measurements. For the diffusion runs, the strips were cut to a size of 0.3 by 3.0 cm. When the isopiastic equilibration of the resin strips was completed, they were hung from a stainless steel hook mounted onto a micrometer screw which allowed moving the strips up or down, so that they could be made to just touch the solution containing the desired radioactive isotope (²²Na⁺ or ^{133m}Ba²⁺ in carrier-free chloride solutions (CNEA, Argentina)) in order to seed the strips. In this way the seeding process could be carried out in a very short time and produced a very convenient thin and straight front of radioactive solution in the strips. The seeded strips were then placed in test tubes containing solutions of the appropriate relative humidity. The test tubes were kept in a thermostat at 25.0 ± 0.1 °C during the period required to complete the diffusion run. The strips were then taken out of the tubes and put between two pieces of adhesive tape which were tightly sealed together.⁸ With a especially designed guillotine, the strips were cut into sections of 0.237 cm, their length always being checked with a mea-

suring microscope. The radioactivity in each section was determined by a scintillation counter (Nuclear). From each strip section a value of the tracer diffusion coefficients was calculated⁸ from the accumulative fraction of radioisotope, f_i , and the distance x_i of the section from the origin of the strip according to the equation which gives the solution of Fick's differential equation for this experimental situation. The expression results:

$$f_i = \text{erf}(x^2/4Dt)^{1/2}$$

where erf is the error function to be found in mathematical tables and t is the diffusion time. The dispersion of the data obtained in every strip was never greater than 3% from the averages which are reported here.

Results

It was important to carry out the measurements of tracer diffusion in the whole series of resin ionic composition at constant V_p (cf. Discussion). Hence the measured water absorption isotherms at each ionic composition were converted into plots of V_p against relative humidity. With these plots the relative humidity necessary to achieve the desired values of V_p could be determined for each ionic composition. These relative humidities were obtained by careful adjustment of the concentration of H₂SO₄ aqueous solutions.

In order to calculate the volume fraction, we assumed that the partial molar volume of water was 17 cm³ mol⁻¹ for the resins at all ionic compositions; this choice is based on data reported in the literature for various poly(styrenesulfonates)⁹ and for films of sodium deoxyribonucleic acid.¹⁰ With this value and the measured density of the various dry resins, V_p was calculated from the water content of the resins determined gravimetrically.

Table I summarizes the data obtained for the tracer diffusion coefficients of Ba²⁺ and Na⁺ in homo- and heteroionic poly(styrenesulfonate) resins with 2.3% cross linking. The ionic composition of the resin is denoted by $X_{\text{Ba}^{2+}}$ which is equal to the fraction of barium ion equivalents in the resin.

Discussion

In order to establish the nature of the functions appearing in eq 1 and 2, we shall deal first with $f(V_p)$. There are several models proposed to account for the tortuosity effect. In 1955 Mackie and Meares⁷ derived an expression for $f(V_p)$ employing a model that considers the hydrated resin as a lattice through which the ions diffuse. The lattice sites which are occupied by the polymeric chains are assumed not to be available for the displacement of the mobile particles. The magnitude of the obstruction produced by the polymeric chains was evaluated in terms of the probability of polymer occupancy of the lattice sites. This probability was related

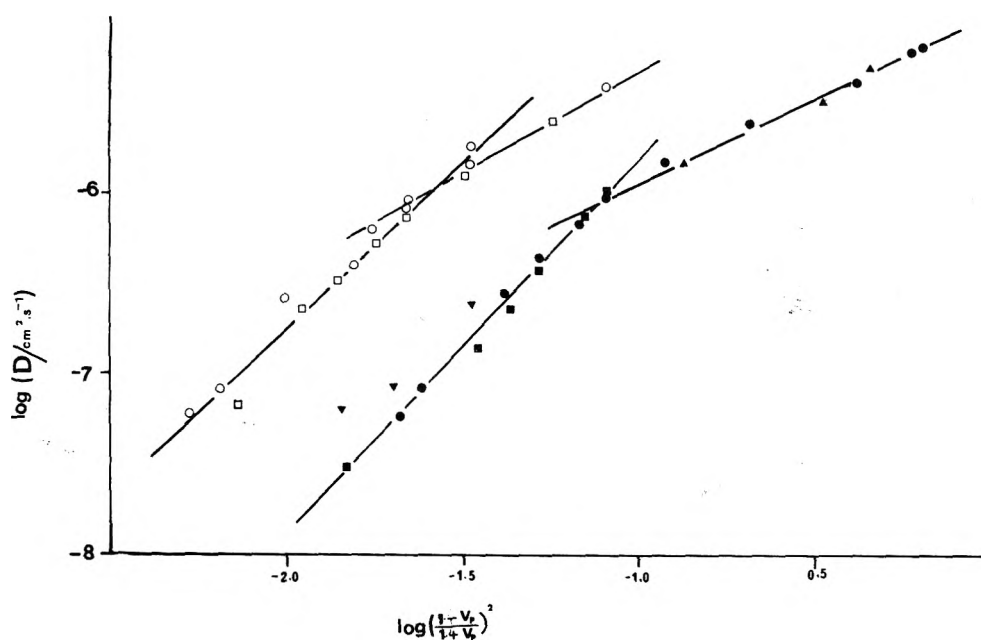


Figure 1. The tortuosity effect in poly(styrenesulfonate) systems according to Mackie and Meares⁷ where $f(V_p)$ is given by eq 3. Na^+ : (●) linear polyelectrolyte;⁹ (■) present work 2.3% cross linking; (▲) commercial resins with 1.7, 4, and 8% cross linking; (▼) 2.3% cross linking.⁸ Cs^+ : (○) 4.5% cross linking; (□) 2.4% cross linking.⁸

directly to the volume fraction of resin. The resulting expression was

$$f(V_p) = \frac{(1 - V_p)^2}{(1 + V_p)^2} \quad (3)$$

The theory of Mackie and Meares has been employed successfully for the diffusion of ions and small neutral solutes through membranes of gelatin, cellulose, and poly(vinyl) compounds,¹¹ as well as for ion-exchange resins.¹² Equation 3 has been found to work for cases where $V_p \leq 0.5$; for the case of ions it was necessary to introduce also an electrostatic interaction to account for the experimental D_i values.³

In order to test this and other expressions for the tortuosity effect we have selected the relatively abundant tracer diffusion data for the sodium ion in poly(styrenesulfonate) aqueous systems. Data are available for the linear polymer,⁹ for commercial ion-exchange resins of various degrees of cross linking,² and for resins synthesized by Lagos⁸ and those employed in the present work. Figure 1 illustrates the plot of $\log(D_i)$ against $\log(f(V_p))$ according to eq 3; the data cover the range 0.1–0.8 of V_p . In Figure 1 we have also included the data of D_{Cs^+} in poly(cesium styrenesulfonate) resin obtained by Lagos.⁸ It may be seen that the data for each ion may be represented by two straight lines, one for the region of low V_p with slopes of 0.9 and 1.0 for Na^+ and Cs^+ , respectively, and the other for high V_p having slopes of 1.96 and 1.75. According to eq 3 the double logarithmic plots in Figure 1 should give straight lines with slopes of unity for the entire range of V_p , hence it may be said that the theory of Mackie and Meares is closely verified for D_{Na^+} up to $V_p = 0.55$ and for D_{Cs^+} up to 0.68. For larger V_p values eq 3 underestimates the decrease of D_i with V_p probably due to the fact that at very high concentration of polymeric material there exists a significant number of polymer chain configurations which completely surround the solvent regions, such that the diffusing species which enter those regions have to move against a chemical potential gradient in order to escape from them and advance then in the direction of the existing chemical potential gradient.

Yasuda et al.¹³ showed that the permeability of NaCl passing through hydrophilic membranes could be correctly accounted for by an expression derived by them from the free volume theory of Cohen and Turnbull¹⁴ for mass transport in glasses and polymeric systems. Yasuda et al. considered that in a hydrophilic membrane the free volume may be additively expressed by that of water and that of the resinous material. Considering, furthermore, that the moving particles cannot permeate through the regions occupied by the resinous matrix, they concluded that the free volume of the system is given by the fraction of water²² times its free volume. Thus

$$f(V_p) = \exp(-bV_p/(1 - V_p)) \quad (4)$$

This rather straight forward extension of Cohen and Turnbull's theory is not extent of criticism, e.g., the free volume of water in the resin is taken to be the same as that in pure water. Hence the physical significance of the constant b in eq 4 is rather obscure. Figure 2 is a plot of the tracer diffusion data for Na^+ and Cs^+ ions in poly(styrenesulfonate) resins already plotted in Figure 1. It may be seen that the data covering the whole range of V_p are correctly represented by a single straight line as predicted by eq 4. The least-squares analysis of the data is summarized in Table II. Equation 4 has been reported¹¹ to apply for $V_p \leq 0.5$ as well as eq 3 for the diffusion of neutral molecules through various hydrophilic membranes, and it also applies for Na^+ tracer diffusion in concentrated films of the sodium salt of deoxyribonucleic acid where the slope is almost parallel to that reported in Table II for Na^+ in poly(sodium styrenesulfonate).¹⁰ On the other hand, the values of $D_i^{(e)}$ in Table II are significantly smaller than D_i^0 indicating the existence of an electrostatic effect ($D_{\text{Na}^+}^0 = 1.333 \times 10^{-5} \text{ cm}^2 \text{ s}^{-1}$ and $D_{\text{Cs}^+}^0 = 2.057 \times 10^{-5} \text{ cm}^2 \text{ s}^{-1}$).

The change in the tracer diffusion coefficients of Na^+ and Ba^{2+} with the resin ionic fraction in heteroionic resins was employed to evaluate the electrostatic contribution to eq 1. First, let us consider the change in diffusion coefficients that would be predicted by polyelectrolyte theory when the Na^+ counterion is replaced by Ba^{2+} . Due to the preferential condensation of multivalent counterions⁵ when Ba^{2+} ions are

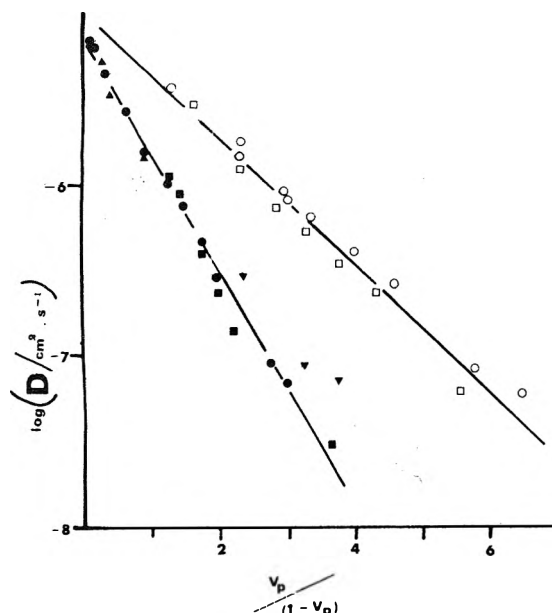


Figure 2. The tortuosity effect in poly(styrenesulfonate) systems according to Yasuda et al. where $f(V_p)$ is given by eq 4. Symbols are the same as in Figure 1.

present in the resin only as a trace, they will be strongly attracted by the macroion as well as a fraction of the sodium counterions. When $X_{Ba^{2+}}$ increases, a fraction of barium ions becomes relatively free and the fraction of free Na^+ also increases. Consequently, the tracer diffusion coefficients of both ions would be expected to increase with $X_{Ba^{2+}}$ at constant V_p , i.e., with the fraction of free counterions.¹⁵

In an important and classical study, Soldano and Boyd¹⁶ have observed the opposite behavior in Na^+/Zn^{2+} heteroionic poly(styrenesulfonate) resins. Nevertheless, their measurements were carried out under conditions which maintained the water activity almost constant, and it is a well-known fact verified in the present work that at the same water activity the bivalent resin has a lower water content than the sodium resin; in other words, at constant water activity V_p increases with the fraction of bivalent counterion in the resin. This implies an increased tortuosity and may be deemed responsible for the observed behavior of the tracer diffusion coefficients in the work of Soldano and Boyd.¹⁶ For this reason we have measured the values of D_{Na^+} and $D_{Ba^{2+}}$ in various heteroionic resins at constant V_p , a condition that proved to be experimentally tedious and difficult to carry out (cf. Results). Figure 3 is a plot of the data reported in Table I for both ionic tracer diffusion coefficients at constant V_p as a function of $X_{Ba^{2+}}$. Figure 3 shows that, from the point of view of "dilute polyelectrolytes", the behavior is still anomalous in spite of the fact that a minimum in the curves is observed which appears to shift to lower $X_{Ba^{2+}}$ values as V_p decreases, suggesting that the predictions of polyelectrolyte theory might be verified at low V_p .

In view of the results illustrated in Figure 3, it is tempting to argue that in sufficiently concentrated ion-exchange resins, the electrostatic effect is not a relevant quantity. This would be the case if under such conditions the counterions moved along the chains of the polymeric backbone through essentially equipotential paths. In this case the electrostatic polyelectrolyte effect would not be acting since it really accounts for the decrease in ionic mobility when the ions travel from positions near the chains in the polymeric domains toward the

TABLE II

Ion	$10^5 D_i^{(el)}/cm^2 s^{-1}$	b_i	Std deviation
Na^+	0.56 ₉	1.42	3%
Cs^+	1.0 ₉	0.87 ₆	2%

$V_p = \text{const.}$

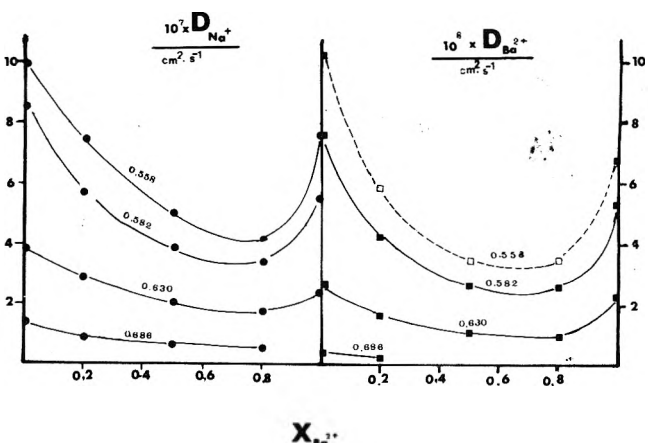


Figure 3. Tracer diffusion coefficients of Na^+ and Ba^{2+} against $X_{Ba^{2+}}$ in Na^+/Ba^{2+} heteroionic poly(styrenesulfonate) resins at constant V_p . For $D_{Ba^{2+}}$ at $V_p = 0.558$ the open symbols were obtained by extrapolation of the data at other V_p values.

domain boundaries.^{3,17} Consequently, if counterions moved along electrostatic equipotential paths close to the chains, $D_i^{(el)}$ in eq 2 should equal D_i^0 and, furthermore, the counterions would follow closely the contour of the resin chains so that the slowest counterions would block the paths to the fastest ones; i.e., since Ba^{2+} has the largest hydrated radius, D_i would decrease with $X_{Ba^{2+}}$.

In order to check this hypothesis, the $\log(D_i)$ values for sodium and barium ions in the heteroionic resins are plotted in Figure 4 against $V_p/(1 - V_p)$ according to eq 4. The slope of $\log(D_{Na^+})$ for the pure sodium resin is somewhat different from that in Figure 3 where all available data for poly(sodium styrenesulfonate) systems were plotted. This discrepancy is attributed to experimental uncertainties which are smoothed out when data in a wider V_p range are considered.

It is surprising to note that according to Figure 4 and Table III the data for $X_{Ba^{2+}} \leq 0.8$ give straight lines which are almost exactly parallel for each diffusing ion at all ionic compositions of the resin. The values of b_i reported in Table III indicate that this parameter in eq 4 depends on the nature of the moving ion but is independent of the particular ionic composition of the resin, an interesting conclusion which also supports our previous contention that the slope b_i in eq 4 has in these media a different meaning to that in the theory of Cohen and Turnbull.

The data for the pure barium resin do not fall on straight lines as illustrated in Figure 4. No satisfactory explanation could be found for this fact; a careful analysis of the corresponding runs make it unlikely that a systematic error may have affected the data.

A consequence of eq 1 and 2 is that the ratios

$$\frac{D_{Na^+}^{(el)}/D_{Na^+}^0}{D_{Ba^{2+}}^{(el)}/D_{Ba^{2+}}^0} = \frac{z_{Ba^{2+}}}{z_{Na^+}} = 2$$

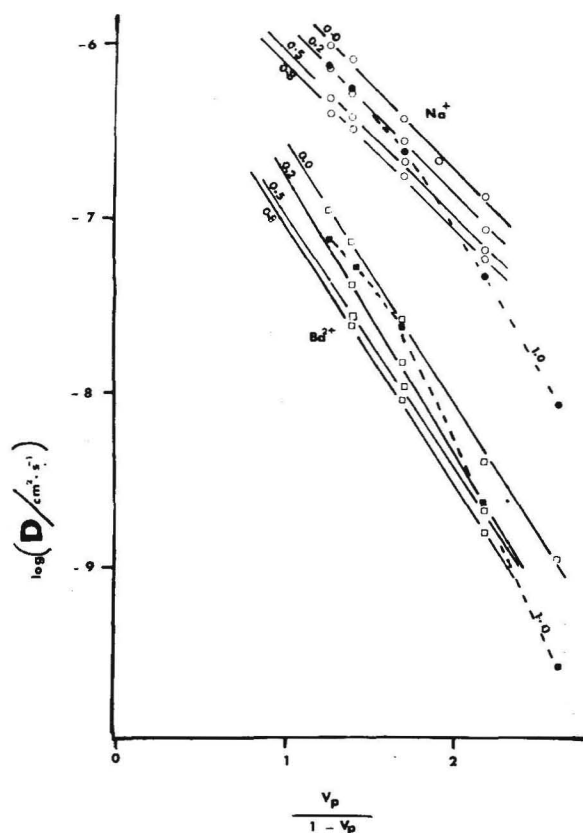


Figure 4. Tracer diffusion coefficients of Na^+ and Ba^{2+} against $V_p/(1 - V_p)$ in $\text{Na}^+/\text{Ba}^{2+}$ heteroionic poly(styrenesulfonate) resins. Full symbols correspond to $X_{\text{Ba}^{2+}} = 1.0$.

for each ionic composition. The ratios obtained from the lines drawn in Figure 4 are reported in Table III, the average value of the ratios being 1.7 ± 0.3 . This would imply that the electrostatic field around the chains is a relevant quantity in determining the diffusion of ions at high V_p values, but the value of Φ would not correspond to that calculated from theories that apply to dilute polyelectrolyte solutions.

Finally it is important to analyze whether it is possible to consider that the absolute mobility of the ions in the resins at high V_p is the same as that in pure water, i.e., that D_i^0 in eq 2 is the tracer diffusion coefficient of ion i at infinite dilution. There are a variety of data on the activation energy for ionic mobilities in resins which show in general that these are of the same order of magnitude as in pure water, except when the diffusing species is large enough to be affected by a sieve effect. In Table IV some recent activation energy data for ionic transport in poly(styrene) resins are compared to those in water; column two of the Table IV gives the degree of cross linking of the resins. It may be observed that the activation energies are only slightly larger than in water except for I^- and for NMe_4^+ ; for the latter ion Boyc¹⁹ considers that sieve effect is operative and responsible for the rather large activation energy.

When the data in Table IV are compared to those for alkali metal ions in glasses²¹ which are several times larger, they seem to indicate that the mechanism of transport in ion-exchange resins is akin to that in water and quite different from those in anhydrous ionic viscoelastic media.

Conclusions

(1) The variation of ionic tracer diffusion coefficient in ion-exchange resins with V_p is well represented by eq 4.

TABLE III: Counterion Tracer Diffusion Coefficients in Heteroionic Resins and Parameters of the Equation: $D_i = D_i^{(el)} \exp(-b_i V_p/(1 - V_p))$ ^a

$X_{\text{Ba}^{2+}}$	b_{Na^+}	$b_{\text{Ba}^{2+}}$	$\frac{D_{\text{Na}^+}^{(el)}/D_{\text{Na}^+}^0}{D_{\text{Ba}^{2+}}^{(el)}/D_{\text{Ba}^{2+}}^0}$
0.0	2.3	3.45	1.46
0.2	2.3	3.65	1.43
0.5	2.3	3.45	1.87
0.8	2.3	3.45	1.98
			1.7 ± 0.3

$$^a D_{\text{Na}^+}^0 = 1.333 \times 10^{-5} \text{ cm}^2 \text{ s}^{-1}; D_{\text{Ba}^{2+}}^0 = 0.846 \times 10^{-5} \text{ cm}^2 \text{ s}^{-1}$$

TABLE IV: Activation Energies of Ionic Mobilities in Poly(styrene) Type Resins

Ion	% cross linking	E^\ddagger	$E^\ddagger_{\text{H}_2\text{O}}^a$	Ref
Na^+	8	5.2	4.20	19
Na^+	30	5.3 ₉	4.20	18
Cs^+	30	4.15	3.65	18
Sr^{2+}	30	4.82	4.76	18
Mg^{2+}	30	4.87	4.48	18
NMe_4^+	8	7.0	3.46	19
Cl^-	4	2.51	3.92	20
Cl^-	8	3.56	3.92	20
Cl^-	16	5.17	3.92	20
I^-	6	8.7	3.84	20

^a Calculated from the conductivity at infinite dilution data in R. A. Robinson and R. H. Stokes in "Electrolyte Solutions", Butterworths, London, 1959.

(2) The slope b_i in eq 4 depends on the nature of the moving ion and not on the nature of the ionic matrix of the resin. Thus eq 1 becomes

$$D_i = D_i^{(el)} f(b_i, V_p) \quad (5)$$

(3) The electrostatic predictions of polyelectrolyte theories are not met in heteroionic resins at large V_p . However, the electrostatic potential still plays an important role.

(4) The activation energy data for ionic transport in resins suggests that the real friction coefficient is closely related to that in dilute aqueous solutions.

Acknowledgment. We thank the Consejo Nacional de Investigaciones Científicas y Técnicas (Argentina) for partial financial support.

References and Notes

- (1) J. A. Marinsky, *J. Phys. Chem.*, **71**, 4349 (1967).
- (2) M. J. Pikal and G. E. Boyd, *J. Phys. Chem.*, **77**, 2918 (1973).
- (3) G. S. Manning, *J. Chem. Phys.*, **46**, 2324 (1967).
- (4) R. Fernández-Prini and A. E. Lagos, *J. Polym. Sci.*, **2A**, 2917 (1964).
- (5) G. S. Manning, *J. Chem. Phys.*, **51**, 924, 934 (1969).
- (6) A. Katchalsky, Z. Alexandrowicz, and O. Kedem in "Chemical Physics of Ionic Solutions", B. E. Conway and R. G. Barradas, Ed., Wiley, New York, N.Y., 1966, p 295; A. Katchalsky, *Pure Appl. Chem.*, **26**, 327 (1971).
- (7) J. M. Mackie and P. Meares, *Proc. R. Soc. London, Ser. A*, **232**, 498 (1955).
- (8) A. E. Lagos, Thesis, University of London, 1960; A. E. Lagos and J. A. Kitchener, *Trans. Faraday Soc.*, **56**, 1245 (1960).
- (9) E. O. Timmermann, *Z. Phys. Chem. (Frankfurt am Main)*, **70**, 195 (1970); **72**, 140 (1970).
- (10) R. Fernández-Prini and A. L. Obaid, submitted for publication.

- (11) H. W. Oosterhoudt, *J. Phys. Chem.*, **78**, 408 (1974).
 (12) A. Despić and G. J. Hills, *Trans. Faraday Soc.*, **53**, 1262 (1957).
 (13) A. Yasuda, C. E. Lamze, and L. D. Ikenberry, *Makromol. Chem.*, **118**, 19 (1968).
 (14) M. H. Cohen and D. Turnbull, *J. Chem. Phys.*, **31**, 1164 (1959).
 (15) M. Rinaudo, B. Loiseleur, M. Milas, and P. Varoqui, *C. R. Acad. Sci.*, **272**, 1003 (1971).
 (16) B. A. Soldano and G. E. Boyd, *J. Am. Chem. Soc.*, **75**, 6107 (1953).
 (17) S. Lifson and J. L. Jackson, *J. Chem. Phys.*, **36**, 2410 (1962).
 (18) J. H. B. George, R. A. Horne, and C. R. Schlaikjer, *J. Electrochem. Soc.*, **117**, 892 (1970).
 (19) G. E. Boyd, *J. Phys. Chem.*, **78**, 735 (1974).
 (20) M. D. Kalinina and N. I. Nikolaev, *Russ. J. Phys. Chem.*, **45**, 1290 (1971).
 (21) G. L. McVay and D. E. Day, *J. Am. Ceram. Soc.*, **53**, 508 (1970); J.-P. Lacharme, *C. R. Acad. Sci.*, **270**, 1350 (1970).
 (22) Yasuda assumed this fraction to be the weight fraction of water, while we have taken it as equal to $(1 - V_p)$, the volume fraction of water.

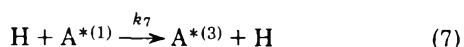
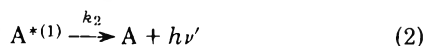
COMMUNICATIONS TO THE EDITOR

Multiplicity of the Reacting State in the Photoaddition of Carbon Tetrachloride to Anthracene

Publication costs assisted by the National Institutes of Health

Sir: The photochemical addition of carbon tetrachloride to anthracene has been known for some time.¹ Although it has been assumed to be a reaction occurring from the excited singlet state of anthracene,¹⁻³ Hardwick concluded from flash spectroscopic studies of triplet quenching⁶ that the reaction is very likely to take place entirely from the anthracene triplet state.⁷

Because of our interest in quenching of excited triplet states⁸ and in heavy atom elucidation of photochemical and photophysical processes,^{9,10} we have investigated the photoaddition of carbon tetrachloride to anthracene in benzene solutions containing varying concentrations of bromobenzene as a heavy atom additive. Assuming that the only effect of bromobenzene is to convert anthracene excited singlets to triplets,¹¹ the following kinetic scheme may be written for the case in which the photoaddition takes place from the anthracene singlet state.¹²



If this formulation is correct, the Stern-Volmer slope for bromobenzene quenching of anthracene fluorescence (from plots of F'/F vs. [bromobenzene], where F' and F are the fluorescence intensities (both in the presence of CCl_4) in the absence and presence of bromobenzene, respectively) and the Stern-Volmer slope for bromobenzene quenching of anthracene disappearance (from plots of Φ_d'/Φ_d vs. [bromobenzene], where Φ_d' and Φ_d are the disappearance quantum yields in the absence and presence of bromobenzene, respectively) should be the same.

Using solutions of 2.4×10^{-3} M anthracene and 0.13 M CCl_4 in benzene, with bromobenzene concentrations of 0, 1.2, 1.52, 1.9, and 2.3 M and following the photochemical reaction by monitoring the decrease of anthracene absorbance at 378 nm, we observed a Stern-Volmer slope of 0.68 M^{-1} (standard deviation, 0.02) for fluorescence quenching and a Stern-Volmer slope of 0.72 M^{-1} (standard deviation, 0.06) for reaction quenching. Since these slopes are the same within experimental error, we conclude that the photochemical reaction of anthracene with carbon tetrachloride takes place entirely from the singlet state of anthracene.

At our experimental concentrations we observed a 480- μs lifetime for the anthracene triplet in the absence of carbon tetrachloride and a k_q for CCl_4 quenching of anthracene triplets of $1.5 \times 10^4 \text{ M}^{-1} \text{ s}^{-1}$, in good agreement with the k_q value determined by Hardwick.⁶ At the CCl_4 concentration used in this study, half of the anthracene triplets were quenched by carbon tetrachloride. Since photochemical adduct formation does not appear to follow, we conclude that the net result of triplet quenching is enhanced radiationless decay of the triplet excited state.

Charge transfer interactions have been proposed in the CCl_4 quenching of naphthalene triplets by Schulte-Frohlinde.¹³ In the present case, an electron transfer complex can be calculated from the equation of Weller¹⁴ and from anthracene and CCl_4 redox data¹⁵ to lie 1.97 ± 0.1 eV above the ground state. Since this is slightly higher than the 1.82-eV energy of the anthracene triplet, electron transfer would require thermal activation. In that case homolysis of the C-Cl bond, which is thought to lead to adduct formation,^{1,2} may be less likely than other processes which lead to ground states.

This study provides another example of the elucidation of photochemical reactions through the use of heavy atom effects.¹⁶ The technique should find use in still other investigations.

Acknowledgment. This work was supported by a National Institutes of Health Research Grant (GM 15238).

References and Notes

- (1) E. J. Bowen and K. K. Rohatgi, *Discuss Faraday Soc.*, **14**, 146 (1953), and references therein.
- (2) M. I. Ivanoff, *Bull. Soc. Chim. Belg.*, **71**, 759 (1962).
- (3) Oster⁴ has presented results which suggest that diphenylanthracene gives radicals from CCl₄ quenching of the singlet excited state only, but that both excited singlet and triplet states of benzene react with CCl₄ to produce radicals. Results for anthracene are not explicitly given. See also the discussion of Birks.⁵ We thank a referee for pointing out these references.
- (4) G. K. Oster, *Acta Phys. Polon.*, **26**, 435 (1964).
- (5) J. B. Birks, "Photophysics of Aromatic Molecules", Wiley-Interscience, New York, N.Y., 1970, pp 439-441.
- (6) S. Kusuhara and R. Hardwick, *J. Chem. Phys.*, **41**, 2386 (1964).
- (7) S. Kusuhara and R. Hardwick, *J. Chem. Phys.*, **41**, 3943 (1964).
- (8) J. K. Roy, F. A. Carroll, and D. G. Whitten, *J. Am. Chem. Soc.*, **96**, 6349 (1974).
- (9) A. R. Gutierrez and D. G. Whitten, *J. Am. Chem. Soc.*, **96**, 7128 (1974).
- (10) (a) F. A. Carroll and F. H. Quina, *J. Am. Chem. Soc.*, **98**, 1 (1976); (b) F. H. Quina, Z. Hamlet, and F. A. Carroll, submitted for publication.
- (11) For evidence supporting this assumption, see T. Medinger and F. Wilkinson, *Trans. Faraday Soc.*, **61**, 620 (1965).
- (12) The dimerization of anthracene is also included as a singlet process: cf. E. J. Bowen, *Adv. Photochem.*, **1**, 23 (1963).
- (13) S. Ander, H. Blume, G. Heinrich, and D. Schulte-Frohlinde, *Chem. Commun.*, 745 (1968).
- (14) H. Knibbe, D. Rehm, and A. Weller, *Ber. Bunsenges. Phys. Chem.*, **72**, 267 (1968).
- (15) C. K. Mann and K. K. Barnes, "Electrochemical Reactions in Non-Aqueous Systems", Marcel Dekker, New York, N.Y., 1970.
- (16) For related applications, see F. Wilkinson and J. T. Dubois, *J. Chem. Phys.*, **48**, 2651 (1968); R. B. Cundall, D. A. Robinson, and A. J. R. Voss, *J. Photochem.*, **2**, 239 (1973-1974); W. I. Ferree, Jr., B. F. Plummer, and W. W. Schloman, Jr., *J. Am. Chem. Soc.*, **96**, 7741 (1974); R. H. Fleming, F. H. Quina, and G. S. Hammond, *ibid.*, **96**, 7738 (1974); D. O. Cowan and J. C. Koziar, *ibid.*, **97**, 249 (1975); A. Gupta, R. J. Kelley, E. M. Evleth, and G. S. Hammond, *J. Chem. Phys.*, **63**, 5496 (1975).
- (17) Department of Chemistry, Davidson College, Davidson, N.C. 28036.

Department of Chemistry
University of North Carolina
Chapel Hill, North Carolina 27514

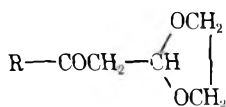
Felix A. Carroll*¹⁷
David G. Whitten*

Received February 23, 1976

Effect of Ring Closure on the Diamagnetic Susceptibility Contributions of Oxygen Atoms

Sir: The present study of the diamagnetic susceptibility of cyclic β-ketoacetals was undertaken to reveal how the contribution of an oxygen atom to the total diamagnetic susceptibility is affected when a second oxygen atom is attached to the same carbon atom.

Cyclic alkyl β-ketoacetals were synthesized by the standard methods³ and their diamagnetic susceptibilities (all the sus-



ceptibility values are in -10⁻⁶ cgs units) were measured with a sensitive Gouy balance calibrated with a number of standard substances. The accuracy of the determination of the Gouy

TABLE I: Diamagnetic Susceptibility of Cyclic β-Ketoacetals

R	Expt	Calcd		χ _O
		From Baudet's method ^a	From Haberditzl's method ^b	
CH ₃	70.45	80.96	69.80	3.45
C ₂ H ₅	82.01	92.35	81.15	3.55
n-C ₃ H ₇	93.88	103.66	92.50	3.56
n-C ₃ H ₁₁	116.19	126.36	115.20	3.60

^a References 4 and 5. ^b Reference 6.

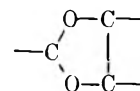
force was on the order of ±0.05 mg and reproducibility of the results was quite satisfactory. The Gouy tube was hung in such a manner that its one end remained in the field so that the susceptibility may be calculated by the well established method. χ_M values of these compounds have also been calculated by Baudet's wave mechanical method^{4,5} and the data are recorded in Table I. χ_M is given by the relation

$$\chi_M(\text{theor}) = \chi_{BE} + \chi_{ISE} + \chi_{NBE} + \chi_{\pi \text{ electrons}}$$

where BE, ISE, and NBE represent bonding electrons, inner shell electrons, and nonbonding electrons, respectively. The near constancy of the deviation for the homologous series suggests that the factor which is responsible for the deviation may be common and contributing almost to the same extent in these compounds. The reason for the poor agreement between the experimental and calculated χ_M values is that the contributions of the electrons in different states do affect diamagnetism and have not been fully accounted for in theoretical calculation.

Haberditzl⁶ has modified Baudet's method and has taken into account the contribution of the electrons in different states. χ_M values calculated by Haberditzl's method show a good agreement between the calculated and experimental χ_M values (Table I).

The diamagnetic contribution of the oxygen atoms present in the form



has been calculated taking the most reliable values as χ_{CH₂} = 11.36, χ_{CH₃} = 13.36, χ_{CH} = 9.36, and χ_{CO} = 6.75 in ketones² and following the additivity rule, χ_{O(av)} in this class of compounds is 3.5 against χ_O = 5.3⁷ in alcohols and ether; χ_O = 5.4 for glycols;¹ and χ_O = 4.7 for alkyl noncyclic β-keto acetals, R-CO-CH₂-CH(OR')₂.

These values indicate that ring closure is primarily responsible for the low value of χ_O in cyclic acetals, rather than the fact that a second oxygen is attached to the same carbon atom.

Acknowledgment. The author expresses his sincere thanks to Professors R. C. Mehrotra, K. C. Joshi, and J. N. Gaur for providing facilities in this department.

References and Notes

- (1) R. R. Gupta, Ph.D. Thesis, Rajasthan University, Jaipur, 1968.
- (2) R. L. Mital and R. R. Gupta, *Indian J. Chem.*, **8**(4), 369 (1970).
- (3) A. E. Pohl and W. R. Benson, *Chem. Rev.*, **66**, 161 (1966).
- (4) J. Baudet, *J. Chim. Phys.*, **58**, 228 (1961).
- (5) J. Baudet, J. Tillieu, and J. Guy *C. R. Acad. Sci.*, **224**, 2920 (1957).
- (6) W. Haberditzl, *Sitzungsber. Dtsch. Akad. Wiss. Berlin, Kl. Chem. Geol. Biol.*, No. 2, 34 (1964).
- (7) E. W. Abel, R. P. Bush, C. R. Jenkins, and T. Zobel, *Trans. Faraday Soc.*, **60**, 1214 (1964).

Department of Chemistry
University of Rajasthan
Jaipur-4, India

R. R. Gupta

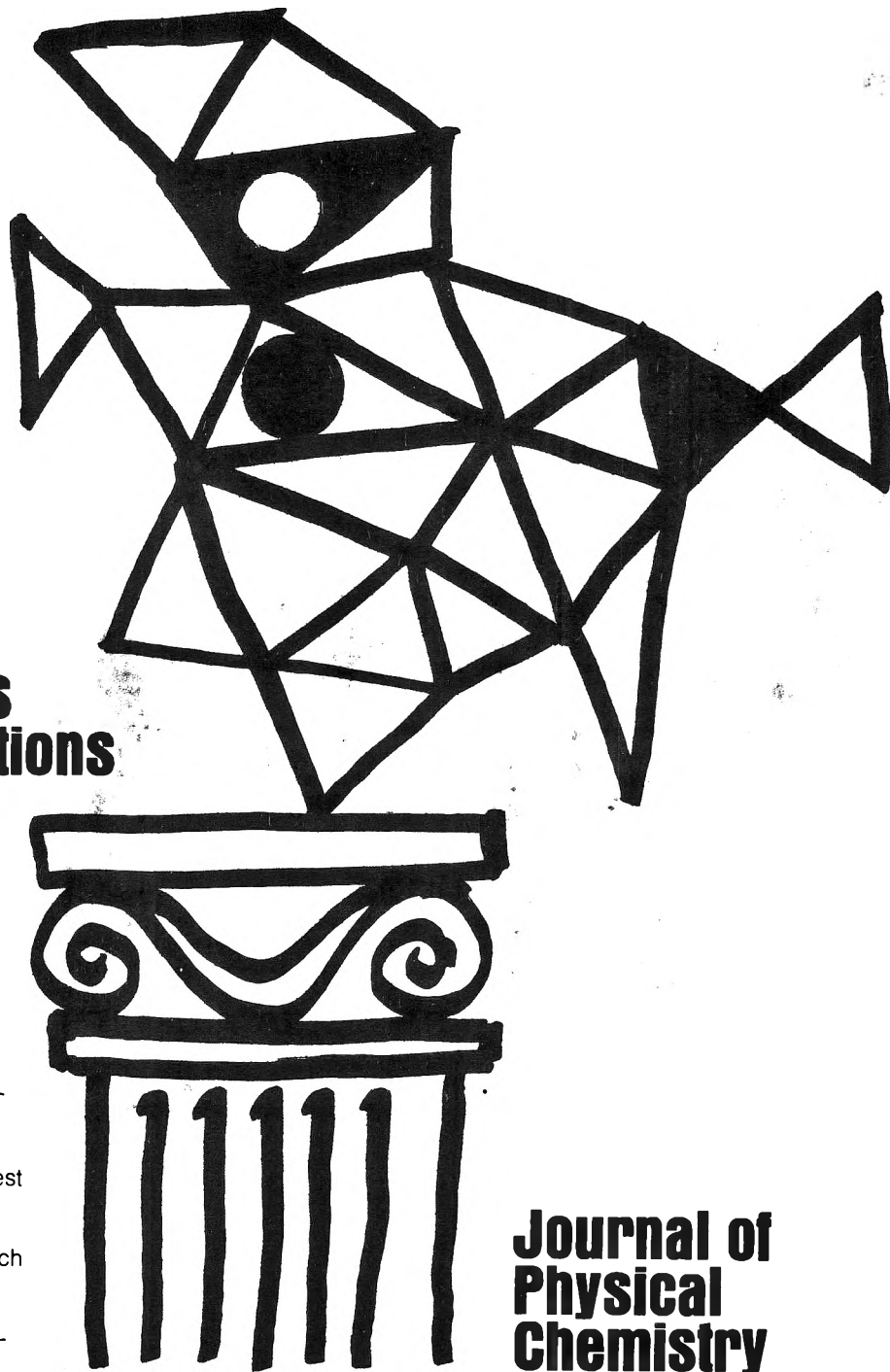
Received June 9, 1975, Revised Manuscript Received May 13, 1976

**New concepts
new techniques
new interpretations**

**... together
with valuable reports
on classical areas**

They are all waiting for you between the covers of our well-balanced JOURNAL OF PHYSICAL CHEMISTRY. Whatever your particular interest in physical chemistry, you'll find the JOURNAL's broad range of experimental and theoretical research reports are relevant and beneficial to your work. Each biweekly issue brings you an average of 30 authoritative, comprehensive reports on fundamental aspects of atomic and molecular phenomena, as well as timely notes, communications and reports plus the proceedings of selected symposia.

Join your fellow physical chemists who rely on JPC as an excellent biweekly source of data in both new and classical areas. Just complete and return the form to start your own subscription.



**Journal of
Physical
Chemistry**

**The Journal of Physical Chemistry
American Chemical Society**

1155 Sixteenth Street, N.W.
Washington, D.C. 20036

1976

Yes, I would like to receive the JOURNAL OF PHYSICAL CHEMISTRY at the one-year rate checked below:

	U.S.	Canada**	Latin America**	Other Nations**
ACS Member One-Year Rate*	<input type="checkbox"/> \$24.00	<input type="checkbox"/> \$30.25	<input type="checkbox"/> \$29.75	<input type="checkbox"/> \$30.25
Nonmember	<input type="checkbox"/> \$96.00	<input type="checkbox"/> \$102.25	<input type="checkbox"/> \$101.75	<input type="checkbox"/> \$102.25

Bill me Bill company Payment enclosed

Air freight rates available on request.

Name _____

Street _____

Home
Business

City _____

State _____

Zip _____

Journal subscriptions start January '76

*NOTE: Subscriptions at ACS member rates are for personal use only. **Payment must be made in U.S. currency, by international money order, UNESCO coupons, U.S. bank draft, or order through your book dealer.



... another ACS service

Important Additions

TO THE JOURNAL OF PHYSICAL AND CHEMICAL REFERENCE DATA.

Two comprehensive reference volumes, each, like the Journal itself, published by The American Institute of Physics, The National Bureau of Standards and The American Chemical Society . . . your triple assurance of their accuracy, immediacy, and usefulness.

SUPPLEMENT NO. 1 TO VOLUME 2

"Physical and Thermodynamic Properties of Aliphatic Alcohols"

by R. C. Wilhoit and B. J. Zwolinski, *Thermodynamics Research Center, Department of Chemistry, Texas A&M University.*

The most exhaustive review and critical analysis of selected physical and thermodynamic properties of aliphatic alcohols that has been published. Coverage of the important properties of the liquid, vapor, and ideal gaseous states as well as pertinent solid state data necessary for equilibrium calculations ordinarily encountered in chemical and chemical engineering applications. All available quantitative data on each property for each aliphatic alcohol are fully documented and critically analyzed providing a "data bank" for the 640 monohydroxy alcohols in the carbon range of C₁ to C₅₀. Internally consistent tables of critical, standard, or selected "best" values are tabulated for each compound. Index included.

SUPPLEMENT NO. 1 TO VOLUME 3

"Thermal Conductivity of the Elements: A Comprehensive Review"

by C. Y. Ho, R. W. Powell, and P. E. Lilly, *1974 Thermophysical Properties Research Center, Purdue University.*

Comprehensive review of the world's thermal conductivity data presents recommended or estimated values for all 105 elements. Reliable thermal

conductivity data for those elements which can be used as standard reference materials to calibrate or check apparatus. Original data, specimen characterization and measurement information for 5200 sets of raw data. Detailed discussions for each element, review of the available experimental data and considerations by which the authors arrived at final assessments. Complete bibliographic citations for 1658 references. Only original sources have been used. All cited documents are available at TPRC in standard microfiche.

Special Issue Sales

American Chemical Society
1155 16th St., N.W., Washington, D. C. 20036

Please send _____ copies of the 420 page supplement to the Journal of Physical and Chemical Reference Data, Volume 2, "Physical and Thermodynamic Properties of Aliphatic Alcohols," at the prices checked below.

Members: Hard cover edition: \$33.00
Nonmembers: Hard cover edition: \$33.00
Members: Soft cover edition: \$10.00
Nonmembers: Soft cover edition: \$30.00

Please send _____ copies of the 796 page supplement to the Journal of Physical and Chemical Reference Data, Volume 3, "Thermal Conductivity of the Elements: A Comprehensive Review," at the prices checked below.

Members: Hard cover edition: \$60.00
Nonmembers: Hard cover edition: \$60.00
Members: Soft cover edition: \$25.00
Nonmembers: Soft cover edition: \$55.00

Check or money order must accompany order. \$1.00 extra for foreign postage and handling.

Name _____

Address _____

City _____ State _____ Zip _____



American Chemical Society

18 02.2519